Nonlinear Vibrations Produced by Unbalanced Motors

Doctoral Thesis

Javier González Carbajal

Supervised by

Prof. Jaime Domínguez and **Prof. Daniel García**

Department of Mechanical and Manufacturing Engineering

Faculty of Engineering

University of Seville

March 2017

Contents

Acknowledgements

Tras estos cuatro años de tesis, estoy en deuda con muchas personas y me gustaría poder incluirlas a todas en este agradecimiento. Confío en que sepan disculparme las que, por falta de espacio o por mi despiste existencial, no aparezcan expresamente nombradas.

En primer lugar, quiero agradecer a mis directores, Jaime y Dani, todos sus buenos consejos y el clima de libertad que han propiciado desde el principio de este trabajo. Estoy convencido de que no podría haber tenido mejores maestros. Gracias también al profesor Emilio Freire, por orientarme sabiamente cuando me adentraba en terrenos matemáticos pantanosos.

I would like to express my gratitude to Professor Gaëtan Kerschen for my stay at the University of Liège. Working with his group was a wonderful research experience, in an environment which could not have been friendlier. Thanks to Peppe, who kindly contributed to correct typos in the thesis, Lionel, Thibaut, Chiara, Edouard, Vincent, Iván, Mirco and many more good friends that I hope to keep for many years and made my stay in Liège warm and enjoyable.

Thanks to Professor Jan A. Sanders, who was very willing to advise me about the attraction properties of averaged systems. His keen e-mail responses were truly helpful for the development of Chapter 5 in the thesis.

Gracias a Joselu, compañero de fatigas desde los míticos tiempos en que inventamos la rosca cuadrada, a Aceituno, Jorge Julio, Sergio, Merche, Juan, David y al resto de compañeros del departamento, porque ha sido una alegría poder trabajar rodeado de buenos amigos. Extiendo con gusto este agradecimiento al gran Guido, pese a su obsesión posesiva con el espacio de trabajo y con las papas fritas.

A Charly, Merchante, Diego, Ortega, Bill, Angelito, Andrés, Miguel, Yoshua, Koctel, Nacho, Derey, Valera y muchos más, por los buenos ratos y cervezas que una tesis necesita, aunque sigan pensando que la mía trata de tornillos.

A Marta, mi equipo alpha particular, que ha sabido animarme como nadie y hacerlo todo muy llevadero estos últimos meses.

Muchas gracias a mis padres, que son el mejor ejemplo que tengo, y a Pablo y Ana, por su apoyo y su cariño diarios. También al resto de mi gran familia, desde mis abuelas y abuelos hasta Julia y Rafilla. Este trabajo habría sido mucho más duro si no hubiera estado tan bien rodeado.

Y principalmente gracias a Dios, a quien le debo todo.

1 INTRODUCTION

The linear theory of vibrations is one of the most useful tools in the handbook of a mechanical engineer. It furnishes a solid and well-established mathematical framework for concepts such us *resonance* and *linear modes* of vibration, which are central for the modal analysis of structures and mechanical systems.

A most appealing quality of this linear theory is its relative simplicity. Linear models exhibit special attributes which make them particularly useful from a practical point of view, such us the principle of superposition –whereby the response to a linear combination of excitations can be obtained as the linear combination of individual responses– or the fact that several attractors never coexist –the stationary motion of a forced, damped, linear system, is independent of the initial conditions–. It is thanks to these properties, together with the fact that many real structures are well represented by linear models in their ranges of operation,

that linear vibration analysis has become a chief tool in the design of mechanical systems and structures in industry.

However, linearity is clearly an idealization. Nature is not linear in general, although it can be approximately represented by linear models in some cases. For instance, the linear theory of elasticity is known to give good results for structures undergoing small displacements and small strains. However, as soon as displacements become significant, nonlinear effects need to be considered (Luongo, Rega, & Vestroni, 1986). Some other possible sources of nonlinearity in mechanical systems are (Thomsen, 2003)

- Material nonlinearities due to a nonlinear relation between stresses and strains in some materials.
- Nonlinear body forces, such as magnetic or aerodynamic interactions.
- Nonlinearities due to the physical configuration, such as those associated to discontinuous couplings, clearances or stops.

Nonlinearity plays a key role in the dynamic behaviour of numerous real-world applications. Some examples are the motion of large wind turbines, the crashworthiness of vehicles or the vibrocompaction of granular materials. The aeronautical industry, with great interest in minimizing weight, is increasingly producing very light and slender structures, with the subsequent activation of geometrical nonlinearities. The use of materials such as carbon-fiber composites in aerospace applications can also produce a significant deviation from linearity. It is evident that, in all these situations, a linearized model would not be able to capture the real system dynamics. Thus, in order to have reliable predictions, nonlinearity would need to be included in the model, which in turn implies entering the complex field of nonlinear dynamics.

Nonlinear dynamics is the branch of mathematics which intends to uncover the temporal evolution of nonlinear dynamical systems. Unlike its linear counterpart, nonlinear dynamics is not a closed subject –not even a mature one–. The main reason is that, while all linear systems are essentially the same, each nonlinear

system is nonlinear in its own way. This means that, in general, conclusions about the behaviour of a particular nonlinear system cannot be generalized to any other. Besides, the dynamics of nonlinear systems is extremely rich, exhibiting a wide range of phenomena which cannot occur in linear systems, such as multistability, chaos or limit cycles. All this complexity renders it extremely hard to obtain analytical solutions to the nonlinear differential equations governing the system dynamics. In general, it is necessary to resort to numerical computations in order to get some insight into the system behaviour.

From the above considerations, it is clear that a significant research effort needs to be oriented to a better comprehension of the dynamic behaviour of nonlinear mechanical systems. This will hopefully lead to efficient predictions about the performance of systems where nonlinearity has a significant effect, and will also motivate the design and development of new nonlinear components which are able to outperform their linear counterparts. It is the aim of this thesis to contribute to this general objective, by analysing in detail a particular class of nonlinear systems, namely those excited by unbalanced motors.

The motion of unbalanced rotors constitutes one of the most common vibration sources in mechanical engineering (Boyaci, Lu, & Schweizer, 2015; Yang et al., 2016). Vibrations due to unbalance may occur in any kind of rotating systems, such as turbines, flywheels, blowers or fans (Shabana, 1996). Actually, in practice, rotors can never be completely balanced because of manufacturing errors such as porosity in casting, non-uniform density of the material, manufacturing tolerances, etc. (Xu & Marangoni, 1994). Even a subsequent balancing process will never be perfect due to the tolerances of the balancing machines. Moreover, some amount of unbalance generally appears during the operation of the machine, as a consequence of uneven wear, corrosion or unequal build-up of deposits (dirt, lime, etc.).

Usually, rotor unbalance has a harmful effect on rotating machinery, since vibration may damage critical parts of the machine, such as bearings, seals, gears and couplings (Xu & Marangoni, 1994). However, there are applications where

unbalanced rotors are used to generate a desired vibration. Some examples are the feeding, conveying and screening of bulk materials, or the vibrocompaction of quartz agglomerates, which makes use of unbalanced motors to compact a quartz-resin mixture.

A simple 2-DOF model to analyse the dynamic response of a structure to the excitation produced by an unbalanced motor is sketched in Fig. 1.1. The simplest approach to this problem consists in assuming the rotor speed to be either constant or a prescribed function of time. In the constant speed case, the centrifugal force of the unbalance produces a harmonic excitation on the vibrating system, whose amplitude scales with the square of the rotating speed and whose frequency coincides with the rotating speed (Shabana, 1996; Thomson, 1996).

Note that, with this approach, it is implicitly being assumed that the rotational motion of the motor is independent of the vibration of the structure. This property is what defines an ideal excitation: it remains unaffected by the vibrating system response. Thus, the amplitude and frequency of an ideal excitation are known a priori, before solving the vibration problem. Obviously, this notion of ideality is applicable to any kind of excitation, and not only to the one produced by an unbalanced motor.

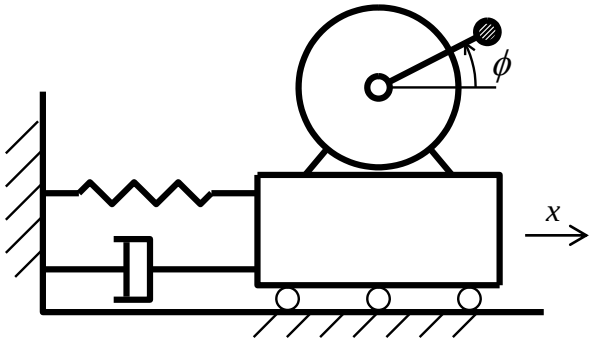

Fig. 1.1 Simple 2-DOF model of a structure excited by an unbalanced motor

1.1 State of the Art

The ideality assumption is valid, with good approximation, in many real problems. However, there are situations where it is not. In 1904, Sommerfeld (Sommerfeld, 1904), whose pioneering work inspired many subsequent investigations, found experimentally kinds of behaviour which could not be explained upon the ideality hypothesis. He mounted an unbalanced electric motor on an elastically supported table and monitored the input power as well as the frequency and amplitude of the response (Nayfeh & Mook, 1995). The experiment consisted in increasing continuously the power input in order to make the rotor speed pass through the resonance frequency of the table. When the rotor speed was close to resonance, an increment of the input power produced only a very slight increase in the rotor speed, while the oscillation amplitude increased considerably. This means that, in this part of the experiment, the increasing input power was not making the motor rotate faster, but was giving rise to larger oscillations. With larger increase of the input power, the rotor speed jumped abruptly to a frequency above resonance and, at the same time, the vibration amplitude jumped to a much smaller quantity than measured in the resonance region. This anomalous behaviour is usually referred to as '**The Sommerfeld Effect**'.

The Sommerfeld effect is closely related to the more general notion of '**resonant capture**' (Quinn, Rand, & Bridge, 1995; Sanders, Verhulst, & Murdock, 2007). This phenomenon occurs when a nonlinear system becomes locked in the vicinity of a particular surface of the phase space, known as a 'resonance manifold', which usually corresponds to a critical value of one of the frequencies present in the system. The alternative, known as '**passage through resonance**', occurs when the system undergoes a transient motion near the resonance manifold and, after some time, it sets out towards the non-resonant region of the phase space.

In 1969, Kononenko (Kononenko, 1969) published a book entirely devoted to the study of nonideal excitations. He considered different configurations of vibrating systems excited by nonideal motors and applied the Averaging Method (Sanders et

al., 2007) to the equations of motion. By taking into account the two-way interaction between the motor and the vibrating structure, he was able to explain the Sommerfeld effect. After Kononenko, numerous investigations have been conducted in order to get more insight into the effect of nonideal excitations on mechanical systems.

An interesting real case of nonideal excitation was reported by Rand et al (Rand, Kinsey., & Mingori, 1992). The system is a dual-spin spacecraft, consisting of two bodies (platform and rotor) connected by a bearing assembly which allows relative rotation. When the spacecraft is first placed in orbit, platform and rotor rotate together with zero relative spin rate. Then, a 'despin maneuver' is initiated, where an internal motor provides a torque intended to increase the bearing axis component of the rotor angular speed, while decreasing the bearing axis component of the platform angular speed. Ideally, this continues until the platform is inertially nonrotating, yet some failures can interfere with the process, channelling the energy provided by the motor into motions other than the intended rotation. When this happens, the condition of the spacecraft after the despin maneuver becomes far from the desired state.

Rand et al. (Rand et al., 1992) investigated one of these possible failures, known as 'precession phase lock', which appears when the rotation of the rotor around the bearing axis becomes synchronized with the precession of the spacecraft around its angular momentum vector. They concluded that the equations describing the spacecraft dynamics are similar to those of an unbalanced motor attached to the fixed frame by a linear spring and driven by a constant torque.

Quinn et al. investigated approximate analytical methods to distinguish initial conditions leading to capture or passage through resonance (Quinn et al., 1995).

Dimentberg et al. analysed experimentally how to promote the passage through resonance by a sudden shift in the system stiffness (Dimentberg, Mcgovern, Norton, Chapdelaine, & Harrison, 1997). They also estimated the decrease in the needed

input power needed for a dynamic passage through resonance, with respect to a quasistatic passage.

Although the most usual analytical approach to the problem is based on averaging procedures, Blekhman (Blekhman, 2000) proposed an alternative approximation to the stationary solutions by using the method of 'Direct Separation of Motions', which shows some similarities with averaging. The main idea behind this technique consists in assuming the motion to be the sum of two terms, one of them evolving much faster than the other. Then, the system displacement is decomposed into a 'slow motion' and a 'fast motion'. By averaging over the fast time, the method allows including the effect of the fast motion into the slow dynamics of the system.

Fidlin (Fidlin, 2006) addressed a weakness of the asymptotic solutions obtained by averaging, namely the fact that approximate solutions near resonance are only valid for a short time scale. He proposed a hierarchic averaging procedure to enlarge the time validity of the approximations.

It should also be noted that some authors have found chaotic motions in systems excited by nonideal power sources (Belato, Weber, Balthazar & Mook, 2001; Krasnopolskaya & Shvets, 1993).

1.2 Motivation and Objectives

The present study of the dynamics of structures excited by unbalanced motors has been motivated by our interest in an industrial process where unbalanced motors are used to compact a quartz-resin mixture. In this process, manufacturers find some unexpected behaviours of the compacting machine, which yield an imperfect compaction of the mixture. It is clear that a good understanding and modelling of the process, including all relevant physical phenomena, would be extremely helpful to explain and avoid these adverse scenarios. Although the models studied and developed in this thesis are still far from being a reliable representation of real

vibrocompaction machines, some of the intrinsic nonlinearities of the real system have been considered, like the nonideal coupling between motor and vibrating structure in Chapters 3-7, and also impacts and a nonlinear constitutive law for the quartz-resin mixture in Chapter 8. Thus, the present work may be envisaged as a first step towards a more complex modelling of vibrocompaction processes.

The objectives of this doctoral thesis are

- Progressing further in the knowledge of the response of nonlinear vibrating systems to nonideal excitations, with special interest in the different kinds of stationary motions that can be found.
- Giving some first steps in modelling and simulating the vibrocompation of quartz agglomerates. Based on the developments of this thesis, some more realistic models will hopefully be constructed in the future, for the purpose of reliably predicting the effect of different factors (speed of the motors, value of the unbalance, granulometry of the mixture…) in the final result of the real process.

1.3 Organization of the Document

Most of this thesis (Chapters 3-7) is aimed at uncovering the behaviour of a 2-DOF system, which can be used to model unbalance-induced vibrations. It consists of an unbalanced motor attached to the fixed frame by a nonlinear spring and a linear damper. The driving torque produced by the motor is assumed to be given by its torque-speed curve, or motor characteristic. The relative simplicity of the model allows for an analytical treatment, based on searching for asymptotic approximations to the exact solutions. These analytical developments furnish much significant information about the system dynamics, which is validated through numerical simulations. After the analysis of this simplified model, a more complex one is considered which intends to be a more accurate representation of the vibrocompaction process of quartz agglomerates.

During the present investigation, it has been realized that the slope of the motor characteristic curve is a chief parameter of the problem. Actually, the system exhibits different behaviours, and requires different mathematical approaches, depending on the order of magnitude of this slope. Thus, two scenarios are analysed separately, depending on whether the slope is *large* (Chapters 3, 4) or *small* (Chapters 5, 6). Hence the document is organized as follows.

In Chapter 2, the main mathematical methods and techniques that are used throughout the thesis are introduced.

Chapter 3 addresses the equations of motion for the simplified system under study and states the assumptions on which the analysis is based, for the case of large slope characteristic. A new analytical approach to this problem is proposed, based on the application of the Singular Perturbation Theory, besides the Averaging Method. With this novel combination of two different perturbation techniques, the original 4D system is transformed into a reduced 2D system, much easier to analyse. The fixed points of this reduced system are obtained, and their stability is studied, finding conditions for the existence of Hopf bifurcations, which have not been reported before, to the best of the author's knowledge. The Hopf bifurcations are analysed in detail, and a simple criterion is encountered to distinguish whether the bifurcation is subcritical or supercritical. The Poincaré-Béndixson theorem is applied as well, in order to show that, under appropriate conditions, all system trajectories are attracted towards a stable limit cycle.

In Chapter 4, a number of numerical simulations are carried out, with the aim of validating the analytical results of Chapter 3 and investigating the global bifurcations which make the limit cycles disappear.

Chapter 5 presents the analytical treatment of the problem when the slope of the motor characteristic is small. Once again, averaging techniques are used to simplify the original system. However, the presence of a resonance manifold in the phase space enforces the construction of two different approximate systems, valid close (*inner region)* or far (*outer region)* from the resonance manifold, respectively. The

fixed points of both averaged systems are obtained and their stability is analysed. Admittedly, some of the developments of this Chapter are not totally new, but a reformulation of already published treatments of the problem. However, the stability of the stationary motions of the system near resonance was not totally solved hitherto. By using attraction arguments, a detailed stability analysis of these solutions is conducted.

Chapter 6 presents numerical results which validate the results and conclusions of Chapter 5.

In Chapter 7, an alternative approximate method is used to obtain the stationary solutions of the system studied in previous chapters. This approach is based on the Method of Direct Separation of Motions, proposed by Blekhman (Blekhman, 2000) and has the advantage of providing a graphical representation of the stationary motions which is highly convenient with a view to the vibrocompaction analysis of the next chapter. Furthermore, this alternative procedure provides a very clear graphical comparison between the cases of *large* and *small* slope considered in preceding chapters.

A new model is introduced in Chapter 8, more complex than the one analysed in previous chapters. This system is a first attempt to model the vibrocompaction process, which has not been done before, to the author's knowledge. In addition to the nonlinearity intrinsically associated to nonideality, the model includes contact and impacts between the mixture and the platform supporting the unbalanced motor, and also between the mixture and the mould where it is contained. Furthermore, a nonlinear constitutive law for the mixture, which allows modelling the compaction itself, is proposed. It is shown that, under some conditions, this model can be transformed into the simpler system analysed in Chapters 3-7, which makes the preceding analytical developments useful for the vibrocompaction analysis. Several numerical simulations illustrate how the proposed model can be used to investigate the effect of different parameters on the final level of compaction achieved.

Finally, Chapter 9 summarises the conclusions of this work and proposes possible further investigations.

2 MATHEMATICAL METHODS

Before the analysis of the problem under study, a brief description of the mathematical methods used within the thesis is presented.

2.1 First Order Averaging

Perturbation methods constitute a broad class of mathematical techniques aimed at finding approximate solutions to a problem, based on the solution of a simpler related problem. In particular, averaging procedures are among the most widely used perturbation methods, presenting two relevant strengths (Sanders et al., 2007):

- They are supported by rigorously proved theorems.
- They can be systematically extended to any order of accuracy.

In order to understand the basic idea behind averaging, consider a system of the form $\dot{\boldsymbol{x}} = \epsilon \boldsymbol{f}(\boldsymbol{x}, t)$, where ϵ is a small parameter and $\boldsymbol{f}$ is T-periodic in t. The

dynamics of such systems contains two different time scales: a fast scale, associated to the fact that $\boldsymbol{f}$ depends on t, and a slow scale, associated to the fact that $\boldsymbol{x}$ is a slow variable ($\dot{\boldsymbol{x}} = O(\epsilon)$). Then, it can be shown that the essential features of the system are maintained when it is replaced by its corresponding averaged system $\dot{\boldsymbol{z}} = \epsilon \frac{1}{T} \int_0^T \boldsymbol{f}(\boldsymbol{z}, s) ds = \epsilon \bar{\boldsymbol{f}}(\boldsymbol{z})$. The idea is to take into account the mean effect of the fast oscillatory dynamics through averaging, so that the second system retains the long term behaviour of the first one. This transformation is useful because the averaged system is autonomous and, therefore, considerably easier to analyse than the non-autonomous original system.

Although the above description has been given for averaging over time, it is sometimes useful to average over fast rotating angles, which play essentially the same role as time. Once the intuitive idea has been explained, some more rigorous results are now given, which will be used throughout the thesis.

Then, consider an initial value problem of the form

$$\left.\begin{matrix} \dot{\boldsymbol{x}} = \epsilon \boldsymbol{X}(\boldsymbol{x}, \phi) \\ \dot{\phi} = \Omega^0(\boldsymbol{x}) + \epsilon \Omega^1(\boldsymbol{x}, \phi) \end{matrix}\right\}, \qquad \begin{matrix} \boldsymbol{x}(0) = \boldsymbol{x}_0 \\ \phi(0) = \phi_0 \end{matrix}, \qquad \begin{matrix} \boldsymbol{x} \in D \subset \mathbb{R}^n \\ \phi \in S^1 \end{matrix} \tag{2.1}$$

where $\boldsymbol{x}$ is a vector of slow variables, ϕ is a fast rotating phase and ϵ is a sufficiently small, positive, dimensionless parameter, $0 < \epsilon \ll 1$. Note that S^1 represents the circumference. Hence to say that $\phi \in S^1$ merely means that $\phi \in \mathbb{R}$, with functions $\boldsymbol{X}$ and Ω^1 being 2π-periodic in ϕ.

Let z be the solution of

$$\dot{\boldsymbol{z}} = \epsilon \bar{\boldsymbol{X}}(\boldsymbol{z}), \quad \boldsymbol{z}(0) = \boldsymbol{x}_0, \tag{2.2}$$

where

$$\overline{\boldsymbol{X}}(\cdot) \equiv \frac{1}{2\pi}\int_0^{2\pi} \boldsymbol{X}(\cdot,\varphi)d\varphi \,. \tag{2.3}$$

Then, if $\boldsymbol{z}(t)$ remains in $D_0 \subset D$,

$$\boldsymbol{x}(t) = \boldsymbol{z}(t) + O(\epsilon), \qquad \text{for } t = O(1/\epsilon). \tag{2.4}$$

The proof can be found in (Sanders et al., 2007).

This is the standard version of the theorem for first order averaging over angles. Note that, thanks to this theorem, an asymptotic approximation to the solution $\boldsymbol{x}(t)$ can be obtained by replacing the original system (2.1) with the approximate system (2.2). In other words, it is possible to reduce the system dimension, from $n+1$ to n, upon averaging over the fast rotating phase.

Note also that, as explicitly stated in (2.4), the approximation obtained through averaging is only valid during a limited time scale. This is a general feature of perturbation approaches, which can be overcome in some situations (e.g. when attraction exists, as described later on in this section). The limitation in the time scale where the approximation is valid will prove to be crucial in Section 5.2.

Generalization to multi-frequency systems

The generalization of this theorem to multi-frequency systems is straightforward (Sanders et al., 2007). The only caveat that needs to be taken into account is that function $\boldsymbol{X}$ must be written as a sum of functions, each of one depending on only one of the fast angles. Thus, consider the multi-frequency system given by

$$\left\{\begin{matrix} \dot{\boldsymbol{x}} = \epsilon\boldsymbol{X}(\boldsymbol{x},\boldsymbol{\phi}) \\ \dot{\boldsymbol{\phi}} = \boldsymbol{\Omega}^0(\boldsymbol{x}) + \epsilon\boldsymbol{\Omega}^1(\boldsymbol{x},\boldsymbol{\phi}) \end{matrix}\right\}, \quad \begin{matrix} \boldsymbol{x}(0) = \boldsymbol{x}_0 \\ \boldsymbol{\phi}(0) = \boldsymbol{\phi}_0 \end{matrix}, \quad \begin{matrix} \boldsymbol{x} \in D \subset \mathbb{R}^n \\ \boldsymbol{\phi} \in \mathbb{T}^m \end{matrix}, \tag{2.5}$$

where $\mathbb{T}^m$ represents the m-torus. Then, assuming that function $\boldsymbol{X}$ can be written as

$$\boldsymbol{X}(\boldsymbol{x},\boldsymbol{\phi}) = \sum_{i=1}^{m} \boldsymbol{X}_i(\boldsymbol{x},\phi_i), \tag{2.6}$$

the first order averaged system can be obtained as

$$\dot{\boldsymbol{z}} = \epsilon \sum_{i=1}^{m} \bar{\boldsymbol{X}}_i(\boldsymbol{z}), \quad \boldsymbol{z}(0) = \boldsymbol{x}_0, \tag{2.7}$$

with $\bar{\boldsymbol{X}}_i$ defined as in (2.3). Then, the error estimate is given by

$$\boldsymbol{x}(t) = \boldsymbol{z}(t) + O(\epsilon), \quad \text{for } t = O(1/\epsilon). \tag{2.8}$$

This multi-frequency version of the theorem will be used in Section 5.1.

The concept of 'Resonance Manifold'

A crucial point of this averaging process is that, for the approximation to be valid, each frequency $\Omega_i^0(\boldsymbol{x})$ must be bounded away from zero. The reason is that, when any $\Omega_i^0(\boldsymbol{x})$ approaches zero, a vanishing denominator appears in the higher order terms of eqs. (2.4) and (2.8). (This will be seen clearly in equation (2.12) of Section 2.2.)

The sets of $\boldsymbol{x}$ for which one or more functions $\Omega_i^0(\boldsymbol{x})$ vanish are called '**resonance manifolds**'. The failure of averaging in the vicinity of resonances can be easily understood by noticing that, near a resonance manifold, one or more angles $\boldsymbol{\phi}_i$ are not fast and, consequently, we cannot average over them.

The main consequence is the following: away from resonances, it is possible to average over all angles. However, in the vicinity of a resonance manifold, we can only average over particular angles, namely those whose frequencies remain bounded away from zero. This distinction will be necessary in Chapter 5.

Averaging with Attraction

Asymptotic approximations obtained by averaging are, in general, valid on a time scale $1/\epsilon$. However, this time scale can be enlarged if there exists attraction in the averaged system (Sanders et al., 2007).

Consider again a system of the form (2.1), with averaged system (2.2).

Suppose $\boldsymbol{z} = \boldsymbol{a}$ is an asymptotically stable fixed point of system (2.2), with domain of attraction $D_0 \subset D$. Then, for all $\boldsymbol{x}_0 \in K \subset D_0$, it can be shown that

$$\boldsymbol{x}(t) = \boldsymbol{z}(t) + O(\epsilon), \qquad \text{for } t \in [0, \infty) \tag{2.9}$$

Thus, the approximation is uniformly valid –i.e. valid for all time– for solutions of the averaged system which are attracted by an asymptotically stable fixed point. Two different proofs of this theorem have been given by Sánchez-Palencia (Sanchez-Palencia, 1975) and Eckhaus (Wiktor Eckhaus, 1975).

A similar result holds for trajectories of the averaged system which are attracted by an asymptotically stable limit cycle. In this case, the approximate solution is valid on $t \in [0, \infty)$ for all variables except the angular one, i.e. the variable which measures the flow on the closed orbit (Sanders et al., 2007). This is equivalent to say that the closeness to the limit cycle can be uniformly approximated, yet not the position on it. The reason is that any small deviation on the frequency is accumulated over the cycles, giving rise to large errors after a sufficient number of periods.

2.2 Second Order Averaging

In some situations, more accurate approximations than those provided by a first order averaging (Section 2.1) are required, as will be the case in Chapter 5 of this

thesis. Fortunately, there exist general results for n^{th} order averaging which allow increasing the precision of the approximation as much as needed. Here we only show some results for order 2, which is enough for the purpose of this thesis. Hence consider a system of the form

$$\left.\begin{cases}\dot{\boldsymbol{x}} = \epsilon \boldsymbol{X^1}(\boldsymbol{x},\phi) + \epsilon^2 \boldsymbol{X^2}(\boldsymbol{x},\phi) + \epsilon^3 \boldsymbol{X^{[3]}}(\boldsymbol{x},\phi,\epsilon) \\ \dot{\phi} = \Omega^0 + \epsilon\Omega^1(\boldsymbol{x})\end{cases}\right\}, \begin{matrix}\boldsymbol{x}(0) = \boldsymbol{x}_0 \quad \boldsymbol{x} \in D \subset \mathbb{R}^n \\ \phi(0) = \phi_0, \quad \phi \in S^1\end{matrix}, \tag{2.10}$$

where, following the notation in (Sanders et al., 2007), brackets are used in $\boldsymbol{X^{[3]}}$ to stress that this term is a remainder of an expansion in powers of ϵ. This is also noted by the fact that $\boldsymbol{X^1}$ and $\boldsymbol{X^2}$ do not.

Let $\{\boldsymbol{y}(t), \psi(t)\}$ be the solution of

$$\left.\begin{cases}\dot{\boldsymbol{y}} = \epsilon \bar{\boldsymbol{X}}^{\boldsymbol{1}}(\boldsymbol{y}) + \epsilon^2 \bar{\boldsymbol{X}}^{\boldsymbol{2}}_*(\boldsymbol{y}) \\ \dot{\psi} = \Omega^0 + \epsilon\Omega^1(\boldsymbol{y})\end{cases}\right\}, \quad \begin{matrix}\boldsymbol{y}(0) = \boldsymbol{x}_0 - \epsilon \boldsymbol{u}^1(\boldsymbol{x}_0, \phi_0) \\ \psi(0) = \phi_0\end{matrix}, \tag{2.11}$$

where $\bar{\boldsymbol{X}}^{\boldsymbol{1}}$ is defined as in (2.3) and

$$\boldsymbol{u}^1(\boldsymbol{y},\psi) = \frac{1}{\Omega^0} \int_{\psi_0}^{\psi} \left[\boldsymbol{X^1}(\boldsymbol{y},\phi) - \bar{\boldsymbol{X}}^{\boldsymbol{1}}(\boldsymbol{y})\right] d\phi, \tag{2.12}$$

$$\bar{\boldsymbol{X}}^{\boldsymbol{2}}_*(\boldsymbol{y}) = \frac{1}{2\pi} \int_0^{2\pi} \left[\boldsymbol{X^2}(\boldsymbol{y},\phi) + \boldsymbol{DX^1}(\boldsymbol{y},\phi) \cdot \boldsymbol{u}^1(\boldsymbol{y},\phi)\right] d\phi. \tag{2.13}$$

Constant ψ_0 in (2.12) is chosen in such a way that

$$\int_0^{2\pi} \boldsymbol{u}^1(\boldsymbol{y},\psi) d\psi = 0, \tag{2.14}$$

while symbol $\boldsymbol{D}$ in (2.13) represents differentiation with respect to $\boldsymbol{y}$. Then, the error estimate is

$$\boldsymbol{x}(t) = \boldsymbol{y}(t) + \epsilon \boldsymbol{u}^1\big(\boldsymbol{y}(t), \psi(t)\big) + O(\epsilon^2), \qquad \text{for } t = O(1/\epsilon) \tag{2.15}$$

This result will be used in Chapter 5. The proof can be found in (Sanders et al., 2007).

Note the presence of Ω^0 in the denominator of expression (2.12), in connection with the concept of 'resonance manifold' explained in Section 2.1. A vanishing frequency Ω^0 would make $\boldsymbol{u}^1$ unbounded and, according to (2.15), the approximation would not be valid anymore. In other words, the averaging transformation becomes singular when Ω^0 approaches zero.

2.3 Singular Perturbation Theory

The Singular Perturbation Theory (SPT) explains the behaviour of a particular class of fast-slow systems (Hunter, 2004; Lesne, 2006; Verhulst & Bakri, 2006). As has been done with averaging, an intuitive description of the theory is first given, followed by the exposition of some more rigorous results which will be used later on in the thesis.

Systems where the SPT is applicable are those exhibiting a *singular limit*. This means that the system depends on a parameter in such a way that, when the parameter approaches some limiting value, the general solution of the problem is qualitatively different to the solution of the limiting problem. Typically, systems of this type exhibit two separate time scales –or space scales– with very different behaviours. A well-known example is the *boundary layer theory* in fluid mechanics, where the effects of viscosity are relevant in a very thin layer of fluid, close to a bounding surface, while being negligible for the rest of the domain.

When the independent variable corresponds to time, systems with a singular limit usually contain fast and slow variables. The global behaviour is then composed of two consecutive stages of time: during a first short stage, the fast variables change significantly, with the slow variables remaining almost constant. At the second stage, much longer, the fast variables become slaved to the slow ones. In other words, the fast variables can be written as functions of the slow ones. This kind of composite behaviour can be observed in Fig. 2.1, where x and y represent the slow and fast variables, respectively.

The main usefulness of this theory lies in the fact that, during the second stage, the system dimension is actually reduced, since the fast variables are not anymore needed to specify the state of the system (they can be directly obtained from the slow variables). Thanks to this property, the original system can be replaced by a simpler reduced system during the second stage.

Now, some more rigorous results are shown, which will be used later on in the thesis. Consider an autonomous system of the form

$$\begin{cases} \dot{\boldsymbol{x}} = \epsilon \boldsymbol{f}(\boldsymbol{x}, \boldsymbol{y}) + O(\epsilon^2) \\ \dot{\boldsymbol{y}} = \boldsymbol{g}(\boldsymbol{x}, \boldsymbol{y}) + O(\epsilon) \end{cases}, \qquad \begin{matrix} \boldsymbol{x} \in D_x \subset \mathbb{R}^n \\ \boldsymbol{y} \in D_y \subset \mathbb{R}^m, \end{matrix} \qquad \begin{matrix} \boldsymbol{x}(0) = \boldsymbol{x}_0 \\ \boldsymbol{y}(0) = \boldsymbol{y}_0 \end{matrix} \tag{2.16}$$

Suppose the following two conditions are fulfilled:

1. The equation $\boldsymbol{g}(\boldsymbol{x}, \boldsymbol{y}) = \boldsymbol{0}$ has one only solution, given in the form $\boldsymbol{y} = \boldsymbol{Y}(\boldsymbol{x})$. This corresponds to a particular surface in the phase space, referred to as the *Slow Manifold*.
2. For every fixed $\boldsymbol{x} \in D_x$, we have that $\boldsymbol{y} = \boldsymbol{Y}(\boldsymbol{x})$ is a globally attracting and asymptotically stable fixed point of the system $\dot{\boldsymbol{y}} = \boldsymbol{g}(\boldsymbol{x}, \boldsymbol{y})$.

Then, the behaviour of the system can be shown to be composed of two consecutive stages of time.

First stage. For $t = O(1)$, the system can be written as

$$\begin{Bmatrix} \boldsymbol{x} = \boldsymbol{x}_0 + O(\epsilon) \\ \dot{\boldsymbol{y}} = \boldsymbol{g}(\boldsymbol{x}_0, \boldsymbol{y}) + O(\epsilon) \end{Bmatrix} \tag{2.17}$$

During this phase, $\boldsymbol{x}$ remains nearly constant, while $\boldsymbol{y}$ is attracted towards $\boldsymbol{Y}(\boldsymbol{x}_0)$. Thus, the trajectory approaches the Slow Manifold.

Second stage. For $t = O(1/\epsilon)$, the system slowly drifts along the Slow Manifold:

$$\begin{Bmatrix} \dot{\boldsymbol{x}} = \boldsymbol{\epsilon f}\big(\boldsymbol{x}, \boldsymbol{Y}(\boldsymbol{x})\big) + O(\epsilon^2) \\ \boldsymbol{y} = \boldsymbol{Y}(\boldsymbol{x}) + O(\epsilon) \end{Bmatrix}. \tag{2.18}$$

In summary, the system is first rapidly attracted towards the Slow Manifold, with the slow variables being almost constant. Next, the trajectory evolves close to the Slow Manifold, which allows reducing the system dimension from $n + m$ to n, as can be observed by neglecting the h.o.t in (2.18):

$$\dot{\boldsymbol{x}} = \epsilon \boldsymbol{f}\big(\boldsymbol{x}, \boldsymbol{Y}(\boldsymbol{x})\big), \qquad \boldsymbol{x} \in \mathbb{R}^n \tag{2.19}$$

An example of the referred behaviour is represented in Fig. 2.1, for $n = m = 1$. For a more detailed exposition and justification of the theory, see (Hunter, 2004; Lesne, 2006; Verhulst & Bakri, 2006).

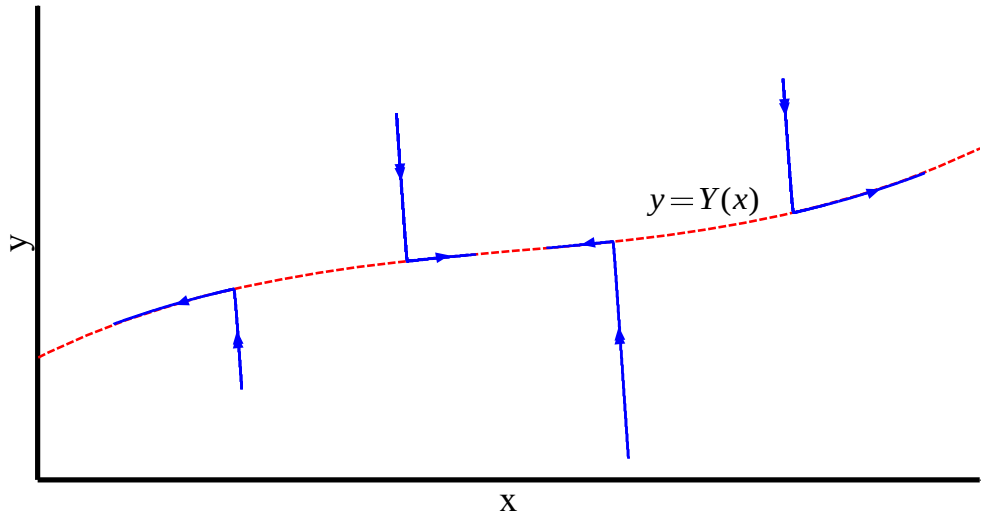

Fig. 2.1 Representative phase portrait for a system of the form (2.16), with $n = 1$, $m = 1$, when conditions 1 and 2 are satisfied. A single arrow stands for the slow motion, while a double arrow represents fast motion.

2.4 Hopf Bifurcations

Hopf bifurcations constitute a common mechanism whereby a fixed point of a dynamical system loses stability. As is well known, the stability of an equilibrium point is given by the real parts of the eigenvalues of the system jacobian matrix. A Hopf bifurcation occurs –with the exception of some degenerate cases– when two complex conjugate eigenvalues cross the imaginary axis. A very interesting feature of Hopf bifurcations is the appearance of limit cycles surrounding the bifurcating equilibrium point. Extensive analysis of this matter can be found in (Guckenheimer & Holmes, 1983; Kuznetsov, 1998).

In the following, a classical result concerning the classification of Hopf bifurcations is explained, which will be useful in Chapter 3. Hence consider a system of the form

$$\dot{\boldsymbol{x}} = \boldsymbol{f}(\boldsymbol{x}, \alpha), \qquad \boldsymbol{x} \in \mathbb{R}^n, \tag{2.20}$$

where α is a scalar parameter. Suppose that the system exhibits a fixed point $\boldsymbol{x}_0$, which undergoes a Hopf Bifurcation for $\alpha = \alpha_c$ such that, for $\alpha < \alpha_c$, the equilibrium is stable, while it becomes unstable for $\alpha > \alpha_c$.

The Hopf bifurcation generates a limit cycle in the vicinity of the fixed point, and is classified as subcritical or supercritical according to the following rule: we call the bifurcation subcritical (supercritical) if it creates an unstable (stable) limit cycle for $\alpha < \alpha_c$ $(\alpha > \alpha_c)$, as depicted in Fig. 2.2. In other words, when the bifurcation is subcritical, there is an unstable limit cycle coexisting with a stable fixed point, while, when it is supercritical, there is a stable limit cycle coexisting with an unstable fixed point. Note that Fig. 2.2 exhibits an additional property of Hopf Bifurcations: the amplitude of the created limit cycle grows, for small values of $|\alpha - \alpha_c|$, as $\sqrt{|\alpha - \alpha_c|}$.

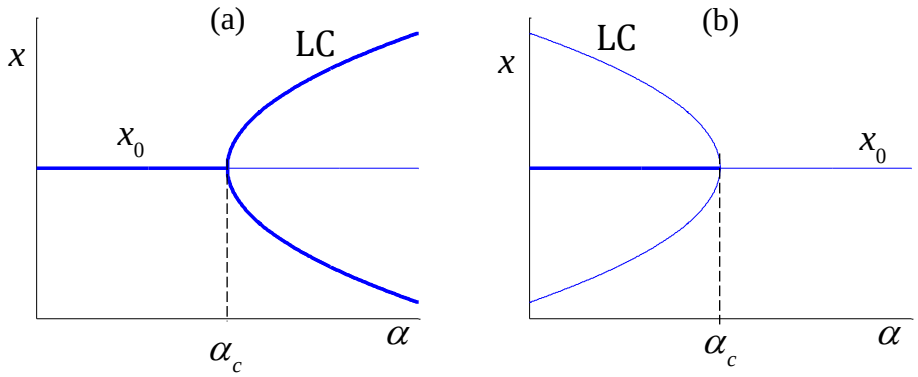

Fig. 2.2 Classification of Hopf bifurcations

(a) Supercritical (b) Subcritical

Thick (thin) lines represent stable (unstable) solutions

The distinction between these two types of bifurcation is crucial from a practical point of view. Subcritical bifurcations are, in general, much more dangerous, since they can give rise to abrupt jumps in the system behavior (Kuznetsov, 1998). The

reason is that, once a fixed point has lost its stability through a subcritical bifurcation, there exist no attractors in the vicinity of the equilibrium (see Fig. 2.2(b)) and, consequently, the system will jump towards an attractor which can be considerably far away from the bifurcating fixed point.

Fortunately, an analytical criterion exists which allows distinguishing supercritical and subcritical bifurcations. In order to apply the criterion to a general system, it should first be noted that any n-dimensional system can be reduced to a 2D system in the vicinity of a Hopf bifurcation, by virtue of the Center Manifold Theorem (Kuznetsov, 1998). Then, with some changes of variables, the system can always be written, at the bifurcation, in the form

$$\begin{bmatrix}\dot{z_1}\\ \dot{z_2}\end{bmatrix} = \begin{bmatrix}0 & -\omega\\ \omega & 0\end{bmatrix}\begin{bmatrix}z_1\\ z_2\end{bmatrix} + \begin{bmatrix}f(z_1,z_2)\\ g(z_1,z_2)\end{bmatrix}, \tag{2.21}$$

where functions f and g, containing the nonlinear terms of the system, can be expanded as Taylor series:

$$\begin{aligned} f(z_1,z_2) &= \sum_{i+j\geq 2} \frac{1}{i!\,j!} f_{ij} z_1^i z_2^j \\ g(z_1,z_2) &= \sum_{i+j\geq 2} \frac{1}{i!\,j!} g_{ij} z_1^i z_2^j \end{aligned} \tag{2.22}$$

Once the system of interest is written as (2.21), a number of variable transformations are conducted, including transformation in complex form, near-identity transformation and transformation in polar coordinates (Habib & Kerschen, 2015). This is a standard procedure whose details can be found in (Guckenheimer & Holmes, 1983; Kuznetsov, 1998). After this procedure, system (2.21) can be written in its Normal Form

$$\dot{r} = \delta r^3, \tag{2.23}$$

which governs the radial dynamics at the bifurcation. As shown in (Guckenheimer & Holmes, 1983), coefficient δ can be computed as

$$16\delta = \left\{ \begin{array}{c} f_{30} + f_{12} + g_{21} + g_{03} \\ +\frac{1}{\omega}[f_{11}(f_{20} + f_{02}) - g_{11}(g_{20} + g_{02}) + f_{02}g_{02} - f_{20}g_{20}] \end{array} \right\}. \tag{2.24}$$

Once parameter δ is known, the criterion is simple: if $\delta < 0$, the bifurcation is supercritical; if $\delta > 0$, the bifurcation is subcritical.

2.5 The Poincaré-Béndixson Theorem

This is a central result in the global theory of nonlinear systems (Perko, 2001). One of the main implications of the theorem is that, for 2-dimensional systems, the possible kinds of dynamical behaviours are very limited. In particular, it proves that chaos cannot occur in 2 dimensions. It is also one of the few results which allow establishing the existence of closed orbits in dynamical systems (Strogatz, 1994). We present here the simplest version of the theorem. For a more rigorous and detailed exposition of its content, see (Perko, 2001).

Consider a 2D dynamical system and a closed, bounded region R of the phase plane which does not contains any fixed points. Then, every trajectory which is confined in R –it starts in R and remains in R for all future time– is a closed orbit or spirals towards a closed orbit as $t \to \infty$.

In practice, the usual way to guarantee that there exists a trajectory which is confined in region R consists in showing that the vector field on the boundary of R

is oriented inwards, as depicted in Fig. 2.3. Then, all trajectories which start inside R are restricted to remain inside.

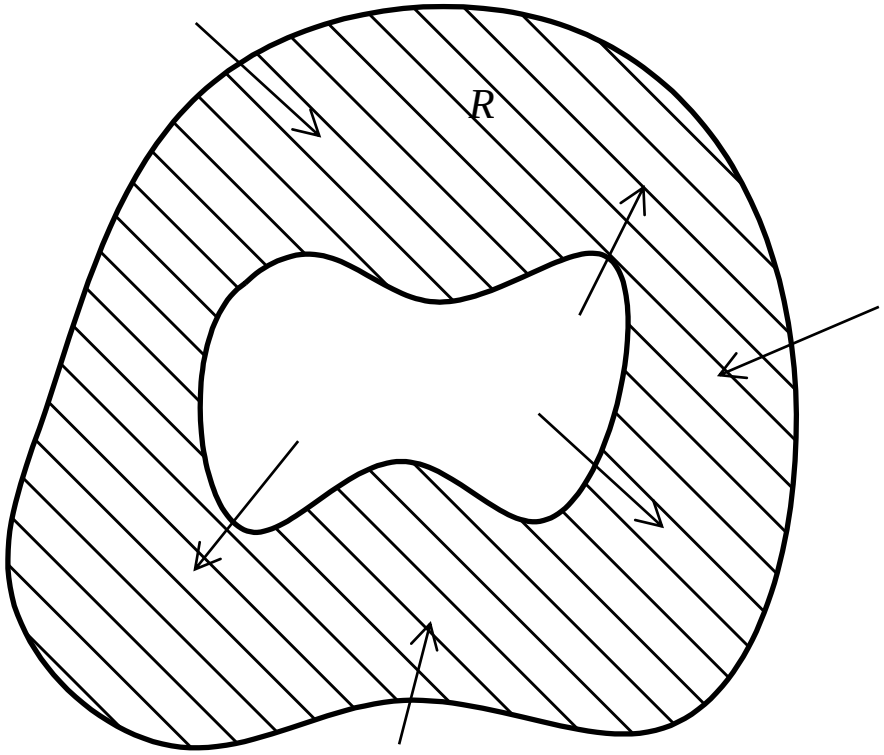

Fig. 2.3 Phase portrait showing a closed, bounded region R with the flow directed inwards at the boundaries. If R contains no fixed points, then it contains at least one stable limit cycle.

3 THE CASE OF LARGE SLOPE OF THE MOTOR CHARACTERISTIC: ANALYTICAL APPROACH

This Chapter investigates the dynamics of a 2-DOF system consisting in an unbalanced motor attached to the fixed frame by a nonlinear spring and a linear damper. As commented in the introduction, two different scenarios need to be considered separately, depending on the order of magnitude of the slope of the motor characteristic. The Case of a Large Slope is considered in this Chapter and the following, while the alternative situation will be studied in Chapters 5 and 6.

3.1 Problem Statement and Assumptions

Consider the system depicted in Fig. 3.1. It consists in an unbalanced motor attached to a fixed frame by a nonlinear spring –whose force has linear and cubic components– and a linear damper. The cubic component of the spring gives the possibility to model a nonlinear behavior for the structure supporting the motor (Mettler, 1962). The effect of gravity can be shown to have no relevance (Dimentberg et al., 1997) and, therefore, it will not be included in the model.

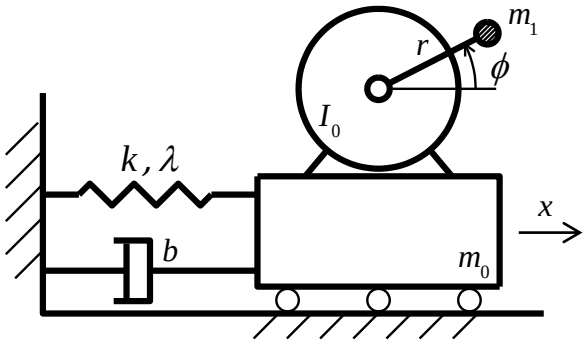

Fig. 3.1 Model

Variable x stands for the linear motion, ϕ is the angle of the rotor, m_1 is the unbalanced mass with eccentricity r, m_0 is the rest of the vibrating mass, I_0 is the rotor inertia (without including the unbalance), b is the viscous damping coefficient and k and λ are, respectively, the linear and cubic coefficients of the spring. The equations of motion for the coupled 2-DOF system are (El-Badawy, 2007)

$$\begin{aligned} m\ddot{x} + b\dot{x} + kx + \lambda x^3 &= m_1 r\left(\dot{\phi}^2 \cos\phi + \ddot{\phi} \sin\phi\right) \\ I\ddot{\phi} &= L_m\left(\dot{\phi}\right) + m_1 r\ddot{x} \sin\phi\,, \end{aligned} \tag{3.1}$$

where $m = m_0 + m_1$, $I = I_0 + m_1 r^2$ and an overdot represents differentiation with respect to time, t.

Function $L_m\left(\dot{\phi}\right)$ is the driving torque produced by the motor –given by its torque-speed curve, also known as static characteristic– minus the losses torque due to

friction at the bearings, windage, etc. We assume this net torque to be a linear function of the rotor speed:

$$L_m(\dot{\phi}) = A + D\dot{\phi}. \tag{3.2}$$

Although $L_m(\dot{\phi})$ includes the damping of rotational motion, we will usually refer to it shortly as '**the motor characteristic'**.

As will be seen later, it is convenient for the purpose of this chapter to write the driving torque in an alternative way. Then, denoting by ω_n the linear natural frequency of the oscillator, given by $\omega_n = \sqrt{k/m}$, the motor torque can be written as

$$L_m(\dot{\phi}) = C + D(\dot{\phi} - \omega_n), \tag{3.3}$$

where C represents the driving torque at resonance ($L_m(\omega_n) = C$). From equations (3.2) and (3.3), the relation between constants A and C can be directly deduced:

$$C = A + D\omega_n. \tag{3.4}$$

Along the whole thesis, the motor characteristic will be written as (3.2) or (3.3), depending on the situation. It should be kept in mind that these two expressions are totally equivalent. The important point is that the driving torque is assumed to follow a linear relation with the rotor speed. It is further assumed that $D < 0$ –the driving torque decreases with the rotor speed–, as is usual for most kinds of motor. This assumption will prove to be of major importance.

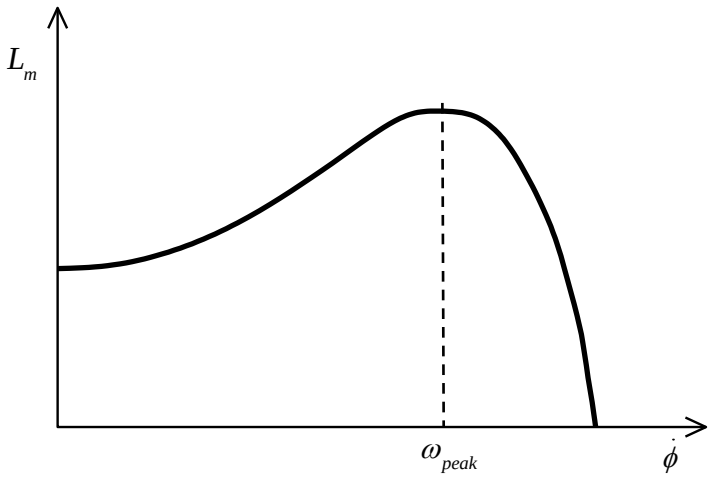

Fig. 3.2 Typical static characteristic for an asynchronous motor

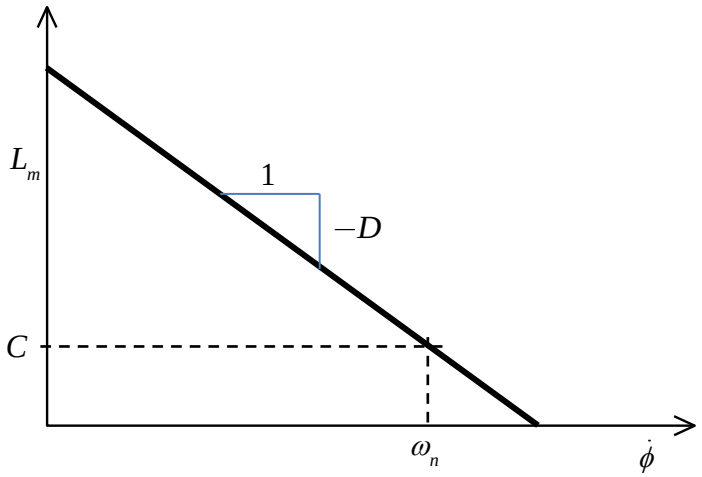

Fig. 3.3 Static characteristic corresponding to equation (3.3)

As an example, the static characteristic of an induction motor is depicted in Fig. 3.2. Note that such a motor is usually designed to work on the region $\dot{\phi} > \omega_{peak}$, where the curve could be reasonably approximated by a straight line with negative slope. The simplified motor characteristic given at (3.3) is represented in Fig. 3.3.

In the second of equations (3.1), which imposes the equilibrium of the rotor, the last term is of great significance, since it accounts for the torque on the rotor caused by linear motion of the system. Its physical interpretation can be readily understood with the aid of Fig. 3.4. Due to displacement $x(t)$, a horizontal inertial force acts on the unbalanced mass and generates a torque with respect to the rotor axis. This particular term of the equations of motion is what makes the excitation nonideal, for it takes into account how vibration influences rotation. If this torque due to vibration did not exist –or if it was negligible–, the rotor equilibrium equation would reduce to $I\ddot{\phi} = L_m(\dot{\phi})$, and it could be solved for $\phi(t)$ regardless of the linear motion. Then, this solution $\phi(t)$ could be introduced in the first of equations (3.1) as a prescribed excitation.

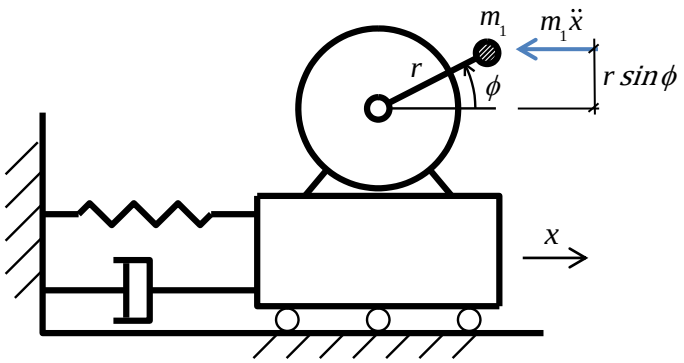

Fig. 3.4 Torque on the rotor due to vibration

By defining

$$R_m = m_1/m\,, \qquad R_I = m_1 r^2/I\,, \qquad \xi = \frac{b}{2\sqrt{km}}, \qquad \alpha = \frac{R_I R_m}{2\xi}$$
$$c = \frac{C}{I\omega_n^2}, \qquad d = \frac{D}{I\omega_n}, \qquad \tau = \omega_n t, \qquad u = \frac{x}{r}\frac{2\xi}{R_m}, \qquad \rho = \frac{\lambda r^2}{k}\left(\frac{R_m}{2\xi}\right)^2, \tag{3.5}$$

the equations of motion can be written in a more convenient dimensionless form

$$\ddot{u} + u = -2\xi\dot{u} - \rho u^3 + 2\xi\left(\dot{\phi}^2\cos\phi + \ddot{\phi}\sin\phi\right)$$
$$\ddot{\phi} = c + d\left(\dot{\phi} - 1\right) + \alpha\ddot{u}\sin\phi\,, \tag{3.6}$$

where a dot now represents differentiation with respect to dimensionless time, τ.

In order to apply perturbation techniques to system (3.6), some assumptions on the order of magnitude of the system parameters have to be made. Thus, we assume the damping, the unbalance and the nonlinearity to be small. This is expressed by making the corresponding coefficients proportional to a sufficiently small, positive and dimensionless parameter ϵ:

$$\xi = \epsilon\xi_0, \qquad \alpha = \epsilon\alpha_0, \qquad \rho = \epsilon\rho_0, \tag{3.7}$$

where parameters with subscript '0' are ϵ-independent. It is also assumed that the torque generated by the motor at resonance $(\dot{\phi} = 1)$ is sufficiently small:

$$c = \epsilon c_0 \tag{3.8}$$

Finally, the slope of the motor characteristic is assumed to be of the order of unity, i.e. independent of ϵ:

$$d = d_0 \tag{3.9}$$

This assumption corresponds to what we have called 'large slope characteristic'. The case of small slope, with d proportional to ϵ, is treated in Chapters 5 and 6.

Taking the proposed scaling (3.7)-(3.9) into account and dropping the subscript '0' for convenience, system (3.1) takes the form

$$\begin{aligned} \ddot{u} + u &= \epsilon\left[-2\xi\dot{u} - \rho u^3 + 2\xi\left(\dot{\phi}^2\cos\phi + \ddot{\phi}\sin\phi\right)\right] \\ \ddot{\phi} &= d\left(\dot{\phi} - 1\right) + \epsilon[c + \alpha\ddot{u}\sin\phi]. \end{aligned} \tag{3.10}$$

3.2 Alternative First Order Averaging

Before turning to the treatment of system (3.10) through some perturbation techniques, an alternative averaging procedure is developed in this section, which will be useful in what follows. In order to make the procedure as general as possible, consider a system of the form

$$\left.\begin{cases} \dot{\boldsymbol{x}} = \epsilon[\boldsymbol{A}\boldsymbol{y} + \boldsymbol{X}(\boldsymbol{x},\phi)] + O(\epsilon^2) \\ \dot{\boldsymbol{y}} = \boldsymbol{B}\boldsymbol{y} + \boldsymbol{Y}(\boldsymbol{x},\phi) + O(\epsilon) \\ \dot{\phi} = \Omega + O(\epsilon) \end{cases}\right\}, \quad \begin{matrix} \boldsymbol{x} \in D \subset \mathbb{R}^n \\ \boldsymbol{y} \in R \subset \mathbb{R}^m \\ \phi \in S^1, \end{matrix} \tag{3.11}$$

where $\boldsymbol{A}$ and $\boldsymbol{B}$ are matrices of constant coefficients and Ω is a scalar constant, bounded away from zero. It will be shown in the next section that system (3.10) can be written in the form (3.11).

Suppose that we try to perform a first order averaging on system (3.11) over angle ϕ. According to the results explained in Section 2.1, such a technique is not applicable in this case, because the set of variables $\boldsymbol{y}$ is not slow. In order to use the theorem of Section 2.1 we would need to have $\dot{\boldsymbol{x}} = O(\epsilon)$ and $\dot{\boldsymbol{y}} = O(\epsilon)$, which is not the case. This justifies the introduction of the modified technique presented below.

First, the averaged variables are defined as

$$\overline{\boldsymbol{x}}(t) \equiv \frac{1}{T}\int_{t-T/2}^{t+T/2} \boldsymbol{x}(s)ds\,, \qquad \overline{\boldsymbol{y}}(t) \equiv \frac{1}{T}\int_{t-T/2}^{t+T/2} \boldsymbol{y}(s)ds \tag{3.12}$$

where $T = 2\pi/\Omega$. As illustrated in Fig. 3.5, the effect of the operator defined in (3.12) is to smooth out the short-term fluctuations of each variable, while retaining the long-term behavior.

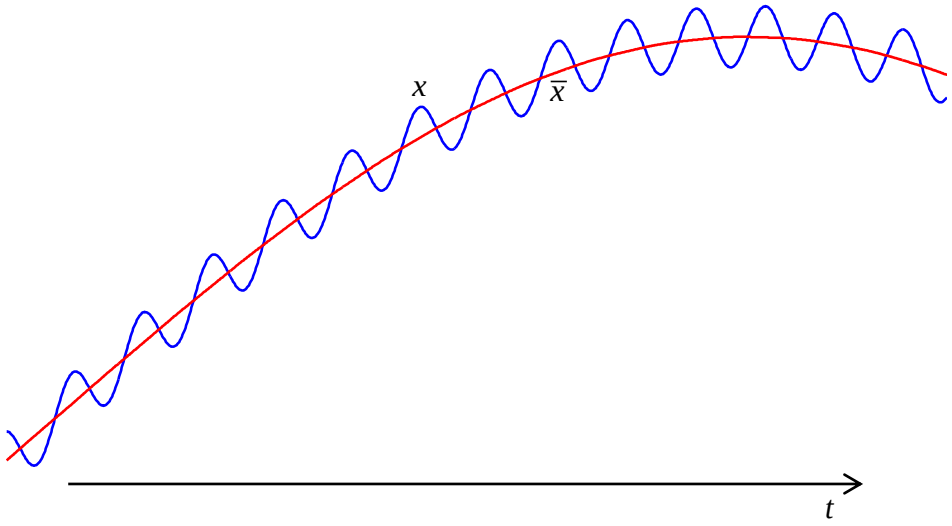

Fig. 3.5 Definition of the averaged variables

Suppose we are interested in the evolution of the averaged variables $\bar{\boldsymbol{x}}(t)$ and $\bar{\boldsymbol{y}}(t)$. Then, we can average the first two equations in (3.11), which yields

$$\left\{\begin{array}{l} \dot{\bar{\boldsymbol{x}}} = \epsilon\left[\boldsymbol{A}\bar{\boldsymbol{y}} + \dfrac{1}{T}\displaystyle\int_{t-T/2}^{t+T/2} \boldsymbol{X}\big(\boldsymbol{x}(s),\phi(s)\big)ds\right] + O(\epsilon^2) \\ \dot{\bar{\boldsymbol{y}}} = \boldsymbol{B}\bar{\boldsymbol{y}} + \dfrac{1}{T}\displaystyle\int_{t-T/2}^{t+T/2} \boldsymbol{Y}\big(\boldsymbol{x}(s),\phi(s)\big)ds + O(\epsilon) \end{array}\right\}, \tag{3.13}$$

where it has been used that the average, as defined in (3.12), is a linear operator (the average of the sum is the sum of the averages).

The next step consists in transforming the integrals in (3.13). Since the process is exactly the same for both integrals, we only focus on the first of them.

First, we can write

$$\frac{1}{T}\int_{t-T/2}^{t+T/2}\boldsymbol{X}\big(\boldsymbol{x}(s),\phi(s)\big)ds=\frac{1}{T}\int_{t-T/2}^{t+T/2}\boldsymbol{X}\big(\boldsymbol{x}(t),\phi(s)\big)ds+O(\epsilon), \tag{3.14}$$

where it has been used the property that, in one period T, $\boldsymbol{x}(t)$ can only change by $O(\epsilon)$, according to (3.11). Thus, we can write $\boldsymbol{x}(s)=\boldsymbol{x}(t)+O(\epsilon)$. Changing the integration variable from s to ϕ yields

$$\frac{1}{T}\int_{t-T/2}^{t+T/2}\boldsymbol{X}\big(\boldsymbol{x}(t),\phi(s)\big)ds+O(\epsilon)=\frac{1}{2\pi}\int_{\phi(t-T/2)}^{\phi(t+T/2)}\boldsymbol{X}(\boldsymbol{x}(t),\phi)d\phi+O(\epsilon), \tag{3.15}$$

where the last of relations (3.11) has been used $\big(d\phi=\Omega ds+O(\epsilon)\big)$. The integration limits can also be transformed by using again $\dot{\phi}=\Omega+O(\epsilon)$:

$$\frac{1}{2\pi}\int_{\phi(t-T/2)}^{\phi(t+T/2)}\boldsymbol{X}(\boldsymbol{x}(t),\phi)d\phi+O(\epsilon)=\frac{1}{2\pi}\int_{\phi(t)-\pi}^{\phi(t)+\pi}\boldsymbol{X}(\boldsymbol{x}(t),\phi)d\phi+O(\epsilon). \tag{3.16}$$

Finally, as function $\boldsymbol{X}$ is 2π-periodic in ϕ, we can write

$$\frac{1}{2\pi}\int_{\phi(t)-\pi}^{\phi(t)+\pi}\boldsymbol{X}(\boldsymbol{x}(t),\phi)d\phi+O(\epsilon)=\frac{1}{2\pi}\int_{0}^{2\pi}\boldsymbol{X}(\boldsymbol{x}(t),\phi)d\phi+O(\epsilon). \tag{3.17}$$

By comparing this last expression to definition (2.3), system (3.13) can be rewritten as

$$\begin{Bmatrix}\dot{\bar{\boldsymbol{x}}}=\epsilon[\boldsymbol{A}\bar{\boldsymbol{y}}+\bar{\boldsymbol{X}}(\bar{\boldsymbol{x}})]+O(\epsilon^2)\\ \dot{\bar{\boldsymbol{y}}}=\boldsymbol{B}\bar{\boldsymbol{y}}+\bar{\boldsymbol{Y}}(\bar{\boldsymbol{x}})+O(\epsilon)\end{Bmatrix}. \tag{3.18}$$

Then, we have been able to derive an autonomous system for the averaged variables, where the fast angle no longer appears –except in the higher order terms of (3.18)–. Note that the proposed approach exploits a particular property of system (3.11), namely the fact that the vector of fast variables $\boldsymbol{y}$ only appears linearly on the r.h.s. of the equations. This feature, together with the linearity of the averaging operator, allows applying an averaging technique to system (3.11), despite it containing fast variables (in addition to the fast rotating phase ϕ).

Finally, it is convenient to remark the difference between the original and averaged variables. From equations (3.11), variations of $\boldsymbol{x}$ and $\boldsymbol{y}$ in one period T are $O(\epsilon)$ and $O(1)$, respectively. Therefore, we can write

$$\boldsymbol{x}(t) = \overline{\boldsymbol{x}}(t) + O(\epsilon), \qquad \boldsymbol{y}(t) = \overline{\boldsymbol{y}}(t) + O(1). \tag{3.19}$$

3.3 Perturbation Approach: Derivation of the Reduced System

Going back to the mechanical system under study, equations (3.10) constitute an autonomous dynamical system of dimension 4, with state variables $\{u, \dot{u}, \phi, \dot{\phi}\}$. A perturbation approach is proposed in this section, whereby (3.10) is transformed into an approximate 2D system, much easier to analyse.

First, it is convenient to perform a change of variables, from $\{u, \dot{u}\}$ to polar coordinates (Sanders et al., 2007):

$$\begin{aligned} u &= a\cos(\phi + \beta) \\ \dot{u} &= -a\sin(\phi + \beta)\,. \end{aligned} \tag{3.20}$$

This step does not include any approximation, since it consists in just replacing the pair of variables $\{u(\tau), \dot{u}(\tau)\}$ with the pair of amplitude-phase variables $\{a(\tau), \beta(\tau)\}$.

By differentiating the first of relations (3.20) we obtain

$$\dot{u} = \dot{a}\cos(\phi+\beta) - a\left(\dot{\phi}+\dot{\beta}\right)\sin(\phi+\beta). \tag{3.21}$$

Comparing (3.21) with the second of relations (3.20) yields

$$\dot{a}\cos(\phi+\beta) - a\left(\dot{\phi}-1+\dot{\beta}\right)\sin(\phi+\beta) = 0. \tag{3.22}$$

On the other hand, if (3.20) is introduced into the first of equations (3.10), we have

$$\begin{gathered} -\dot{a}\sin(\phi+\beta) - a\left(\dot{\phi}-1+\dot{\beta}\right)\cos(\phi+\beta) = \\ = \epsilon\left[2\xi a\sin(\phi+\beta) - \rho a^3\cos^3(\phi+\beta) + 2\xi\left(\dot{\phi}^2\cos\phi + \ddot{\phi}\sin\phi\right)\right] \end{gathered} \tag{3.23}$$

Equations (3.22) and (3.23) together form a linear system for $\dot{a}$ and $\dot{\beta}$ that can be readily solved:

$$\begin{gathered} \dot{a} = -\epsilon\sin(\phi+\beta)\left[2\xi a\sin(\phi+\beta) - \rho a^3\cos^3(\phi+\beta) + 2\xi\left(\dot{\phi}^2\cos\phi + \ddot{\phi}\sin\phi\right)\right] \\ \dot{\beta} = 1-\dot{\phi} - \epsilon\frac{\cos(\phi+\beta)}{a}\left[2\xi a\sin(\phi+\beta) - \rho a^3\cos^3(\phi+\beta) + 2\xi\left(\dot{\phi}^2\cos\phi + \ddot{\phi}\sin\phi\right)\right] \end{gathered} \tag{3.24}$$

It is also suitable to define a new variable for the rotor speed:

$$\Omega \equiv \dot{\phi}. \tag{3.25}$$

Then, the dynamical system, written in terms of the new variables, becomes

$$\left\{\begin{array}{c} \dot{a} = -\epsilon\sin(\phi+\beta)\,F_1(a,\beta,\phi,\Omega) + O(\epsilon^2) \\ \dot{\beta} = 1-\Omega-\epsilon\dfrac{\cos(\phi+\beta)}{a}F_1(a,\beta,\phi,\Omega) + O(\epsilon^2) \\ \dot{\Omega} = d(\Omega-1) + \epsilon(c-\alpha a\sin\phi\cos(\phi+\beta)) + O(\epsilon^2) \\ \dot{\phi} = \Omega, \end{array}\right\}, \tag{3.26}$$

where

$$F_1 = 2\xi a \sin(\phi+\beta) - \rho a^3 \cos^3(\phi+\beta) + 2\xi[\Omega^2 \cos\phi + d(\Omega-1)\sin\phi]. \quad (3.27)$$

A new 4D autonomous dynamical system (3.26) has been derived, with state variables $\{a, \beta, \phi, \Omega\}$, which is fully equivalent to (3.10).

Consider now a general set of initial conditions $\{a_0, \beta_0, \phi_0, \Omega_0\}$ and let us investigate how the variables evolve with time. In the next subsections, it will be shown that the dynamics of (3.26) is composed of three consecutive stages of time, with different qualitative behaviours.

First stage

For the moment, consider only the evolution equations for variables β and Ω, which can be written as

$$\left\{\begin{array}{l} \dot{\beta} = 1 - \Omega + O(\epsilon) \\ \dot{\Omega} = d(\Omega-1) + O(\epsilon) \end{array}\right\}. \quad (3.28)$$

It is clear that, to first order of approximation, the evolution of β and Ω only depends on Ω. This first order approximation corresponds to neglecting the $O(\epsilon)$ terms in (3.28):

$$\left\{\begin{array}{l} \dot{\beta} = 1 - \Omega \\ \dot{\Omega} = d(\Omega-1) \end{array}\right\}. \quad (3.29)$$

The relation between exact system (3.28) and (3.29) is established by the Regular Perturbation Theory (Sanders et al., 2007), which assures that solutions of (3.29) are $O(\epsilon)$–approximations to solutions of (3.28), for $\tau = O(1)$. Thus, we proceed to solve system (3.29):

$$\left.\begin{aligned}\beta &= \beta_0^* + \frac{1-\Omega_0}{d}e^{d\tau} \\ \Omega &= 1 + [\Omega_0 - 1]e^{d\tau}\end{aligned}\right\}, \tag{3.30}$$

with

$$\beta_0^* \equiv \beta_0 + \frac{\Omega_0 - 1}{d}. \tag{3.31}$$

It is clear from (3.30) that both variables tend exponentially to constant values:

$$\beta \to \beta_0^*, \qquad \Omega \to 1. \tag{3.32}$$

This is due to the assumption $d < 0$ (otherwise, the exponentials in (3.30) would be divergent). Taking into account the approximation made when transforming (3.28) into (3.29), it can be stated that, after a time interval $\tau = O(1)$, we have

$$\beta = \beta_0^* + O(\epsilon), \qquad \Omega = 1 + O(\epsilon). \tag{3.33}$$

Once β and Ω are at an $O(\epsilon)$–distance from β_0^* and 1, respectively, the first stage of the motion is over. Note that, during this stage, the rotor speed evolves monotonically towards the resonance region.

During this first phase, variable a remains nearly constant. Since $\dot{a} = O(\epsilon)$ –see (3.26)–, variable a needs a time length $\tau = O(1/\epsilon)$ to evolve significantly. Thus, at the end of the first stage, we have

$$a = a_0 + O(\epsilon). \tag{3.34}$$

In summary, the first stage corresponds to a time length $\tau = O(1)$. It starts at $\tau = 0$ and it ends when β and Ω have reached an $O(\epsilon)$–distance to β_0^* and 1, respectively.

Second stage

At the beginning of the second stage, the rotor speed is already in the vicinity of resonance. Consequently, it can be naturally expanded as

$$\Omega = 1 + \epsilon\sigma. \tag{3.35}$$

A new variable σ has been introduced in (3.35), which will be very widely used throughout the thesis. Notice that σ is a detuning coordinate, which measures how much the rotor speed deviates from the system natural frequency.

If system (3.26) is written using variable σ instead of Ω, it becomes

$$\left\{\begin{array}{c} \dot{a} = -\epsilon \sin(\phi+\beta)\, F_2(a,\beta,\phi) + O(\epsilon^2) \\ \dot{\beta} = -\epsilon\sigma - \epsilon \dfrac{\cos(\phi+\beta)}{a} F_2(a,\beta,\phi) + O(\epsilon^2) \\ \dot{\sigma} = c + d\sigma - \alpha a \sin\phi \cos(\phi+\beta) + O(\epsilon) \\ \dot{\phi} = 1 + \epsilon\sigma \end{array}\right\}, \tag{3.36}$$

where

$$F_2 = 2\xi a \sin(\phi+\beta) - \rho a^3 \cos^3(\phi+\beta) + 2\xi \cos\phi. \tag{3.37}$$

Notice that the closeness between the rotor speed and the natural frequency of the system has transformed β into a slow variable. Note also that system (3.36) is of the form (3.11), with $\{a, \beta\}$ playing the role of vector $\boldsymbol{x}$ and σ that of vector $\boldsymbol{y}$. Therefore, the averaging technique presented in Section 3.2 can be readily applied to (3.36), in order to obtain the evolution of the averaged variables.

The averaged system, which in the general case is given by (3.18), takes in the present case the form

$$\left\{\begin{array}{c} \dot{\bar{a}} = -\epsilon\xi\left(\bar{a} + \sin\bar{\beta}\right) + O(\epsilon^2) \\ \dot{\bar{\beta}} = -\epsilon\left(\bar{\sigma} + \xi\dfrac{\cos\bar{\beta}}{\bar{a}} - \dfrac{3}{8}\rho\bar{a}^2\right) + O(\epsilon^2) \\ \dot{\bar{\sigma}} = c + d\bar{\sigma} + \dfrac{\alpha}{2}\bar{a}\sin\bar{\beta} + O(\epsilon) \end{array}\right\}, \tag{3.38}$$

where the averaged variables $\{\bar{a}, \bar{\beta}, \bar{\sigma}\}$ are defined as in (3.12). System (3.38) has dimension 3, since variable ϕ no longer appears.

It is convenient to highlight the relation between the original and the averaged variables. Particularizing the general expression (3.19) to the system under analysis, we find

$$\begin{array}{l} a = \bar{a} + O(\epsilon) \\ \beta = \bar{\beta} + O(\epsilon) \\ \sigma = \bar{\sigma} + O(1). \end{array} \tag{3.39}$$

Observe that, even with an $O(1)$ error in σ, the rotor speed is still known with $O(\epsilon)$ precision, according to (3.35). From now on, the overbars will be omitted, unless otherwise stated.

The task now is to investigate system (3.38). As pointed out before, this is a fast-slow system, with two slow variables a and β and one fast variable σ. This difference in the time scales allows exploiting the Singular Perturbation Theory (Hunter, 2004; Lesne, 2006; Verhulst & Bakri, 2006).

In order to apply the SPT to system (3.38), the 2 conditions specified in Section 2.3 need to be verified:

1. It is clear that the solution of equation

$$c + d\sigma + \frac{\alpha}{2}a\sin\beta = 0 \tag{3.40}$$

can be written as

$$\sigma = \sigma^*(a,\beta) \equiv -\frac{c}{d} - \frac{\alpha}{2d} a \sin\beta, \tag{3.41}$$

which is the expression of the Slow Manifold: a 2D surface in the 3D phase space. Thus, the first condition is satisfied.

2. For fixed values of a and β, it is found that $\sigma = \sigma^*(a,\beta)$ is a globally asymptotically stable fixed point of the 1D system

$$\dot{\sigma} = c + d\sigma + \frac{\alpha}{2} a \sin\beta, \tag{3.42}$$

provided that assumption $d < 0$ holds. Therefore, the second condition is also fulfilled.

Once both requirements have been verified, it can be stated that system (3.38) displays two qualitatively different behaviors at two sequential time scales –see Section 2.3–, which correspond to the second and third stages of the original system (3.26). Using the results of Section 2.3, we have that, at the first of these stages –second stage of (3.26)–, the system can be written as

$$\begin{aligned} a &= a_0 + O(\epsilon) \\ \beta &= \beta_0^* + O(\epsilon) \\ \dot{\sigma} &= c + d\sigma + \frac{\alpha}{2} a_0 \sin\beta_0^* + O(\epsilon), \end{aligned} \tag{3.43}$$

where it has been taken into account that, at the beginning of stage 2, $a = a_0 + O(\epsilon)$ and $\beta = \beta_0^* + O(\epsilon)$. Then, at this stage, the system is attracted towards the Slow Manifold, with the slow variables remaining nearly constant:

$$\sigma \to \sigma^*(a_0, \beta_0^*). \tag{3.44}$$

Summing up, the second stage corresponds to a time length $\tau = O(1)$, just as the first one. It ends once variable σ has reached an $O(\epsilon)$–distance to $\sigma^*(a_0, \beta_0^*)$. During this phase of the motion, a and β do not change significantly.

Third stage

The third stage of the original system (3.26) –which is the second stage of the averaged system (3.38)– occurs at a time scale $\tau = O(1/\epsilon)$. This can be easily understood by noticing that, once the system is near the slow manifold, variable σ becomes slow (introducing (3.41) in (3.38) leads to $\dot{\sigma} = O(\epsilon)$). Therefore, near the slow manifold, all variables are slow and, as a consequence, the system natural time scale is $\tau = O(1/\epsilon)$.

By introducing the expression of the slow manifold in (3.38), the equations corresponding to the third phase of the motion are obtained:

$$\left\{\begin{array}{c} \dot{a} = -\epsilon\xi(a + \sin\beta) + O(\epsilon^2) \\ \dot{\beta} = -\epsilon\left(\sigma^*(a,\beta) + \xi\dfrac{\cos\beta}{a} - \dfrac{3}{8}\rho a^2\right) + O(\epsilon^2) \\ \sigma = \sigma^*(a,\beta) + O(\epsilon). \end{array}\right\} \tag{3.45}$$

As usual, higher order terms in (3.45) can be eliminated, giving rise to an $O(\epsilon)$ approximation for a time length $\tau = O(1/\epsilon)$:

$$\left\{\begin{array}{c} \dot{a} = -\epsilon\xi(a + \sin\beta) \\ \dot{\beta} = -\epsilon\left(\sigma^*(a,\beta) + \xi\dfrac{\cos\beta}{a} - \dfrac{3}{8}\rho a^2\right) \\ \sigma = \sigma^*(a,\beta). \end{array}\right\} \tag{3.46}$$

It is convenient to observe that, although (3.46) contains three equations, only two of them are differential equations. Thus, (3.46) represents a 2D autonomous dynamical system. The evolution of a and β no longer depends on σ, once σ is written as a function of a and β. The last equation is written with the only purpose of tracking the evolution of variable σ.

In summary, the third stage corresponds to a time length $\tau = O(1/\epsilon)$. At this phase of the motion, the averaged system evolves along the slow manifold given by (3.41). Variables a, β and σ obey equations (3.46), with $O(\epsilon)$ precision.

Fig. 3.6 shows a schematic representation of the three different stages of the system dynamics, summing up the results obtained in the present section. Note that, in Fig. 3.6, the use of overbars for the averaged variables is recovered. The most relevant result is that, once the initial transient corresponding to the first two stages has finished, the evolution of variables a and β is governed by equations (3.46) –within an $O(\epsilon)$ error–.

From Fig. 3.6, it is clear that suitable initial conditions for system (3.46) are $\{a_0, \beta_0^*\}$. Recalling definition (3.31), this can be written as $\{a_0, \beta_0 + (\Omega_0 - 1)/d\}$, where $\{a_0, \beta_0, \phi_0, \Omega_0\}$ is the set of initial conditions for system (3.26)

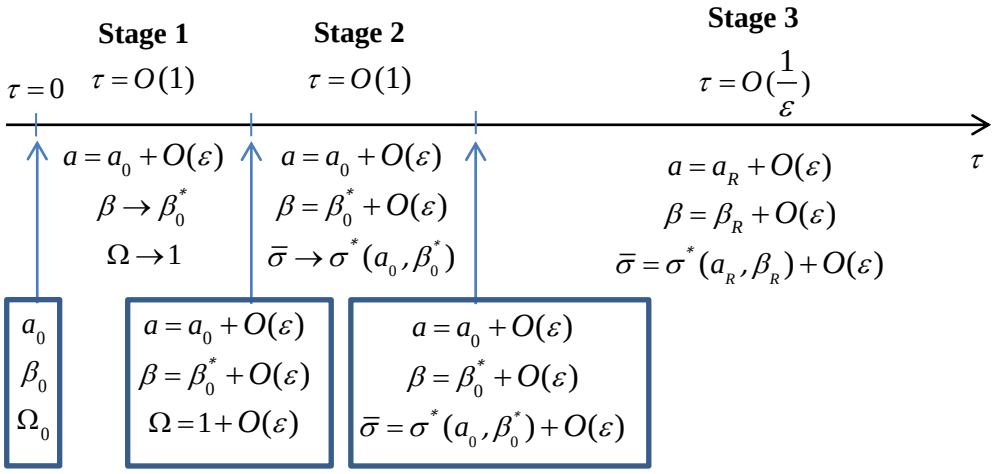

Fig. 3.6 Overview of the system dynamics, with $\{a_R, \beta_R\}$ being the solution of system (3.46) with appropriate initial conditions.

However, we may be interested in a particular set of initial conditions for system (3.10), given as $\{u_0, \dot{u}_0, \phi_0, \dot{\phi}_0\}$. It is, then, convenient, to express the initial conditions for (3.46) as functions of the initial conditions for (3.10):

$$\begin{aligned} a_0 &= \sqrt{u_0^2 + \dot{u}_0^2} \\ \beta_0^* &= \tan^{-1}\left(\frac{-\dot{u}_0}{u_0}\right) - \phi_0 + \frac{\dot{\phi}_0 - 1}{d}, \end{aligned} \tag{3.47}$$

as can be readily deduced from relations (3.20), (3.25) and (3.31).

Recapitulating, we have been able to eliminate from the formulation variable ϕ by Averaging, and variable σ by applying the Singular Perturbation Theory.

3.4 Analysis of the Reduced System

This section focuses on the behaviour of system (3.46), once it has been shown to capture, with $O(\epsilon)$ precision, the dynamics of the original system (3.10) during the third stage of the motion.

Firstly, it is useful to make a comparison between the system under study and its ideal counterpart, where the rotor speed is constant. Clearly, for this ideal case, the equation of motion of the system shown in Fig. 3.1 is given by

$$m\ddot{x} + b\dot{x} + kx + \lambda x^3 = m_1 r \dot{\phi}^2 \cos\phi, \tag{3.48}$$

with $\dot{\phi}$ fixed. Equation (3.48) describes a Duffing oscillator, subjected to harmonic excitation. This is a very well-known problem, which has been widely studied in the literature (Brennan, Kovacic, Carrella, & Waters, 2008; Fidlin, 2006; Nayfeh & Mook, 1995; Thomsen, 2003). Under the assumptions of small damping, small

nonlinearity, small unbalance and near-resonant excitation $\left(\dot{\phi} = 1 + \epsilon\sigma_0\right)$, the Averaging Method can be applied to system (3.48), leading to

$$\left\{\begin{array}{c} \dot{a} = -\epsilon\xi(a + \sin\beta) \\ \dot{\beta} = -\epsilon\left(\sigma_0 + \xi\dfrac{\cos\beta}{a} - \dfrac{3}{8}\rho a^2\right) \end{array}\right\}, \tag{3.49}$$

where all the parameters and variables are defined as in Sections 3.1 and 3.3. It is easy to verify that system (3.49) is exactly the same as (3.46), with the only difference of replacing $\sigma^*(a,\beta)$ by the constant value σ_0. This is a clear illustration of the concept of nonideal excitation. In the ideal case, the rotor speed appears in equations (3.49) as a constant value σ_0, externally imposed by the motor. However, in the nonideal case, the rotor speed enters equations (3.46) as a function of the system vibratory motion, $\sigma^*(a,\beta)$.

It is also important to observe that an ideal motor displays a vertical static characteristic, corresponding to the limit case $d \to -\infty$. The motor is, then, able to generate any torque for the same rotor speed. This suggests the idea that a real motor with a static characteristic of very large slope (in absolute value) is more likely to behave in an ideal manner than another one with a smaller slope.

Fixed points

Going back to the objective of analyzing system (3.46), it is first convenient to look for its fixed points, $\{a_{eq}, \beta_{eq}, \sigma_{eq}\}$:

$$\begin{array}{c} a_{eq} = -\sin\beta_{eq} \\ \sigma^*\left(a_{eq},\beta_{eq}\right) = \dfrac{3}{8}\rho a_{eq}^2 - \xi\dfrac{\cos\beta_{eq}}{a_{eq}} \\ \sigma_{eq} = \sigma^*\left(a_{eq},\beta_{eq}\right). \end{array} \tag{3.50}$$

From the first of equations (3.50), we have

$$\cos\beta_{eq} = -z\sqrt{1-a_{eq}^2}, \qquad z = \pm 1. \tag{3.51}$$

Combining (3.41), (3.50) and (3.51) yields

$$-\frac{c}{d} + \frac{\alpha}{2d}a_{eq}^2 = \frac{3}{8}\rho a_{eq}^2 + z\xi\frac{\sqrt{1-a_{eq}^2}}{a_{eq}}. \tag{3.52}$$

Solutions of (3.52), for both values of z, give a_{eq} for all the fixed points of (3.46). This can be done analytically, but the expressions become cumbersome and difficult to interpret. An alternative procedure is proposed, which leads to the fixed points of (3.46) in a graphical way. To this end, the last of equations (3.46) can be rewritten as

$$c + d\sigma = -\frac{\alpha}{2}a\sin\beta, \tag{3.53}$$

where definition (3.41) has been used. Now, recall the last of equations (3.38), which governs the evolution of the rotor speed for the averaged system:

$$\dot{\sigma} = c + d\sigma + \frac{\alpha}{2}a\sin\beta + O(\epsilon). \tag{3.54}$$

In the light of (3.54), (3.53) can be interpreted as an equilibrium between two torques on the rotor. The left hand term in (3.53) represents the driving torque produced by the motor, while the right hand term represents the resisting torque due to vibration. Thus, the fact that the averaged system is on the slow manifold –which is expressed in equation (3.53)– can be understood as a torque equilibrium condition.

Equation (3.53), particularized for the fixed point $\{a_{eq}, \beta_{eq}, \sigma_{eq}\}$, takes the form

$$c + d\sigma_{eq} = \frac{\alpha}{2} a_{eq}^2, \tag{3.55}$$

where (3.50) has been used. We now define the following functions:

$$\begin{aligned} T_m(\sigma) &\equiv c + d\sigma \\ T_v(a) &\equiv \frac{\alpha}{2} a^2. \end{aligned} \tag{3.56}$$

Clearly, according to the comments below equation (3.54), T_m represents the driving torque produced by the motor, while T_v corresponds to the resisting torque due to vibration. Then, (3.55) can be rewritten as

$$T_m(\sigma_{eq}) = T_v(a_{eq}), \tag{3.57}$$

which is the torque equilibrium condition, particularized for the fixed point.

In order to solve (3.57) in a graphical way, it would be desirable to write both torques explicitly in terms of σ_{eq}. However, this would in turn need explicitly writing a_{eq} in terms of σ_{eq}, which produces long and complicated expressions. Thus, an implicit procedure for the graphical representation is proposed. Combining (3.50) and (3.51) results in

$$\sigma_{eq} = \sigma_v(z, a_{eq}), \tag{3.58}$$

where function $\sigma_v(z, a)$ is defined as

$$\sigma_v(z, a) \equiv \frac{3}{8}\rho a^2 + z\xi \frac{\sqrt{1 - a^2}}{a}. \tag{3.59}$$

The proposed representation can be constructed as follows: first, graph T_m versus σ according to (3.56). Then, graph on the same plot the parametric curve given by

$\{\sigma_v(z,a), T_v(a)\}$, for $z = \pm 1$ and $a \in (0,1]$. The fact that a is strictly positive comes from the definition of a as the radius of a polar coordinate transformation –see (3.20)–. On the other hand a_{eq} cannot be greater than 1, according to the first of equations (3.50).

The above procedure gives rise to a plot like that shown in Fig. 3.7. Considering equation (3.57), the fixed points can be found as the intersections of the two torque curves. In the particular case displayed in Fig. 3.7, there are three equilibrium points, marked with circles. Note that the curve associated to the vibration torque is composed of two branches, which collide at the maximum of the curve. They correspond to the two possible values of parameter z, as specified in Fig. 3.7.

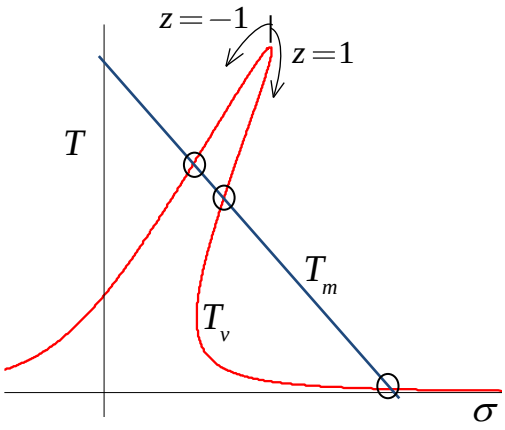

Fig. 3.7 Fixed points of system (3.46)

We note that the 'Sommerfed effect', which was described in the introduction, can be readily explained by using Fig. 3.7. For such an explanation, the interested reader can refer to (Blekhman, 2000; Dimentberg et al., 1997; Kononenko, 1969; Nayfeh & Mook, 1995).

Stability Analysis

Once the fixed points of the reduced system have been obtained, it is convenient to investigate their stability. For a 2D system, this reduces to calculating the trace and determinant of the jacobian matrix, evaluated at the equilibrium point of interest:

$$J_{eq} = \epsilon \begin{bmatrix} -\xi & z\xi R_{eq} \\ \left(-\frac{\alpha}{2d} + \frac{3\rho}{4}\right) a_{eq} - \frac{z\xi R_{eq}}{a_{eq}^2} & -\frac{z\alpha a_{eq} R_{eq}}{2d} - \xi \end{bmatrix}, \tag{3.60}$$

where R_{eq} stands for $\sqrt{1 - a_{eq}^2}$.

The conditions for a fixed point to be asymptotically stable are

C1. $tr(J_{eq}) < 0$ (3.61)

C2. $det(J_{eq}) > 0$. (3.62)

After some algebra, these conditions can be expressed as

C1. $\frac{z\alpha a_{eq} R_{eq}}{4d} + \xi > 0$ (3.63)

C2. $\begin{Bmatrix} \frac{1}{\eta} - \frac{1}{d} < 0, & if\ z = 1 \\ \frac{1}{\eta} - \frac{1}{d} > 0, & if\ z = -1 \end{Bmatrix}$, (3.64)

where η denotes the slope of the T_v curve at the considered equilibrium point (see Fig. 3.8 and Fig. 3.9), and has the expression

$$\frac{1}{\eta} = -\frac{z\xi}{\alpha a_{eq}^3 R_{eq}} + \frac{3\rho}{4\alpha}, \tag{3.65}$$

as can be deduced from (3.56), (3.59).

Conditions (3.63) and (3.64) are now applied to evaluate stability regions in different scenarios. The procedure is as follows. Consider parameters α, ξ, ρ fixed, so that the T_v curve –see Fig. 3.7– is fixed too. Consider a pair of values (c, d) which gives a particular curve $T_m(\sigma)$. The intersections between the two curves represent the equilibrium points of the system. Select one of them –if there are more than one– and let parameters (c, d) vary in such a way that the selected equilibrium point remains an equilibrium point. In other words, let parameters (c, d) vary so as to make the curve $T_m(\sigma)$ rotate around the selected equilibrium point, satisfying restriction $d < 0$. Finally, use conditions (3.63) and (3.64) to analyze how the stability of the fixed point is affected by the slope d of the motor characteristic.

Fig. 3.8 displays the outcome of applying the above procedure for a fixed point located at the left branch of the vibration torque curve $(z = -1)$. Two scenarios are considered, depending on the sign of slope η, evaluated at the fixed point under consideration. It is observed that a change of stability occurs when both torque curves become tangent $(d = \eta)$. This can be shown to correspond to a transcritical bifurcation. Note that, in Fig. 3.8, the motor curve corresponding to $d = \eta$ has been directly labeled as $d = \eta$, instead of $T_m(d = \eta)$. This shortened notation will be widely used in the figures of the document.

Fig. 3.9 shows analogous results for a fixed point located at the right branch of the vibration torque curve $(z = 1)$. The system behavior is richer in this case, since stability may change in two different ways, depending on the comparison $\eta \lessgtr d_H$ where d_H is defined below.

We define critical slope d_H as the value of d which makes $\mathrm{tr}(J_{eq}) = 0$. Recall that the stability condition $\mathrm{tr}(J_{eq}) < 0$ was written as (3.63). Therefore, d_H takes the form

$$d_H(\alpha, \xi, a_{eq}) = -\frac{\alpha a_{eq} R_{eq}}{4\xi}. \tag{3.66}$$

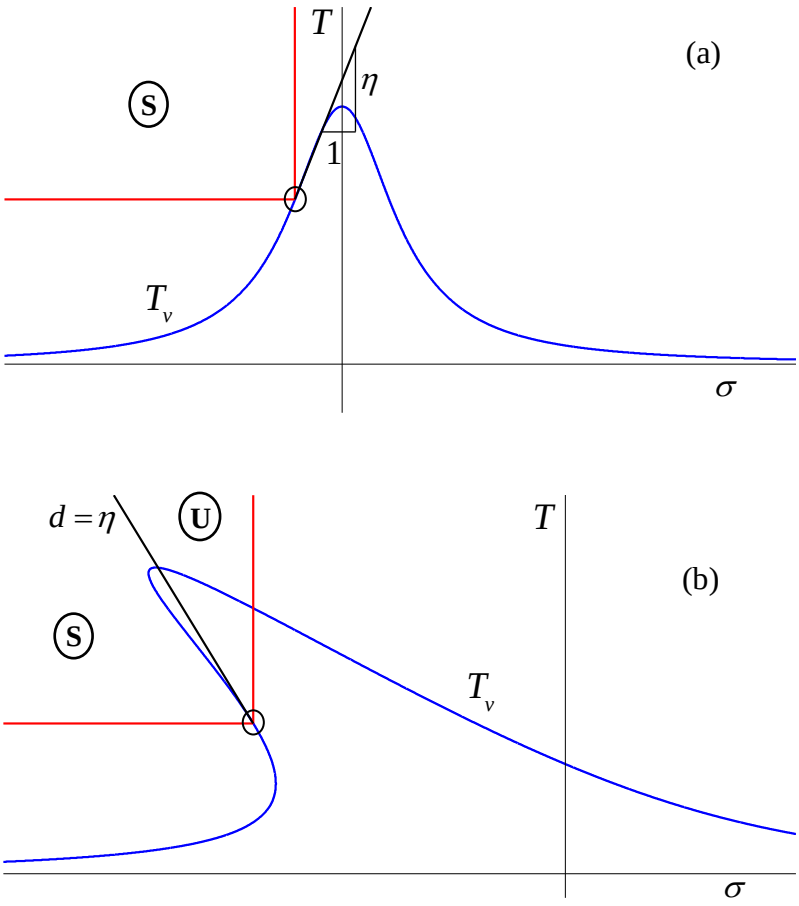

Fig. 3.8 Stability regions for $z = -1$. *S* and *U* label the stable and unstable regions, respectively. (a) $\eta > 0$, (b) $\eta < 0$

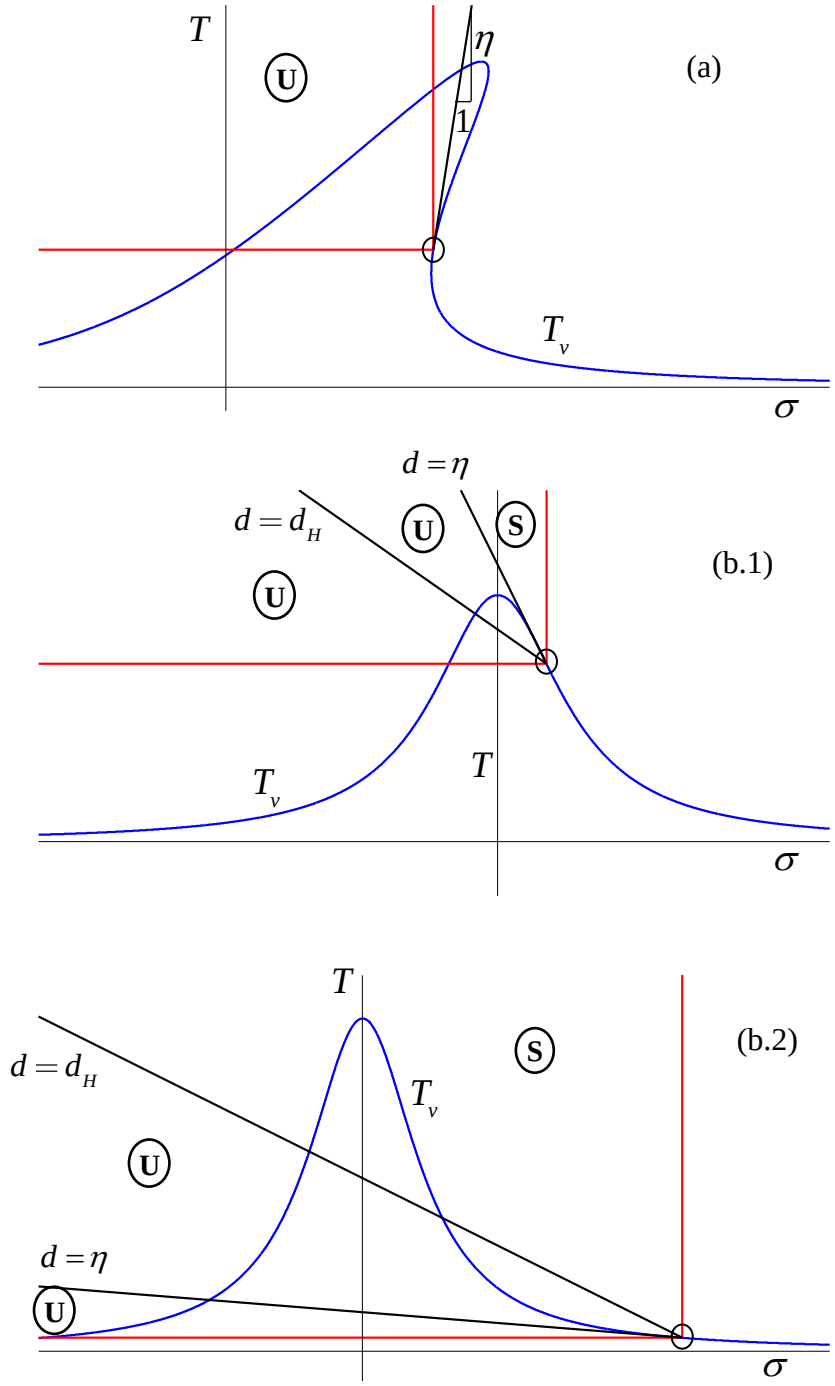

Fig. 3.9 Stability regions for $z = 1$. *S* and *U* label the stable and unstable regions, respectively.

(a) $\eta > 0$, (b.1) $\eta < d_H < 0$, (b.2) $d_H < \eta < 0$

Below, the different possibilities for $z = 1$ are considered.

If $\eta > 0$ (Fig. 3.9a), condition **C2** is never fulfilled, so the fixed point is unstable regardless the value of slope d.

If $\eta < d_H < 0$ (Fig. 3.9b.1), the critical condition –i.e. the one which produces the stability change– is **C2**. In this case, a transcritical bifurcation can be shown to occur when both torque curves are tangent $(d = \eta)$. Note that this result is analogous to that obtained for the left branch (Fig. 3.8).

If $d_H < \eta < 0$ (Fig. 3.9b.2), the critical condition is **C1**. In this case, the stability change occurs at $d = d_H$ through a Hopf bifurcation, after which parameter d_H was named.

To better understand the nature of the different bifurcations, notice the following correspondence between conditions **C1** and **C2,** and the eigenvalues of J_{eq}, according to (3.61), (3.62):

- **C1** is the critical condition $\rightarrow \begin{Bmatrix} \mathrm{tr}(J_{eq}) = 0 \\ \det(J_{eq}) > 0 \end{Bmatrix}$ both eigenvalues of J_{eq}, being complex conjugates, cross the imaginary axis.

- **C2** is the critical condition $\rightarrow \begin{Bmatrix} \mathrm{tr}(J_{eq}) < 0 \\ \det(J_{eq}) = 0 \end{Bmatrix}$ a single, real eigenvalue of J_{eq} crosses the imaginary axis.

It is worth stressing that most of the literature on nonideal excitations maintains that stability changes when the torque curves become tangent (Blekhman, 2000; Dimentberg et al., 1997; Kononenko, 1969; Nayfeh & Mook, 1995). This is consistent with our results, with the important exception of case $z = 1, d_H < \eta < 0$ (Fig. 3.9b.2). Thus, one of the main contributions of this Chapter consists in having found a case where the usual rule of thumb for stability is not valid. In this scenario, the stable region is in fact smaller than predicted by usual theories (see Fig. 3.9b.2).

Not taking this into account may be dangerous in real applications, since it could lead to unexpected instabilities.

Finally, the conditions for the existence of a Hopf bifurcation in the linear case ($\rho = 0$) are investigated in more detail. As stated above, a Hopf bifurcation exists if

$$z = 1, \qquad d_H < \eta < 0. \tag{3.67}$$

By substituting expressions (3.65) and (3.66) in (3.67), for $\rho = 0$, we have

$$z = 1, \qquad -\frac{\alpha a_{eq} R_{eq}}{4\xi} < -\frac{\alpha a_{eq}^3 R_{eq}}{\xi} < 0. \tag{3.68}$$

Simplifying (3.68) yields

$$z = 1, \qquad a_{eq} < 0.5. \tag{3.69}$$

Therefore, if the system under study has no structural nonlinearity ($\rho = 0$), it is particularly easy to predict the existence of a Hopf bifurcation, by simply checking condition (3.69).

3.5 Classification of the Hopf bifurcations

Clearly, it would be of great interest to characterize the Hopf bifurcation encountered in last section as subcritical or supercritical. In the former case, an unstable limit cycle coexists with the stable fixed point, while in the latter case there is a stable limit cycle coexisting with the unstable fixed point, as represented in Fig. 3.10.

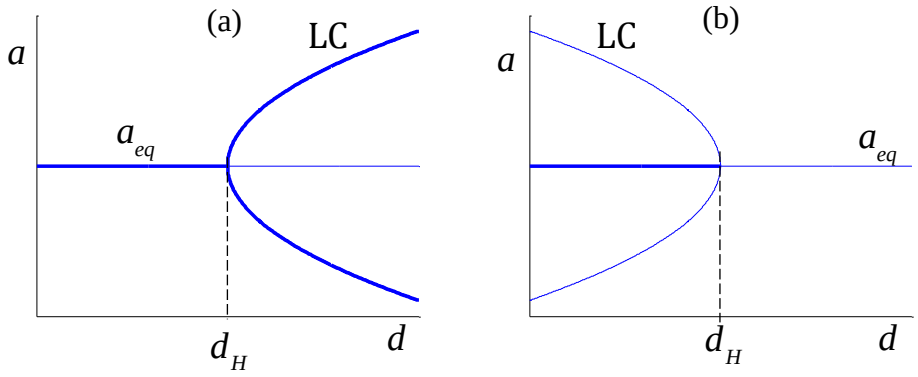

Fig. 3.10 Classification of Hopf bifurcations.
(a) Supercritical (b) Subcritical
Thick (thin) lines represent stable (unstable) solutions.

Characterizing the bifurcations require several transformations of system (3.46), that are detailed below.

Transformation to Cartesian Coordinates

We assume the system parameters are such that there exists a fixed point on the right branch of curve T_v $(z = 1)$, satisfying condition (3.67) and, thereby, undergoing a Hopf bifurcation. By defining change of variables

$$\left.\begin{matrix}\tilde{x} = a\cos\beta \\ \tilde{y} = a\sin\beta\end{matrix}\right\}, \tag{3.70}$$

system (3.46), particularized for the bifurcation point $(d = d_H)$, can be rewritten as

$$\left.\begin{matrix}\dot{\tilde{x}} = -\epsilon\left[\xi\tilde{x} + \frac{c}{d_H}\tilde{y} + \frac{\alpha}{2d_H}\tilde{y}^2 + \frac{3}{8}\rho\tilde{y}(\tilde{x}^2+\tilde{y}^2)\right] \\ \dot{\tilde{y}} = \epsilon\left[-\xi - \xi\tilde{y} + \frac{c}{d_H}\tilde{x} + \frac{\alpha}{2d_H}\tilde{x}\tilde{y} + \frac{3}{8}\rho\tilde{x}(\tilde{x}^2+\tilde{y}^2)\right]\end{matrix}\right\}. \tag{3.71}$$

Displacement of the origin

In order to characterize the bifurcation, it is convenient to locate the origin of the coordinate system at the fixed point under investigation. Then, we define change of variables

$$\begin{Bmatrix} x = \tilde{x} - a_{eq}\cos\beta_{eq} \\ y = \tilde{y} - a_{eq}\sin\beta_{eq} \end{Bmatrix}. \tag{3.72}$$

Using the new coordinates, system (3.71) takes the form

$$\begin{Bmatrix} \dot{x} = \epsilon\left[-\left[\xi + \frac{3}{4}\rho a^3 R\right]x - \left[\frac{3}{4}\rho a^4 + \xi\left(\frac{2a}{R} - \frac{R}{a}\right)\right]y + \frac{3}{8}\rho a^2 x^2 + \left[\frac{2\xi}{aR} + \frac{9}{8}\rho a^2\right]y^2 + \frac{3}{4}\rho aRxy - \frac{3}{8}\rho y[x^2 + y^2]\right] \\ \dot{y} = \epsilon\left[\left[\frac{3}{4}\rho a^2 R^2 - \xi\frac{R}{a}\right]x + \left[\xi + \frac{3}{4}\rho a^3 R\right]y - \frac{9}{8}\rho aRx^2 - \frac{3}{4}\rho aRy^2 - \left[\frac{2\xi}{aR} + \frac{3}{4}\rho a^2\right]xy + \frac{3}{8}\rho x[x^2 + y^2]\right] \end{Bmatrix}. \tag{3.73}$$

where a_{eq} and R_{eq} are shortly written as a and R, respectively, in order to make the expression more manageable. This abbreviated notation will also be used in the Appendix. Note that system (3.73) is of the form

$$\begin{bmatrix} \dot{x} \\ \dot{y} \end{bmatrix} = \epsilon\left(\boldsymbol{A}\begin{bmatrix} x \\ y \end{bmatrix} + \boldsymbol{h}(x, y)\right) \tag{3.74}$$

where matrix $\boldsymbol{A}$ is given by

$$\boldsymbol{A} = \begin{bmatrix} -\left(\xi + \frac{3}{4}\rho a_{eq}^3 R_{eq}\right) & -\left[\frac{3}{4}\rho a_{eq}^4 + \xi\left(\frac{2a_{eq}}{R_{eq}} - \frac{R_{eq}}{a_{eq}}\right)\right] \\ \frac{3}{4}\rho a_{eq}^2 R_{eq}^2 - \xi\frac{R_{eq}}{a_{eq}} & \xi + \frac{3}{4}\rho a_{eq}^3 R_{eq} \end{bmatrix} \tag{3.75}$$

and vector $\boldsymbol{h}(x, y)$ contains the nonlinear terms of the system.

Transformation to the real eigenbasis of matrix $\boldsymbol{A}$

A new change of variables, using the real eigenbasis of matrix $\boldsymbol{A}$, is defined:

$$\begin{bmatrix} x \\ y \end{bmatrix} = \boldsymbol{T} \begin{bmatrix} z_1 \\ z_2 \end{bmatrix}, \tag{3.76}$$

where the columns of matrix $\boldsymbol{T}$ are the real and imaginary parts of the complex conjugate eigenvectors of $\boldsymbol{A}$, denoted by $\boldsymbol{v}_{1,2}$:

$$\boldsymbol{v}_{1,2} = \begin{bmatrix} c_1 \\ c_2 \end{bmatrix} \pm i \begin{bmatrix} \omega_0 \\ 0 \end{bmatrix} \rightarrow \boldsymbol{T} = \begin{bmatrix} c_1 & \omega_0 \\ c_2 & 0 \end{bmatrix}, \tag{3.77}$$

with

$$\begin{aligned} c_1 &= \xi + \frac{3}{4}\rho a_{eq}^3 R_{eq} \\ c_2 &= \xi \frac{R_{eq}}{a_{eq}} - \frac{3}{4}\rho a_{eq}^2 R_{eq}^2 \\ \omega_0 &= \sqrt{\left(\frac{1 - 4a_{eq}^2}{a_{eq}^2}\right)\xi^2 - \frac{3}{4}\rho \xi a_{eq} R_{eq}}. \end{aligned} \tag{3.78}$$

System (3.73), written in terms of the new variables, takes the form

$$\begin{bmatrix} \dot{z}_1 \\ \dot{z}_2 \end{bmatrix} = \epsilon \left(\begin{bmatrix} 0 & -\omega_0 \\ \omega_0 & 0 \end{bmatrix} \begin{bmatrix} z_1 \\ z_2 \end{bmatrix} + \begin{bmatrix} f(z_1, z_2) \\ g(z_1, z_2) \end{bmatrix} \right), \tag{3.79}$$

where functions f and g, containing the nonlinear terms of the system, can be written as Taylor series:

$$f(z_1, z_2) = \sum_{i+j=2}^{3} \frac{1}{i!\,j!} f_{ij} z_1^i z_2^j$$
$$g(z_1, z_2) = \sum_{i+j=2}^{3} \frac{1}{i!\,j!} g_{ij} z_1^i z_2^j \tag{3.80}$$

Coefficients f_{ij} and g_{ij} are specified in the Appendix.

Note that the system is finally written in the form (2.21). Thus, the result explained in Section 2.4 can be directly applied.

Transformation to Normal Form

System (3.79) can be transformed to its Normal Form by a standard procedure (Guckenheimer & Holmes, 1983; Kuznetsov, 1998), as described in Section 2.4:

$$\dot{r} = \epsilon \delta r^3, \tag{3.81}$$

where parameter δ is obtained as

$$16\delta = \left\{ \begin{array}{c} f_{30} + f_{12} + g_{21} + g_{03} \\ + \frac{1}{\omega_0}[f_{11}(f_{20} + f_{02}) - g_{11}(g_{20} + g_{02}) + f_{02}g_{02} - f_{20}g_{20}] \end{array} \right\}. \tag{3.82}$$

In summary, it can be said that, after a large number of variable transformations, system (3.46) can be written as (3.81), from which it is concluded that the bifurcation is supercritical (subcritical) if $\delta < 0$ ($\delta > 0$).

Despite the fact that coefficients f_{ij} and g_{ij} are of rather complicated form, we find –with the aid of software for symbolic computation (Matlab)– that the condition for supercriticality or subcriticality can be expressed in a surprisingly simple manner:

$$\begin{aligned}\text{Supercritical} \Rightarrow \delta < 0 \Rightarrow \rho < -\frac{8\xi}{3a_{eq}R_{eq}} \\ \text{Subcritical} \Rightarrow \delta > 0 \Rightarrow \rho > -\frac{8\xi}{3a_{eq}R_{eq}}\end{aligned} \tag{3.83}$$

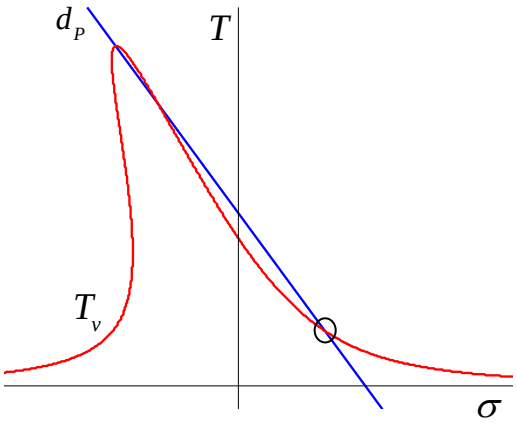

Fig. 3.11 Definition of slope d_P

From (3.83), it is clear that a nonlinearity of the softening type $(\rho < 0)$ is needed to have a supercritical bifurcation.

It is also worth noting that conditions (3.83) admit a very clear graphical interpretation. Consider a curve T_m which intersects T_v at the equilibrium point under consideration and also at the **peak** of curve T_v. Let d_P denote the slope of this particular motor characteristic, as depicted in Fig. 3.11.

In order to obtain d_P, the coordinates of the two points defining the straight line are defined below. First, the highest peak of curve T_v can be shown to correspond to $a = 1$. Substituting this condition in (3.56) and (3.59) yields

$$\sigma = \frac{3}{8}\rho, \qquad T = \frac{\alpha}{2} \tag{3.84}$$

On the other hand, the (σ, T) coordinates of the equilibrium point under study are directly given in (3.56) and (3.59):

$$\sigma = \frac{3}{8}\rho a_{eq}^2 + \xi \frac{R_{eq}}{a_{eq}}, \qquad T = \frac{\alpha}{2} a_{eq}^2 \tag{3.85}$$

Then, from (3.84) and (3.85), the expression of d_P can be readily obtained:

$$\frac{1}{d_P} = \frac{3\rho}{4\alpha} - \frac{2\xi}{\alpha a_{eq} R_{eq}}, \tag{3.86}$$

By comparing (3.86) and (3.66), conditions (3.83) can be expressed as

$$\begin{array}{l} \text{Supercritical} \Rightarrow d_H < d_P \\ \text{Subcritical} \Rightarrow d_H > d_P. \end{array} \tag{3.87}$$

This last manner of characterizing the bifurcation is certainly appealing from a graphical point of view, since the basic information about the bifurcation can be directly observed from the torque–speed curves, as shown in Fig. 3.12 for two particular examples.

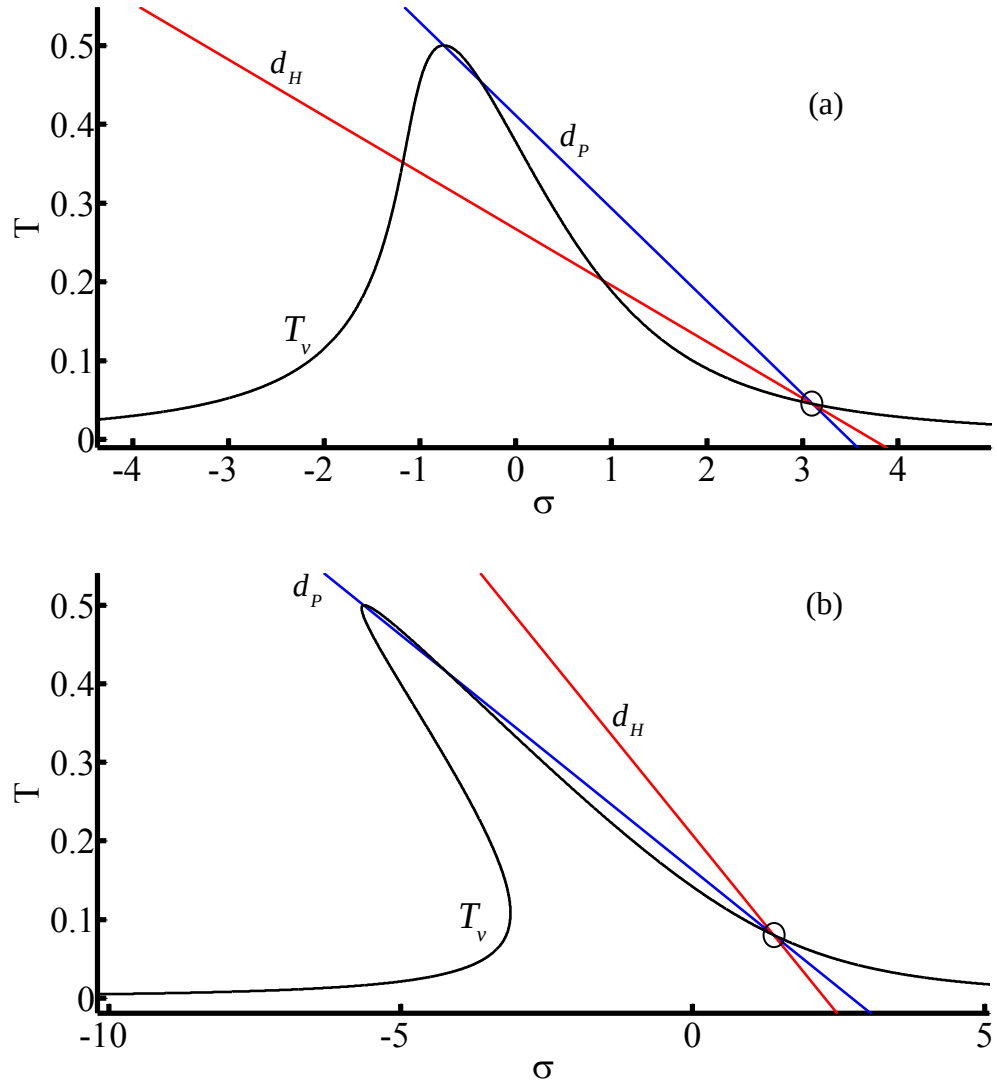

Fig. 3.12 Examples of (a) subcritical and (b) supercritical bifurcations.

(a) $\xi = 1, \alpha = 1, \rho = -2, a_{eq} = 0.3$

(b) $\xi = 1, \alpha = 1, \rho = -15, a_{eq} = 0.4$

3.6 Conditions under which all System Trajectories are Attracted towards a Limit Cycle

In Section 3.5, a simple condition has been obtained to ascertain whether the Hopf bifurcation under study is subcritical or supercritical, which in turn allows predicting the kind of limit cycle generated by the bifurcation (see Fig. 3.10). Although this distinction is relevant, it is based on a local analysis and, consequently, it only gives local information about the system behaviour. This is so in two senses: the analysis of Section 3.5 provides insight into the system dynamics

- for values of d close enough to d_H (results are local in the parameter space) and

- for trajectories close enough to the investigated fixed point (results are local in the phase plane).

In view of the aforementioned limitations, this section addresses a new global result that complements those of Section 3.5. It will be shown that, under certain circumstances, the Poincaré-Bendixson (P-B) theorem can be used to prove that all trajectories of the system under study are attracted towards a limit cycle. For a brief explanation of the theorem, see Section 2.5.

First, it can be easily deduced from (3.46) that

$$a > 1 \Rightarrow \dot{a} < 0. \tag{3.88}$$

Let a and β represent polar coordinates on the phase plane, according to (3.70), and let D denote a circle centred at the origin of the phase plane with a radius slightly greater than 1, say 1.01. From (3.88), it can be said that every trajectory starting outside region D will enter D and remain inside for all subsequent time. Obviously, trajectories starting inside D will also remain inside forever. This kind of behavior would present D as a suitable candidate for the role of region R in the P-B theorem –see Section 2.5 –, if it were not for the presence of fixed points inside D.

Consider now the following particular situation:

$$\begin{Bmatrix}\text{The system has only one fixed point}\\ z = 1, \qquad d_H < d < \eta < 0\end{Bmatrix}, \tag{3.89}$$

whose torque curves are depicted in Fig. 3.13. We suppose that the only fixed point of the system is on the right branch of curve T_v and undergoes a Hopf bifurcation. It is also assumed that the actual slope of the motor characteristic is $d > d_H$ and, therefore, the equilibrium is unstable.

First, let us prove that the fixed point is a repeller. Since the equilibrium is already known to be unstable, we only need to prove that it is not a saddle. Let J_{eq} be the jacobian matrix of system (3.46), evaluated at the equilibrium point. Taking into account that a saddle point has two real eigenvalues λ_1, λ_2 with different signs, we can state

$$\text{If } det(J_{eq}) = \lambda_1\,\lambda_2 > 0, \qquad \text{then the equilibrium is not a saddle.} \tag{3.90}$$

With some simple algebra, it can be shown that, for $z = 1$, condition $det(J_{eq}) > 0$ can be written as $d < \eta$. Then, it is clear that, for a fixed point satisfying (3.89), we have $det(J_{eq}) > 0$. Thus, the equilibrium is a repeller.

A new region Q is now defined as D minus a circle of infinitesimal radius around the equilibrium point. From the above considerations –all trajectories enter D and the fixed point is a repeller–, it is clear that the flow on the boundary of Q is directed inwards, as depicted in Fig. 3.14.

In summary, a closed, bounded region Q of the phase plane has been obtained, which contains no fixed points and such that all trajectories of the system enter Q and remain inside forever. Then, all conditions of the P-B theorem are fulfilled, and it can be assured that any trajectory of the system is attracted towards a closed orbit as $t \to \infty$, if it is not a closed orbit itself.

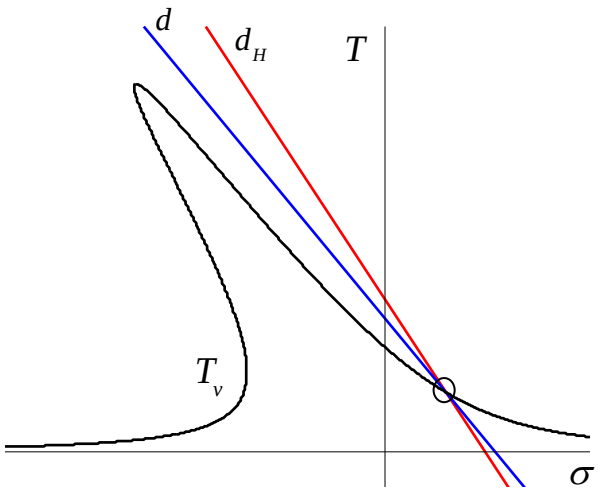

Fig. 3.13 Schematic view of the torque curves corresponding to conditions (3.89)

Finally, it should be noted that, although the P-B theorem does not guarantee that all trajectories tend to the same closed orbit, all the numerical experiments conducted within this thesis show the presence of only one stable limit cycle, namely that created by the Hopf bifurcation. This suggests that, for a system verifying (3.89), all the system dynamics is attracted towards a unique limit cycle.

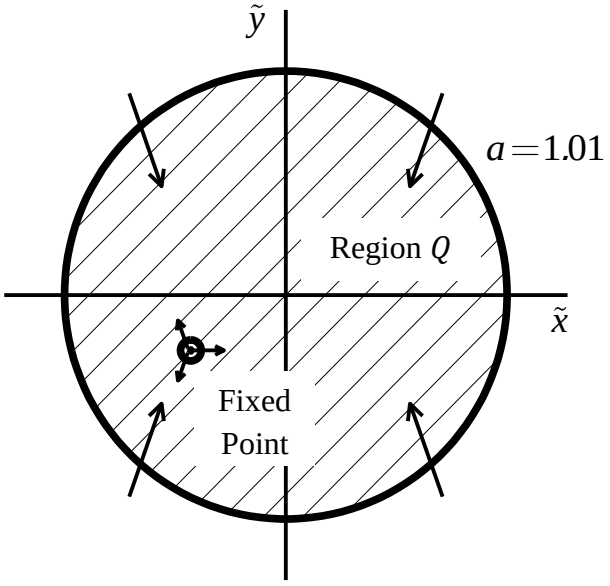

Fig. 3.14 Flow on the boundary of region Q (dashed), under conditions (3.89)

3.7 Discussion

Time Validity

A crucial point in any perturbation analysis is the time scale for which the obtained approximate solution is valid. It has been shown in Section 3.3 that the solution given by the reduced system is valid, at least, for a time scale $\tau = O(1/\epsilon)$ –see Fig. 3.6–.

However, the situation is even better than that. As described in Section 2.1 (Averaging with Attraction), the asymptotic approximations attained through averaging are valid for all time, whenever they are attracted by a stable fixed point or a stable limit cycle. In the latter case, the uniform validity holds for all variables except the angular one, i.e. the variable which measures the flow on the limit cycle. As will be seen later, all the numerical solutions obtained in Chapter 4 fulfill the above condition of attraction.

Comparison with other authors' results

In this subsection, the presented approach and results are compared to some proposed by other authors.

First of all, as far as the authors know, there has been no attempt in the literature to use the SPT for the analysis of nonideally excited systems. Thus, the analytical procedure addressed in this Chapter appears to be a novel approach to the problem.

On the other hand, the possibility of a Hopf bifurcation on the right branch of the vibration torque curve (Fig. 3.9b.2) has been addressed. An important implication of this result is that the stability of the stationary solutions near resonance does not only depends on the comparison between the slopes of the two torque curves ($\eta \lessgtr d$), as commonly stated in the literature (Blekhman, 2000; Dimentberg et al., 1997; Kononenko, 1969; Nayfeh & Mook, 1995). Let us try to explain this divergence in the results.

Kononenko's book (Kononenko, 1969) is one of the most relevant references in the subject. He considered several linear and nonlinear systems excited by nonideal motors. By using the averaging method, he was able to analytically investigate the stationary motions of the motor and their stability. His approach was as follows. Considering the rotor speed to be in the vicinity of resonance, he expanded it as

$$\dot{\phi} = 1 + \Delta, \qquad \Delta = \epsilon\sigma. \tag{3.91}$$

Thus, he found equations of motion of the form

$$\left\{\begin{array}{c} \dot{a} = O(\epsilon) \\ \dot{\beta} = -\epsilon\sigma + O(\epsilon) \\ \dot{\Delta} = O(\epsilon) \\ \dot{\phi} = 1 + \Delta \\ \Delta = \epsilon\sigma \end{array}\right\}, \tag{3.92}$$

which is a system analogous to (3.36). Then, he averaged (3.92) over the fast angle ϕ, obtaining an averaged system of the form

$$\left\{\begin{array}{c} \dot{\bar{a}} = O(\epsilon) \\ \dot{\bar{\beta}} = -\epsilon\bar{\sigma} + O(\epsilon) \\ \dot{\bar{\Delta}} = O(\epsilon) \\ \bar{\Delta} = \epsilon\bar{\sigma} \end{array}\right\}. \tag{3.93}$$

This averaged system is completely analogous to system (3.38), obtained in the present chapter. The only difference lies in the fact that Kononenko used the evolution equation for $\bar{\Delta}$, instead of that for $\bar{\sigma}$. This has an important consequence. From (3.38), it is clear that $\bar{\sigma}$ is a fast variable, while $\bar{a}$ and $\bar{\beta}$ are slow. This property was exploited in Section 3.3 to obtain a reduced 2D system (3.46), by using the SPT. The analysis of the fixed points of this reduced system and their stability has revealed the possibility of Hopf bifurcations, and conditions for their appearance have been derived in Section 3.4. However, the form of the averaged equations (3.93), used by Kononenko, doesn't evidence so clearly the fact that $\bar{\sigma}$ is a fast variable. Then, instead of taking advantage of this separation in the time scales through the SPT, he directly investigated system (3.93), which did not allow him to obtain analytical conditions for the existence of Hopf bifurcations.

While several authors followed Kononenko's approach (Dimentberg et al., 1997; Nayfeh & Mook, 1995), Blekhman proposed a completely different one, based on the 'method of direct separation of motions' (Blekhman, 2000). With this procedure, he came to the conclusion that the system dynamics is governed by equation

$$I\ddot{\phi} = L_m(\dot{\phi}) + V(\dot{\phi}) \tag{3.94}$$

where dimensional variables have been used. In (3.94), $V(\dot{\phi})$ represents the torque on the rotor due to vibration. Based on this equation, Blekhman deduced the same

result as Kononenko regarding the stability of stationary solutions, namely, that stability changes when the driving torque curve and the vibration torque curve are tangent.

It is worth noting that Blekhman's approach is not applicable under the assumptions of the present chapter. The reason is that, in general, the torque on the rotor due to vibration depends on the linear motion of the system, as observed in the second of equations (3.1). This feature is maintained in the averaged system (3.38) obtained in this Chapter, where the vibration torque appears as a function of a, β.

On the contrary, in (Blekhman, 2000), the vibration torque is written as a function of the rotor speed –see (3.94)–, which implies neglecting the dynamics associated to variables a and β. This would only be valid if the rotor speed was a much slower variable than those associated to the linear vibration (a, β). To better understand this point, suppose that, in system (3.1), the rotor inertia was $O(1/\epsilon)$, with the rest of the parameters being $O(1)$. Then, writing $I = \tilde{I}/\epsilon$, system (3.1) would take the form

$$\left\{\begin{matrix} m\ddot{x} + b\dot{x} + kx + \lambda x^3 = m_1 r\dot{\phi}^2 \cos\phi + O(\epsilon) \\ \tilde{I}\ddot{\phi} = \epsilon\left[A + D\dot{\phi} + m_1 r\ddot{x}\sin\phi\right] \end{matrix}\right\}. \tag{3.95}$$

With this particular scaling of the parameters, Blekhman's approach would be valid because the dynamics of linear motion would be much faster than that of the rotor speed. Then, as predicted by the SPT, the variables associated to the linear motion would be slaved to the rotor speed, in the same sense that fast variable $\boldsymbol{y}$ becomes slaved to slow variable $\boldsymbol{x}$ in Section 2.3 (see Fig. 2.1). This would in turn allow writing the vibration torque as a function of the rotor speed, as in (3.94).

As pointed out above, the assumptions of the present chapter (3.7)-(3.9) are not compatible with the results in (Blekhman, 2000), because the required difference in the time scales of the different variables is not satisfied. This can be observed in the averaged system (3.38), where we find $\left\{\dot{a} = O(\epsilon), \dot{\beta} = O(\epsilon), \dot{\sigma} = O(1)\right\}$.

More recently, Bolla et al. (Bolla, M. R., Balthazar, J. M., Felix, J. L. P., Mook, 2007) used the Multiple Scales method to solve the same problem studied in this Chapter, under the same assumptions. However, after obtaining system (3.38), they conducted the stability analysis considering only the first two equations in (3.38) and taking σ as a fixed parameter. As explained at the beginning of Section 3.4, this corresponds to studying the ideal case, where the rotor speed is externally imposed. Consequently, they did not find the Hopf bifurcations that have been identified within this work. In fact, Bolla et al. explicitly stated the impossibility of Hopf bifurcations: '*This fact eliminates the possibility of a pair eigenvalue pure imaginary, so this eliminates Hopf bifurcation kind*'. Thus, the present Chapter can be envisaged as an extension of (Bolla, M. R., Balthazar, J. M., Felix, J. L. P., Mook, 2007), where new bifurcations are encountered due to the nonideal interaction between motor and vibrating system.

4 THE CASE OF LARGE SLOPE OF THE MOTOR CHARACTERISTIC: NUMERICAL SIMULATIONS

This Chapter presents two main purposes. First, a numerical investigation of the reduced system (3.46) is conducted in order to analyze the global bifurcations of limit cycles. While Section 3.5 analyzes how the Hopf bifurcations give rise to the appearance of limit cycles, Section 4.1 gives some insight about the dynamical mechanisms whereby the limit cycles are destroyed. A second section is presented where, by comparing numerical solutions of the original and reduced systems – (3.10) and (3.46), respectively– the proposed approach is validated. The objective is

to demonstrate that the conclusions attained for the reduced system are also valid for the original system.

4.1 Global Bifurcations of the Limit Cycles

In Section 3.5, the creation of limit cycle oscillations (LCOs) through Hopf bifurcations has been investigated. Now, the opposite question is examined: once a limit cycle is born, does it exist for every $d > d_H$ in the supercritical case –for every $d < d_H$ in the subcritical case–, or is it destroyed at any point? In the latter case, it would also be interesting to know the dynamical mechanism which makes the limit cycle disappear.

The aim of this Section is to analyse the global dynamics of the system, tracking the evolution of the limit cycles in order to find out how they are destroyed –if they are destroyed at all–. Since this task is in general too difficult to be carried out analytically, we resort to numerical computation.

The Subcritical Case

Consider the following set of dimensionless parameters:

$$\xi = 1, \qquad \alpha = 1, \qquad \rho = 0, \qquad a_{eq} = 0.3, \qquad z = 1, \tag{4.1}$$

which might be associated to dimensional parameters

$$\left\{ \begin{array}{c} m = 1\text{kg} \\ k = 1\,\text{N/m} \\ b = 0.002\,\text{Ns/m} \\ m_1 = 0.001\text{kg} \\ \lambda = 0\,\text{N/m}^3 \\ r = 0.1\text{m} \\ I = 5 \cdot 10^{-3}\text{m}^2\text{kg} \end{array} \right\}, \tag{4.2}$$

with $\epsilon = 0.001$. Obviously, (4.2) is only one of the many possible sets of dimensional parameters giving rise to (4.1).

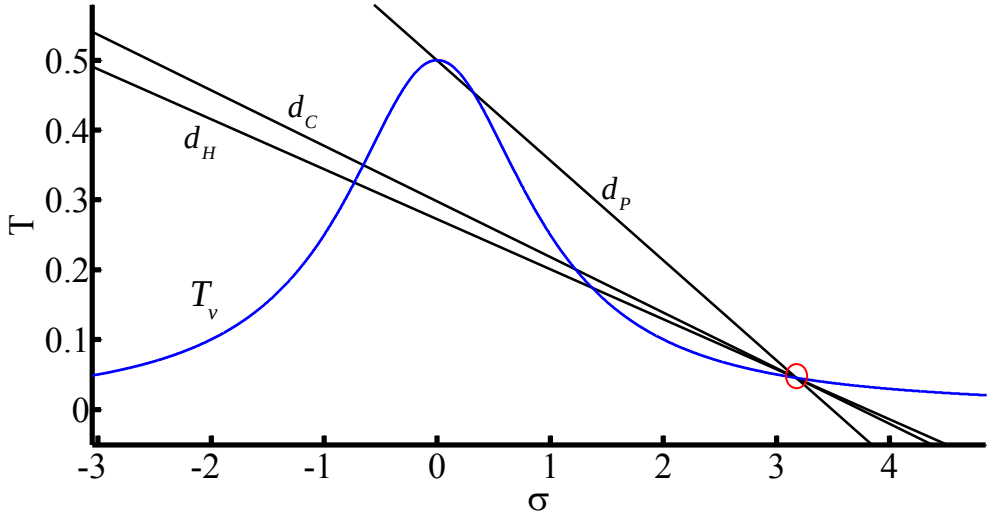

Fig. 4.1 Torque curves corresponding to parameters (4.1)

By using equations (3.66) and (3.86), slopes d_H and d_P can be obtained, as depicted in Fig. 4.1.

$$d_H = -0.0715, \qquad d_P = -0.1431 \tag{4.3}$$

According to criterion (3.87), the Hopf bifurcation is found to be subcritical. Thus, as represented in Fig. 3.10, an unstable limit cycle is known to exist for $d < d_H$, within a certain neighborhood of d_H. We are interested in tracking the evolution of this limit cycle as slope d decreases. By numerically integrating system (3.46), using embedded Runge-Kutta formulae of orders 4 and 5, for different values of d, the limit cycle is found to disappear at $d = d_C$ –see Fig. 4.1–, with

$$d_C = -0.0795 \tag{4.4}$$

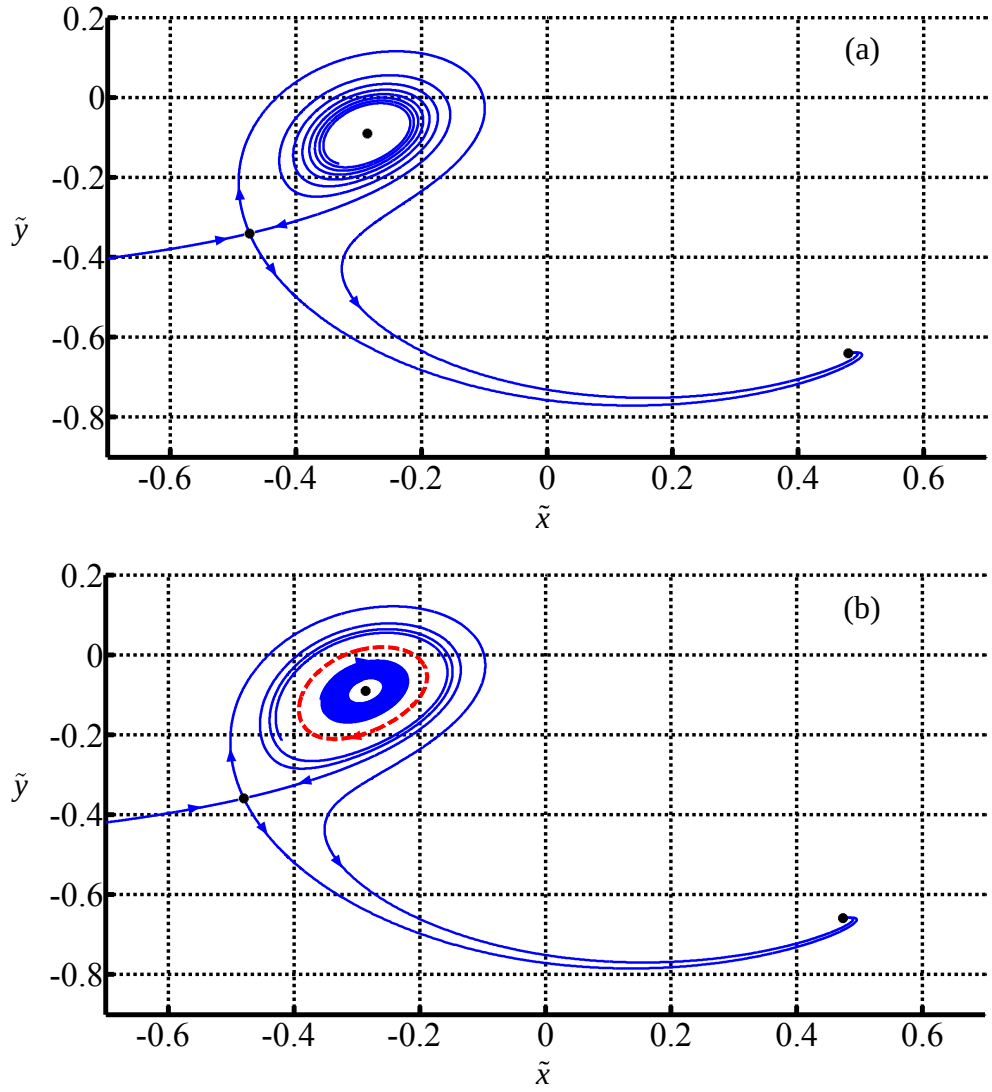

Fig. 4.2 Phase portraits corresponding to parameters (4.1). The fixed points are marked with dots. The dashed loop represents the unstable limit cycle (a) $d = -0.070$, (b) $d = -0.073$

The dynamical mechanism whereby the limit cycle is destroyed, which turns out to be a homoclinic bifurcation (Kuznetsov, 1998), is shown in Fig. 4.2 and Fig. 4.3. Let us follow the evolution of the phase portrait. From Fig. 4.2 (a) to Fig. 4.2 (b), the Hopf bifurcation takes place: the focus becomes stable, while an unstable limit cycle is born around it. In Fig. 4.3(a), the cycle has swelled considerably and passes close to saddle point S. The homoclinic bifurcation occurs when the cycle touches

the saddle point ($d = d_C$), becoming a homoclinic orbit. In Fig. 4.3(b), we have $d < d_C$ and the loop has been destroyed.

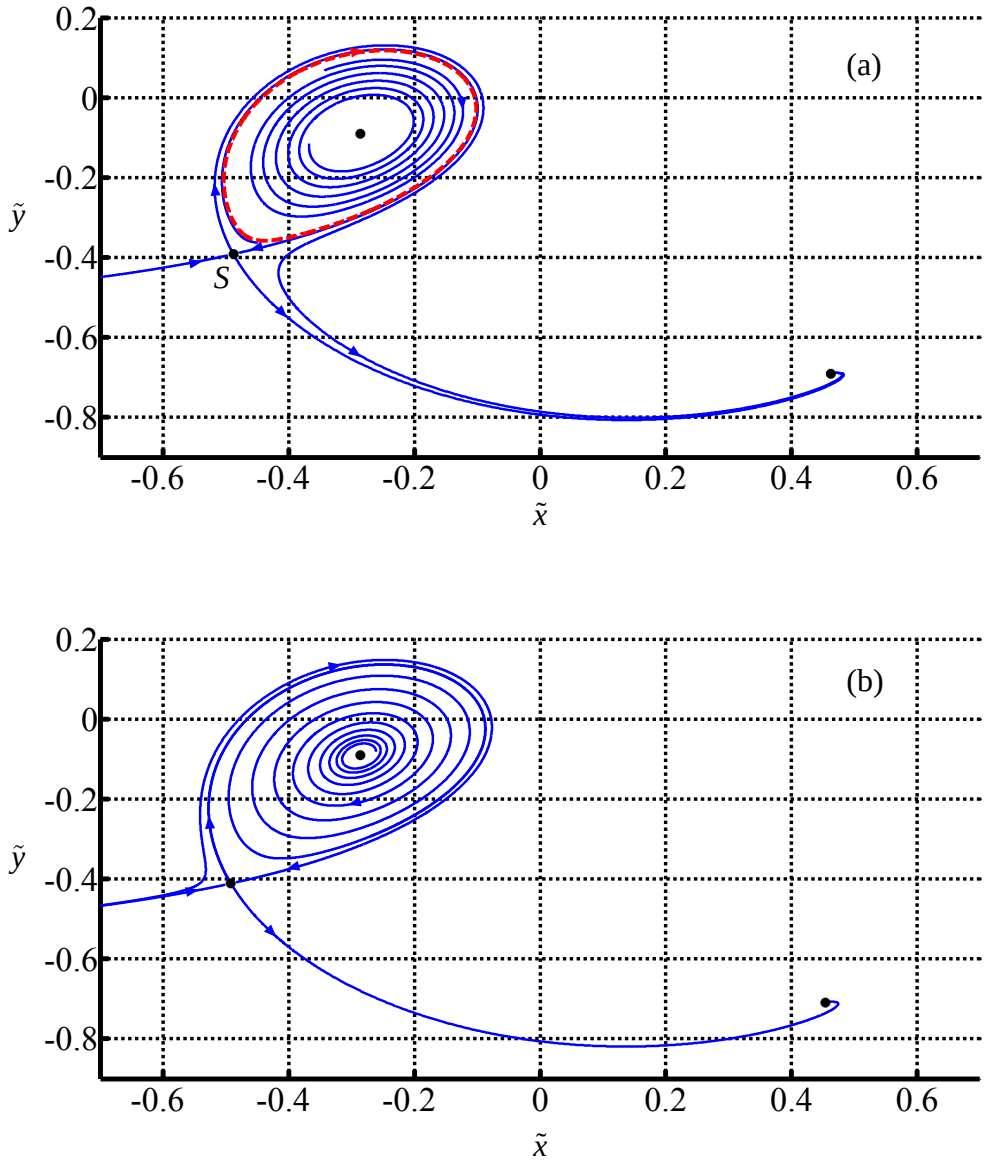

Fig. 4.3 Phase portraits corresponding to parameters (4.1). The fixed points are marked with dots. The dashed loop represents the unstable limit cycle (a) $d = -0.078$, (b) $d = -0.081$

It is worth noting that, when the unstable limit cycle exists –namely, for $d_C < d < d_H$–, it acts as a frontier between the domains of attraction of the two stable equilibrium points of the system –see Fig. 4.2(b) and Fig. 4.3(a)–.

Many other cases exhibiting a subcritical bifurcation, which are not shown here, have also been numerically solved. In all of them, the unstable limit cycle has been found to disappear through a homoclinic bifurcation.

The Supercritical Case

Consider the following set of dimensionless parameters:

$$\xi = 1, \qquad \alpha = 2, \qquad \rho = -10, \qquad a_{eq} = 0.5, \qquad z = 1, \tag{4.5}$$

which might be associated to dimensional parameters

$$\left\{ \begin{array}{c} m = 1\text{kg} \\ k = 1\,\text{N/m} \\ b = 0.002\,\text{Ns/m} \\ m_1 = 0.001\text{kg} \\ \lambda = -4\,\text{N/m}^3 \\ r = 0.1\text{m} \\ I = 2.5 \cdot 10^{-3}\text{m}^2\text{kg} \end{array} \right\}, \tag{4.6}$$

with $\epsilon = 0.001$. Equations (3.66) and (3.86) yield the values of slopes d_H and d_P, depicted in Fig. 4.4.

$$d_H = -0.2165, \qquad d_P = -0.1650 \tag{4.7}$$

Criterion (3.87) allows characterizing the bifurcation as supercritical. Then, as represented in Fig. 3.10, it can be assured that a stable limit cycle encircles the unstable equilibrium for $d > d_H$, within a certain neighborhood of d_H. As a matter of fact, the results of Section 3.6 can be used here to investigate the range of slopes d for which the limit cycle exists.

Consider the curve T_m which intersects T_v at the fixed point under study and is **tangent** to curve T_v at another point. Let d_T stand for the slope of that particular torque curve, as displayed in Fig. 4.4. Then, it is straightforward to show that, for $d_H < d < d_T$, conditions (3.89) are fulfilled and, consequently, it can be assured that all system trajectories tend to a periodic orbit. In the case under analysis, we have

$$d_T = -0.1697 \tag{4.8}$$

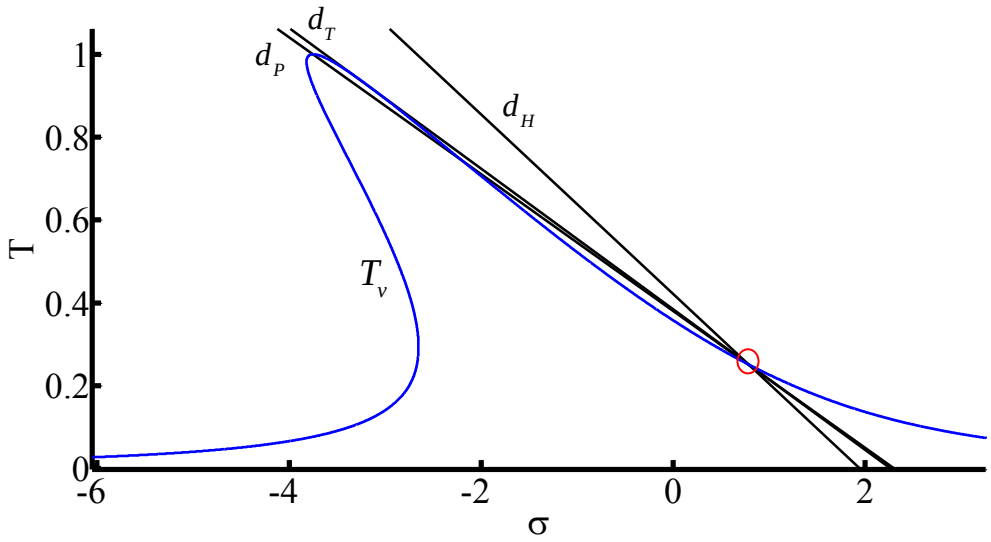

Fig. 4.4 Torque curves corresponding to parameters (4.5)

Note that the Poincaré-Bendixson Theorem gives sufficient, but not necessary, conditions for the existence of a stable periodic orbit. Thus, it cannot be deduced from the Theorem whether the limit cycle survives or not when $d > d_T$. To the end of answering this question, we resort again to a numerical resolution of system (3.46), for increasing values of d. The results are displayed in Fig. 4.5 and Fig. 4.6.

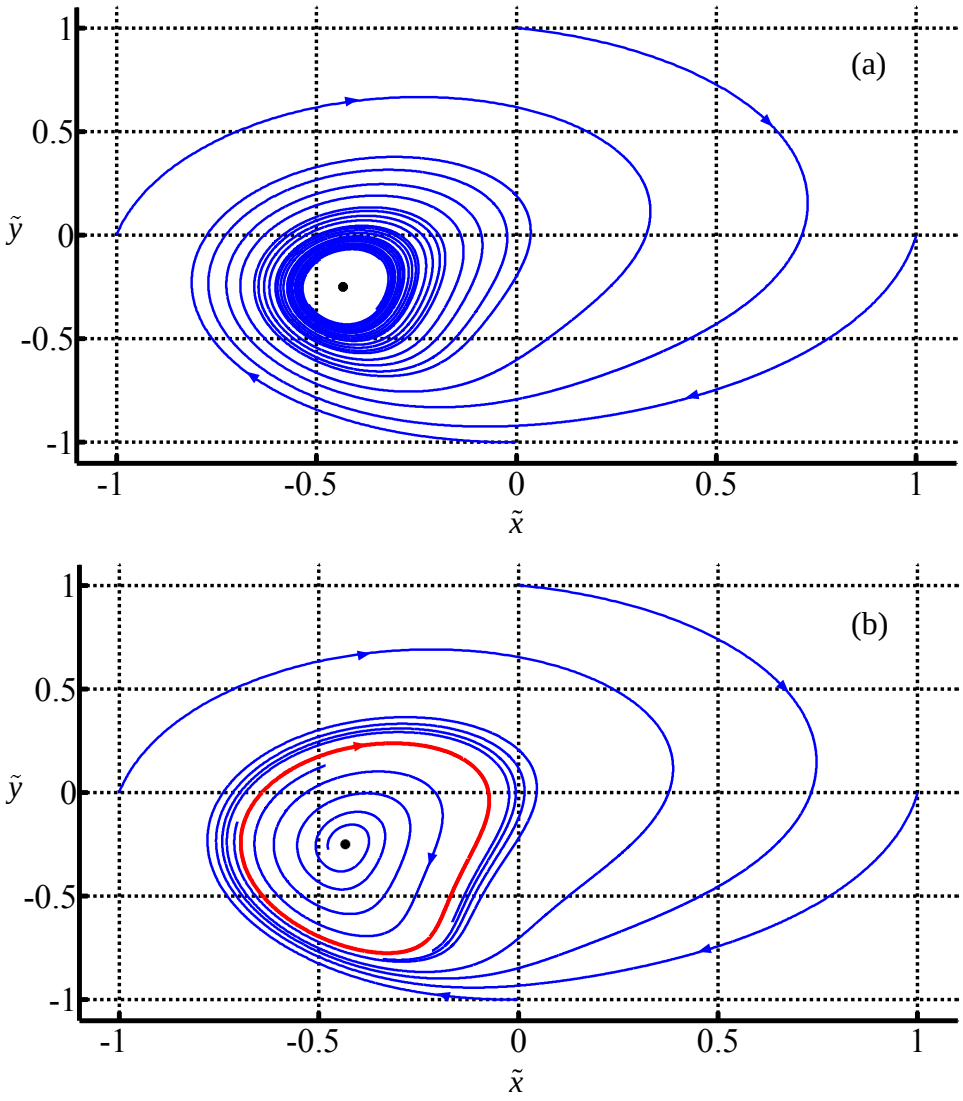

Fig. 4.5 Phase portraits corresponding to parameters (4.5). The fixed points are marked with dots. The solid loop represents the stable limit cycle $(a)\ d = -0.22$, (b) $d = -0.19$

Let us track the evolution of the phase portrait. In Fig. 4.5(a) we have $d < d_H$ and all system trajectories are attracted towards the only fixed point of the system. It may seem from Fig. 4.5(a) that trajectories are actually attracted towards a limit cycle surrounding the fixed point. The reason for this false impression is that the attraction of the fixed point is very weak, as it is close to becoming unstable (d is

close to d_H). Hence the required time for trajectories to approach the equilibrium is extremely long.

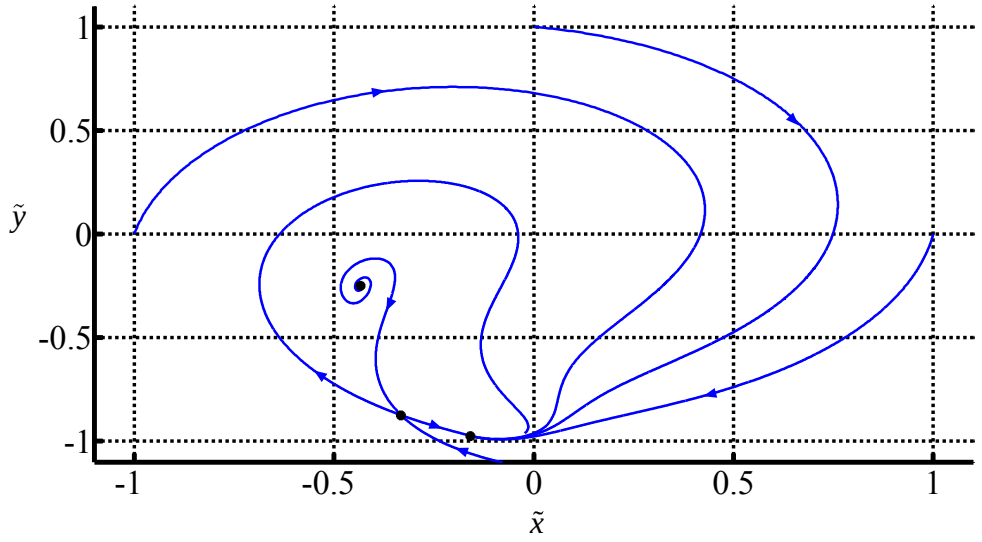

Fig. 4.6 Phase portraits corresponding to parameters (4.5), for $d = -0.169$. The fixed points are marked with dots. The solid loop represents the stable limit cycle

Fig. 4.5b corresponds to $d_H < d < d_T$. The Hopf bifurcation has occurred and, therefore, the focus has lost its stability at the same time that a stable limit cycle has appeared around it. Note that, in Fig. 4.5(b), conditions (3.89) hold. Consequently, all system trajectories are attracted towards a periodic orbit. Actually, Fig. 4.5b can be observed as a particular example of the general picture shown in Fig. 3.14.

The numerical results mentioned above are only useful to confirm the analytical developments of previous sections. By contrast, Fig. 4.6 does provide new information about the global dynamics of the system. It shows that the stable limit cycle is destroyed through a saddle-node homoclinic bifurcation (Kuznetsov, 1998), which occurs at $d = d_T$. This means that the cycle disappears exactly when conditions (3.89) are not fulfilled anymore. The mechanism is as follows. At $d = d_T$ a new fixed point, which immediately splits into a saddle and a node, is created through a saddle-node bifurcation. This new equilibrium appears precisely on the limit cycle, transforming it into a homoclinic orbit. What is found at $d > d_T$,

as observed in Fig. 4.6, is that the limit cycle has been replaced by a couple of heteroclinic orbits connecting the saddle and the node.

It has been shown that, for the particular set of parameters (4.5), conditions (3.89) are necessary and sufficient for the existence of a stable limit cycle. Thus, the periodic orbit never coexists with any other attractor of the system. Nevertheless, it should be stressed that this is not always the case. In fact, cases have also been found where the stable limit cycle is destroyed through a homoclinic bifurcation, just like in the subcritical case. In these situations, the global bifurcation occurs at certain slope $d_C > d_T$ and, therefore, the limit cycle coexists with a stable equilibrium for $d_T < d < d_C$.

As an example, consider a case with d_H satisfying $d_T < d_H < d_P$. Clearly, according to (3.87), the Hopf bifurcation is supercritical. However, it is not possible for the limit cycle to be destroyed through a saddle-node homoclinic bifurcation, because the saddle and the node are created before the limit cycle. In fact, in these cases, the closed orbit has been found to die in the same way as the unstable limit cycle shown in Fig. 4.3, i.e. through a homoclinic bifurcation due to the presence of a saddle point.

In summary, the simulations carried out suggest that, while unstable limit cycles are destroyed by homoclinic bifurcations, the stable ones can disappear either through homoclinic bifurcations or saddle-node homoclinic bifurcations.

4.2 Numerical Validation of Analytical Results

A Subcritical Case

Consider again the set of parameters given at (4.1), which gives rise to a subcritical Hopf bifurcation, as depicted in Fig. 4.2 and Fig. 4.3. Two different scenarios are studied, corresponding to the following slopes of the motor characteristic:

$$d_1 = -0.078, \qquad d_2 = -0.070. \tag{4.9}$$

By comparing (4.9) with Fig. 4.2 and Fig. 4.3, it can be verified that, for $d = d_1$, the system has a stable focus surrounded by an unstable limit cycle, while, at $d = d_2$, the focus has become unstable through a Hopf bifurcation. As pointed out in Section 4.1, the unstable limit cycle for $d = d_1$ is the boundary which separates the basins of attraction of the two attracting fixed points present in the system–see Fig. 4.3(a)–.

For $d = d_1$, two sets of initial conditions, I.C. (1) and I.C. (2), are selected, outside and inside the limit cycle, respectively:

$$\text{I. C. (1)} \begin{Bmatrix} a_0 = 0.2 \\ \beta_0^* = -2.8 \end{Bmatrix}, \qquad \text{I. C. (2)} \begin{Bmatrix} a_0 = 0.1 \\ \beta_0^* = -2.8 \end{Bmatrix}. \tag{4.10}$$

Then, by using relations (3.47), corresponding initial conditions for the original system can be computed:

$$\text{I. C. (1)} \begin{Bmatrix} u_0 = 0.2 \\ \dot{u}_0 = 0 \\ \phi_0 = 2.8 \\ \dot{\phi}_0 = 1 \end{Bmatrix}, \qquad \text{I. C. (2)} \begin{Bmatrix} u_0 = 0.1 \\ \dot{u}_0 = 0 \\ \phi_0 = 2.8 \\ \dot{\phi}_0 = 1 \end{Bmatrix}. \tag{4.11}$$

Note that this step has not a unique solution, because different sets of original initial conditions can produce the same reduced initial conditions.

The obtained numerical solutions are shown in Fig. 4.7, for $\epsilon = 10^{-3}$. A good agreement between solutions of both systems is observed. Clearly, the two considered sets of initial conditions lead the system to different attractors.

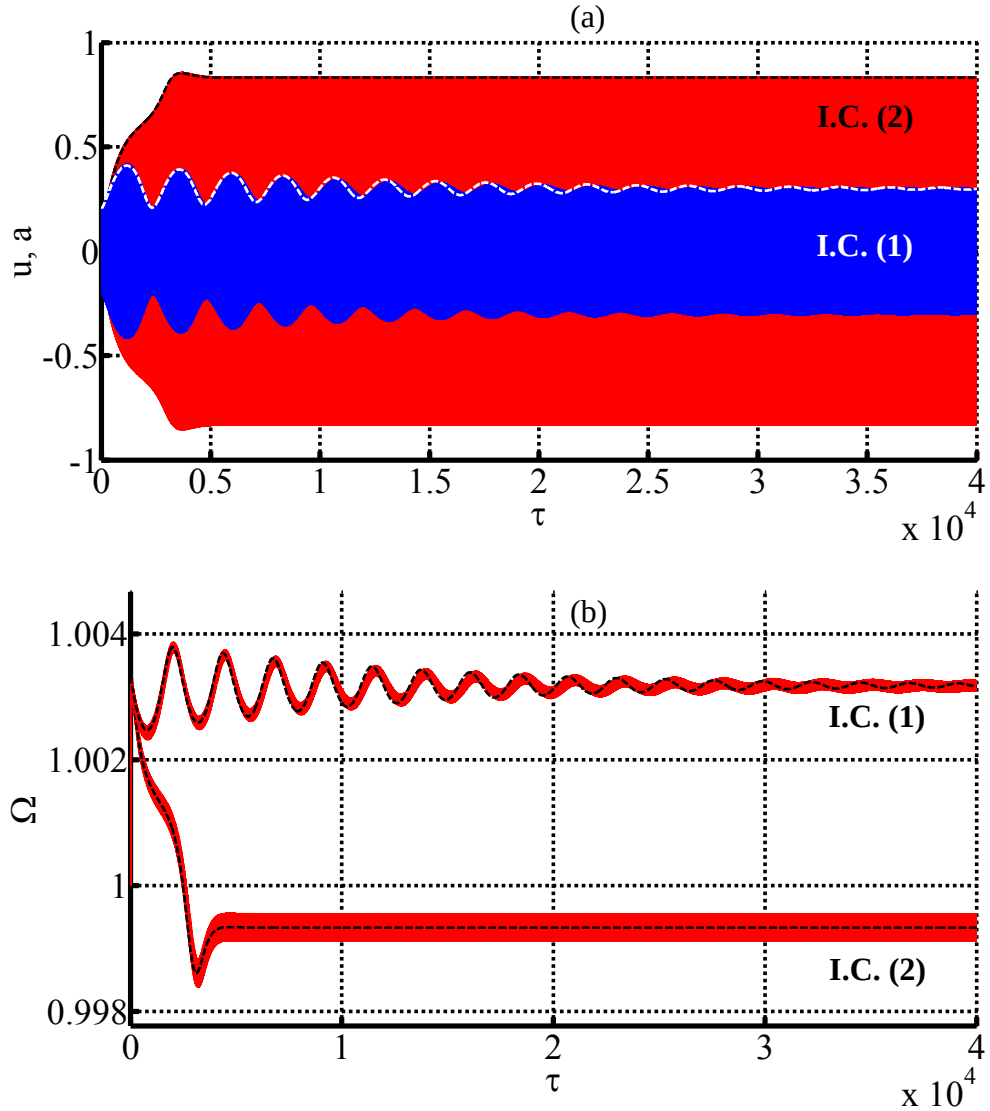

Fig. 4.7 Comparison of numerical solutions of the original (solid line) and reduced (dashed line) systems for parameters (4.1), $\epsilon = 10^{-3}$ and $d = d_1 = -0.078$

(a) Displacements

(b) Rotor Speed

It is convenient to make here an observation about the size of parameter ϵ. The procedure used in Chapter 3 to transform the original system into a simpler reduced system is based on perturbation methods. These techniques are useful for dynamical systems which contain a small parameter ϵ, and they explain how such systems behave for a *sufficiently small* ϵ. This means that the smaller ϵ is, the more accurate

perturbation predictions are. Fig. 4.7 shows that, for the case under consideration, a value of $\epsilon = 10^{-3}$ gives a remarkable accordance between solutions of the original and reduced system. As an illustrative example, the same numerical computation is done, for initial conditions I.C. (2) and $\epsilon = 10^{-2}$. This larger ϵ gives rise to a less accurate prediction, as displayed in Fig. 4.8. The required ϵ to have an accurate result depends on the case under study. For instance, in the following simulation (Fig. 4.9), it was necessary to take $\epsilon = 10^{-4}$ for a good matching between solutions of the exact and approximate systems. However, in the majority of simulations conducted within this work, $\epsilon = 10^{-3}$ proved to be small enough.

Consider now the case $d = d_2$ where, according to Fig. 4.2(a), the focus is unstable and there is a unique attracting fixed point in the system. Initial conditions

$$\text{I. C. (3)} \begin{Bmatrix} a_0 = 0.25 \\ \beta_0^* = -2.65 \end{Bmatrix} \tag{4.12}$$

are selected for the reduced system, from which corresponding initial conditions for the original system can be obtained:

$$\text{I. C. (3)} \begin{Bmatrix} u_0 = 0.25 \\ \dot{u}_0 = 0 \\ \phi_0 = 2.65 \\ \dot{\phi}_0 = 1 \end{Bmatrix}. \tag{4.13}$$

The original and reduced systems are numerically solved with $\epsilon = 10^{-4}$ and initial conditions (4.13) and (4.12), respectively. The results are displayed in Fig. 4.9, where it is clearly observed how the system moves away from the unstable focus, as the oscillation amplitude increases, until it is attracted to the stable node.

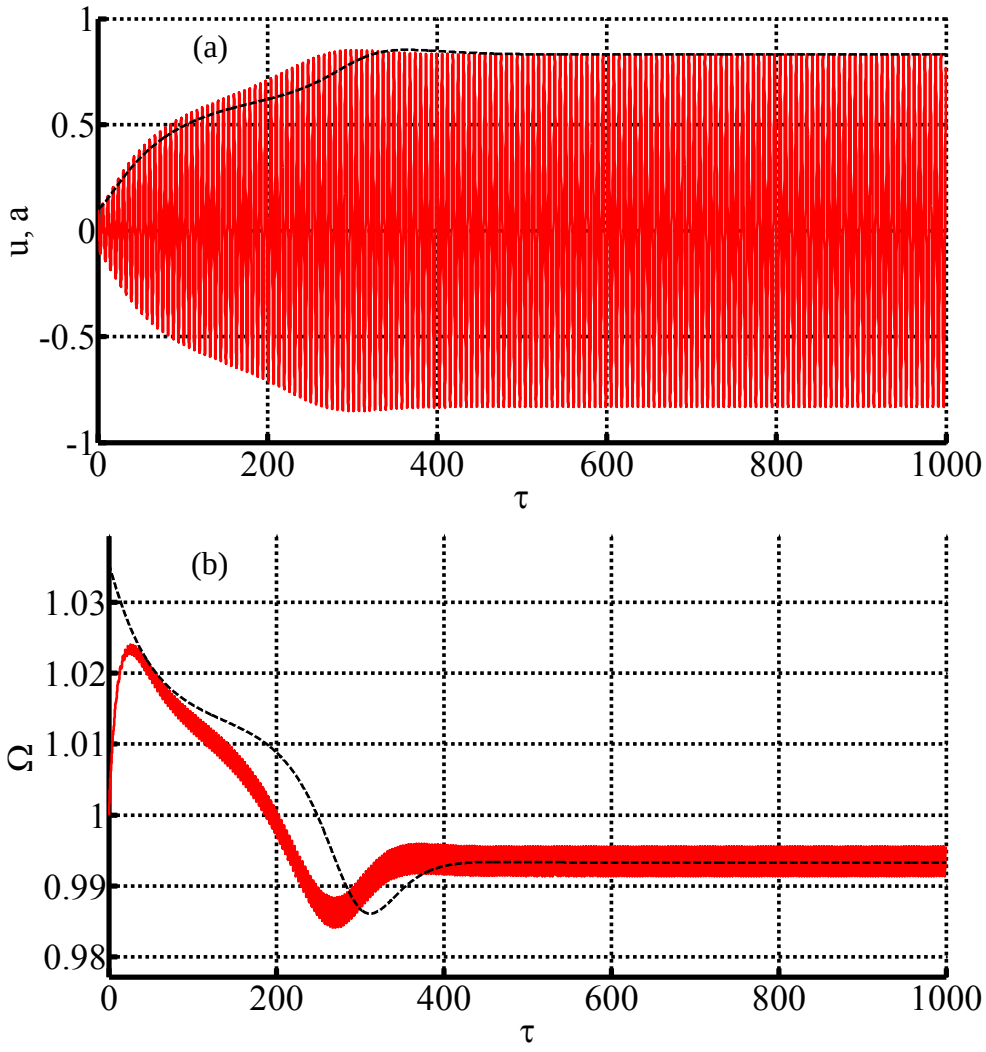

Fig. 4.8 Comparison of numerical solutions of the original (solid line) and reduced (dashed line) systems for parameters (4.1), initial conditions I. C. (2), $\epsilon = 10^{-2}$ and $d = d_1 = -0.078$

(a) Displacements

(b) Rotor Speed

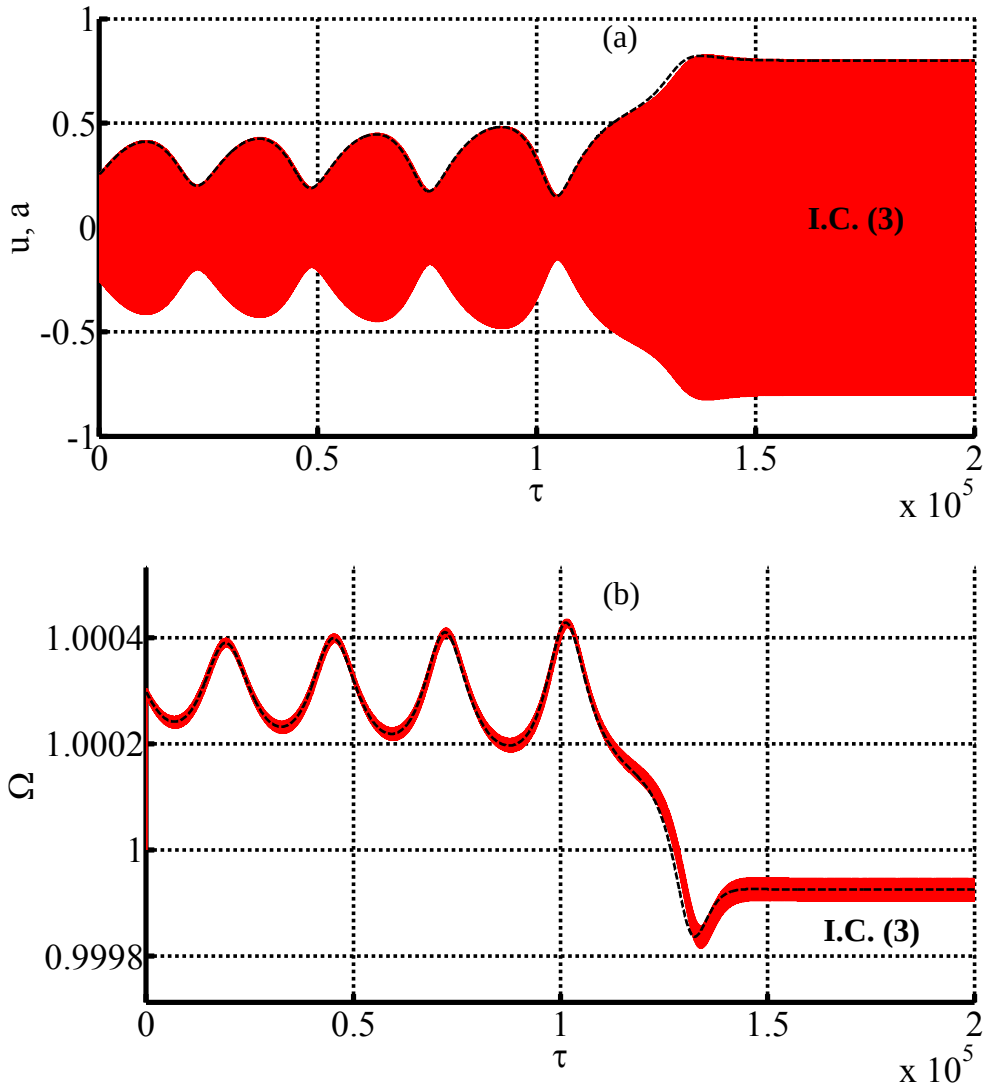

Fig. 4.9 Comparison of numerical solutions of the original (solid line) and reduced (dashed line) systems for parameters (4.1), $\epsilon = 10^{-4}$ and $d = d_2 = -0.070$

(a) Displacements

(b) Rotor speed

A Supercritical Case

In order to observe limit cycle oscillations in the original system, we need to consider a case where a supercritical Hopf bifurcation occurs, giving birth to a stable limit cycle. Thus, consider again the set of parameters given at (4.5) and a motor characteristic with slope $d = -0.19$, which corresponds to the phase portrait exhibited in Fig. 4.5(b). With these parameters, the original system of equations (3.10) is numerically solved for $\epsilon = 10^{-3}$ and initial conditions

$$\left\{\begin{matrix} u_0 = 0.1 \\ \dot{u}_0 = 0 \\ \phi_0 = 0 \\ \dot{\phi}_0 = 0 \end{matrix}\right\}. \tag{4.14}$$

The reduced system (3.46) is numerically integrated as well for comparison. The associated initial conditions for the reduced system can be computed with the aid of relations (3.47):

$$\left\{\begin{matrix} a_0 = 0.1 \\ \beta_0^* = 5.263 \end{matrix}\right\}. \tag{4.15}$$

With these sets of initial conditions, the obtained results for both systems are represented in Fig. 4.10 and Fig. 4.11, exhibiting very good agreement.

It is worth stressing that, as depicted in Fig. 4.10 and Fig. 4.11, a new kind of behaviour has been found for the mechanical system under study, which consists in a vibratory motion of the structure with slowly oscillating amplitude, due to the nonideal interaction between exciter and vibrating system. The periodic solutions of the averaged system correspond to quasiperiodic solutions of the original one.

This type of motion had not been addressed before, to the author's knowledge, in the literature about nonideal excitations. Note that the LCOs give rise, in this case, to very large variations of the amplitude. Thus, the effect of the studied instability may be of great importance in real applications.

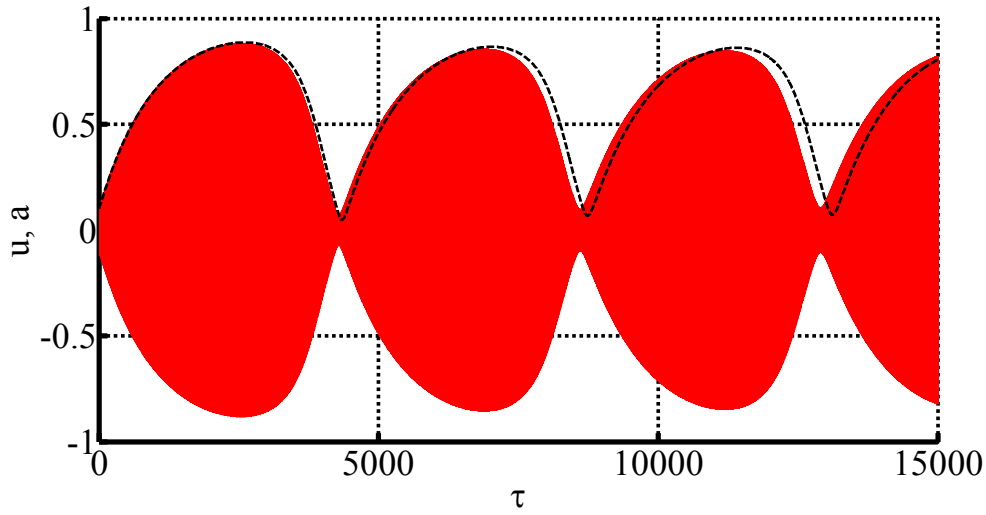

Fig. 4.10 Comparison of displacements obtained by numerical resolution of the original (solid line) and reduced (dashed line) systems for parameters (4.5), $\epsilon = 10^{-3}$ and $d = -0.19$

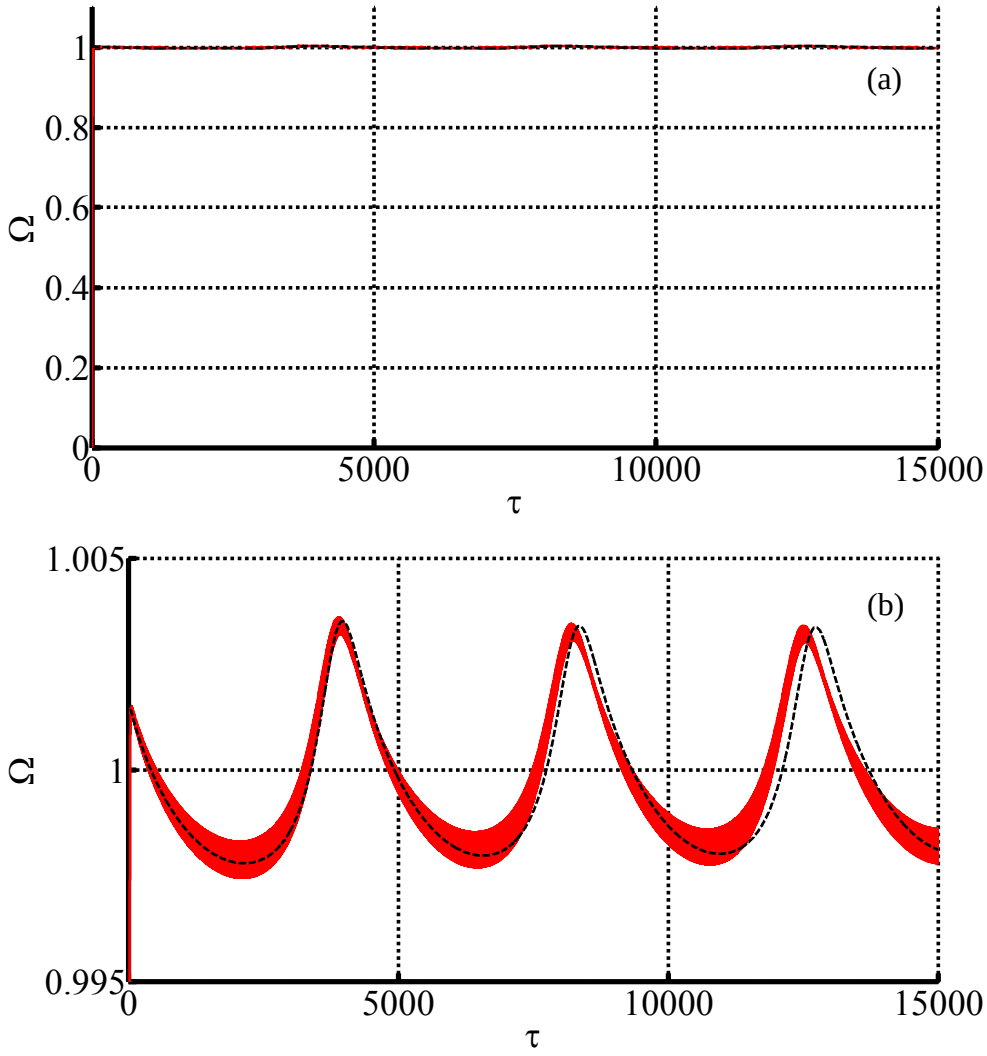

Fig. 4.11 Comparison of the rotor speed obtained by numerical resolution of the original (solid line) and reduced (dashed line) systems for parameters (4.5), $\epsilon = 10^{-3}$ and $d = -0.19$

(a) Full view

(b) Close-up around resonance

5 THE CASE OF SMALL SLOPE OF THE MOTOR CHARACTERISTIC: ANALYTICAL APPROACH

As commented in the Introduction to the thesis, the behaviour of the vibrating system under study is different depending on the order of magnitude of the slope of the motor characteristic. Then, in this Chapter, the system depicted in Fig. 3.1 and governed by equations (3.6) is considered again, maintaining the assumptions (3.7) and (3.8) –small damping, small unbalance, small nonlinearity coefficient and small

torque at resonance–, and replacing assumption (3.9) –large slope of the motor characteristic– with

$$d = \epsilon d_0. \tag{5.1}$$

The assumption $d < 0$ is kept within this chapter. Moreover, we assume $c > 0$, with c defined in (3.5).

With these new assumptions, the dimensionless equations of motion are

$$\begin{aligned} \ddot{u} + u &= \epsilon\left[-2\xi\dot{u} - \rho u^3 + 2\xi\left(\dot{\phi}^2\cos\phi + \ddot{\phi}\sin\phi\right)\right] \\ \ddot{\phi} &= \epsilon\left[c + d\left(\dot{\phi} - 1\right) + \alpha\ddot{u}\sin\phi\right], \end{aligned} \tag{5.2}$$

where subscript '0' has been dropped for convenience.

It is useful to transform system (5.2), according to change of variables

$$\left\{\begin{matrix} u = a\cos(\phi + \beta) \\ \dot{u} = -a\sin(\phi + \beta) \end{matrix}\right\} \tag{5.3}$$

and define a new variable for the rotor speed:

$$\Omega \equiv \dot{\phi}. \tag{5.4}$$

Notice that the procedure followed in Chapter 3 is being repeated: a change to polar coordinates is performed by replacing the pair of variables $\{u(\tau), \dot{u}(\tau)\}$ with the pair of amplitude–phase variables $\{a(\tau), \beta(\tau)\}$. Thus, the intermediate steps can be skipped, since they are exactly the same as in Chapter 3. The system, written in the new variables, takes the form

$$\left\{\begin{array}{c} \dot{a} = -\epsilon \sin(\phi+\beta)\, F_1(a,\beta,\phi,\Omega) + O(\epsilon^2) \\ \dot{\Omega} = \epsilon[c + d(\Omega-1) - \alpha a \sin\phi \cos(\phi+\beta)] + O(\epsilon^2) \\ \dot{\beta} = 1 - \Omega - \epsilon \dfrac{\cos(\phi+\beta)}{a} F_1(a,\beta,\phi,\Omega) + O(\epsilon^2) \\ \dot{\phi} = \Omega \end{array}\right\}, \tag{5.5}$$

where

$$F_1 = 2\xi a \sin(\phi+\beta) - \rho a^3 \cos^3(\phi+\beta) + 2\xi\Omega^2 \cos\phi. \tag{5.6}$$

Equations (5.5) and (5.6) are analogous to (3.26) and (3.27).

A direct inspection of system (5.5) reveals that it contains two non-angular real variables $\{a, \Omega\}$ which are slow –they evolve with rate $O(\epsilon)$– and two angular variables $\{\beta, \phi\}$ which are, in principle, fast –they evolve with rate $O(1)$ unless $\Omega \approx 0$ or $\Omega \approx 1$–. Hence this is a suitable scenario for averaging over the fast angles. However, in order to average over several angles, the system needs to be written in the form (2.5), (2.6), as explained in Section 2.1. To this end, new angular variables are defined:

$$\varphi_1 \equiv \beta, \qquad \varphi_2 \equiv \phi + \beta, \qquad \varphi_3 \equiv 2\phi + \beta. \tag{5.7}$$

Then, by expanding the products of sines and cosines in (5.5), the system can be written as

$$\left\{\begin{array}{c} \dot{a} = \epsilon\left[-\xi a - \xi \sin\varphi_1 + \xi a \cos(2\varphi_2) - \xi\Omega^2 \sin\varphi_3 + \rho a^3\left(\dfrac{1}{4}\sin(2\varphi_2) + \dfrac{1}{8}\sin(4\varphi_2)\right)\right] + O(\epsilon^2) \\ \dot{\Omega} = \epsilon\left[c + d(\Omega-1) + \dfrac{\alpha}{2} a \sin\varphi_1 - \dfrac{\alpha}{2} a \sin\varphi_3\right] + O(\epsilon^2) \\ \dot{\varphi}_1 = 1 - \Omega + O(\epsilon) \\ \dot{\varphi}_2 = 1 + O(\epsilon) \\ \dot{\varphi}_3 = 1 + \Omega + O(\epsilon) \end{array}\right\} \tag{5.8}$$

Now, assume a positive rotor speed, $\Omega > 0$. Then, the only resonance manifold present in system (5.8) is given by condition

$$\Omega = 1 \tag{5.9}$$

As explained in Section 2.1, it is necessary to distinguish between two scenarios, depending on whether or not the system is close to the resonance manifold.

5.1 Outer Region

Suppose the rotor speed Ω is away from 1. Then, we can average system (5.8) over the three fast angles φ_1, φ_2 and φ_3. The resulting averaged system is

$$\left\{\begin{array}{c} \dot{a} = -\epsilon\xi a \\ \dot{\Omega} = \epsilon H_m(\Omega) \end{array}\right\}, \tag{5.10}$$

where

$$H_m(\Omega) \equiv c + d(\Omega - 1). \tag{5.11}$$

According to the averaging theorem stated in Section 2.1, system (5.10) is valid on a time scale $\tau = O(1/\epsilon)$, with $O(\epsilon)$ precision.

A straightforward analysis of system (5.10) yields the conclusion that it has one only fixed point, given by

$$\left\{\begin{array}{c} a = 0 \\ H_m(\Omega) = 0 \end{array}\right\} \Rightarrow \left\{\begin{array}{c} a = 0 \\ \Omega = \widetilde{\Omega} \equiv 1 - \dfrac{c}{d} \end{array}\right\}, \tag{5.12}$$

which is globally asymptotically stable as long as $d < 0$.

Note that, according to assumptions $c > 0$, $d < 0$, the equilibrium point (5.12) corresponds to a post-resonant regime, $\Omega > 1$. This solution has a very clear physical interpretation. First, note by comparing (5.11) to (3.3) that function $H_m(\Omega)$ is simply a dimensionless version of the motor characteristic $L_m(\dot{\phi})$:

$$H_m(\Omega) = \frac{L_m(\omega_n \Omega)}{\epsilon I \omega_n^2} \tag{5.13}$$

Clearly, $\widetilde{\Omega}$ is the only zero of $H_m(\Omega)$, as represented in Fig. 5.1. Then, the outer fixed point (5.14) corresponds to a post-resonant motion where the oscillation amplitude is zero and the rotor speed takes the value which makes the motor torque vanish. Note that this holds for the averaged system (5.10), whose solutions are at an $O(\epsilon)$ distance to those of the original system (5.2). Then, regarding the original system, it can be said that the outer fixed point (5.14) represents a post-resonant motion with small oscillation amplitudes $a = O(\epsilon)$ and with the rotor speed close to the zero of the motor characteristic $\Omega = \widetilde{\Omega} + O(\epsilon)$.

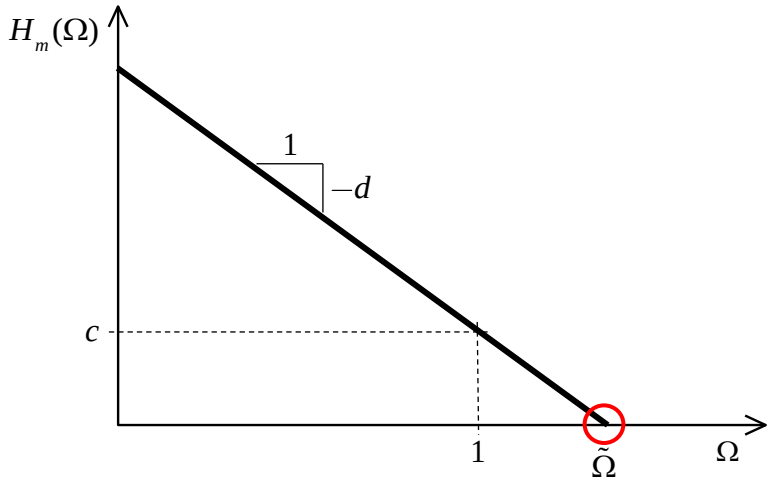

Fig. 5.1 Dimensionless motor characteristic $H_m(\Omega)$

In physical terms, it is consistent that a non-resonant excitation produces a small oscillation of the vibrating system. Note that, for such small oscillations, the torque

on the rotor due to vibration is very small $\left(\epsilon\alpha\ddot{u}\sin\phi = O(\epsilon^2)\right)$. Then, during this post-resonant motion, the motor does not have to provide any significant torque to maintain the system vibration and, consequently, the rotor speed takes such a value that the driving torque is virtually zero: $\Omega = \widetilde{\Omega} + O(\epsilon) \Rightarrow \epsilon[c + d(\Omega - 1)] = O(\epsilon^2)$.

Two different scenarios can be considered:

- If $\Omega(0) > 1$, system (5.10) is exponentially attracted towards equilibrium (5.12) without approaching the resonance manifold. Then, according to Section 2.1 (Averaging with Attraction), the outer averaged system is valid for all $\tau > 0$.
- If $\Omega(0) < 1$, system (5.10) is also exponentially attracted by equilibrium (5.12). However, in its way towards the equilibrium, the system will necessarily reach the vicinity of the resonance manifold, making system (5.10) no longer valid. There are, in principle, two options:
    - The system remains close to the resonance manifold for all subsequent time (**resonant capture**).
    - The system stays near the resonance manifold for some finite time, after which it continues its evolution towards fixed point (5.12) (**passage through resonance**).

The next Section investigates the dynamics of (5.5) close to the resonance manifold.

5.2 Inner Region

In order to study the system behavior in the vicinity of the resonance manifold, the rotor speed is expanded as

$$\Omega = 1 + \sqrt{\epsilon}\sigma. \tag{5.14}$$

Note that the definition of the detuning variable σ is not the same as in the case of large slope –compare (5.14) to (3.35)–. The reason is that, under the assumption of small slope made in this chapter, the problem requires a different perturbation approach, which in turn requires a different scaling of the rotor speed. It can be checked that a scaling such as (3.35) would not yield any relevant result in the present case.

Replacing (5.14) in (5.5), (5.6) yields

$$\left\{\begin{array}{c} \dot{a} = -\epsilon \sin(\phi+\beta)\, F_2(a,\beta,\phi) + O\left(\epsilon\sqrt{\epsilon}\right) \\ \dot{\beta} = -\sqrt{\epsilon}\sigma - \epsilon \dfrac{\cos(\phi+\beta)}{a} F_2(a,\beta,\phi) + O\left(\epsilon\sqrt{\epsilon}\right) \\ \dot{\sigma} = \sqrt{\epsilon}[c - \alpha a \sin\phi \cos(\phi+\beta)] + \epsilon d\sigma + O\left(\epsilon\sqrt{\epsilon}\right) \\ \dot{\phi} = 1 + \sqrt{\epsilon}\sigma \end{array}\right\}, \tag{5.15}$$

with

$$F_2 = 2\xi a \sin(\phi+\beta) - \rho a^3 \cos^3(\phi+\beta) + 2\xi \cos\phi. \tag{5.16}$$

Clearly, system (5.15) contains three slow variables $\{a, \beta, \sigma\}$ and a fast rotating phase ϕ. It is, then, suitable for a second order averaging procedure. Following the procedure described in Section 2.2, we arrive at averaged system

$$\left\{\begin{array}{c} \dot{\bar{a}} = -\epsilon\xi\left(\bar{a} + \sin\bar{\beta}\right) \\ \dot{\bar{\beta}} = -\sqrt{\epsilon}\bar{\sigma} + \epsilon\left(\dfrac{3}{8}\rho\bar{a}^2 - \xi\dfrac{\cos\bar{\beta}}{\bar{a}}\right) \\ \dot{\bar{\sigma}} = \sqrt{\epsilon}\left[c + \dfrac{\alpha}{2}\bar{a}\sin\bar{\beta}\right] + \epsilon d\bar{\sigma} \\ \dot{\bar{\phi}} = 1 + \sqrt{\epsilon}\bar{\sigma} \end{array}\right\}, \tag{5.17}$$

where, with an appropriate relation between the initial conditions for the original and averaged systems, the error estimates are

$$\left\{\begin{array}{c} a = \bar{a} + O(\epsilon) \\ \beta = \bar{\beta} + O(\epsilon) \\ \sigma = \bar{\sigma} + \sqrt{\epsilon}\frac{\alpha}{4}\bar{a}\cos\left(2\bar{\phi} + \bar{\beta}\right) + O(\epsilon) \\ \phi = \bar{\phi} + O\left(\sqrt{\epsilon}\right) \end{array}\right\}, \qquad \text{for} \quad \tau = O\left(\frac{1}{\sqrt{\epsilon}}\right). \tag{5.18}$$

Note that the $O\left(\sqrt{\epsilon}\right)$ terms in the first two of relations (5.18) turn out to be zero in this particular case.

Despite the fact that the evolution $\{\bar{a}, \bar{\beta}, \bar{\sigma}\}$ is independent of $\bar{\phi}$ –as is evident, since this is precisely the purpose of averaging–, system (5.17) includes $\bar{\phi}$ as a state variable. The reason is that variable $\bar{\phi}(\tau)$ is necessary to construct the error estimates in (5.18). However, in order to investigate the dynamics of the averaged system, it is convenient to rewrite it without the fast angle:

$$\left\{\begin{array}{c} \dot{\bar{a}} = -\epsilon\xi\left(\bar{a} + \sin\bar{\beta}\right) \\ \dot{\bar{\beta}} = -\sqrt{\epsilon}\bar{\sigma} + \epsilon\left(\frac{3}{8}\rho\bar{a}^2 - \xi\frac{\cos\bar{\beta}}{\bar{a}}\right) \\ \dot{\bar{\sigma}} = \sqrt{\epsilon}\left[c + \frac{\alpha}{2}\bar{a}\sin\bar{\beta}\right] + \epsilon d\bar{\sigma} \end{array}\right\}. \tag{5.19}$$

A direct analysis of (5.19) allows deducing that, if $c > \alpha/2$, there are no fixed points in the inner region. On the other hand, if $c < \alpha/2$, system (5.19) exhibits two fixed points, given by

$$\left\{\begin{array}{l} a_{eq} = a_0 + \sqrt{\epsilon}a_1 + O(\epsilon) \\ \beta_{eq} = \beta_0 + \sqrt{\epsilon}\beta_1 + O(\epsilon) \\ \sigma_{eq} = \sigma_0 + \sqrt{\epsilon}\sigma_1 + O(\epsilon) \end{array}\right\}, \tag{5.20}$$

with

$$\left\{\begin{array}{ll} a_0 = \sqrt{\dfrac{2c}{\alpha}}, & a_1 = 0 \\ \beta_0 = \tan^{-1}\left(\dfrac{-a_0}{-zR_0}\right), & \beta_1 = 0 \\ \sigma_0 = 0, & \sigma_1 = \dfrac{z\xi R_0}{a_0} + \dfrac{3}{8}\rho a_0^2 \end{array}\right\}, \qquad z = \pm 1 \tag{5.21}$$

where $R_0 \equiv \sqrt{1 - a_0^2}$. The two possible values of z correspond to the two different equilibrium points.

Note that, unlike in the case of large slope –see (3.52)–, the analytical expressions for the fixed points are very simple in the present scenario. However, the torque-speed plots used in Section 3.4 may also be illustrative here and will provide an interesting comparison with the case of large slope.

Thus, consider the equilibrium condition applied to variable $\bar{\sigma}$. From the third of equations (5.19) we have, at first order,

$$c + \frac{\alpha}{2} a_0 \sin\beta_0 = 0. \tag{5.22}$$

On the other hand, condition $\dot{\bar{a}} = 0$ yields

$$\sin\beta_0 = -a_0, \tag{5.23}$$

which allows writing (5.22) as

$$c = \frac{\alpha}{2} a_0^2. \tag{5.24}$$

Equation (5.24) can be clearly interpreted as a torque equilibrium condition:

$$T_m = T_v(a_0), \tag{5.25}$$

with

$$\begin{aligned} T_m &\equiv c \\ T_v(a) &\equiv \frac{\alpha}{2} a^2. \end{aligned} \tag{5.26}$$

T_m represents the driving torque produced by the motor and T_v corresponds to the resisting torque due to vibration. In order to obtain the usual torque-speed plot, we would need to write T_m and T_v in terms of σ_{eq}. Nevertheless, this would in turn require writing a_0 in terms of $\sigma_0, \sigma_1, ...$, and then substitute in (5.25). Since this yields very long and cumbersome expressions, we resort to an alternative implicit procedure for the graphical representation.

From condition $\dot{\bar{\beta}} = 0$, we have

$$\sigma_0 = 0, \qquad \sigma_1 = \frac{3}{8}\rho a_0^2 + \frac{z\xi\sqrt{1-a_0^2}}{a_0}. \tag{5.27}$$

Then, we can write

$$\sigma_1 = \sigma_v(z, a_0), \tag{5.28}$$

where function $\sigma_v(z, a)$ is defined as

$$\sigma_v(z, a) \equiv \frac{3}{8}\rho a^2 + z\xi\frac{\sqrt{1-a^2}}{a}. \tag{5.29}$$

The proposed representation can be constructed as follows. First, graph T_m versus σ (in this case, as $T_m \equiv c$, a constant function is obtained). Then, represent the parametric curve given by $\{\sigma_v(z, a), T_v(a)\}$ for $z = \pm 1$ and $a \in (0,1]$. The fact that a is strictly positive comes from its definition as the radius of a polar coordinate transformation –see (5.3)–, while condition (5.23) forbids a_0 to be greater than 1. This procedure gives rise to a plot like that shown in Fig. 5.2.

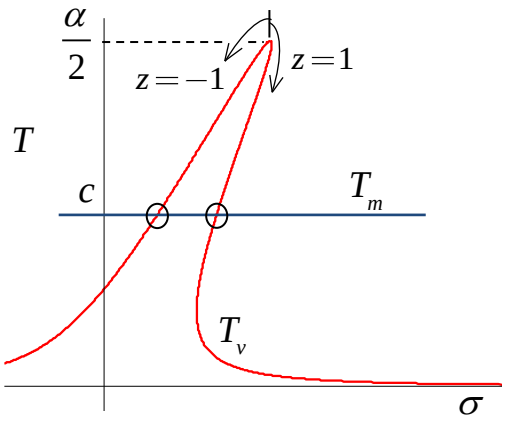

Fig. 5.2 Fixed points of system (5.19)

A direct comparison between Fig. 5.2 and Fig. 3.7 is quite illustrative as for the difference between the two scenarios considered in this thesis. In the case of large (small) slope, the driving torque curve exhibits a slope which is comparable (negligible) with respect to that of the vibration torque curve.

Fig. 5.2 shows the existence of two fixed points, as long as $c < \alpha/2$. The stability of these equilibria is now investigated. To this end, the jacobian matrix of system (5.19) needs to be obtained and evaluated at the equilibrium point of interest:

$$\boldsymbol{J}_{eq} = \sqrt{\epsilon}\boldsymbol{J}_0 + \epsilon\boldsymbol{J}_1 + O\left(\epsilon\sqrt{\epsilon}\right), \tag{5.30}$$

with

$$\boldsymbol{J}_0 = \begin{bmatrix} 0 & 0 & 0 \\ 0 & 0 & -1 \\ -\frac{\alpha}{2}a_0 & -\frac{z\alpha}{2}a_0 R_0 & 0 \end{bmatrix}, \qquad \boldsymbol{J}_1 = \begin{bmatrix} -\xi & z\xi R_0 & 0 \\ -\frac{z\xi R_0}{a_0^2} + \frac{3}{4}\rho a_0 & -\xi & 0 \\ 0 & 0 & d \end{bmatrix}. \tag{5.31}$$

The eigenvalues of matrix $\boldsymbol{J}_{eq}$ are now computed. After some algebra, we find, for the right branch of the torque curve ($z = 1$),

$$z = 1 \rightarrow \left\{ \begin{array}{c} \lambda_1 = -2\epsilon\xi + O\left(\epsilon\sqrt{\epsilon}\right) \\ \lambda_2 = \sqrt{\epsilon}\sqrt{\dfrac{\alpha a_0 R_0}{2}} + O(\epsilon) \\ \lambda_3 = -\sqrt{\epsilon}\sqrt{\dfrac{\alpha a_0 R_0}{2}} + O(\epsilon) \end{array} \right\}, \tag{5.32}$$

which clearly corresponds to an unstable equilibrium of the saddle type. For the left branch ($z = -1$) we obtain

$$z = -1 \rightarrow \left\{ \begin{array}{c} \lambda_1 = -2\epsilon\xi + O\left(\epsilon\sqrt{\epsilon}\right) \\ \lambda_2 = \sqrt{\epsilon}i\sqrt{\dfrac{\alpha a_0 R_0}{2}} + \epsilon\dfrac{d}{2} + O\left(\epsilon\sqrt{\epsilon}\right) \\ \lambda_3 = -\sqrt{\epsilon}i\sqrt{\dfrac{\alpha a_0 R_0}{2}} + \epsilon\dfrac{d}{2} + O\left(\epsilon\sqrt{\epsilon}\right) \end{array} \right\}. \tag{5.33}$$

According to (5.33), the left equilibrium is stable, since all eigenvalues have negative real parts, as long as $d < 0$.

Here the most challenging part of the Chapter is faced. Note that there is a significant difference between the stability of both fixed points. Not only the eigenvalues give information about stability, but also about the time needed by trajectories to be attracted or repelled by the fixed point.

For $z = 1$, we have $Re(\lambda_2) = O\left(\sqrt{\epsilon}\right)$, where λ_2 is the only positive eigenvalue –see (5.32)–. Thus, the characteristic time of repulsion is $\tau = O\left(1/\sqrt{\epsilon}\right)$. Recall, from (5.18), that the time scale in which the inner approximation is valid is precisely $\tau = O\left(1/\sqrt{\epsilon}\right)$. Then, consider a trajectory of (5.19) which starts in the vicinity of the considered fixed point. If the trajectory is tracked for the time length where the averaged system (5.19) is valid, $\tau = O\left(1/\sqrt{\epsilon}\right)$, we find that it is repelled out of the

equilibrium. Therefore, it can be stated that the equilibrium, which is unstable for the averaged system (5.19), is also unstable for the original system (5.5).

On the other hand, for $z = -1$, we have $Re(\lambda_1, \lambda_2, \lambda_3) = O(\epsilon)$, with all three eigenvalues having negative real parts. Thus, the time of attraction is $\tau = O(1/\epsilon)$. Clearly, we have

$$\tau_{attraction} \gg \tau_{validity}. \tag{5.34}$$

With a similar reasoning as for the unstable case, a trajectory of the averaged system starting in a neighborhood of the fixed point can be considered. However, in this case, if the trajectory is followed during $\tau = O\left(1/\sqrt{\epsilon}\right)$, we find that it is neither attracted nor repelled by the equilibrium, because the time scale is not long enough. If a longer time scale is considered, solutions of the averaged system may not be good approximations to those of the original system anymore. Then, the fact that this equilibrium, which is stable for the averaged system (5.19), is also stable for the original system (5.5) needs a deeper justification.

Justification of the equilibrium stability for $z = -1$

As expounded in Section 2.1, attraction properties can be used to enlarge the time of validity of asymptotic approximations. The problem here is that the attraction is very weak, which makes necessary a modified version of the standard result given in Section 2.1. The analysis shown below is based on an example given in (Sanders et al., 2007) –see page 109, 'The Case $n = 2$' in the mentioned reference–.

Consider system (5.15), which belongs to the more general class of systems

$$\left.\begin{cases} \dot{\boldsymbol{x}} = \epsilon \boldsymbol{X^1}(\boldsymbol{x}, \phi) + \epsilon^2 \boldsymbol{X^2}(\boldsymbol{x}, \phi) + \epsilon^3 \boldsymbol{X^{[3]}}(\boldsymbol{x}, \phi, \epsilon) \\ \dot{\phi} = \Omega^0 + \epsilon \Omega^1(\boldsymbol{x}) \end{cases}\right\}, \begin{matrix} \boldsymbol{x}(0) = \boldsymbol{x}_0 \quad \boldsymbol{x} \in D \subset \mathbb{R}^n \\ \phi(0) = \phi_0 \quad \phi \in S^1 \end{matrix} \tag{5.35}$$

Note the change in notation: $\sqrt{\epsilon}$ is now written as ϵ for simplicity. This can be understood as a simple correspondence between two small parameters: $\sqrt{\epsilon_1} = \epsilon_2$.

A second order averaging procedure –see Section 2.2– yields the averaged system

$$\left.\begin{cases} \dot{\boldsymbol{y}} = \epsilon \bar{\boldsymbol{X}}^{\boldsymbol{1}}(\boldsymbol{y}) + \epsilon^2 \bar{\boldsymbol{X}}_*^{\boldsymbol{2}}(\boldsymbol{y}) \\ \dot{\psi} = \Omega^0 + \epsilon \Omega^1(\boldsymbol{y}) \end{cases}\right\}, \qquad \begin{matrix} \boldsymbol{y}(0) = \boldsymbol{x}_0 - \epsilon \boldsymbol{u}^1(\boldsymbol{x}_0, \phi_0) \\ \psi(0) = \phi_0 \end{matrix}, \tag{5.36}$$

where the error estimate is given by

$$\boldsymbol{x}(t) = \boldsymbol{y}(t) + \epsilon \boldsymbol{u}^1\big(\boldsymbol{y}(t), \psi(t)\big) + O(\epsilon^2), \qquad \text{for } t = O(1/\epsilon), \tag{5.37}$$

and function $\boldsymbol{u}^1$ is defined as

$$\boldsymbol{u}^1(\boldsymbol{y}, \psi) = \frac{1}{\Omega^0} \int_{\psi_0}^{\psi} \big[\boldsymbol{X}^{\boldsymbol{1}}(\boldsymbol{y}, \phi) - \bar{\boldsymbol{X}}^{\boldsymbol{1}}(\boldsymbol{y})\big] d\phi, \tag{5.38}$$

with constant ψ_0 chosen in such a way that

$$\int_0^{2\pi} \boldsymbol{u}^1(\boldsymbol{y}, \psi) d\psi = 0, \tag{5.39}$$

Functions $\bar{\boldsymbol{X}}^{\boldsymbol{1}}$ and $\bar{\boldsymbol{X}}_*^{\boldsymbol{2}}$ are defined in (2.3) and (2.13).

As a particularity of the case under study, note from (5.18), that there is only one component of vector $\boldsymbol{u}^1$ which does not vanish. Thus, in our case, vector $\boldsymbol{u}^1(\boldsymbol{y}, \psi)$ is of the form

$$\boldsymbol{u}^1(\boldsymbol{y},\psi) = \left\{ \begin{array}{c} 0 \\ \vdots \\ 0 \\ u_j^1(\boldsymbol{y},\psi) \\ 0 \\ \vdots \\ 0 \end{array} \right\} \tag{5.40}$$

Before proceeding to the stability analysis, it is convenient to draw a relevant conclusion from (5.39). Defining period T as

$$T = \frac{2\pi}{\Omega^0}, \tag{5.41}$$

function $\boldsymbol{u}^1$ can be integrated over one period:

$$\frac{1}{T}\int_{t-T/2}^{t+T/2} \boldsymbol{u}^1\big(\boldsymbol{y}(s),\psi(s)\big)ds = \frac{1}{2\pi}\int_0^{2\pi} \boldsymbol{u}^1(\boldsymbol{y}(t),\psi)d\psi + O(\epsilon), \tag{5.42}$$

as can be deduced by a reasoning analogous to that in equations (3.14)-(3.17). Introducing (5.38) into (5.42) yields

$$\frac{1}{T}\int_{t-T/2}^{t+T/2} \boldsymbol{u}^1\big(\boldsymbol{y}(s),\psi(s)\big)ds = O(\epsilon) \Rightarrow \frac{1}{T}\int_{t-T/2}^{t+T/2} u_j^1\big(\boldsymbol{y}(s),\psi(s)\big)ds = O(\epsilon) \tag{5.43}$$

Thus, u_j^1 is an $O(1)$ function whose integral over a period is $O(\epsilon)$. This implies that u_j^1 necessarily vanishes at least once per period, which can be written as

$$\forall t \geq 0, \qquad \exists t_0 \in [t, t+T] \,/\, \boldsymbol{u}^1\big(\boldsymbol{y}(t_0),\psi(t_0)\big) = \boldsymbol{0}, \tag{5.44}$$

since all other components of vector $\boldsymbol{u}^1$ are always zero. This will prove to be an important point because, at these particular instants, we have $\|\boldsymbol{x}-\boldsymbol{y}\| = O(\epsilon^2)$, in accordance with (5.37).

Suppose that the averaged system, written without the fast angle as

$$\dot{\boldsymbol{y}} = \epsilon\overline{\boldsymbol{X}}^1(\boldsymbol{y}) + \epsilon^2\overline{\boldsymbol{X}}^2_*(\boldsymbol{y}), \tag{5.45}$$

has a fixed point $\boldsymbol{y} = \boldsymbol{y}_{eq}$. Suppose further that the fixed point is asymptotically stable, with

$$Re(\lambda_i) = O_{\#}(\epsilon^2), \tag{5.46}$$

where λ_i is the eigenvalue with the smallest real part in absolute value and symbol $O_{\#}$ represents a sharp estimate (Sanders et al., 2007). Assume that $\boldsymbol{x}(0)$ and $\boldsymbol{y}(0)$ belong to the Poincaré-Lyapunov domain of $\boldsymbol{y}_{eq}$, i.e. to the region of the phase space where the attraction of the equilibrium is exponential.

According to (5.46) the characteristic time of attraction of the equilibrium is

$$t_{attraction} = O\left(\frac{1}{\epsilon^2}\right), \tag{5.47}$$

much longer than the time of validity of the asymptotic approximation, according to (5.37):

$$t_{validity} = O\left(\frac{1}{\epsilon}\right). \tag{5.48}$$

The scenario found when studying the unbalanced motor with small slope characteristic has been sketched here in more general terms.

In order to extend the time of validity of the averaged system by using attraction arguments, the attraction properties of system (5.45) are now investigated. Consider two solutions, $\boldsymbol{y}_1(t)$ and $\boldsymbol{y}_2(t)$, of (5.45) starting in the Poincaré-Lyapunov domain of the fixed point. According to the Poincaré-Lyapunov Theorem (Sanders et al., 2007), we have that the difference between these two solutions decreases exponentially:

$$\|\boldsymbol{y}_1(t) - \boldsymbol{y}_2(t)\| \leq C\|\boldsymbol{y}_1(0) - \boldsymbol{y}_2(0)\|e^{-\mu t}, \qquad \text{with } \mu > 0, C \geq 1 \tag{5.49}$$

Moreover, it is known from (5.46) that the contraction coefficient μ is $O_{\#}(\epsilon^2)$:

$$\mu = \epsilon^2 \mu_0 \tag{5.50}$$

In order to apply a contraction argument, we would need to guarantee that, after a time interval of $O(1/\epsilon)$, the difference between $\boldsymbol{y}_1$ and $\boldsymbol{y}_2$ has decreased. Introducing $t = L/\epsilon$, together with (5.50), into (5.49), we have

$$\begin{aligned}\|\boldsymbol{y}_1 - \boldsymbol{y}_2\| &\leq C\|\boldsymbol{y}_1(0) - \boldsymbol{y}_2(0)\|e^{-\epsilon\mu_0 L} \\ &= C\|\boldsymbol{y}_1(0) - \boldsymbol{y}_2(0)\|\big(1 - \epsilon\mu_0 L + O(\epsilon^2)\big).\end{aligned} \tag{5.51}$$

Equation (5.51) shows that, for the considered time interval, we cannot state $\|\boldsymbol{y}_1 - \boldsymbol{y}_2\| < \|\boldsymbol{y}_1(0) - \boldsymbol{y}_2(0)\|$ because, in general, we have $C \geq 1$. This difficulty would be overcome if we were able to put $C = 1$. Actually, it can be shown that, when the **eigenvectors** of the jacobian are **orthogonal**, (5.49) is satisfied with $C = 1$. Then, a change of variables is performed in order to have orthogonal eigenvectors:

$$\boldsymbol{y} = \boldsymbol{y}_{eq} + \boldsymbol{T}\boldsymbol{q}, \tag{5.52}$$

where $\boldsymbol{T}$ is a real matrix whose columns contain the real eigenvectors of the jacobian of (5.45), evaluated at $\boldsymbol{y} = \boldsymbol{y}_{eq}$. In the case of complex conjugate eigenvectors, the real and imaginary parts are stored in different columns of $\boldsymbol{T}$.

Clearly, change of variables $\boldsymbol{y} \mapsto \boldsymbol{q}$ is composed of two transformations. First, the coordinate system is translated so that the origin coincides with the fixed point. Then, a transformation to the real eigenbasis of the jacobian is performed, by means of matrix $\boldsymbol{T}$.

Vector $\boldsymbol{q}$ contains the state variables of the system, expressed with respect to the basis formed by the eigenvectors of the jacobian. Then, it is clear that these eigenvectors are necessarily orthogonal in the space of coordinates $\boldsymbol{q}$. Consequently, for two solutions starting in the Poincaré-Lyapunov domain, we have

$$\|\boldsymbol{q}_1(t) - \boldsymbol{q}_2(t)\| \leq \|\boldsymbol{q}_1(0) - \boldsymbol{q}_2(0)\| e^{-\mu t}, \qquad \text{with } \mu = \epsilon^2 \mu_0 > 0. \tag{5.53}$$

By considering a time increment $t = L/\epsilon$ in (5.53), we have

$$\|\boldsymbol{q}_1 - \boldsymbol{q}_2\| \leq k \|\boldsymbol{q}_1(0) - \boldsymbol{q}_2(0)\|, \qquad \text{with } 0 < k < 1, \tag{5.54}$$

where

$$k = e^{-\epsilon \mu_0 L} = 1 - \epsilon \mu_0 L + O(\epsilon^2). \tag{5.55}$$

Thus, it has been shown that $\boldsymbol{q}(t)$ exhibits exponential contraction on the time scale $1/\epsilon$, even though this contraction is weak.

Now, variable $\boldsymbol{x}(t)$ –solution of the original system (5.35)– can also be transformed according to (5.52):

$$\boldsymbol{x} = \boldsymbol{y}_{eq} + \boldsymbol{T}\boldsymbol{p}, \tag{5.56}$$

Consider the following partition of time in intervals of $O(1/\epsilon)$:

$$\left[0,\frac{L_1}{\epsilon}\right] \cup \left[\frac{L_1}{\epsilon},\frac{L_2}{\epsilon}\right] \cup \left[\frac{L_2}{\epsilon},\frac{L_3}{\epsilon}\right] \cup \dots, \qquad \text{with } L_{i+1} - L_i = O(1), \tag{5.57}$$

where constants L_i are chosen such that

$$\boldsymbol{u}^1\left(\boldsymbol{y}\left(\frac{L_i}{\epsilon}\right), \psi\left(\frac{L_i}{\epsilon}\right)\right) = \boldsymbol{0}, \qquad \forall i. \tag{5.58}$$

Note that this choice of constants L_i is always possible, because $\boldsymbol{u}^1$ vanishes at least once per period, according to (5.44).

We define

$$\boldsymbol{p}_i = \boldsymbol{p}\left(\frac{L_i}{\epsilon}\right), \qquad \text{with } \boldsymbol{p}(0) = \boldsymbol{T}^{-1}\big(\boldsymbol{x}(0) - \boldsymbol{y}_{eq}\big). \tag{5.59}$$

$$\boldsymbol{q}_i = \boldsymbol{q}\left(\frac{L_i}{\epsilon}\right), \qquad \text{with } \boldsymbol{q}(0) = \boldsymbol{T}^{-1}\big(\boldsymbol{y}(0) - \boldsymbol{y}_{eq}\big). \tag{5.60}$$

$$\boldsymbol{q}_{(i)} = \boldsymbol{q}\left(\frac{L_i}{\epsilon}\right), \qquad \text{with } \boldsymbol{q}\left(\frac{L_{i-1}}{\epsilon}\right) = \boldsymbol{p}_{i-1}. \tag{5.61}$$

Thus, $\boldsymbol{q}_{(i)}$ represents the value of $\boldsymbol{q}$ at the end of an interval when, as an initial condition, $\boldsymbol{q}$ is imposed to be equal to $\boldsymbol{p}$ at the beginning of the interval.

First, we have that

$$\left\|\boldsymbol{p}_i - \boldsymbol{q}_{(i)}\right\| \leq c\epsilon^2, \tag{5.62}$$

as is clear from (5.37),(5.49) and (5.56), using that $\boldsymbol{u}^1 = \boldsymbol{0}$ at the considered instants.

On the other hand, by virtue of relation (5.54), we can write

$$\left\|\boldsymbol{q}_i - \boldsymbol{q}_{(i)}\right\| \leq k\|\boldsymbol{q}_{i-1} - \boldsymbol{p}_{i-1}\|, \qquad \text{with } k = 1 - \epsilon\lambda, \qquad \lambda > 0. \tag{5.63}$$

Combining (5.62) and (5.63), we have

$$\|\boldsymbol{p}_i - \boldsymbol{q}_i\| \leq c\epsilon^2 + k\|\boldsymbol{q}_{i-1} - \boldsymbol{p}_{i-1}\|. \tag{5.64}$$

By using (5.64) recursively, we arrive at

$$\|\boldsymbol{p}_i - \boldsymbol{q}_i\| \leq c\epsilon^2\left(1 + k + \cdots + k^{i-2}\right) + k^{i-1}\|\boldsymbol{q}_1 - \boldsymbol{p}_1\|. \tag{5.65}$$

Note that, according to (5.37), (5.49) and (5.56), we can write

$$\|\boldsymbol{q}_1 - \boldsymbol{p}_1\| \leq c\epsilon^2, \tag{5.66}$$

thanks to the fact that $\boldsymbol{u}^1\left(\boldsymbol{y}(L_1/\epsilon), \psi(L_1/\epsilon)\right) = \boldsymbol{0}$.

Finally, introducing (5.66) into (5.65) and taking the limit for $i \to \infty$ yields

$$\lim_{i\to\infty}\|\boldsymbol{p}_i - \boldsymbol{q}_i\| \leq \frac{c}{1-k}\epsilon^2 \leq \frac{c}{\lambda}\epsilon, \tag{5.67}$$

where (5.55) has been used.

Although (5.67) only holds, in principle, for the particular instants L_i/ϵ, it can be readily generalized for any t. Note that, as stated in (5.44), any $t > 0$ is at $O(1)$–distance from an instant t_0 where $\boldsymbol{u}^1 = \boldsymbol{0}$. Clearly, t_0 could be taken as L_i/ϵ and, therefore, (5.67) holds at t_0. On the other hand, $\boldsymbol{p}$ and $\boldsymbol{q}$ can only undergo $O(\epsilon)$ variations in an $O(1)$ time increment, which justifies the generalization of (5.67) to any t. Then, for $t \to \infty$, we can write

$$\|\boldsymbol{p}(t) - \boldsymbol{q}(t)\| \leq \frac{c}{\lambda}\epsilon \tag{5.68}$$

Recovering the original variables, we have

$$\|\boldsymbol{x}(t) - \boldsymbol{y}(t)\| \leq \|\boldsymbol{T}\|\big\|\big(\boldsymbol{p}(t) - \boldsymbol{q}(t)\big)\big\|, \qquad t \in [0, \infty). \tag{5.69}$$

Finally, introducing (5.68) into (5.69) yields

$$\|\boldsymbol{x}(t) - \boldsymbol{y}(t)\| \leq c_1\epsilon, \qquad t \in [0, \infty), \tag{5.70}$$

where

$$c_1 = \frac{\|\boldsymbol{T}\|c}{\lambda} \tag{5.71}$$

The conclusion is that, for initial conditions close enough to the considered equilibrium, the solution of the averaged system is at an $O(\epsilon)$ distance from the solution of the original system, for all $t > 0$. Then, if the equilibrium is asymptotically stable in the averaged system, it is asymptotically stable as well for the original system.

Now, the obtained result is particularized for the case of the motor with small slope characteristic. Equation (5.70) takes the form

$$\left.\begin{matrix} a = \bar{a} + O\left(\sqrt{\epsilon}\right) \\ \beta = \bar{\beta} + O\left(\sqrt{\epsilon}\right) \\ \sigma = \bar{\sigma} + O\left(\sqrt{\epsilon}\right) \end{matrix}\right\}, \qquad \text{for} \quad \tau \in [0, \infty), \tag{5.72}$$

for solutions starting close enough to the fixed point (5.20), (5.21), with $z = -1$. By comparing (5.70) with (5.18), it is clear that the time validity of the approximation has been extended, paying the price of a less accurate solution.

Final Remarks

In summary, the system has been found to exhibit two equilibrium points in the resonance region as long as $c < \alpha/2$. Fig. 5.2 represents both equilibria on a torque-speed plot, where the fixed point on the right branch is unstable and the one on the left branch is stable. Note that the existence of a stable fixed point in the inner region justifies the possibility of 'resonance capture'.

Recall that the system reaches the resonance manifold whenever $\Omega(0) < 1$. For some sets of initial conditions, the trajectory will enter the Poincaré-Lyapunov domain of the stable fixed point and, therefore, it will remain near resonance for all subsequent time –resonant capture–. Clearly, there may also be sets of initial conditions such that the trajectory does not reach the Poincaré-Lyapunov domain of the stable fixed point. In these cases, the system will probably leave the inner region and evolve towards fixed point (5.12) in the outer region –passing through resonance–.

In principle, it would also be possible that the system was attracted by a different object in the inner region, such as a stable limit cycle or a chaotic attractor. This would represent another kind of resonance capture, not due to the presence of the stable fixed point analysed in this section. However, the numerical simulations carried out have not revealed the existence in the inner region of any attractor other than the analysed fixed point.

Note also that this chapter has coped with the inner and outer approximations separately. We have not tried to construct a 'composite expansion' by matching the inner and outer solutions, which is a rather intricate and complex subject, treated, for example, in (W. Eckhaus, 1979; Sanders et al., 2007).

Before showing numerical results to confirm the analytical developments of this Chapter, it is convenient to comment some other works on the subject.

Sanders, Verhulst and Murdock considered the system studied in this Section as an illustrative example in Chapters 7 and 8 of their book (Sanders et al., 2007). Regarding the outer region of the phase space, they conducted the same analysis as in this Chapter, averaging over the three fast angles in (5.8) and obtaining equilibrium (5.12). However, in the inner region they only carried out a first order averaging in contrast to the second order averaging addressed in this Chapter. This procedure did not allow them to analyse the stability of the fixed points near resonance, since a first order averaging is not accurate enough for this purpose.

In addition, Alexander Fidlin devoted Chapter 5 of his book (Fidlin, 2006) to the study of nonideal excitations, taking system (5.2) as a relevant example. He focused only on the resonance region, arriving at a system analogous to (5.19) after a second order averaging. However, there are two main differences between his results and those presented in the present Chapter:

- According to the analysis proposed in this thesis, the equilibrium point for $z = -1$ is stable as long as $d < 0$. However, Fidlin came to the conclusion that the condition for stability is $d - \xi < 0$. The reason for this difference is a small erratum in the eigenvalues computation in (Fidlin, 2006), namely in the step from equation (5.21) to (5.22) of the mentioned reference: where it reads $\frac{1}{4}\epsilon^2 k \cos\vartheta_{20} \sin\vartheta_{20}$, it should read $\frac{1}{2}\epsilon^2 k \cos\vartheta_{20} \sin\vartheta_{20}$.
- Fidlin addressed the short time scale where the inner averaged system is valid, $\tau = O\left(1/\sqrt{\epsilon}\right)$, as an important limitation of the analysis. He proposed a hierarchic averaging procedure as a way to enlarge the time of validity of the approximation (Pechenev, 1992). However, this method fails precisely in the vicinity of the equilibrium point of interest, because the required variable transformation becomes singular at that point. Therefore, the hierarchic averaging scheme cannot be used to justify the asymptotic stability of the fixed point.

In conclusion, the chief contribution of this Chapter with respect to previous published works is the rigorous justification of the asymptotic stability of one of the stationary motions of the system near resonance, which in turn gives a solid explanation of the possibility of resonant capture, or ‘locking into resonance’.

6 THE CASE OF SMALL SLOPE OF THE MOTOR CHARACTERISTIC: NUMERICAL SIMULATIONS

This Chapter is intended to verify the results of Chapter 5 by means of numerical simulation. Following an analogous scheme to that in Chapter 4, particular values are assigned to the system parameters and both the original and approximate systems are numerically solved in order to compare the obtained solutions.

Thus, consider the following parameters

$$\xi = 2, \qquad \alpha = 4, \qquad \rho = 5, \qquad c = \frac{1}{2}, \qquad d = -1, \tag{6.1}$$

which might be associated to dimensional parameters

$$\left\{ \begin{array}{c} m = 100\text{kg} \\ k = 100\,\text{N/m} \\ b = 0.4\,\text{Ns/m} \\ m_1 = 0.1\text{kg} \\ \lambda = 50\,\text{N/m}^3 \\ r = 0.4\text{m} \\ I = 1\text{m}^2\text{kg} \\ C = 5 \cdot 10^{-4}\text{Nm} \\ D = -1 \cdot 10^{-3}\text{Nms} \end{array} \right\}, \tag{6.2}$$

with $\epsilon = 0.001$. This set of parameters gives rise to the torque-speed curves depicted in Fig. 6.1. Note that condition $c < \alpha/2$ is fulfilled, which implies that there exist two fixed points in the inner region of the phase space, corresponding to the two intersections between T_v and T_m in Fig. 6.1.

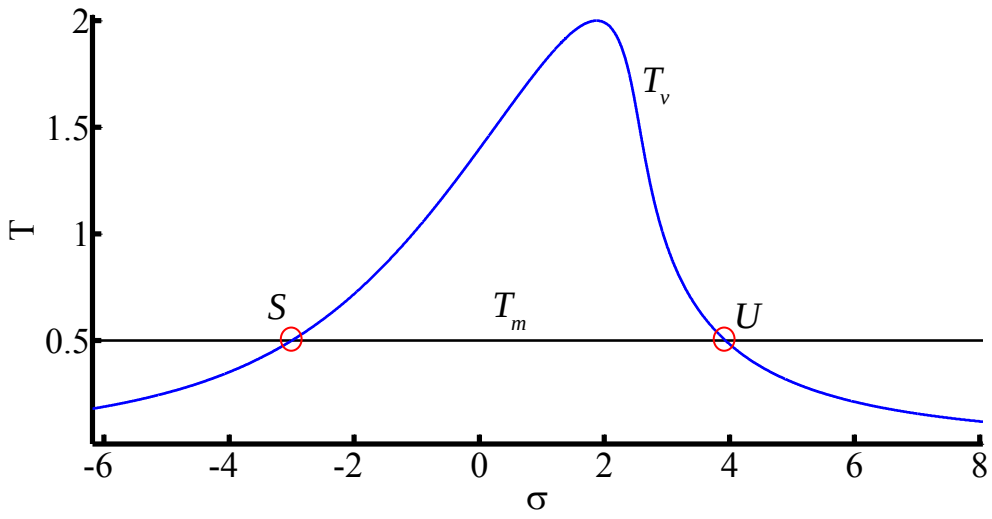

Fig. 6.1 Torque-speed curves corresponding to parameters (6.1).
S and U label the stable and unstable fixed points, respectively.

As discussed in Chapter 5, the equilibrium on the left branch of curve T_v is stable, while the one on the right branch is unstable. The fixed points can be readily computed by introducing (6.1) into (5.21):

$$\left\{\begin{matrix} a_0 = 0.5 & \beta_0 = -0.52 & \sigma_0 = 0 \\ a_1 = 0 & \beta_1 = 0 & \sigma_1 = -3 \end{matrix}\right\} \text{ STABLE} \tag{6.3}$$

$$\left\{\begin{matrix} a_0 = 0.5 & \beta_0 = -2.62 & \sigma_0 = 0 \\ a_1 = 0 & \beta_1 = 0 & \sigma_1 = 3.93 \end{matrix}\right\} \text{ UNSTABLE} \tag{6.4}$$

The third equilibrium, in the outer region of the phase space, can be obtained by introducing (6.1) into (5.12):

$$\left\{\begin{matrix} a = 0 \\ \Omega = 1.5 \end{matrix}\right\}. \tag{6.5}$$

The simulations have been carried out as follows. A set of initial conditions for the original system (5.2) is chosen with $\Omega(0) < 1$, i.e. in the pre-resonant region of the phase space. Then, the original system of equations is numerically solved for a time interval $[0, \tau_f]$ which is long enough to ascertain whether the system is captured or passes through resonance.

Suppose the system passes through resonance. Looking at the numerical solution of the original equations, two particular instants, τ_1 and τ_2 are defined, at which the system enters and leaves the resonance region, respectively. Although the choice of these two values is somewhat arbitrary, they give an approximation to the limits between the inner and outer solutions. Then, the outer approximate system (5.10) is solved for $\tau \in [0, \tau_1]$ and $\tau \in [\tau_2, \tau_f]$, with the initial conditions obtained as the solution of the original system evaluated at $\tau = 0$ and $\tau = \tau_2$, respectively. The inner approximate system (5.17) is solved for $\tau \in [\tau_1, \tau_2]$, with the initial conditions corresponding to the solution of the original equations particularized at $\tau = \tau_1$. Finally, the solutions of the original, outer and inner systems are represented

together, in order to confirm the accordance between the outer (inner) approximation and the original solution far away from (close to) resonance.

In the event of resonance capture, instant τ_2 does not exist. Then, the outer and inner averaged systems are solved for $\tau \in [0, \tau_1]$ and $\tau \in [\tau_1, \tau_f]$, respectively.

It is worth noting that, regarding the inner approximation, we do not represent the solution $\{\bar{a}, \bar{\beta}, \bar{\sigma}, \bar{\phi}\}$ of system (5.17), but the more accurate solution given by $\left\{\bar{a}, \bar{\beta}, \bar{\sigma} + \sqrt{\epsilon}\frac{\alpha}{4}\bar{a}\cos(2\bar{\phi} + \bar{\beta}), \bar{\phi}\right\}$, according to (5.18).

For the first simulation, consider the following set of initial conditions for the original system:

$$\begin{Bmatrix} u_0 = 0.2 \\ \dot{u}_0 = 0 \\ \phi_0 = 3 \\ \dot{\phi}_0 = 0.2 \end{Bmatrix}. \tag{6.6}$$

The obtained numerical solution, together with the corresponding solutions of the outer and inner approximate systems, is represented in Fig. 6.2. In this particular case, the outer solution has been depicted for the whole time range, in order to clearly see how this approximation actually captures the original system behaviour until reaching the resonance region. From this point on, the outer approximation loses all accuracy.

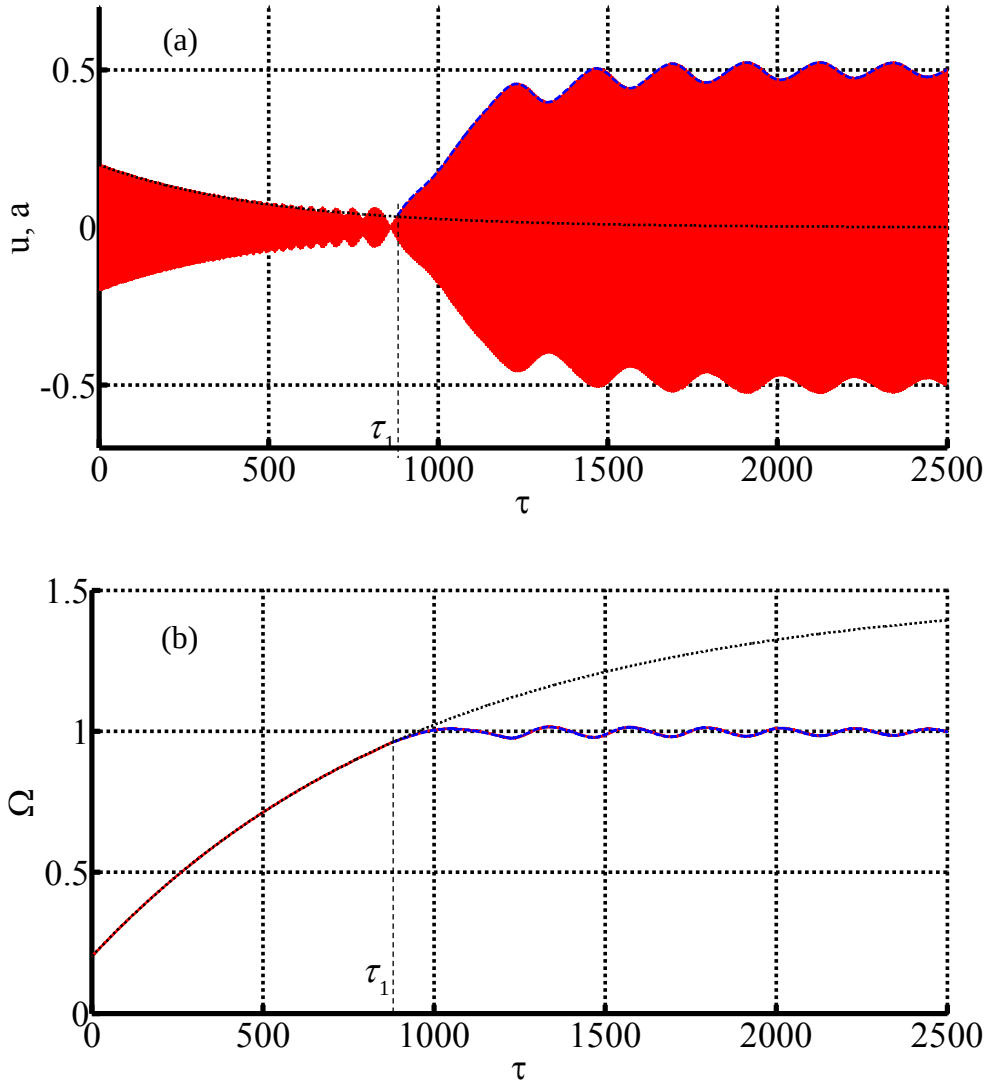

Fig. 6.2 Numerical solutions for parameters (6.1), initial conditions (6.6) and $\epsilon = 10^{-3}$. Solid, dashed and dotted lines correspond to the original, inner and outer systems, respectively

a) Displacements

b) Rotor speed

Fig. 6.2 shows a clear scenario of resonance capture, with a remarkably good accordance between solutions of the original and approximate systems. In fact, it

may not be easy to distinguish the different curves because they are virtually coincident.

The oscillation observed in the resonance region resembles the limit cycles encountered in the case of large slope (see Fig. 4.10 and Fig. 4.11), which may lead us to consider it a sustained oscillation. However, a closer look at the curves reveals that the amplitude of this variation decreases with time, as trajectories approaches the stable equilibrium given at (6.3). The mentioned oscillation is just the typical spiralling of an orbit which approaches a stable focus. This can be clearly observed Fig. 6.3(a). With an even closer look at the rotor speed near resonance in Fig. 6.3(b), we can also see the small, fast oscillation given by the $O\left(\sqrt{\epsilon}\right)$-term in the third of equations (5.18).

We note here the relation between the above comments and some experimental results published in (Dimentberg et al., 1997). Dimentberg et al. used an experimental setup, similar to the model studied within this thesis, to look for the threshold between passage and locking into resonance. Fig. 6.4 displays the results of one of their experiments, which clearly corresponds to resonance capture. It is interesting to observe the similarity between Fig. 6.2 and Fig. 6.4. Dimentberg et al. were inclined to think that the oscillations in the vibrating amplitude and rotor speed may represent a chaotic motion of the system. However, in the light of the last paragraph, we can put forth the possibility that these variations actually correspond to the same phenomenon as in Fig. 6.2. This could be ascertained by simply recording experimental data for a longer time interval, in order to see whether or not the rotor speed stabilizes on a constant value (apart from the small and fast oscillation displayed in Fig. 6.2(d)).

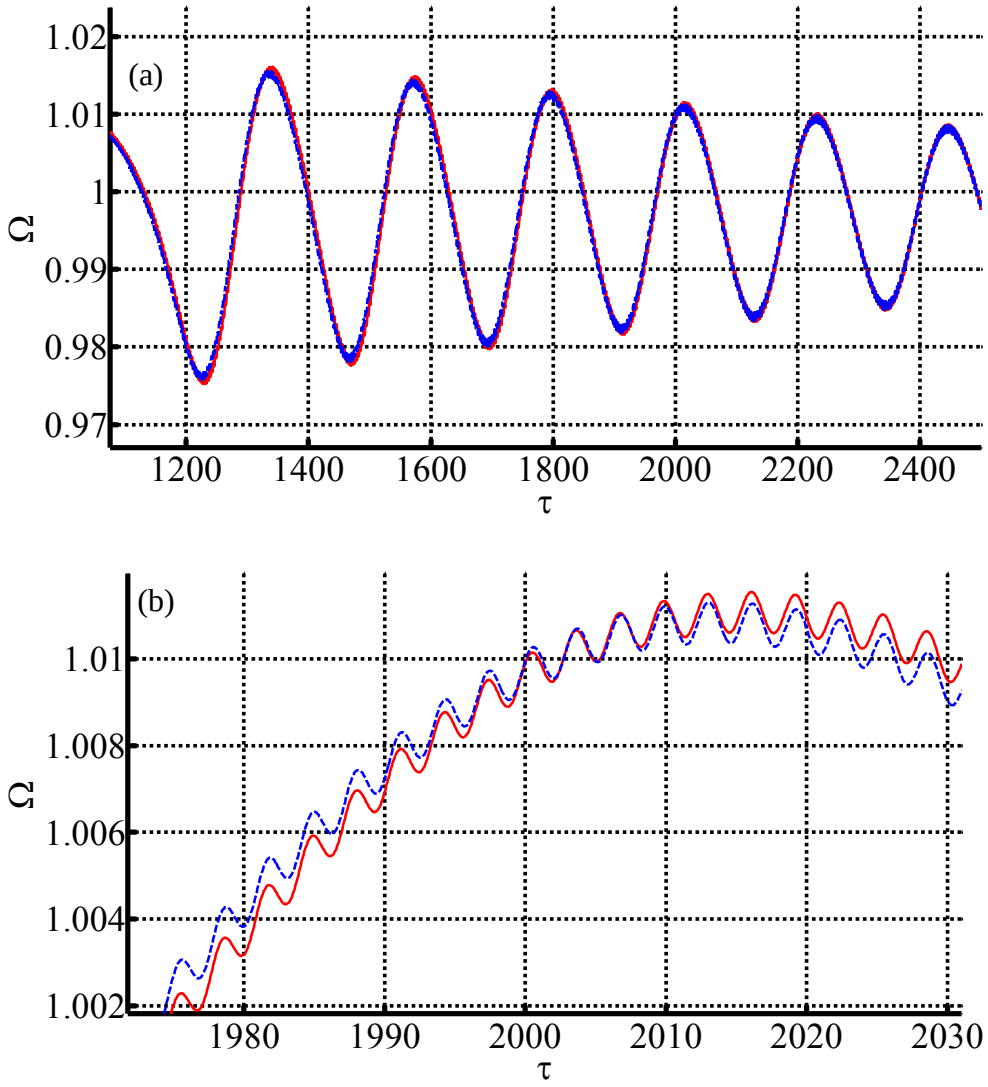

Fig. 6.3 Numerical evolution of the rotor speed for parameters (6.1), initial conditions (6.6) and $\epsilon = 10^{-3}$. Solid and dashed lines correspond to the original and inner systems, respectively

a) Close-up around resonance

b) Narrower close-up to show the fast oscillation

Consider now a different set of initial conditions for the original system,

$$\begin{Bmatrix} u_0 = 0.1 \\ \dot{u}_0 = 0 \\ \phi_0 = 2 \\ \dot{\phi}_0 = 0.1 \end{Bmatrix}, \tag{6.7}$$

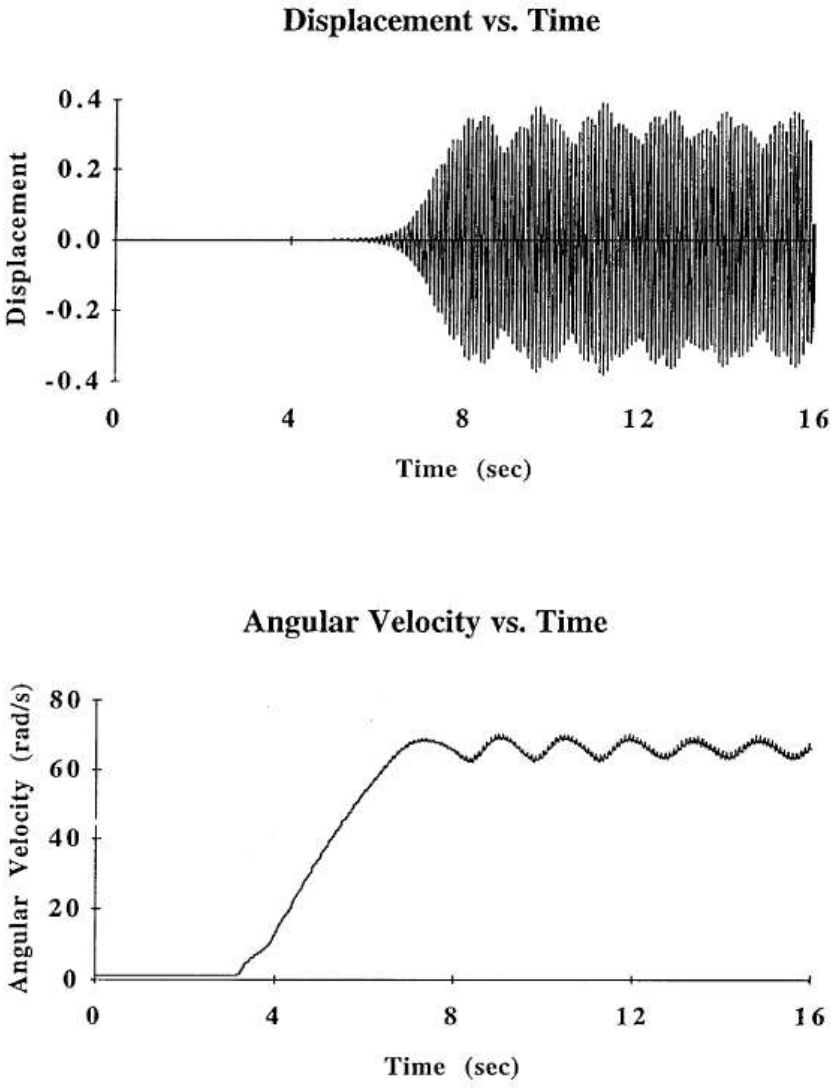

Fig. 6.4 Experimental results for resonance capture found by Dimentberg, taken from (Dimentberg et al., 1997)

which yields the numerical results displayed in Fig. 6.5.

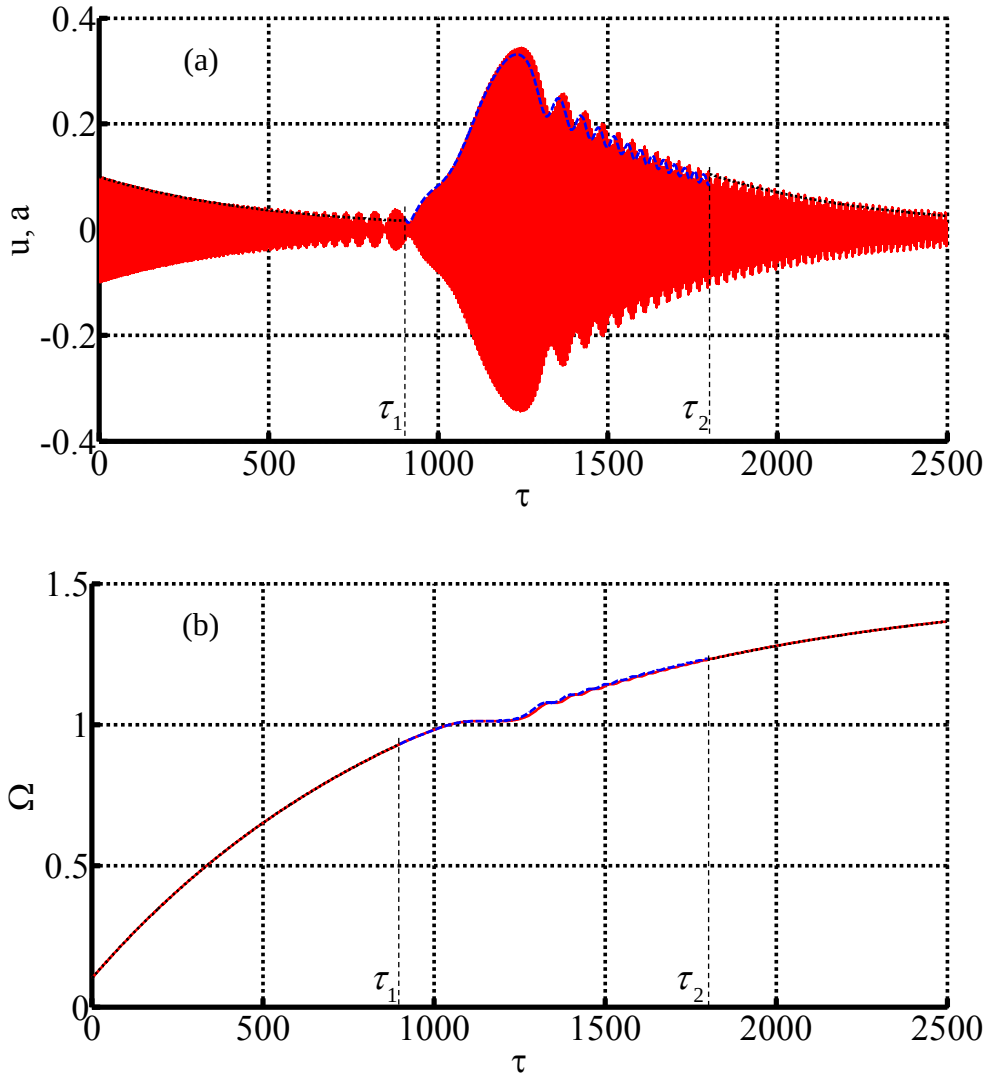

Fig. 6.5 Numerical solutions for parameters (6.1), initial conditions (6.7) and $\epsilon = 10^{-3}$. Solid, dashed and dotted lines correspond to the original, inner and outer systems, respectively

a) Displacement

b) Rotor speed

Unlike in the previous case, the system is now found to pass through resonance, with an acceptably good accordance between the solutions of the original and

approximate equations. Once the system has overcome the resonance region, it evolves towards the outer stable equilibrium given by (6.5).

It is also illustrative to consider a different situation. Suppose parameter c is increased until there are no fixed points in the averaged system near resonance. The condition to meet is $c > \alpha/2 = 2$. Then, consider the following set of parameter values:

$$\xi = 2, \qquad \alpha = 4, \qquad \rho = 5, \qquad c = 2.1, \qquad d = -1, \tag{6.8}$$

which is exactly the same as (6.1) except for a larger driving torque at resonance. The torque-speed graph for this scenario, obtained through relations (5.26) and (5.29), is depicted in Fig. 6.6, exhibiting no intersections between the curves.

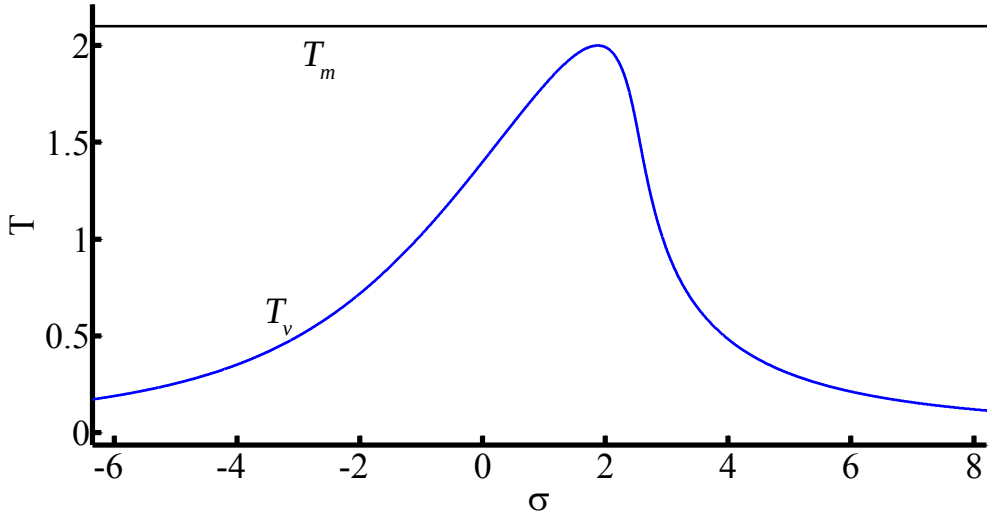

Fig. 6.6 Torque-speed curves corresponding to parameters (6.8)

Clearly, resonance capture cannot occur in this situation, unless an attractor other than a fixed point existed in the inner region. As stated before, no numerical evidence of such an attractor has been found. The conclusion is that the system will pass through resonance for any pre-resonant initial condition and will lead towards the outer stable equilibrium, which is now given by

$$\begin{Bmatrix} a = 0 \\ \Omega = 3.1 \end{Bmatrix}, \tag{6.9}$$

as can be obtained by introducing (6.8) into (5.12):

Despite the resonance being not active –i.e. there are no attractors in the resonance region–, it can be expected that trajectories are somehow distorted when passing through the resonance manifold. To the end of observing this effect, two different simulations have been conducted with different initial conditions:

$$\begin{Bmatrix} u_0 = 0.05 \\ \dot{u}_0 = 0 \\ \phi_0 = 0 \\ \dot{\phi}_0 = 0.3 \end{Bmatrix}. \tag{6.10}$$

$$\begin{Bmatrix} u_0 = 3 \\ \dot{u}_0 = 0 \\ \phi_0 = 0 \\ \dot{\phi}_0 = 0.3 \end{Bmatrix}. \tag{6.11}$$

The results are displayed in Fig. 6.7-Fig. 6.9. Note that, for initial conditions (6.10), the evolution of the rotor speed is nearly unaffected by resonance, while there is a significant effect on the vibration amplitude. It is interesting that exactly the opposite case is encountered for initial conditions (6.11): whereas the structure vibration is almost unaltered by resonance, the rotor speed undergoes significant oscillations when the system passes through the resonance manifold. Thus, it is clear that the influence of resonance on the system behaviour depends on the initial conditions. In general, we can state that some transient resonant effects can be expected in the system, even when there are no attractors in the resonance region.

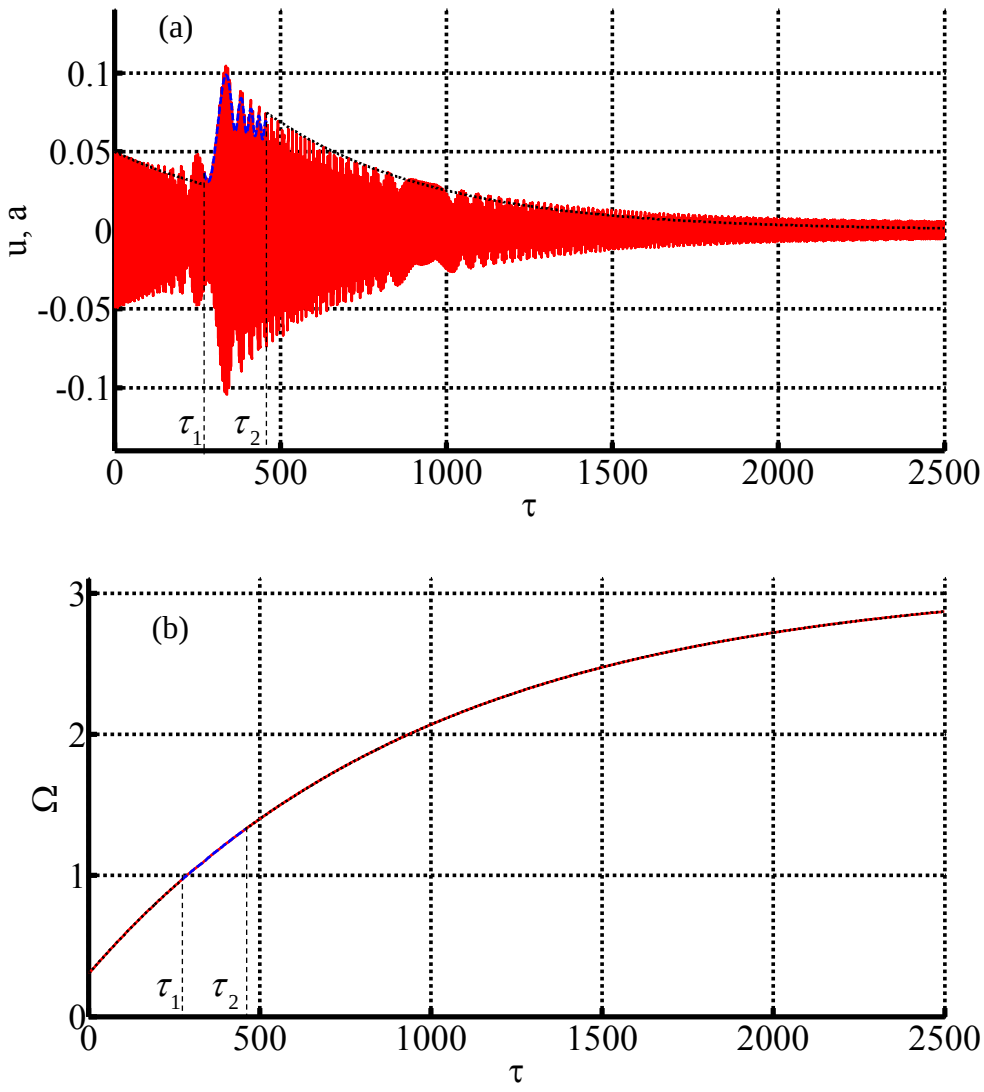

Fig. 6.7 Numerical solutions for parameters (6.1), initial conditions (6.10) and $\epsilon = 10^{-3}$. Solid, dashed and dotted lines correspond to the original, inner and outer systems, respectively

a) Displacement

b) Rotor speed

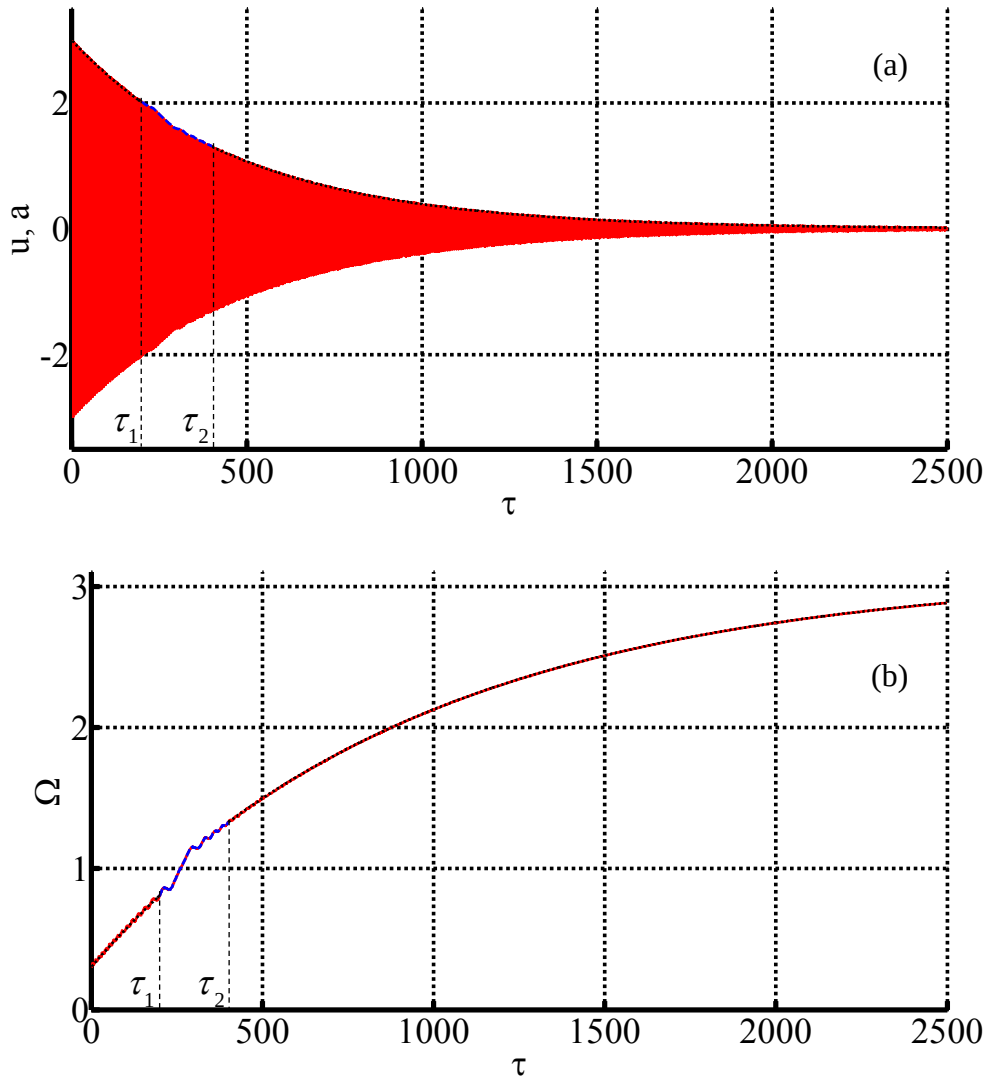

Fig. 6.8 Numerical solutions for parameters (6.1), initial conditions (6.11) and $\epsilon = 10^{-3}$. Solid, dashed and dotted lines correspond to the original, inner and outer systems, respectively

a) Displacement

b) Rotor speed

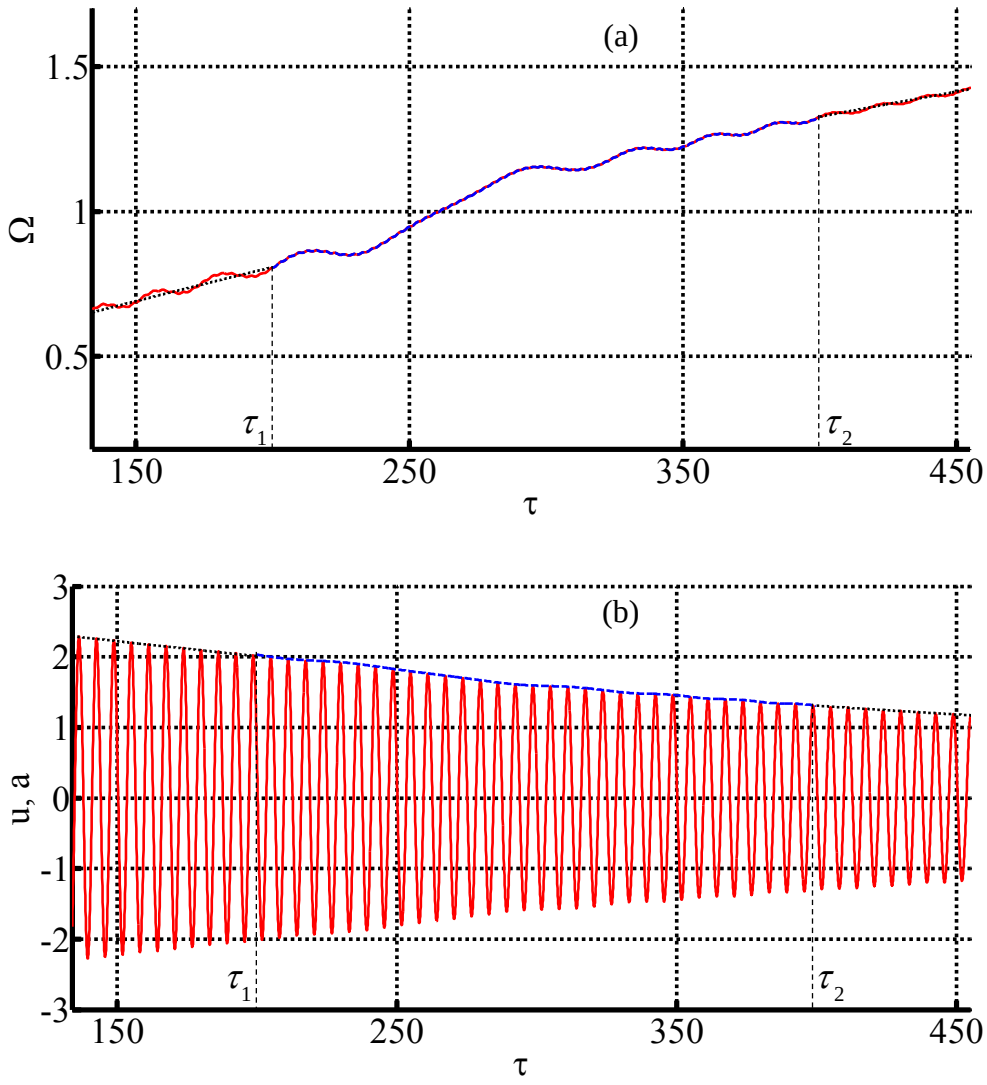

Fig. 6.9 Close-up around resonance of numerical solutions for parameters (6.1), initial conditions (6.11) and $\epsilon = 10^{-3}$. Solid, dashed and dotted lines correspond to the original, inner and outer systems, respectively

a) Displacement

b) Rotor speed

7 TORQUE-SPEED CURVES FOR THE WHOLE FREQUENCY RANGE

This Chapter serves as a connector between the analyses presented in Chapters 3-6 and the study of the vibrocompaction process expounded in Chapter 8. Recall that torque-speed curves have already been successfully used to obtain the stationary motions of the vibrating unbalanced motor in Chapters 3-6. However, in these previous approaches, the torque-speed plot is only represented for the resonance region, like in Fig. 3.7 and Fig. 5.2, or for the non-resonant region, like in Fig. 5.1. This necessary distinction between resonant and non-resonant regions of the phase

space is a direct consequence of the perturbation approaches that have been utilized in previous chapters.

The objective is now to generalize the use of these curves, so that the vibration torque and the motor torque can be plotted together in a single graph for the whole frequency range, thereby representing the resonant and non-resonant stationary motions of the motor. This will turn out to be very useful in the next chapter, as will be seen, and will also provide a clear global perspective of the problem studied in Chapters 3-6.

7.1 Computation of the Torque-Speed Curves

Consider again the mechanical system shown in Fig. 3.1, whose equations of motion (3.1) are rewritten below.

$$\begin{aligned} m\ddot{x} + b\dot{x} + kx &= m_1 r\left(\dot{\phi}^2 \cos\phi + \ddot{\phi}\sin\phi\right) \\ I\ddot{\phi} &= L_m\left(\dot{\phi}\right) + m_1 r\ddot{x}\sin\phi\,, \end{aligned} \tag{7.1}$$

Note that the cubic nonlinearity is now assumed to be zero for simplicity. As usual, the motor characteristic is assumed to be a linear function of the rotor speed:

$$L_m\left(\dot{\phi}\right) = A + D\dot{\phi}, \tag{7.2}$$

with $D < 0$.

We note that the analysis shown in what follows is based on Blekhman's approach of *direct separation of motions* (Blekhman, 2000). In order to approximately obtain the stationary motions of the system, it is reasonable to look for solutions where the rotor speed has the form

$$\dot{\phi}(t) = \Omega_0 + \Omega_1(t), \tag{7.3}$$

with Ω_0 constant and $\Omega_1(t)$ a periodic function of time with zero average. It is also assumed that the solution satisfies

$$\left.\begin{matrix}\Omega_1(t) \ll \Omega_0 \\ \dot{\Omega}_1(t) \ll \Omega_0^2\end{matrix}\right\} \forall t. \tag{7.4}$$

Conditions (7.4) will be verified afterwards. Introducing (7.3) into the first of equations (7.1) yields

$$m\ddot{x} + b\dot{x} + kx = m_1 r\left[(\Omega_0 + \Omega_1)^2 \cos\phi + \dot{\Omega}_1 \sin\phi\right]. \tag{7.5}$$

By taking (7.4) into account, equation (7.5) can be approximated as

$$m\ddot{x} + b\dot{x} + kx \approx m_1 r\Omega_0^2 \cos(\Omega_0 t), \tag{7.6}$$

where $\phi(0) = 0$ has been assumed for simplicity. Note that, to first approximation, the small oscillation of the rotor speed $\Omega_1(t)$ does not affect the system vibration.

It may seem from (7.6) that the problem has been rendered linear with the proposed approximation. In fact, equation (7.6) represents a harmonically forced linear oscillator. However, the system as a whole is still nonlinear, due to the nonideal interaction with the exciter. This can be seen by noticing that constant Ω_0 in (7.6) is not known a priori. Hence the linear motion $x(t)$ needs to be solved as a function of Ω_0. Then, the torque produced by this vibration will be introduced in the rotor equilibrium equation –second of equations (7.1)–, which will allow obtaining Ω_0. Therefore, there is still a two-way coupling between vibration and rotation.

The stationary solution of (7.6) is very well-known from linear vibration theory:

$$x(t) = x_{max}\cos(\Omega_0 t + \varphi_1), \tag{7.7}$$

with

$$x_{max} = \frac{\frac{m_1}{m} r \left(\frac{\Omega_0}{\omega_n}\right)^2}{\sqrt{\left[\left(\frac{\Omega_0}{\omega_n}\right)^2 - 1\right]^2 + \left[2\xi\frac{\Omega_0}{\omega_n}\right]^2}}, \qquad \varphi_1 = \tan^{-1}\left(\frac{-2\xi\frac{\Omega_0}{\omega_n}}{1 - \left(\frac{\Omega_0}{\omega_n}\right)^2}\right), \tag{7.8}$$

where $\omega_n = \sqrt{k/m}$, $\xi = b/(2m\omega_n)$. The vibration amplitude x_{max} is represented against the average rotor speed Ω_0 in Fig. 7.1, according to (7.8).

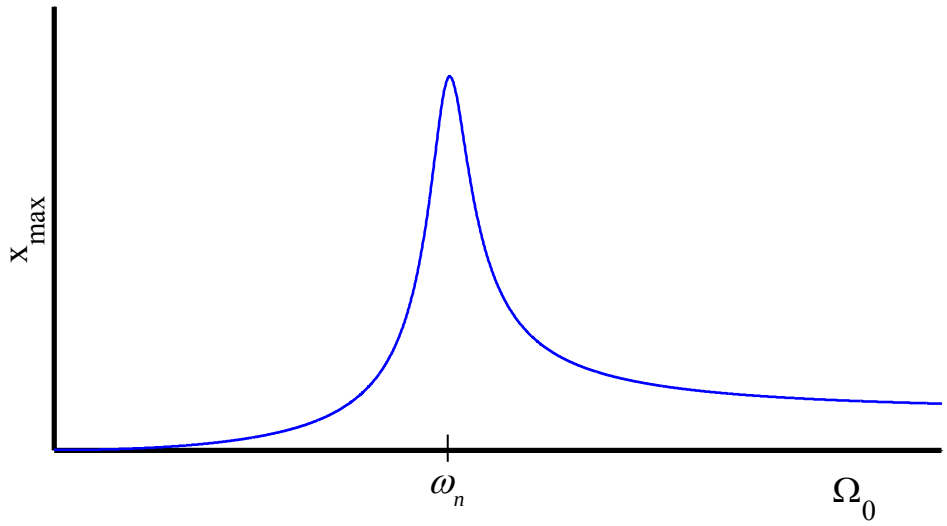

Fig. 7.1 Amplitude of the stationary vibration versus averaged rotor speed, corresponding to equation (7.8)

Once the linear motion has been obtained, it can be introduced in the rotor equilibrium equation in order to compute the stationary rotor speed. First, the proposed solution for the rotor speed (7.3) is replaced in the second of equations (7.1):

$$I\dot{\Omega}_1 \approx L_m(\Omega_0) + D\Omega_1 + m_1 r\ddot{x}\sin(\Omega_0 t), \tag{7.9}$$

where assumption (7.4) has been used. Then, introducing solution (7.7) into (7.9) yields

$$I\dot{\Omega}_1 \approx L_m(\Omega_0) + D\Omega_1 - \Omega_0^2 m_1 r x^{max}\cos(\Omega_0 t + \varphi_1)\sin(\Omega_0 t). \tag{7.10}$$

It is convenient to rewrite the last term in (7.10) as the sum of its mean value and an oscillating component:

$$\begin{aligned} I\dot{\Omega}_1 \approx L_m(\Omega_0) + D\Omega_1 &+ \frac{1}{2}\Omega_0^2 m_1 r x_{max}\sin\varphi_1 \\ &- \frac{1}{2}\Omega_0^2 m_1 r x_{max}\sin(2\Omega_0 t + \varphi_1). \end{aligned} \tag{7.11}$$

Note that (7.11) contains constant and oscillating terms with zero average. Clearly, if equation (7.11) is averaged, only the constant terms remain:

$$0 = L_m(\Omega_0) + \frac{1}{2}\Omega_0^2 m_1 r x_{max}\sin\varphi_1. \tag{7.12}$$

Substracting (7.12) to (7.11) yields

$$I\dot{\Omega}_1 = D\Omega_1 - \frac{1}{2}\Omega_0^2 m_1 r x_{max}\sin(2\Omega_0 t + \varphi_1). \tag{7.13}$$

Equation (7.12) can be interpreted as an equilibrium conditions between the average torques acting on the rotor during the stationary motion. Actually, by inserting (7.8) into (7.12), the following relation is obtained:

$$L_m(\Omega_0) = L_v(\Omega_0), \tag{7.14}$$

where function L_v is defined as

$$L_v(\dot{\phi}) \equiv k\xi \left(\frac{m_1 r}{m}\right)^2 \frac{\left(\frac{\dot{\phi}}{\omega_n}\right)^5}{\left[\left(\frac{\dot{\phi}}{\omega_n}\right)^2 - 1\right]^2 + \left[2\xi \frac{\dot{\phi}}{\omega_n}\right]^2}. \tag{7.15}$$

Equation (7.14) is the most important outcome of this chapter. It allows obtaining the average stationary rotor speed as the intersection between two curves, which represent the driving torque produced by the motor (L_m) and the resisting torque due to vibration (L_v). This graphical representation, which had been already obtained in (Blekhman, 2000), is given in Fig. 7.2.

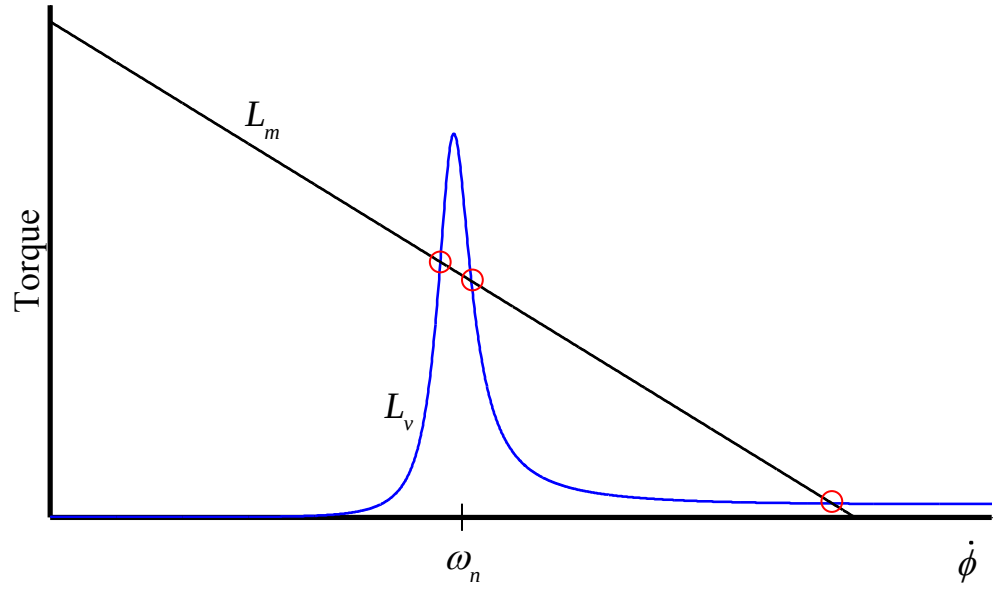

Fig. 7.2 Graphical representation of the torque-speed curves, corresponding to equation (7.14). The three intersections, marked with circles, give the three possible values of the average rotor speed, Ω_0, at the stationary motion of the system.

Surely, the described way of obtaining the stationary motions of the unbalanced motor will remind the reader similar results obtained in previous chapters. Actually,

in Chapter 3 (large slope), the stationary motions near resonance were graphically obtained from the equality between the motor torque and the vibration torque, $T_m = T_v$ (see equation (3.57) and Fig. 3.7). The philosophy was exactly the same in Chapter 5 (small slope), both for the stationary motions away from resonance (see equation (5.12) and Fig. 5.1) and in the resonance region (see equation (5.25) and Fig. 5.2). It is recalled here that, in Fig. 5.1, the stationary solution is obtained as the speed which makes the motor torque zero because the vibration torque is negligible outside the resonance region, under the assumptions of Chapter 5.

Two aspects are important regarding the relation between the approach presented in this chapter and those in Chapters 3 and 5:

- Functions T_m and T_v in Fig. 3.7 and Fig. 5.2 represent, respectively, dimensionless versions of the torques L_m and L_v used within the present chapter. In the same way, curve H_m in Fig. 5.1 is also a dimensionless version of L_m. Actually, T_m in Chapter 5 is obtained by particularizing H_m for the resonance region of the phase space. Dimensional variables have been preferred for this chapter because the results they provide are more convenient with a view to the vibrocompaction model presented in Chapter 8.
- The torque-speed curves used in previous chapters of the thesis are only valid in the resonance region (like in Fig. 3.7 and Fig. 5.2) or far away from resonance (like in Fig. 5.1). Conversely, the curves given at (7.2), (7.15), and represented in Fig. 7.2, are valid for the whole frequency range. In fact, it can be checked that expression (7.15), particularized for $\dot{\phi}$ close to ω_n, after neglecting the higher order terms and transforming to dimensionless variables, gives the vibration torque curve used in previous chapters and defined by equations (3.56), (3.59). In view of this, it is reasonable to wonder why the approaches presented in Chapters 3 and 5 have been used at all, instead of directly applying the scheme of the present chapter. The reason is twofold. First, the approach of this chapter assumes that the spring which connects the motor to the fixed frame is linear. The extension of this

analytical scheme to the case of a nonlinear spring is not straightforward. Second, and more importantly, the method described in this chapter does not provide the stability of the stationary solutions. In fact, the stability analysis requires the use of a rigorous perturbation technique, such as those presented in Chapters 3 and 5.

Finally, the time-varying part of the rotor speed can be obtained from (7.13). This is a first order linear differential equation in $\Omega_1(t)$. Since the forcing term in (7.13) is harmonic with frequency $2\Omega_0$, so must the stationary response be. Then, we look for a solution of the form

$$\Omega_1(t) = \Omega_1^{max} \sin(2\Omega_0 t + \varphi_2) \tag{7.16}$$

Introducing (7.16) in (7.13), the amplitude Ω_1^{max} is readily obtained:

$$\Omega_1^{max} = \frac{\frac{1}{2}\Omega_0^2 m_1 r x_{max}}{\sqrt{D^2 + (2I\Omega_0)^2}} \tag{7.17}$$

The value of constant φ_2 is not given because it is of no special interest. It should be noticed that expressions (7.16), (7.17) are in complete accordance with the result obtained in Chapter 5 for the small oscillation of the rotor speed in the case of small slope, as can be checked by carefully comparing (7.16), (7.17) with the third of equations (5.18).

In order to verify whether or not assumptions (7.4) are fulfilled by solution (7.16), expression (7.17) is divided by Ω_0 and x_{max} is substituted by using (7.8), which gives

$$\frac{\Omega_1^{max}}{\Omega_0} = \frac{\frac{1}{2} R_I R_m \left(\frac{\Omega_0}{\omega_n}\right)^3}{\sqrt{d^2 + \left(\frac{2\Omega_0}{\omega_n}\right)^2} \sqrt{\left[\left(\frac{\Omega_0}{\omega_n}\right)^2 - 1\right]^2 + \left[2\xi \frac{\Omega_0}{\omega_n}\right]^2}}, \tag{7.18}$$

where dimensionless parameters R_I, R_m and d, defined in (3.5), have been used. It is easy to see that, for small values of the damping coefficient ξ, the curve Ω_1^{max}/Ω_0 –as a function of (Ω_0)– exhibits a global maximum at $\Omega_0 \approx \omega_n$. The value of this maximum can be approximately obtained by inserting $\Omega_0 = \omega_n$ in (7.18):

$$\left.\frac{\Omega_1^{max}}{\Omega_0}\right]_{\Omega_0=\omega_n} = \frac{\frac{1}{2} R_I R_m}{2\xi\sqrt{d^2+4}} < \frac{R_I R_m}{8\xi}. \tag{7.19}$$

Taking into account that (7.19) represents the maximum possible value of the amplitude of oscillation of $\Omega_1(t)$, it gives an upper bound for $\Omega_1(t)$:

$$\frac{\Omega_1(t)}{\Omega_0} < \frac{R_I R_m}{8\xi} = \frac{\alpha}{4}, \tag{7.20}$$

where $\alpha \equiv R_I R_m / 2\xi$, as defined in (3.5). On the other hand, the expression for $\dot{\Omega}_1(t)$ can be readily obtained by differentiating (7.16) with respect to time:

$$\dot{\Omega}_1(t) = 2\Omega_0 \Omega_1^{max} \cos(2\Omega_0 t + \varphi_2) \tag{7.21}$$

By combining (7.21) and (7.19), an upper bound is also found for $\dot{\Omega}_1(t)$:

$$\frac{\dot{\Omega}_1(t)}{\Omega_0^2} < \frac{\alpha}{2} \tag{7.22}$$

Assuming that α is a small parameter, as was done in all previous chapters –see (3.7)–, it is clear that assumption (7.4) is satisfied by the obtained solution, in the light of (7.20) and (7.22).

7.2 A Global Perspective for the Cases of Large and Small Slope

As was commented in the introduction to the chapter, the presentation of this alternative way of obtaining the torque-speed curves for the system under study has two main purposes. One is directly related to next chapter, where these curves will provide very illustrative and useful information about the vibrocompaction process. The second reason is that the torque-speed curves represented for the whole frequency range give a very clear graphical comparison between the cases of *large* and *small* slope treated in previous chapters.

The curves given by (7.2), (7.15) are represented in Fig. 7.3 and Fig. 7.4 for different motor characteristics, keeping the rest of the system parameters constant. Fig. 7.3 represents a case where the assumptions of Chapters 3 and 4 (*large slope*) are satisfied, whereas Fig. 7.4 corresponds the assumptions of Chapters 5 and 6 (small slope).

Note that the axes have been represented with the same scale in Fig. 7.3 and Fig. 7.4, in order to facilitate the visual comparison.

The plot with a large slope clearly evidences that all the stationary motions of the system –three in the particular case depicted– are in the resonance region, as had already been concluded in Chapter 3. These motions correspond to the fixed points shown in Fig. 3.7, and their stability was investigated in detail in Section 3.4. Applying these stability results, summed up in Fig. 3.8 and Fig. 3.9, to the plot under consideration, it can be stated that the first of the stationary motions (the one

with the lowest frequency) is stable and the second one is unstable. The stability of the third point cannot be deduced with just the information of Fig. 7.3, because of the possibility of a Hopf Bifurcation.

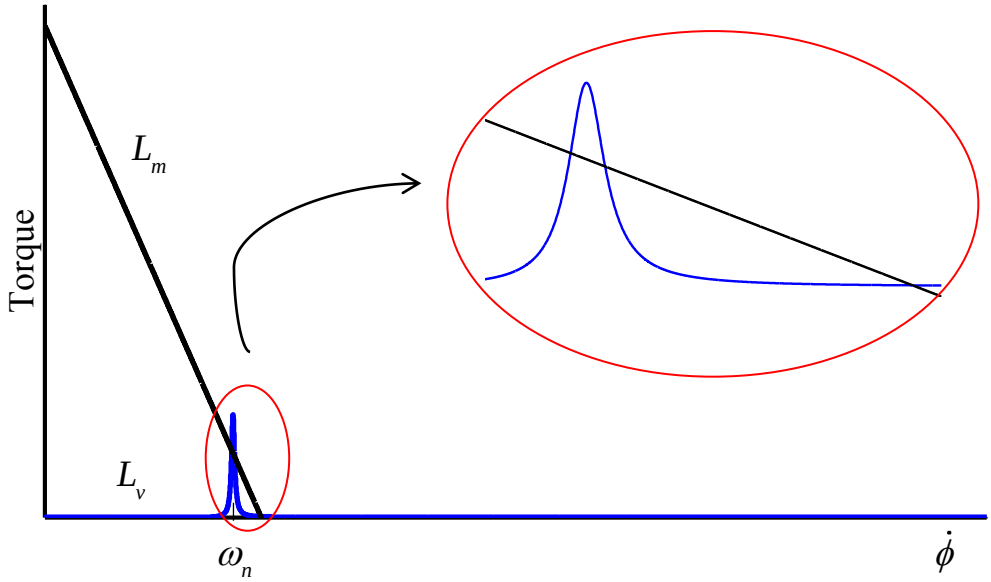

Fig. 7.3 Torque-speed curves corresponding to a case of *large slope* of the motor characteristic

In the case of small slope depicted in Fig. 7.4(a), three stationary motions are encountered as well: two of them in the resonance region and the third far away from resonance, in accordance with the results of Chapter 5. Fig. 7.4(b) represents a different scenario, also with small slope, where there exist no stationary motions near resonance. This occurs when the motor torque at $\dot{\phi} = \omega_n$ is greater than the resonance peak of the vibration torque curve, which implies that there are no intersections between $L_m(\dot{\phi})$ and $L_v(\dot{\phi})$ close to resonance.

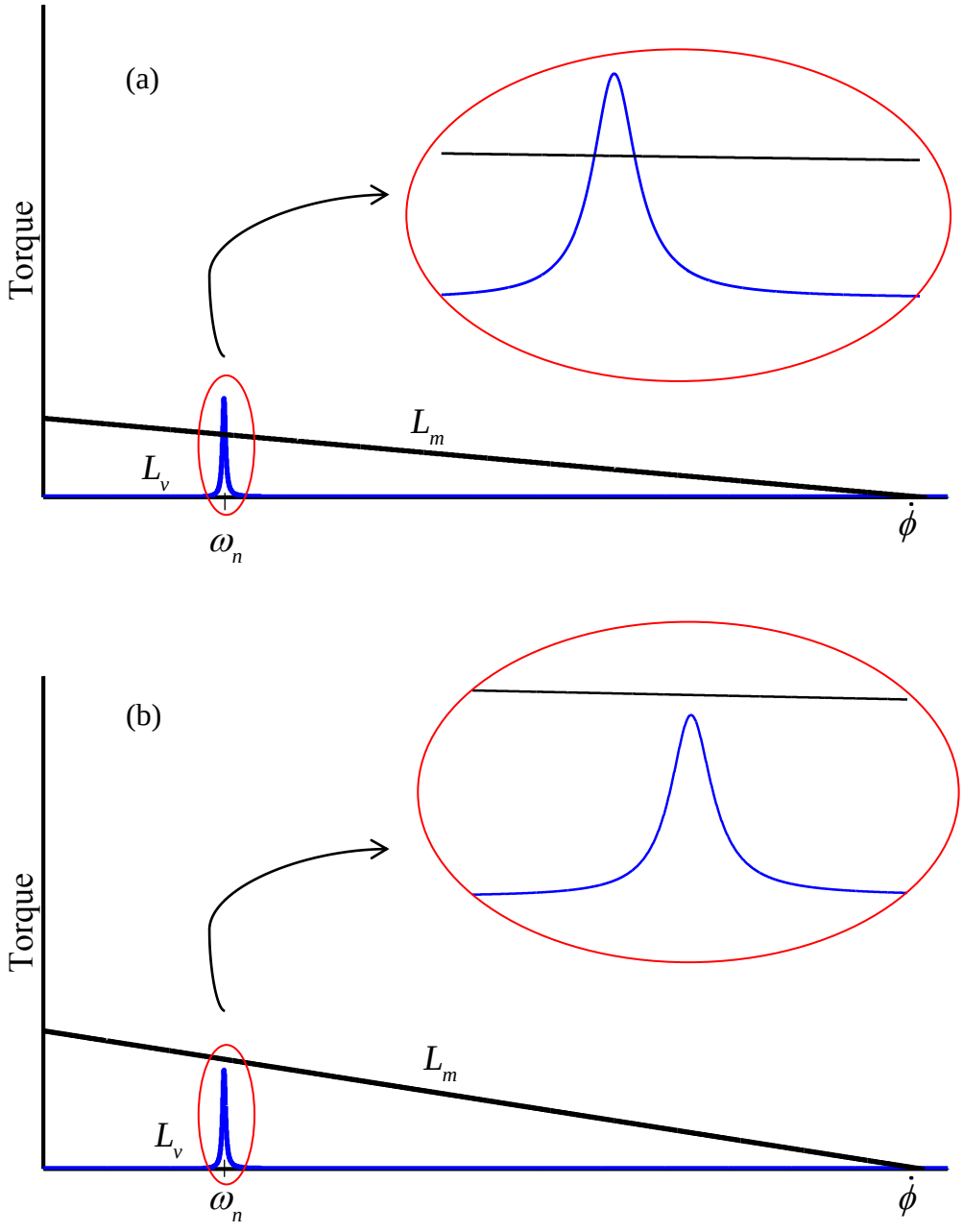

Fig. 7.4 Torque-speed curves corresponding to a case of *small slope* of the motor characteristic

(a) *Resonant capture* can occur

(b) *Resonant capture* does not occur

The near-resonant stationary motions in Fig. 7.4(a) correspond to the fixed points shown in Fig. 5.2. As was widely discussed in Section 5.2, the first of these two fixed points is asymptotically stable, whereas the second one is unstable. The third stationary motion represented in Fig. 7.4(a), which is outside the resonance region, corresponds to the fixed point of the outer averaged system, depicted in Fig. 5.1. This solution was shown to be stable in Section 5.1.

Then, for the case of small slope –assuming the motor torque at resonance to be smaller than the resonance peak of the vibration torque curve–, two stable stationary behaviours exist, one of them in the resonance region, and the other being far away from resonance. For any pre-resonant initial state, the system can be attracted by either the near-resonant or the post-resonant stable stationary motions. These two scenarios are referred to as *resonant capture* and *passage through resonance*, respectively. In the simpler case represented in Fig. 7.4(b), where no stationary motions close to resonance exist, the system always passes through resonance, and evolves towards its only attractor, away from the resonance region.

Hopefully, it has been shown that most of the conclusions about the system behaviour obtained in previous chapters can be summed up and easily retained by using the torque-speed curves described in this chapter. However, the rigorous perturbation approaches of Chapters 3 and 5 are necessary to assess the stability of the stationary motions.

8 MODELLING AND SIMULATION OF THE VIBROCOMPACTION PROCESS

This Chapter focuses on the vibrocompaction process which has motivated the whole thesis. After describing the real industrial procedure, a 4-DOF numerical model of the vibrocompaction system is presented. Although this model is suitable for numerical investigation of the process, it is still too complex for an analytical treatment which may reveal more general information about the system dynamics. Then, a second model with 2 DOFs is derived, through some reasonable simplifications, which turns out to be very useful in order to analyse the process and even tune the parameters of the compacting machine. Finally, numerical simulations on the first model (*full model*) and comparison with the predictions of

the second (*simplified model*) illustrate their ability to predict the effect of different parameters on the final level of compaction achieved.

8.1 Some Notes on the Real Process

Quartz agglomerates, made of granulated quartz mixed with a polyester resin, are widely used as an artificial stone for countertops in kitchens or bathrooms. The manufacturing process of a slab of this material starts with the filling of a mould with the mixture of quartz and resin. Once the mould is full, a conveyor belt carries it to the vibrocompaction zone, where the thickness of the slab is reduced to nearly half of its initial value, by eliminating the air out of the material. Then, the mixture is cured in a kiln, during a specified time interval, at a suitable temperature for the polymerization of the resin. After the resin is polymerized, an air stream is used to cool the slab before it enters the mechanical finishing stage. During this process the edges are cut, producing a slab of prescribed dimensions, and the surfaces are polished. Then, the product is ready for the quality control stage.

It is worth giving some more insight into the vibrocompaction stage of the process, which is the one of interest for the purpose of this study. Before the mixture has been compacted, it is composed of three different phases: solid (the quartz grains), liquid (the resin) and gas (air). The air is present in the material in two different ways: as bubbles within the resin or as gaps between grains of quartz that the resin has not been able to fill. The aim of the compaction process is to eliminate the air out of the mixture, since the presence of pores at the surface of the final countertop is clearly detrimental from a practical point of view: the pores tend to accumulate dirt and are rather difficult to clean.

The compaction is conducted by means of several unbalanced electric motors, mounted on a piston with the dimensions of the slab surface. At the beginning of the vibrocompaction process, the piston descends onto the mixture and exerts a static pressure, due to its weight and to an air pressure applied on it. Then, the air

pressure inside the mould is reduced by using a vacuum system, after which the motors are switched on. The vibration produced by the unbalanced motors is the main responsible for the compaction. During the motion of the system, there can be separations and impacts between the piston and the slab, which are generally beneficial for the compaction, as they produce very high peaks of compression forces. In order to reduce vibrations in the vicinity of the compaction machine, elastic elements are placed between the foundation of the machine and the ground, acting as a vibration absorber and thus protecting nearby equipment. Fig. 8.1 shows a pilot plant used for testing purposes, which preserves the main features of the actual industrial machine. It is interesting to note that there are two motors mounted on the piston, which rotate in opposite directions in order to cancel the horizontal components of the centrifugal forces on the unbalanced masses. Hence the net effect of the rotation of both motors is an oscillating vertical force.

Fig. 8.1 Pilot plant for the analysis of the vibrocompaction process

From the above comments, it is clear that the vibrocompaction process is extremely complex from a physical point of view. A large number of factors –some of them being intrinsically nonlinear– influence the final result of the compaction:

- The quartz granulometry, the rheological properties of the resin and the mass ratio between quartz and resin affect the mechanical behaviour of the compacting mixture. This behaviour is necessarily nonlinear, since the mixture suffers irreversible deformation during compaction. Moreover, an accurate description of this constitutive law would require modelling the motion of the bubbles through the mixture, the friction between quartz particles, the interaction between quartz and resin, etc. Some investigations about the behaviour these types of three-phase mixtures can be found in (Alonso, Gens, & Josa, 1990; Pietruszczak & Pande, 1996; Stickel & Powell, 2005).
- The dynamic properties of the different elements of the machine –the piston, the conveyor belt supporting the mould, the elastomer between the foundation and the ground, etc. – may influence the vibrocompaction as well.
- The speed of the motors, their available power and the amount of unbalance are key parameters of the process.
- The final result of the compaction may also depend on the duration of the process.
- The spatial distribution of the vacuum channels influences the extraction of the air out of the mixture, thereby affecting the compaction.

8.2 Full Model

Building a reliable model of such a complex manufacturing process, able to accurately predict the result of the compaction depending on the system parameters, is an extremely hard task, which clearly exceeds the scope of this thesis. It should be noted that, as far as the author know, such a model is not available yet.

The aim of this Section is to present an approximate model which, without intending to give accurate quantitative predictions, provides useful qualitative results regarding the vibrocompaction process. This may be seen as a first step towards the ambitious goal of achieving a more complex model which reliably captures the dynamics of the real system. Note that the name *full model* is used here only for distinction from the *simplified model* presented in the next section.

The simplification carried out can be observed in Fig. 8.2 and Fig. 8.3. The former shows a schematic picture of the real machine, while the later displays the approximate 4-DOF model.

The quartz-resin mixture is represented in the model by a couple of masses attached to each other by a linear damper and a nonlinear spring, which models the compaction itself by allowing for permanent deformation when the spring is compressed. Then, the distance between both masses would represent the thickness of the compacting mixture. The mould is modelled as a rigid base, while the piston with the unbalanced motors is represented by a mass with a single unbalanced motor. The mixture is in contact –with separations and impacts allowed– with the mould at the bottom and with the piston at the top. The vacuum system is not included in the model.

It should be noted that the model assumes the horizontal motion of the piston to be completely restrained, which makes unnecessary to include a couple of motors rotating in opposite directions.

As represented in Fig. 8.3, the model has 4 DOFs: y_b, y_t, y_p and ϕ, which correspond, respectively, to position of the bottom of the mixture, position of the top of the mixture, position of the piston and rotation of the motor.

The parameters represented in Fig. 8.3 are as follows: m_m stands for the mass of the mixture, m_1 is the unbalanced mass, m_p is the mass of the piston and the motor, r is the eccentricity of the unbalance, I_o is the rotor inertia, b is the damping

coefficient, F_m is the force produced by the nonlinear spring and g is the gravity constant.

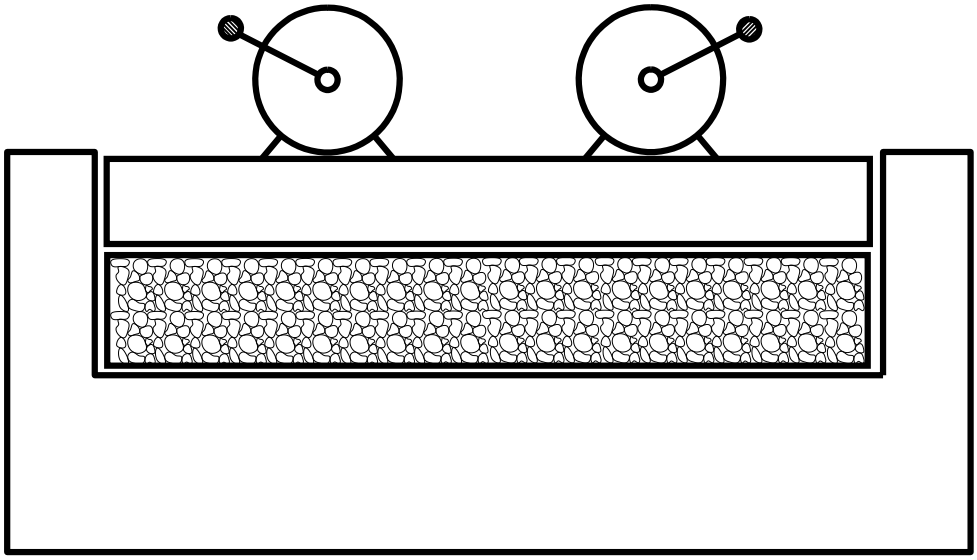

Fig. 8.2 Simplified representation of the compacting machine

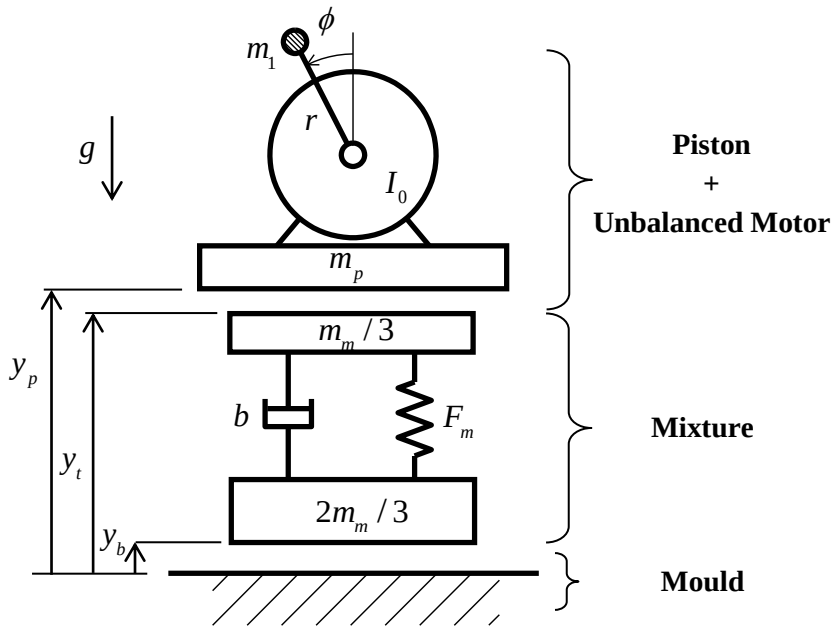

Fig. 8.3 - 4 DOF model of the vibrocompaction process

Notice that the total mass of the mixture is distributed in the proposed model in a particular way: one third corresponds to the upper mass and two thirds to the bottom mass. In order to understand this feature of the model, suppose that, in the real system, the bottom of the mixture is in continuous contact with the mould and, therefore, remains at rest during the system vibration. Assume also that the mass of the mixture is uniformly distributed over the slab thickness. Then, if the deformation is uniform over the slab thickness as well, the effective mass of the mixture during the oscillations can be shown to be one third of its total mass. Note that the assumption of uniform deformation is suitable because the mass of the piston is much greater than that of the mixture and, consequently, it is reasonable to approximate the deformed shape by that corresponding to a concentrated load on the top surface of the slab.

Obviously, if the top mass contains one third of the total mass of the mixture, there have to be two thirds at the bottom mass: when there are separations between mixture and mould and between mixture and piston, it must be the total mass of the slab which moves freely.

As in the models presented in previous chapters, the driving torque provided by the motor minus the losses torque due to friction at the bearings and windage is assumed to be a linear function of the rotor speed:

$$L_m(\dot{\phi}) = A + D\dot{\phi}, \tag{8.1}$$

The equations of motion of the system can be obtained by either equilibrium considerations or any other analytical mechanics approach like Lagrange's method or Hamilton's principle:

$$\left\{\begin{array}{c}\left(m_p+m_1\right)\ddot{y}_p=m_1 r\left(\dot{\phi}^2\cos\phi+\ddot{\phi}\sin\phi\right)+F_{ct}-\left(m_p+m_1\right)g\\ \frac{m_m}{3}\ddot{y}_t+F_m+b(\dot{y}_t-\dot{y}_b)=-F_{ct}-\frac{m_m}{3}g\\ \frac{2m_m}{3}\ddot{y}_b-F_m-b(\dot{y}_t-\dot{y}_b)=F_{cb}-\frac{2m_m}{3}g\\ I\ddot{\phi}=L_m\left(\dot{\phi}\right)+m_1 r\sin\phi\left(\ddot{y}_p+g\right)\end{array}\right\}, \tag{8.2}$$

where $I\equiv I_0+m_1r^2$ and F_{cb}, F_{ct} represent the normal contact force between mixture and mould and between mixture and piston, respectively. Clearly, the most challenging features of this model are the behaviour of the nonlinear spring and the computation of the contact forces. System (8.2), together with the definition of the spring force and the contact forces given in the following, constitutes what we have called *full model* for the vibrocompaction process.

Proposed Nonlinear Spring to Model Compaction

It is rather intuitive that the compaction of a granular material can be described by two main features:

- When a compressive force is applied on the material, it deforms in a nonlinear hardening way. This means that the deforming body stiffens when it becomes more compacted, as a consequence of the increasing packing density of the grains.
- If the compressive load is released, some of the deformation remains – irreversible deformation due to compaction–, while the rest is recovered – elastic deformation–.

Here, a simple model for the nonlinear spring is proposed, following the two rules above. Fig. 8.4 represents force F_m produced by the spring against the spring displacement

$$\Delta L\equiv y_t-y_b-L_0, \tag{8.3}$$

where L_0 is the undeformed length of the spring.

The behaviour is as follows. Starting from the undeformed position O, a compressive force makes the spring follow a parabolic path of the hardening type, with an initial tangent stiffness k_0. Suppose that, at an intermediate state of compaction A, the force is reversed until reaching an unloaded state. The spring follows the straight line AB, which is tangent to the parabolic curve at point A. Note that, already at this stage, the spring stiffness has increased with respect to the initial value k_0. Note also that, at point B, some plastic deformation remains, corresponding to the level of compaction achieved, while the elastic part of the deformation has been recovered.

If a compressive load is applied again, the material deforms along the elastic path BA, followed by the hardening parabolic line. The complete compaction is defined by point C, where the tangent nonlinear stiffness is k_f. Whenever point C is reached, the mixture becomes totally compacted, and any subsequent loading would only produce elastic deformations with stiffness k_f. Parameter d_c in Fig. 8.4 represents the irreversible deformation of the mixture when it is unloaded and totally compacted.

If, at any point of the process, the spring was subjected to a tension load, it would respond linearly and elastically, with the stiffness exhibited by the spring immediately before the tension load was applied. This means that all the linear paths in Fig. 8.4 –each one with its particular slope– can be extended into the region of positive values of F_m. It should be noted that this scenario is not usual, because the large weight of the piston will make the spring work mainly in compression. However, if separations between mixture and piston occur, some tension forces in the spring can be expected.

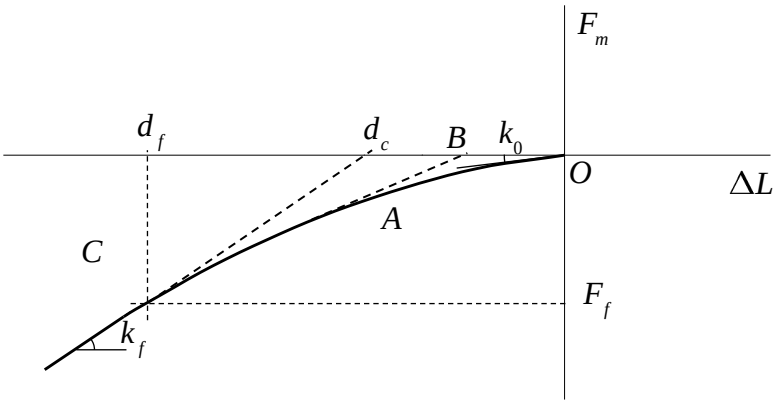

Fig. 8.4 Force-displacement curve of the nonlinear spring

More generally, note that the force between the two masses which model the mixture is given by $F_m + b(\dot{y}_t - \dot{y}_b)$. The fact of this force becoming positive during a particular simulation would imply an internal tension force in the mixture. Observe that this situation –typical during periods of separation at the top and bottom of the mixture– can be physically sound, since the resin provides some adhesion to the mixture, thereby giving it some resistance to tension forces.

The behaviour of the spring is completely defined by specifying F_f, d_f and $R_k \equiv k_0/k_f$. Below it is shown how to obtain the expression of the parabolic path from these three parameters.

The parabola is given by

$$F_m(\Delta L) = c_1 \Delta L^2 + c_2 \Delta L + c_3, \tag{8.4}$$

where the three coefficients can be obtained by imposing the following conditions:

$$F_m(0) = 0 \Rightarrow c_3 = 0 \tag{8.5}$$

$$F_m(d_f) = F_f \Rightarrow F_f = c_1 d_f^2 + c_2 d_f \tag{8.6}$$

$$\left.\begin{matrix} F_m'(d_f) = k_f \Rightarrow 2c_1 d_f + c_2 = k_f \\ F_m'(0) = k_0 \Rightarrow c_2 = k_0 \end{matrix}\right\} \Rightarrow \frac{1}{R_k} = 1 + \frac{2c_1 d_f}{c_2} \tag{8.7}$$

By combining (8.6) and (8.7), c_1 and c_2 can be calculated:

$$\begin{Bmatrix} c_1 \\ c_2 \end{Bmatrix} = \begin{bmatrix} d_f^2 & d_f \\ -2d_f & \dfrac{1-R_k}{R_k} \end{bmatrix}^{-1} \begin{Bmatrix} F_f \\ 0 \end{Bmatrix} \tag{8.8}$$

Once c_1, c_2 and c_3 are known, the initial and final stiffnesses are obtained as

$$k_0 = c_2, \qquad k_f = k_0/R_k\,. \tag{8.9}$$

Finally, it is useful to characterize the quality of the process for a particular simulation by the level of compaction achieved, defined as

$$\gamma = \frac{k_p - k_0}{k_f - k_0}, \tag{8.10}$$

where k_p is the stiffness of the spring once the dynamic compaction process has finished. Thus, $\gamma = 0$ corresponds to a totally uncompacted mixture and $\gamma = 1$ represents a case of complete compaction. It is also practical to define a static level of compaction, in order to distinguish how much of the total compaction is due to the weight of the piston and how much is consequence of the vibration process:

$$\gamma^{st} = \frac{k_{st} - k_0}{k_f - k_0}. \tag{8.11}$$

In equation (8.11), k_{st} represents the system stiffness after the mixture has been statically compacted by the weight of the masses located above the spring –mainly the weight of the piston–. This initial stiffness can be obtained as

$$k_{st} \equiv \frac{dF_m}{d(\Delta L)}\Big]_{\Delta L = d_{st}} = 2c_1 d_{st} + c_2, \tag{8.12}$$

where, as shown in Fig. 8.5, d_{st} stands for the lenght variation of the spring due to the weight of the masses above it:

$$d_{st} = \frac{-c_2 + \sqrt{c_2^2 - 4c_1 mg}}{2c_1}. \tag{8.13}$$

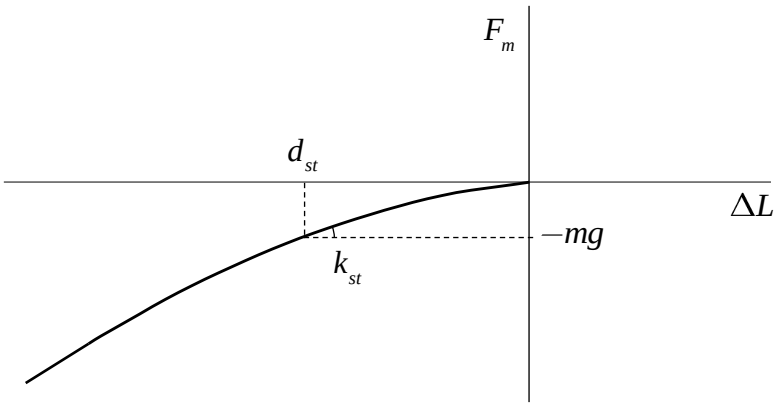

Fig. 8.5 Graphical definition of parameters d_{st} and k_{st}

Finally, note that the proposed spring model, while being very simple, is able to capture the essential features of compaction, thereby representing a reasonable choice for a first attempt to model the vibrocompaction process.

Contact Modelling

Consider now the contact between the mixture and the piston. There are several different ways to model impact/contact, which can be broadly divided into discrete and continuous approaches, according to the classification given in (Gilardi & Sharf, 2002). Discrete models, which were first introduced by Isaac Newton (Newton, 1686), consider impact as an instantaneous process, where contact forces

are impulsive and kinetic variables suffer discontinuous changes. The effect of local deformation due to contact is implicitly taken into account through coefficients such as the *impulse ratio* and the *coefficient of restitution*. Despite being very useful in some scenarios, these models lead to several problems. For example, cases have been found where, in the presence of Coulomb's friction, no solution or multiple solutions exist (Mason & Wang, 1988). Moreover, energy conservation principles may be violated during frictional impacts (Stronge, 1991).

Continuous models are able to overcome these obstacles, by considering that interaction forces act in a continuous manner during impact (Gilardi & Sharf, 2002). Then, the problem can be approached in the usual way, by simply adding the contact forces to the equations of motion during their action periods. Two different continuous approaches are possible. Implicit models take into account the deformation due to contact directly via the flexibility of the contacting bodies, imposing an impenetrability condition. The contact forces can be obtained through the Lagrange multiplier method, or other mathematical techniques (Farahani, Mofid, & Vafai, 2000). Conversely, explicit models assume the normal contact force F_c to be a known function of the indentation δ, which represents the local deformation due to contact, and its rate:

$$F_c = F_c(\delta, \dot{\delta}) \tag{8.14}$$

One of the simplest possibilities consists in modelling contact as a spring-dashpot connection:

$$F_c = k_c\delta + b_c\dot{\delta} \tag{8.15}$$

However, this model gives rise to several drawbacks, the most obvious being the discontinuity of the contact force at the instants of impact and separation. As a consequence, more complex nonlinear models have been developed, such as the

model of Hertz and the model of Hunt and Crossley, which is the one chosen for the present study.

Hunt and Crossley (Hunt & Crossley, 1975) proposed a nonlinear model of the form

$$F_c = k_c \delta^n + b_c \delta^p \dot{\delta}^q, \tag{8.16}$$

where it is standard to set $n = p$, $q = 1$ (Gilardi & Sharf, 2002). Note that the damping term depends on indentation, which is physically sound, since plastic regions are more likely to develop for larger contact deformations. Moreover, the contact force does not exhibit discontinuous changes at the impact and separation instants, thereby overcoming one of the main problems of the spring-dashpot model. The model of Hunt and Crossley has been successfully used in the analysis of a wide variety of contact/impact problems (Bhasin, Dupree, Patre, & Dixon, 2008; Haddadi & Hashtrudi-Zaad, 2008; Ma, 1995; Vukobratović & Potkonjak, 1999).

For simplicity, the exponents in (8.16) are taken as $n = p = q = 1$ for the present analysis, and the contact parameters k_c and b_c are assumed to be the same for both contacts in the model. Then, the expression of the contact forces is given by

$$\begin{Bmatrix} F_{ct} = k_c(y_t - y_p) + b_c(y_t - y_p)(\dot{y}_t - \dot{y}_p) & if\ y_t > y_p \\ F_{ct} = 0 & if\ y_t \leq y_p \end{Bmatrix}. \tag{8.17}$$

$$\begin{Bmatrix} F_{cb} = -k_c y_b + b_c y_b \dot{y}_b & if\ y_b < 0 \\ F_{cb} = 0 & if\ y_b \geq 0 \end{Bmatrix}. \tag{8.18}$$

Flow of Energy in the Model

It is illustrative to consider with some detail how energy enters and leaves the system. Clearly, the only energy input is given by the driving torque of the electric motor. This energy leaves the system in three different ways:

- The damping term of the contact forces (8.17), (8.18) accounts for the energy lost due to contact and impacts between the piston and the mixture and between the mixture and the mould.
- The nonlinear spring is also responsible for some dissipation of energy, which can be obtained as the area enclosed by the path $(\Delta L - F_m)$ followed by the spring during the process. This energy is directly related to the compaction of the mixture. Its physical interpretation may be given in terms of the viscosity associated to the flow of the resin around the grains and also the friction between quartz particles. Fig. 8.6 represents the whole energy dissipated by the spring during a complete compaction.

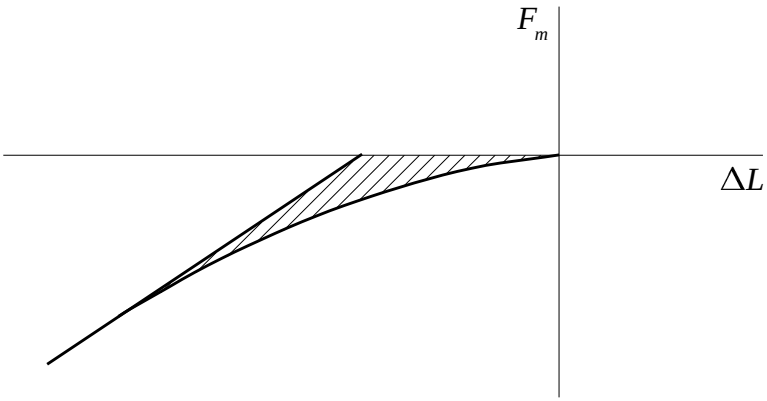

Fig. 8.6 Force-displacement curve of the nonlinear spring. The dashed area is the energy consumed by the nonlinear spring during a complete compaction.

- Damper b in Fig. 8.3 accounts for the energy needed to make the mixture vibrate, but not associated to the compaction itself. To understand this distinction, suppose that the slab has already been totally compacted, but the motor is still working. Then, the mixture would keep oscillating without

any further compaction. Clearly, this motion has some internal damping associated, which is modelled by the linear dashpot b.

8.3 Simplified Model and Torque-Speed Curves

Despite all the simplifying assumptions made, the presented model seems still too complex for an analytical treatment. However, it would be desirable to apply the analytical developments of previous chapters in some approximate way to this model, in order to have an interpretation of numerical results. In particular, it would be extremely useful to plot torque-speed curves for the vibrocompaction problem, so as to find all the possible stationary motions of the system.

Derivation of the Simplified Model

With the aim described above, some approximations are proposed here which allow for a simplification of the equations of motion.

- First, suppose that the motion of interest occurs without separations between mixture and piston nor between mixture and mould. Then, it is reasonable to write $y_t = y_p$, $y_b = 0$, thus reducing the number of DOFs to 2.
- Since this simplified model is built to the end of obtaining the stationary motions of the machine, it is reasonable to assume also that the nonlinear spring is only subjected to elastic deformation. The reason is that, once the system has reached a stationary state of motion, there is no further compaction and the spring follows a straight line in the $\Delta L - F_m$ graph, such as segment AB in Fig. 8.4, with a stiffness $k_i \in [k_0, k_f]$.

With these two assumptions system (8.2) can be written as

$$\left.\begin{matrix} m\ddot{x} + k_i x + b\dot{x} = m_1 r\left(\dot{\phi}^2 \cos\phi + \ddot{\phi}\sin\phi\right) \\ I\ddot{\phi} = L_m\left(\dot{\phi}\right) + m_1 r \sin\phi\,(\ddot{x} + g) \end{matrix}\right\}, \tag{8.19}$$

where $m = m_p + m_m/3 + m_1$ –i.e. the total mass above the spring– and x represents the displacement of the piston with respect to its static equilibrium position. The gravity term in (8.19) can be neglected for the purposes of this chapter, since it becomes zero when averaged over ϕ:

$$\left.\begin{matrix} m\ddot{x} + k_i x + b\dot{x} = m_1 r\left(\dot{\phi}^2 \cos\phi + \ddot{\phi}\sin\phi\right) \\ I\ddot{\phi} = L_m\left(\dot{\phi}\right) + m_1 r\ddot{x}\sin\phi \end{matrix}\right\}, \tag{8.20}$$

Note that (8.20) is exactly the same as system (3.1), which has been analysed in Chapters 3-7, with $\lambda = 0$. Thus, with the assumptions made above, the *full model* for vibrocompaction (8.2) is transformed into a *simplified model* (8.20), already studied in detail in previous chapters.

Torque-Speed Curves for Variable Stiffness

An important outcome of this simplification is the fact that the torque-speed curves obtained in Chapter 7 can be used to represent the stationary motions of the compacting machine. As a relevant particularity of this system, note that the stiffness k_i is not a fixed parameter, but can take different values between k_0 and k_f, depending on the degree of compaction achieved. Then, instead of a single curve for the vibration torque, there will be a family of curves, one of them for each possible value of the spring stiffness.

Although, in principle, the system can exhibit any stiffness between k_0 and k_f, the range of possible values for this parameter is actually narrower during the vibrocompaction. The reason lies in the fact that there is already some static compaction before motor is switched on. Hence the system stiffness at the beginning of the dynamic process is k_{st}, defined in (8.12)

It is clear that, along the dynamic compaction process, the stiffness of the spring can take values $k_i \in [k_{st}, k_f]$. Then, it is pertinent to wonder how the vibration torque curve change when the stiffnes is varied, with all the rest of the dimensional parameters kept constant. A careful analysis of equation (7.15) reveals that the resonance peak of the curve –which approximately corresponds to $\dot{\phi} = \omega_n$– and the resonance frequency ω_n grow in proportion to $k^{3/2}$ and $k^{1/2}$, respectively. This fact is reflected in Fig. 8.7, where several vibration torque curves are plotted for growing values of the spring stiffness.

Assume that the lowest and highest stiffnesses in Fig. 8.7 correspond to k_{st} and k_f, respectively. Then, the collection of curves in the graph is a representative set of the whole family of curves for $k_i \in [k_{st}, k_f]$. If the torque-speed curve of the motor is depicted on the same plot, the possible stationary motions of the machine are graphically obtained as the intersection between the motor curve and each one of the vibration curves.

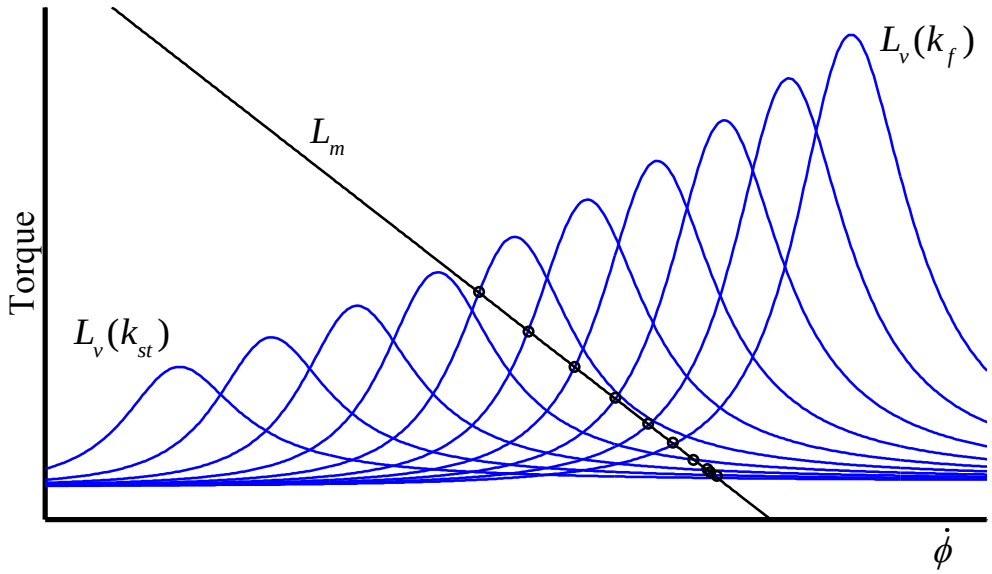

Fig. 8.7 Torque-speed curves for the vibrocompaction process. The stationary motions are marked with circles

As shown in Fig. 8.7 there are many feasible stationary motions for the system. In fact, the amount of possibilities is infinite if all the curves for continuously

increasing stiffness are considered. Clearly, predicting which of these motions will actually attract the machine dynamics would be of great practical interest.

Stability Analysis of the Simplified Model

With the purpose of predicting the final steady motion of the machine, the first obvious step consists in neglecting the unstable solutions, since they do not represent operating conditions which can actually be reached by the vibrating system. This stability analysis requires using the results of Chapters 3 or 5, depending on whether the slope of the motor charateristic is assumed to be *large* or *small*. The practical way of making this distinction is as follows: in the torque-speed plot (such as that in Fig. 8.7), if the slope of the motor curve is much smaller (in absolute value) than that of the vibration torque curves, then the scenario corresponds to the case of small slope. If, conversely, the slopes are comparable, we are in a case of large slope.

In the simulations of this chapter, the parameters have been chosen in such a way that the slope of the characteristic can be considered as *large*. The reason is that the stability properties of the system are richer in the case of large slope, due to the possibility of Hopf bifurctions, as was shown in Section 3.4.

In order to apply the results of Chapter 3 to the system under study, dimensionless variables and parameters should be used:

$$R_m = m_1/m\,, \qquad R_I = m_1 r^2/I\,, \qquad \xi_i = \frac{b}{2\sqrt{k_i m}}, \qquad \alpha_i = \frac{R_I R_m}{2\xi_i}$$
$$\omega_{ni} = \sqrt{k_i/m}\,, \qquad c_i = \frac{C}{I\omega_{ni}^2}, \qquad d_i = \frac{D}{I\omega_{ni}}, \qquad \tau_i = \omega_{ni} t, \qquad u_i = \frac{x}{r}\frac{2\xi_i}{R_m}. \tag{8.21}$$

These are the same parameters and variables already defined in (3.5). Subscript i has been used to emphasize the dependence of some parameters and variables on the variable stiffnes k_i. Then, for instance, the same vibrocompaction system will

exhibit different damping ratios ξ_i depending on the particular value taken by the stiffness.

Together with the assumption of large slope of the motor characteristic, it is assumed here –like in Chapter 3– that the system has small damping, small unbalance and small motor torque at resonance:

$$\xi_i = \epsilon\xi_{i0}, \qquad \alpha_i = \epsilon\alpha_{i0}, \qquad c_i = \epsilon c_{i0}, \qquad d_i = d_{i0}, \tag{8.22}$$

Recall that, in Chapters 3-6, subscript '0' was ommited for brevity in the analytical developments. However, within this chapter, subscript '0' will be kept for the sake of clarity. Once these four dimensionless parameters (8.22) are obtained, for some particular stiffness k_i, all the conclusions of Chapter 3 are directly applicable.

Suppose that one particular vibration torque curve from Fig. 8.7 is selected, and the corresponding dimensionless parameters (8.22) are computed. Then, following the steps of Section 3.4, the stability of the stationary solutions would be investigated by plotting the $\sigma_i - T_i$ curves (see Fig. 3.8 and Fig. 3.9), which are just a dimensionless version of the corresponding $L - \dot{\phi}$ curves in Fig. 8.7. In a typical case with three stationary solutions, such as that represented in Fig. 8.8, the conclusions about stability of Section 3.4 –summed up in Fig. 3.8 and Fig. 3.9– allow stating that the first point is stable, while the second is unstable. However, the stability of the third point is not so direct to obtain, because of the possibility of a Hopf bifurcation. For the stability of this point, two steps would be needed:

1. Check whether or not a Hopf bifurcation exists for that point.
2. If the bifurcation exists, verify the condition $d_i < d_{Hi}$ to ascertain whether the solution of interest is stable or not, where d_{Hi} is the critical slope defined in (3.66).

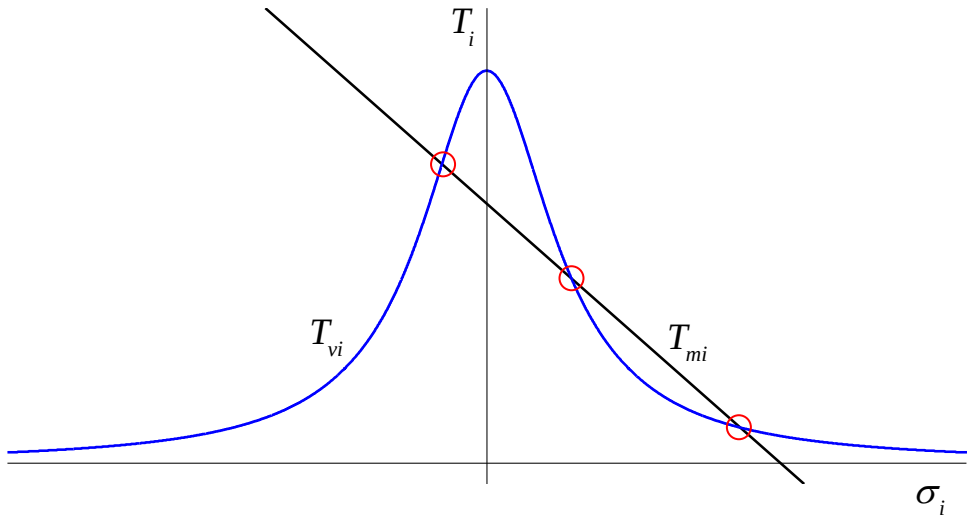

Fig. 8.8 Dimensionless torque-speed curves for a particular stiffness of the spring

Following the procedure explained above, the results of Chapter 3 can be used to evaluate the stability of any of the stationary motions shown in Fig. 8.7. Nevertheless, even if all the unstable solutions are discarded as possible candidates to attract the system dynamics, there are still many feasible stationary motions of the machine. In the following, it will be shown that, under certain circumstances, it is possible to predict what particular stationary motion will actually attract the dynamics of the vibrocompacting system.

8.4 Analytical Investigation of a Quasistatic Vibrocompaction Process

This section is intended to analyse a particular type of vibrocompaction process, where the control settings of the motor are very slowly varied. Then, it is first convenient to say a word about the motor control. An electric motor of any kind is controlled by means of one or more input magnitudes (current, voltage, frequency …). For example, the speed of a 3-phase induction motor is usually controlled by

modifying the amplitude and frequency of the stator voltage, through a variable frequency drive. For each setting of the motor control, the motor characteristic is fixed. In other words, the motor characteristic can be modified by changing the control parameters. In the presented model, where the motor curve is assumed to be given by a straight line, the motor control would allow changing parameters $\{A, D\}$.

Suppose that the effect of the chosen control method consists in displacing the motor characteristic, parallel to itself, when the control settings are changed. This is actually the case, for instance, in simplest control approach for an induction motor, known as the V/f control (Holtz, Paper, & Holtz, 2002). Thus, with such a procedure, the system operating condition would be modified by changing parameter A, while keeping the same slope D.

Now, consider a situation where the motor characteristic is not at its final position from the beginning of the process –as has been the case in all the simulations conducted in previous chapters–. Conversely, the torque-speed curve of the motor is initially set to L_{m0}, as shown in Fig. 8.9, and then it is very slowly displaced upwards. This change in the motor control is assumed to occur *quasistatically*, in the sense that it does not produce any transient effect in the machine, but only a succession of stationary states. Three particular instants of the process are considered, and the corresponding system oscillation is depicted in two representative graphs: the torque-speed plot (Fig. 8.10) and the force-displacement curve of the nonlinear spring (Fig. 8.11).

In the considered process, the vibrocompacting system is initially at rest, under the static load produced by the weight of all its elements. In the $\Delta L - F_m$ graph of Fig. 8.11, this initial point is marked with a triangle. At the instant in which the motor curve is L_{m1}, the system oscillates with some stiffness $k_1 \in (k_{st}, k_f)$, as shown in Fig. 8.11. The motion is depicted as a straight segment with slope k_1, delimited by the maximum and minimum displacements reached during the system vibration. Note the important feature that, according to Fig. 8.11, the minimum displacement

reached by the spring during the vibration coincides with the tangency point between the parabola and the elastic line. This requires some detailed explanation.

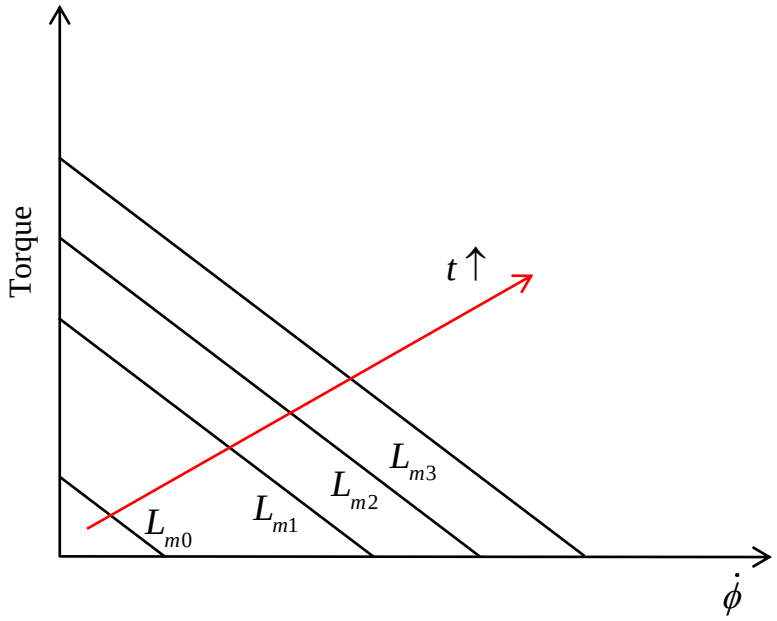

Fig. 8.9 Evolution of the motor characteristic during the *quasistatic* compaction process

The stationary vibration necessarily takes place around the position of static equilibrium of the system, which is different for each particular stiffness, as highlighted in Fig. 8.11 with squares. The static equilibrium position can always be obtained as the intersection between the elastic line of interest and the horizontal line given by $F_m = -mg$. Then, parameter $x^*_{max}(k_i)$ is defined as the distance in ΔL between the static equilibrium position and the tangent point of the elastic line with the parabola for stiffness k_i (see Fig. 8.11):

$$x^*_{max}(k_i) = \frac{-mg - F_{mi}}{k_i}, \tag{8.23}$$

where F_{mi} represents the value of F_m at which the parabolic curve of the spring exhibits a slope k_i.

It is clear that the system cannot oscillate, for stiffness k_i, with a greater amplitude than $x^*_{max}(k_i)$, because that would imply following some length of the parabolic path, with the subsequent increase in the spring stiffness.

On the other hand, oscillations with stiffness k_i and amplitude smaller than $x^*_{max}(k_i)$ are possible in principle. Nonetheless, such a regime of motion would require a process such as that described below:

1. First, the vibration amplitude reaches $x^*_{max}(k_i)$. This is necessary if the spring stiffness is to take value k_i.
2. Then, the amplitude of the oscillation is reduced and the system attains a stationary vibration with amplitude $< x^*_{max}(k_i)$.

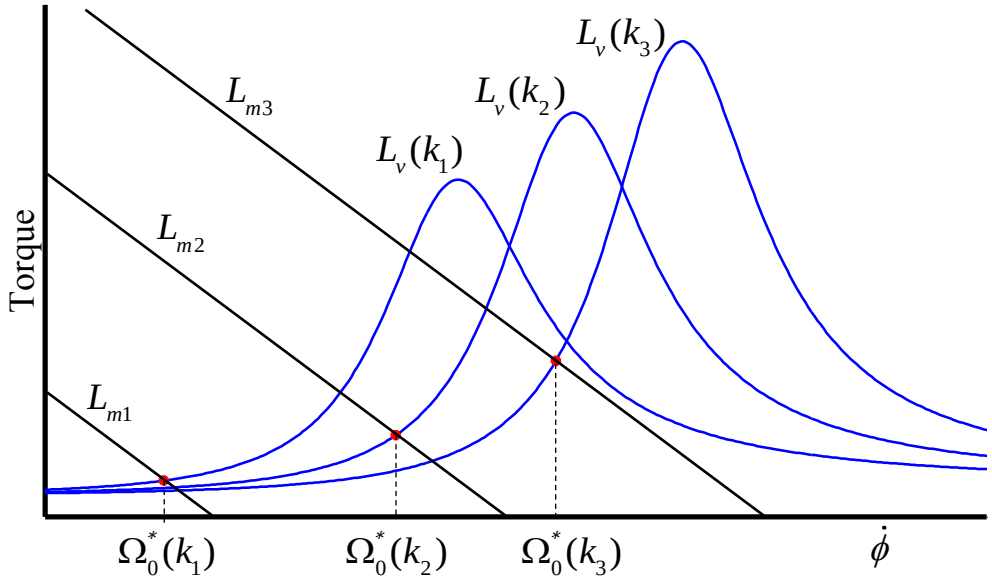

Fig. 8.10 Torque-speed curves at different instants of the quasistatic compaction process

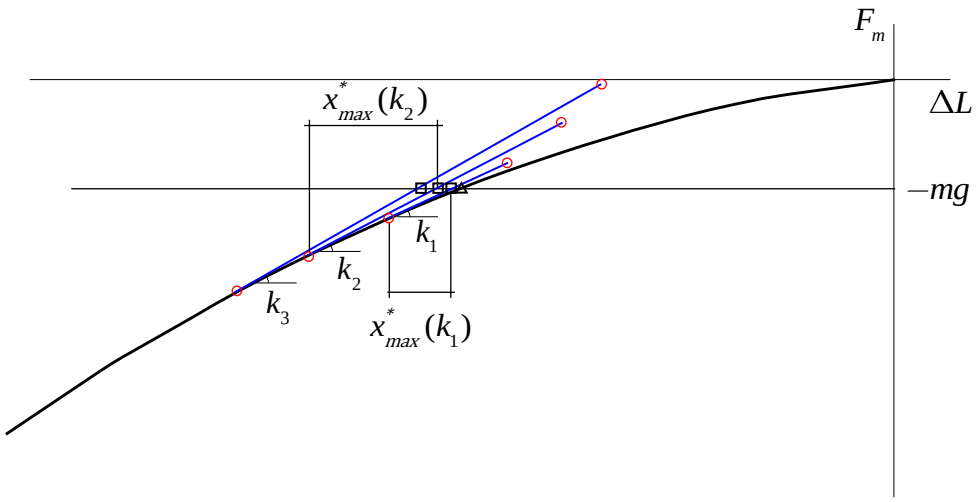

Fig. 8.11 Oscillation of the system at three instants of the quasistatic compaction process

Note that the evolution described above cannot occur in the *quasistatic* process under consideration, where the motion of the system changes from one stationary state to another, with no transient effects. The progressive upwards displacement of the motor characteristic actually gives rise to a monotonous growing of the vibration amplitude, which makes impossible to reach a state where the system vibrates with stiffness k_i and amplitude $< x^*_{max}(k_i)$.

It needs to be noted that there is a relevant exception to the statements of the above paragraph, as will be clearly seen in the numerical simulations of the next section. Under the considered motor control, the vibration amplitude grows monotonically until the point where a jump phenomenon takes place, making the amplitude fall drastically, with the rotor speed rapidly evolving up to a post-resonant value. This is precisely a manifestation of *the Sommerfeld effect*, which was described in the introduction of the thesis (see the first paragraph of Section 1.1). The jump phenomenon at resonance is one of the most classical effects of the nonideal interaction between exciter and vibrating system. An explanation for this effect will be given afterwards in this section.

Then, if the attention is restricted to the fraction of the process before the jump phenomenon, we have that the spring stiffness grows continuously, with the amplitude of the oscillation being given, for each instantaneous k_i, by $x^*_{max}(k_i)$. Since the oscillation amplitude for each k_i is known, the rotor speed can also be computed by using the first of relations (7.8):

$$x^*_{max}(k_i) \rightarrow \Omega^*_0(k_i) \tag{8.24}$$

Notice that there may be two possible rotor speeds for the same vibration amplitude, as observed in Fig. 7.1. Then, care should be taken to choose the pre-resonant solution, which is the one of interest for the process under consideration (see Fig. 8.10). This can be done, if equation (7.8) is to be solved numerically, by appropriately selecting the initial guess for the numerical algorithm.

The conclusion is that, when the system reaches stiffness k_i through the quasistatic procedure being described, it will do so with rotor speed $\Omega^*_0(k_i)$, which can be computed a priori with no need of numerical resolution of the equations of motion. Then, for each vibration torque curve, the corresponding operating point can be directly plotted, as shown in Fig. 8.10.

Giving one more step, a new curve $\Gamma(\dot{\phi})$ can be constructed with the collection of stationary solutions, forgetting about the vibration torque curves. This new curve, depicted in Fig. 8.12, represents the complete sequence of motions followed by the machine during the quasistatic compaction. Clearly, plotting the exact curve would require computing the operating points for all values of the stiffness k_i, which is not practical. Then, an approximation to the curve is obtained by plotting the operating points for a number of values of the stiffness and then connecting them with straight lines (see Fig. 8.12).

Note that curve $\Gamma(\dot{\phi})$ gives very relevant information from a practical perspective. Each point of the curve corresponds to a particular stiffness and, therefore, to a particular degree of compaction γ. Then, the curve reveals the required driving

torque to achieve a particular degree of compaction through a quasistatic process. For instance, reaching stiffness k_i in Fig. 8.12 would require a motor characteristic such as $L_{mi}(\dot{\phi})$.

It is interesting to investigate the end points of curve $\Gamma(\dot{\phi})$ because, as will be seen, they provide very meaningful information about the possibilities of compaction. First, it is clear that, for stiffness k_{st}, the stationary solution is given by $\dot{\phi} = 0, L_v = 0$, corresponding to the initial state of the machine, with the motor at rest. Then, curve $\Gamma(\dot{\phi})$ starts at (0,0). More significant is the final point. In principle, the curve ends at the point associated to the stiffness of the totally compacted mixture, k_f, as shown in Fig. 8.13(a). However, another possibility also exists. Consider the case shown in Fig. 8.13(b), where 10 values of the stiffness have been considered. (As a shortened notation, which will be widely used throughout the rest of the document, the vibration torque curves are directly labelled with the corresponding stiffness k_i, instead of writing $T_v(k_i)$). It is observed that the operating point corresponding to the eighth curve is already close to the maximum of the vibration torque curve. For the ninth and tenth curves, no stationary solution is marked because its corresponding vibration amplitude, $x^*_{max}(k_i)$, turns out to be greater than that of the resonance peak. Then, when $\Omega_0^*(k_i)$ is tried to be computed through relation (7.8), no solution is found. In physical terms, it can be said that, for stiffness k_9 or k_f to be reached through a quasistatic process, the system would need to oscillate with greater amplitude than that of the resonance peak, which is not possible.

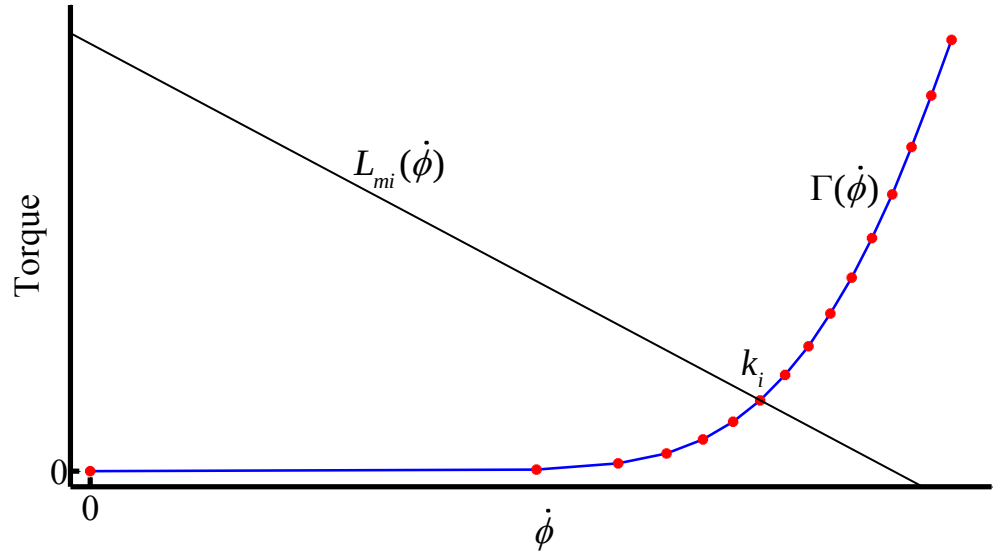

Fig. 8.12 Curve $\Gamma(\dot{\phi})$, representing the complete sequence of motions along the quasistatic compaction

It is clear that, for certain stiffness k_{max} between k_8 and k_9 in Fig. 8.13(b), the operating point coincides with the maximum of the vibration torque curve, constituting the end point of curve $\Gamma(\dot{\phi})$. This critical value k_{max} has a very meaningful interpretation: it is the maximum stiffness that can be achieved through a quasistatic compaction process. Note that k_{max} is totally independent of the motor characteristic: it is a property if the system itself, not related to the motor control. Hence it can be stated that a system with torque-speed curves such as those shown in Fig. 8.13(b) cannot be completely compacted through a quasistatic compaction process. If this total compaction was to be achieved, some properties of the system would need to be changed. For example, an increment in the unbalanced mass would be beneficial in this regard.

Now, consider again the scenario shown in Fig. 8.13(b), and suppose that, once stiffness k_{max} has been reached, the motor characteristic is further displaced upwards. This situation is represented in Fig. 8.14. The initial effect of this translation of the motor curve will be a slight decrease in the vibration amplitude, as the operating point falls through the right branch of the vibration torque curve. This

will occur until reaching the tangency point between both torque curves. If the motor characteristic is further displaced, it is found that there are no more stationary motions near the resonance peak. Actually, at the tangency point, two stationary motions –one stable and one unstable– disappear through a saddle-node bifurcation. Hence the system necessarily evolves towards the only remaining steady solution, which corresponds to a post-resonant motion with small oscillation amplitudes, as evidenced in Fig. 8.14. This is precisely the jump phenomenon observed by Sommerfeld in 1904, and one of the most well-known effects of nonideal excitations.

Summing up the above considerations, and defining parameter k_{max} as the maximum stiffness that can be reached through a quasistatic compaction process, two different scenarios are possible: if $k_{max} = k_f$, then a complete compaction can be quasistatically achieved. Conversely, if $k_{max} < k_f$, the mixture cannot be totally compacted through a quasistatic procedure. This definition of k_{max} can be directly extended to the level of compaction achieved, γ_{max}, defined as

$$\gamma_{max} = \frac{k_{max} - k_0}{k_f - k_0}. \tag{8.25}$$

After the above detailed analysis of the quasistatic compaction, it is reasonable to wonder what the differences are when the process is not quasistatic. This would be the case, for instance, if the motor was switched on with the torque-speed curve being directly in its final position, or if the control settings of the motor were abruptly modified. In these situations, there can be significant transient effects which influence the final stationary motion reached by the machine and, therefore, affect the level of compaction achieved. Some of these transient effects will be discussed in the next section.

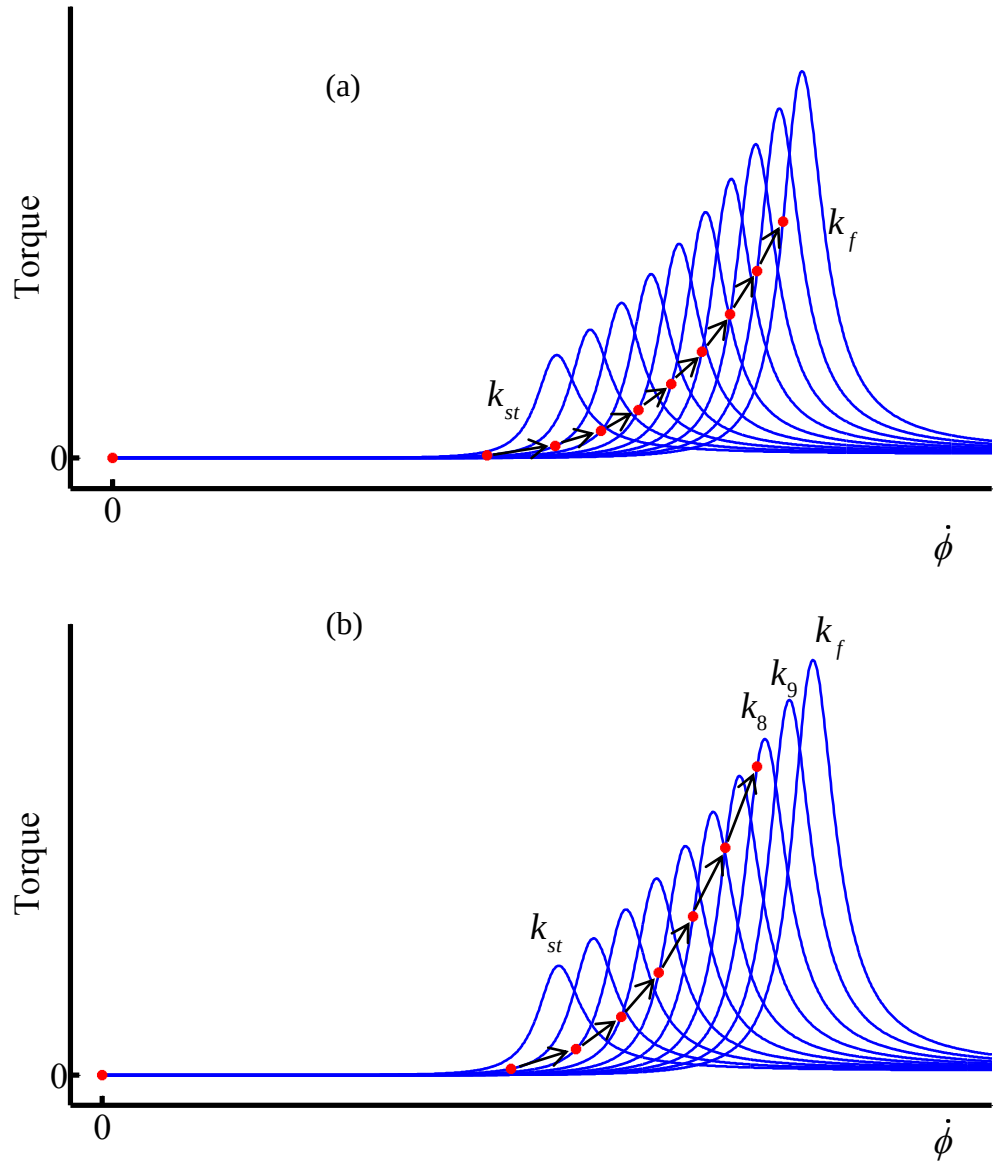

Fig. 8.13 Vibration torque curves for different values of the stiffness. The stationary motion for each stiffness is marked with a dot.

(a) $k_{max} = k_f$

(b) $k_{max} < k_f$

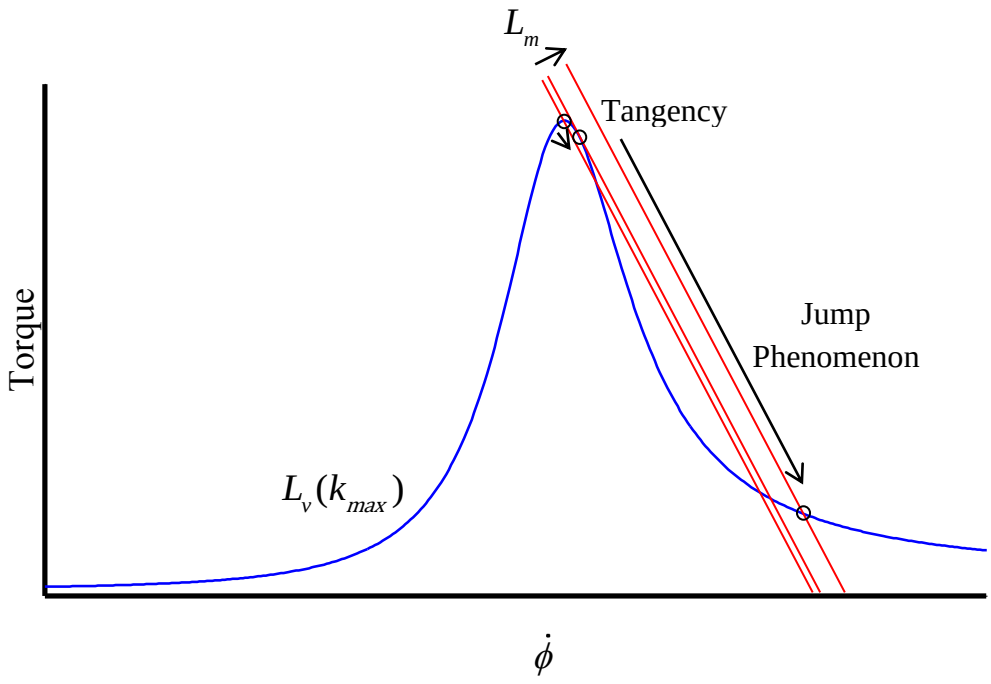

Fig. 8.14 Torque-speed curves for stiffness k_{max} and jump phenomenon

8.5 Numerical Results and Discussion

General Description of the Simulations

In this section, system (8.2) –associated to the full model– is numerically solved for different scenarios. The chosen initial conditions for all the simulations correspond to the static equilibrium position of the system (see Fig. 8.15):

$$\left\{\begin{array}{c} \phi(0)=\pi \\ \dot{\phi}(0)=0 \\ y_b(0)=d_b \\ \dot{y}_b(0)=0 \\ y_t(0)=d_b+L_0+d_{st} \\ \dot{y}_t(0)=0 \\ y_p(0)=d_b+L_0+d_{st}+d_t \\ \dot{y}_p(0)=0 \end{array}\right\}, \tag{8.26}$$

where d_t and d_b are the indentations at the top and bottom contacts, respectively, due to the weight of the elements above the contact:

$$d_t=\frac{-(m_p+m_1)g}{k_c}, \qquad d_b=\frac{-(m_p+m_1+m_m)g}{k_c}. \tag{8.27}$$

With this initial configuration, system (8.2) is solved, using embedded Runge-Kutta formulae of orders 4 and 5, for a simulation time t_f which varies between 30s and 55s. This total time includes three different stages in the simulation, of respective lengths t_1, t_2 and t_3 $(t_f=t_1+t_2+t_3)$:

- During the first stage $(0 \le t < t_1)$ parameter A is linearly increased from A_0 to A_f, with A_0 and A_f being defined for each particular simulation. The slope D is kept constant along the process, which implies that the motor characteristics is displaced parallel to itself. Then, for a sufficiently long t_1, this stage would represent the quasistatic variation described in Section 8.4.
- At the second stage $(t_1 \le t < t_1+t_2)$, parameter A is kept constant at its final value A_f. During this stage, the machine is expected to reach a stationary operating point.
- At time $t=t_1+t_2$, the motor is switched off in order to let the system reach a compacted equilibrium position. Clearly, once the motor is switched off, there is no driving torque on the rotor, and function $L_m(\dot{\phi})$ must only account for the resisting torque due to windage and friction at the

bearings. This is modelled by replacing the motor characteristic with the following curve:

$$L_m(\dot{\phi}) = 0.2 \cdot D\dot{\phi}, \qquad \text{for } t_1 + t_2 \leq t < t_f. \tag{8.28}$$

Hence it is being assumed that the slope of the resisting torque curve is 20% of the slope of the motor characteristic.

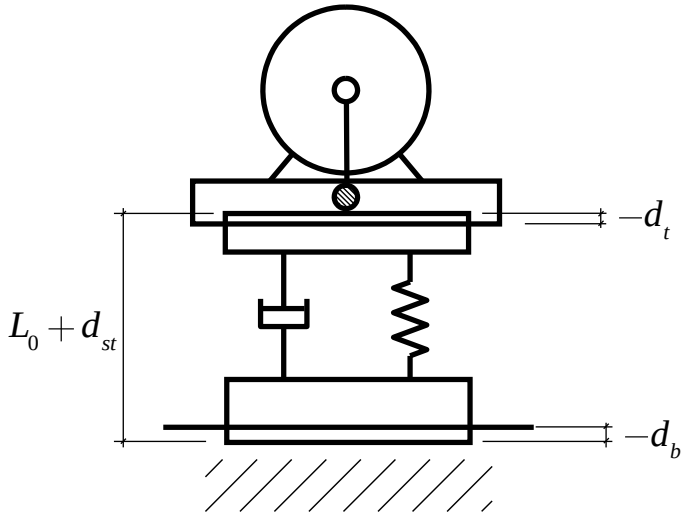

Fig. 8.15 – Initial configuration of the system, with the contact indentations exaggerated for clarity.

Parameters t_2 and t_3 have been chosen as 15s for all the simulations, while t_1 will take different values depending on the case under study.

Case 1

The proposed full model (8.2) is defined by 11 dimensional parameters

$$\{m_1, m_p, m_m, b, r, I_0, d_f, F_f, R_k, k_c, b_c\}, \tag{8.29}$$

besides the two parameters associated to the motor control

$$\{A, D\}. \tag{8.30}$$

For this first simulation, the set of parameters (8.29) is chosen as

$$\left\{\begin{array}{lll} m_1 = 20\text{kg}, & m_m = 240\text{kg}, & m_p = 1.5 \cdot 10^3\text{kg} \\ r = 0.1\text{m}, & I_0 = 0.84\text{kgm}^2, & b = 4 \cdot 10^3\ \text{Ns/m} \\ d_f = -0.1\text{m}, & F_f = -1 \cdot 10^5\text{N}, & R_k = 0.1 \\ k_c = 3 \cdot 10^9\ \text{N/m}, & b_c = 9.5 \cdot 10^6\ \text{Ns/m} & \end{array}\right\}. \tag{8.31}$$

Before the numerical resolution of the equations of motion, it is useful to obtain some previous information about the system by plotting the vibration torque curves. First, from the knowledge of parameters $\{d_f, F_f,\ R_k\}$, stiffnesses k_0 and k_f can be computed through relations (8.8), (8.9):

$$k_0 = 1.82 \cdot 10^5\ \text{N/m}, \qquad k_f = 1.82 \cdot 10^6\ \text{N/m} \tag{8.32}$$

Using (8.12), (8.13) the initial stiffness for the dynamic process can also be obtained, together with the static compaction:

$$k_{st} = 7.39 \cdot 10^5\ \text{N/m} \Rightarrow \gamma_{st} = 34.1\%. \tag{8.33}$$

Now, the vibration torque curves can be plotted for $k_i \in [k_{st}, k_f]$, as shown in Fig. 8.16. From this plot, it is clear that this system belongs to the scenario where $k_{max} < k_f$, since the highest stiffnesses cannot be reached quasistatically. This will also be the case of the rest of the simulations.

The maximum achievable compaction –under quasistatic conditions– can be computed through relation (8.25):

$$k_{max} = 9.71 \cdot 10^5 \text{ N/m} \Rightarrow \gamma_{max} = 48.2\% \tag{8.34}$$

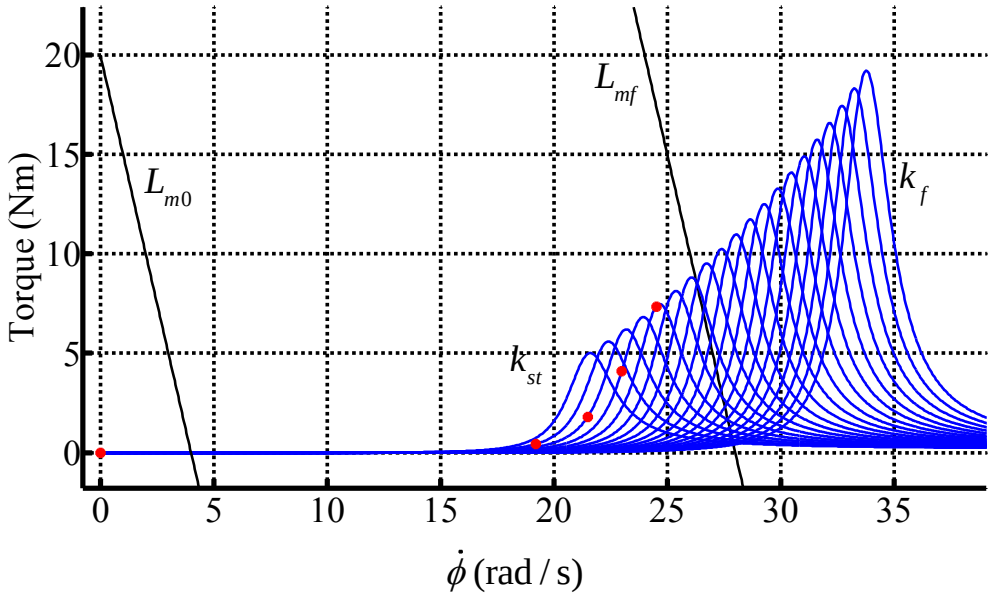

Fig. 8.16 Torque-speed curves for Case 1. The dots represent the stationary motions for a quasistatic compaction process.

A numerical experiment is carried out now, where the motor control parameters are chosen as

$$t_1 = 10\text{s}, \qquad D = -5\text{Nms}, \qquad \text{A}_0 = 20\text{Nm}, \qquad \text{A}_f = 140\text{Nm}. \tag{8.35}$$

The corresponding torque-speed curves are represented in Fig. 8.16, where notation

$$L_{m0} = \text{A}_0 + D\dot{\phi}, \qquad L_{mf} = \text{A}_f + D\dot{\phi} \tag{8.36}$$

has been used. Note that the final motor characteristic, L_{mf}, is located ahead of the final point of curve $\Gamma(\dot{\phi})$. Although this curve has not been explicitly represented for clarity, it can be obtained by simply connecting the dots in Fig. 8.16. Then, the proposed simulation can be envisaged –if the chosen t_1 is long enough– as a

particular case of the general process described in Section 8.4, where a quasistatic frequency sweep is conducted until reaching the maximum compaction, followed by a jump towards a post-resonant regime of motion (see). The numerical results for this simulation are shown in Fig. 8.17 and Fig. 8.18.

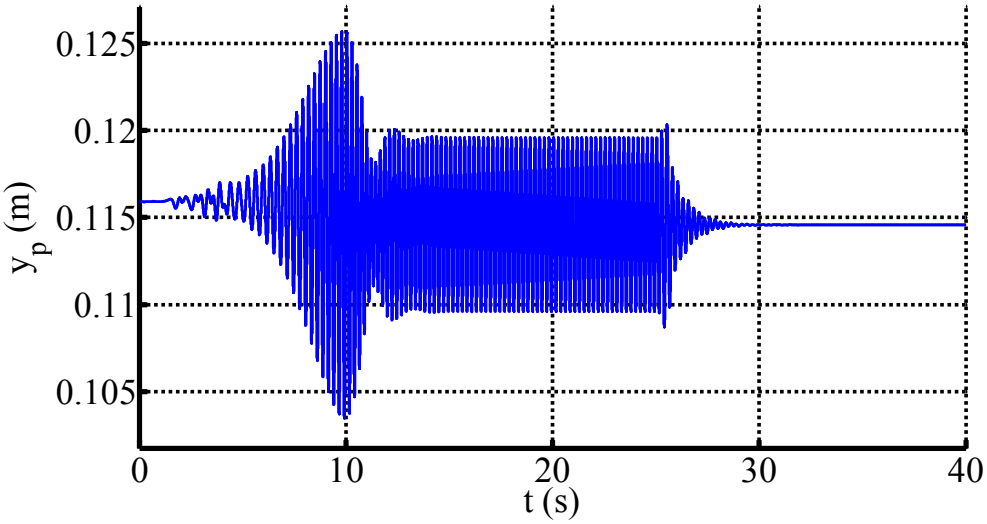

Fig. 8.17 Piston displacement for Case 1

The phenomenon expounded in Section 8.4 is clearly observed here. As the motor curve is displaced upwards between 0 and 10s, the oscillation amplitude grows monotonically, until a point where the jump phenomenon is encountered. During the second stage of the simulation, for $10\text{s} < t < 25\text{s}$, the motor characteristic is fixed at L_{mf}, and the system stabilizes at a post-resonant stationary motion. This is evidenced in Fig. 8.18, where ω_{np} represents the natural frequency of the system during the stationary motion of stage 2. Note also the difference between the initial and final position of the piston in Fig. 8.17, which reveals the compaction due to vibration.

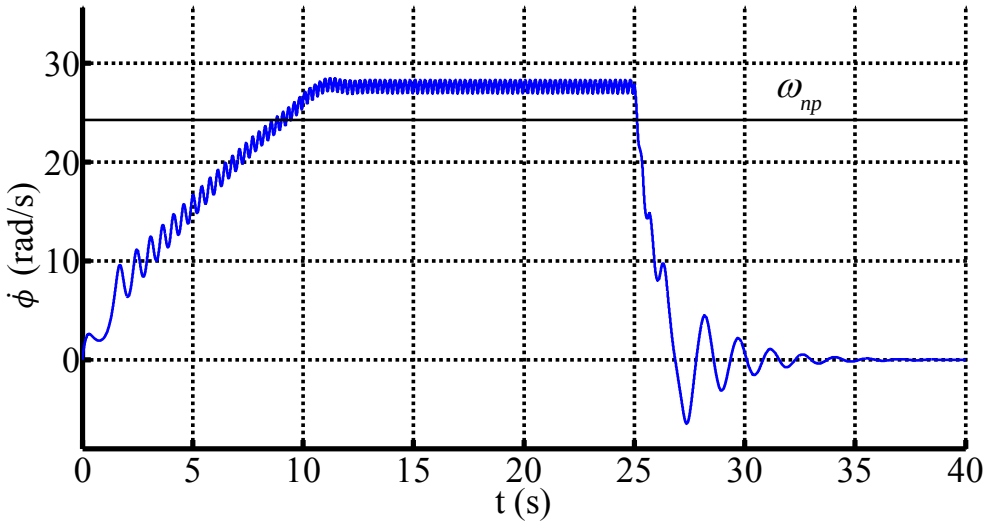

Fig. 8.18 Rotor speed for Case 1

Regarding the top and bottom contacts, no separations or impacts were found in this case. Hence the displacements of the mixture, which do not give much significant information, have not been represented.

The most important outcome of the simulation is the final level of compaction achieved, which turns out to be

$$\gamma_s = 46.5\%. \tag{8.37}$$

A subscript '*s*' is used to emphasize that this result is the outcome of a numerical simulation, in contrast to those obtained analytically.

By comparing (8.37) with (8.34), some difference is encountered between the theoretical and numerical levels of compaction, which can lead to the suspicion that the process may not have been slow enough to consider it as *quasistatic*. Hence a new simulation is conducted in order to validate this hypothesis.

Case 2

For this second scenario, the same set of parameters is chosen as in Case 1. The only difference is in the time associated to the first stage of the simulation, which is now set to

$$t_1 = 20\text{s}. \tag{8.38}$$

The numerical results are shown in Fig. 8.19 and Fig. 8.20.

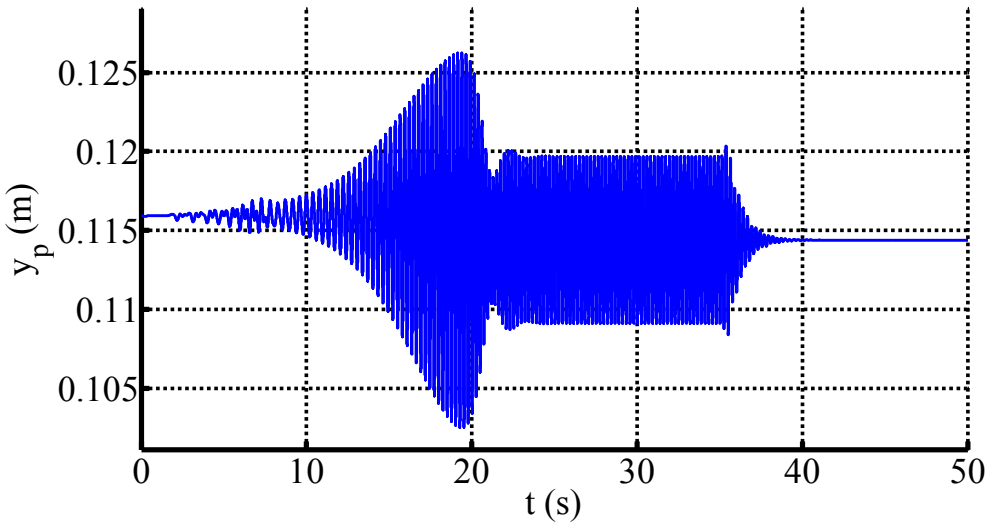

Fig. 8.19 Piston displacement for Case 2

Clearly, the same qualitative behavior than in Case 1 is found here. However, the final level of compaction reached in this case is

$$\gamma_s = 47.5\%, \tag{8.39}$$

which is closer to the theoretical value (8.34) than the compaction achieved in Case 1. This supports the idea that, the slower the displacement of the motor characteristic, the more similar the process is to the ideal quasistatic case.

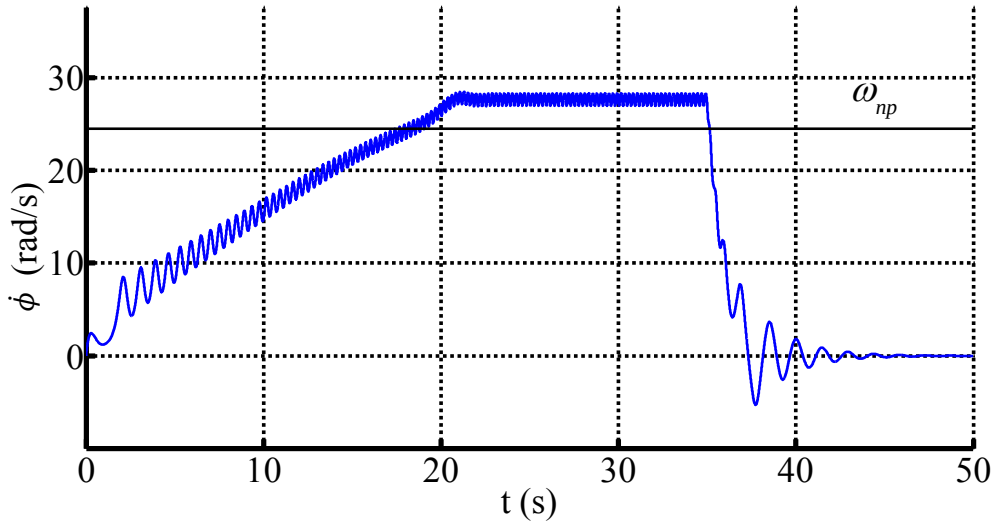

Fig. 8.20 Rotor speed for Case 2

Case 3

In this scenario the set of parameters (8.31) is maintained, which implies that the vibration torque curves and also curve $\Gamma(\dot{\phi})$ are the same as in the two previous cases. On the contrary, the control parameters are now set to

$$t_1 = 15\text{s}, \qquad D = -1.5\text{Nms}, \qquad \text{A}_0 = 22\text{Nm}, \qquad \text{A}_f = 43\text{Nm}. \tag{8.40}$$

The motor characteristics for the present case can be observed in Fig. 8.21. As can be seen, the motor curve does not overtake the final point of $\Gamma(\dot{\phi})$. Hence compaction γ_{max} will not be reached in this case.

In fact, the expected behaviour of the machine is as follows: as the motor characteristic is displaced from L_{m0} to L_{mf} the operating point of the system will follow curve $\Gamma(\dot{\phi})$ (dots in Fig. 8.21). At each instant, the motion of the system will be given by the intersection between $\Gamma(\dot{\phi})$ and the instantaneous motor curve –assuming the process is quasistatic–. Finally, when L_m is fixed at its final position, i.e. during the second stage of the simulation, the machine will keep oscillating at

the operating point given by the intersection between L_{mf} and $\Gamma(\dot{\phi})$, marked with a square in Fig. 8.21. This point is characterized by

$$\Omega_{0a} = 24.2\,\mathrm{rad/s} \tag{8.41}$$

$$k_a = 9.56 \cdot 10^5\,\mathrm{N/m} \rightarrow \gamma_a = 47.3\%, \tag{8.42}$$

where a subscript *a* has been used to stress that these are analytical results, which will be later compared to those obtained numerically. Following the notation of Chapter 7, Ω_0 represents the average rotor speed during the stationary motion of the system.

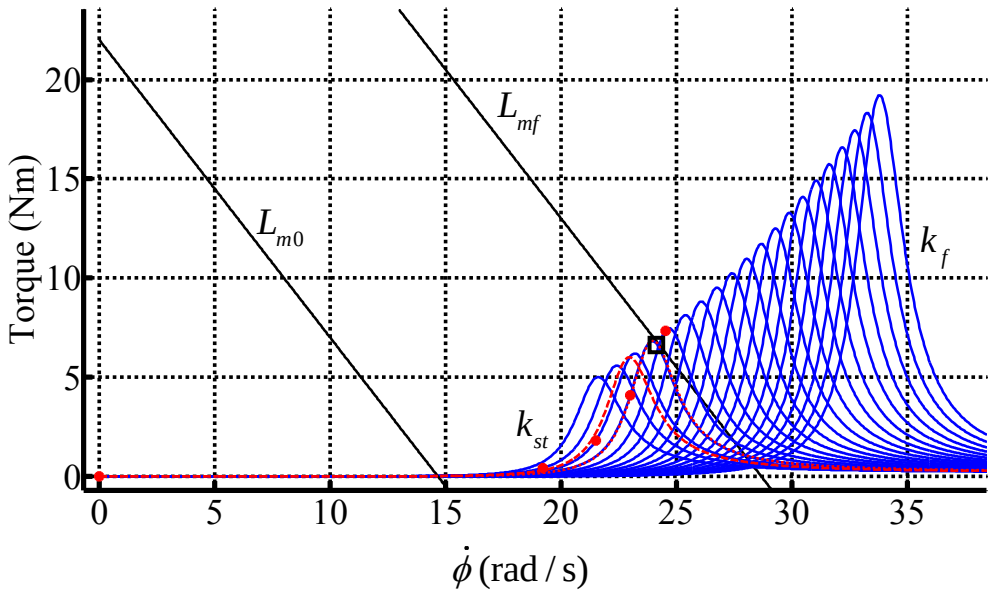

Fig. 8.21 Torque-speed curves for Cases 3 and 4. The dots represent the stationary motions for a quasistatic compaction process. The vibration torque curve in dashed (dotted) line is the one exhibited by the system in Case 4 at $t = 1.5$s (during the stationary motion attained).

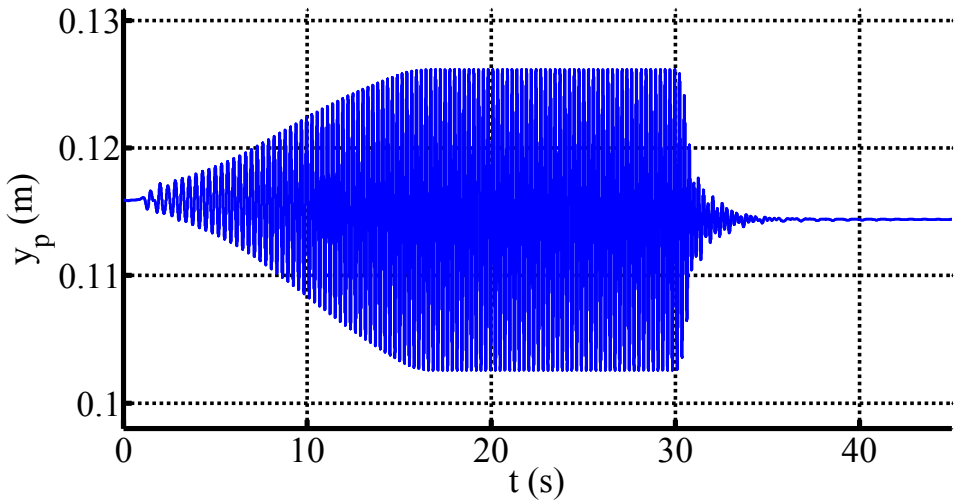

Fig. 8.22 Piston displacement for Case 3

The simulation results are depicted in Fig. 8.22 and Fig. 8.23. No separations or impacts were observed.

From Fig. 8.23, the average value of the rotor speed during the stationary motion of stage 2 is obtained:

$$\Omega_{0s} = 24.2\,\mathrm{rad/s} \tag{8.43}$$

Besides, the final compaction obtained in the simulation is

$$\gamma_s = 47.4\%. \tag{8.44}$$

The remarkable agreement between (8.43), (8.44) and (8.41), (8.42) reveals that, in this case, the analytical approach based on the torque-speed curves is actually able to predict the behaviour of the full model (8.2).

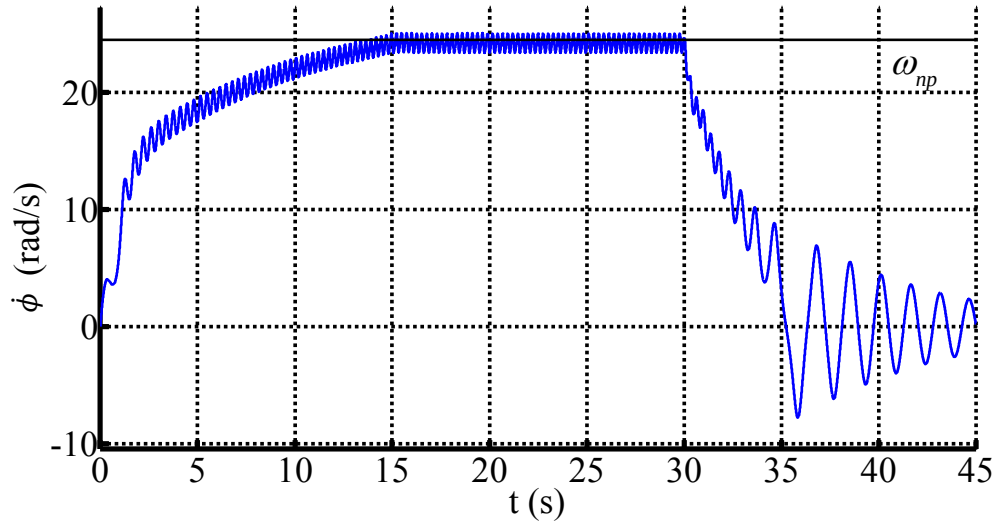

Fig. 8.23 Rotor speed for Case 3

Case 4

This case is intended to investigate the effects of transient motions in the dynamics of compaction. Thus, in the present scenario, the motor is not controlled in such a way that its torque curve is slowly displaced, as in previous cases. Instead, the motor characteristic is now set to its final position from the beginning of the process.

All the parameters in the simulation are like in Case 3, except for the time associated to the first stage, which is now set to

$$t_1 = 0\text{s}. \tag{8.45}$$

This is equivalent to say that there is no motor control. The results of this simulation are shown in Fig. 8.24 and Fig. 8.25, where an utterly different behavior to that of Case 3 is found.

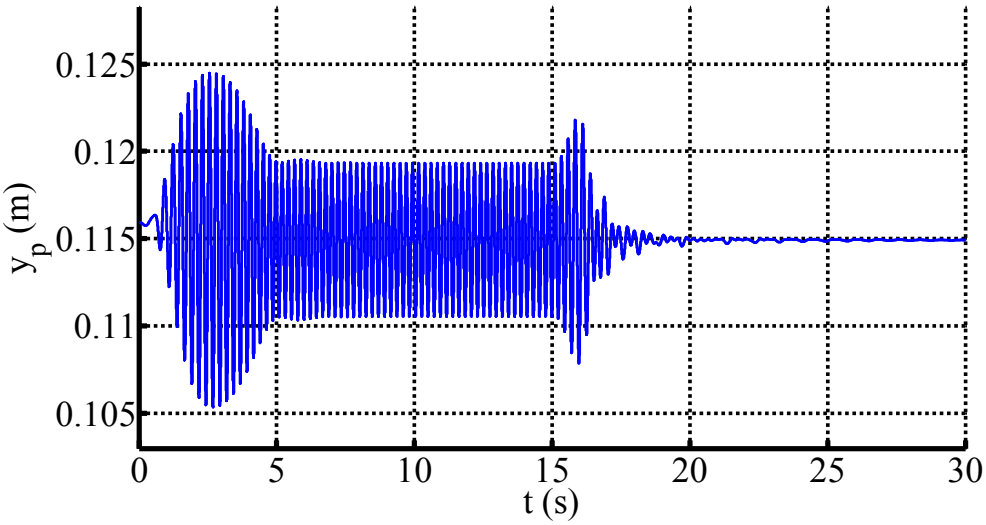

Fig. 8.24 Piston displacement for Case 4

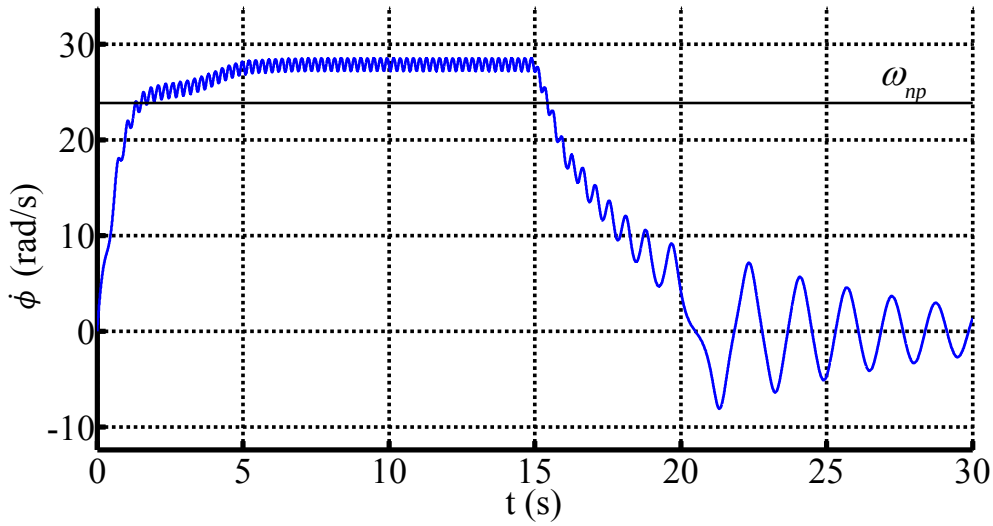

Fig. 8.25 Rotor speed for Case 4

The evolution of the rotor speed evidences that the resonance peak has been overtaken, since the final average speed is above ω_{np}. In fact, the displacement and rotor speed plots are rather typical of a passage through the resonance peak: the displacement undergoes a transient increase when the rotor speed is close to the resonance frequency, followed by a fall to a smaller final value. On the other hand, the increase in the rotor speed is slowed down when passing through the resonance

frequency, since the resisting torque due to vibration is larger in this region. Observe also that an increase in the vibration amplitude exists around $t = 16\text{s}$, once the motor has been shut down. This is due to a reversed passage through the resonance peak, which occurs when the rotor speed decreases to zero.

The level of compaction achieved in this case turns out to be smaller than in Case 3:

$$\gamma_s = 44.6\%. \tag{8.46}$$

Thus, in the present case, the transient motion has a detrimental effect on the result of the process. In what follows, an explanation for this lower compaction is proposed.

Since the motor is not externally controlled, it is the system dynamics itself which determines which of all possible operating points –see Fig. 8.7– is actually reached by the machine. In particular, a relevant feature of the system dynamics is the time needed by the rotor speed and the vibration amplitude to vary significantly. Recall that the increase in the vibration amplitude is directly related to the increase in the system stiffness and, therefore, to the mixture compaction.

Suppose that the rotor speed increases considerably –reaching the resonance region– in a very short time. Then, the vibration amplitude may not have enough time to grow as much as in Case 3 and, consequently, the system stiffness may not be able to reach value k_a, given in (8.42). This may explain the fact that a less effective compaction is obtained here with respect to the previous case.

In order to validate the above hypothesis, consider the particular time instant $t = 1.5\text{s}$. The results of the simulation reveal that, at this point of the process, the rotor speed and the instantaneous stiffness of the spring are

$$t = 1.5\text{s} \rightarrow \left\{ \begin{array}{c} \dot{\phi} = 23.6\,\text{rad/s} \\ k_i = 8.36 \cdot 10^5\,\text{N/m} \end{array} \right\}. \tag{8.47}$$

Clearly, this particular value of the stiffness has a vibration torque curve associated. Then, the torque speed curves for the instant considered are plotted in Fig. 8.26. These curves are also represented in Fig. 8.21 (dashed line for the vibration torque curve), in order to put them in relation with the global behavior of the system. It can be observed that, already at $t = 1.5\text{s}$, the rotor speed has passed through the resonance peak, while the stiffness of the spring is still relatively far from the quasistatic value (compare (8.47) with (8.42)). From Fig. 8.26, it can be expected that the system is attracted towards a post-resonant motion, as is actually the case in the simulation (see Fig. 8.25).

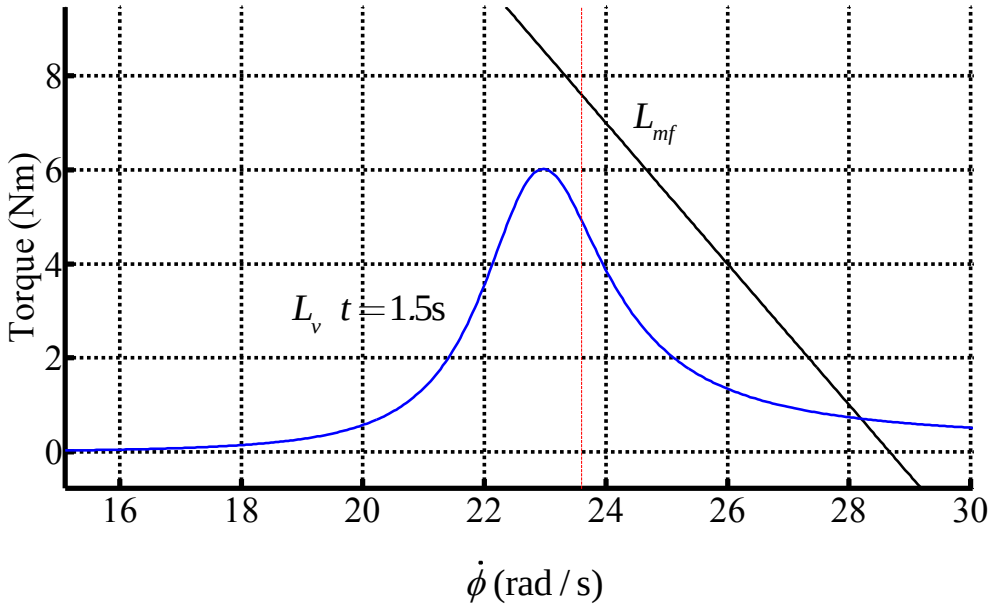

Fig. 8.26 Torque-speed curves of the system at $t = 1.5\text{s}$. The vertical dashed line corresponds to the actual rotor speed at the considered instant.

In summary, it is observed that the lower compaction achieved in this case, with respect to the quasistatic process, is due to the fast variation of the rotor speed. It is interesting to note that the rate at which the rotor speed evolves is directly related to the rotor inertia. Very large rotor inertia would produce a much slower increment in the speed of rotation, making the process analogous to the quasistatic compaction described in Section 8.4. In other words, with sufficiently large rotor inertia, the

system would evolve following a succession of stationary states, as if the average rotor speed was constant at each instant.

It should also be noted that, although the effect of the transient motion turns out to be detrimental for the compaction in this case, it may be beneficial in other scenarios. For example, an abrupt change in the motor control may entail some overshoot in the evolution of the vibration amplitude, which may in turn provide a better compaction than the quasistatic process.

In general, it can be said that, although transient effects may have beneficial results for the compaction in some cases, letting the process depend on these transients leads to the possibility of an undesired and premature passage through the resonance peak, with the subsequent reduction in the compaction quality.

Finally, with an illustrative purpose, the stability of the stationary motion reached by the machine in the present case is analysed. Clearly, this solution is stable according to the numerical results (otherwise, it could not be attained by the system). The objective now is to verify if the analytical predictions about stability (Section 3.4) are consistent with this result.

Hence the stability analysis of the simplified model, described in Section 8.3, is conducted here. The first step is to obtain the stiffness exhibited by the system during the motion of interest. The numerical results reveal that, during the steady motion of the machine (roughly corresponding to $5\text{s} < t < 15\text{s}$), the spring stiffness is $k_i = 9.12 \cdot 10^5\ \text{N/m}$. Then, dimensionless parameters (8.22) corresponding to this stiffness can be obtained by using relations (8.21) and taking $\epsilon = 0.01$:

$$\left\{\begin{matrix}\xi_{i0} = 5.24 \\ \alpha_{i0} = 2.30 \\ c_{i0} = 1.21 \\ d_{i0} = -0.06\end{matrix}\right\} \tag{8.48}$$

Once dimensionless parameters (8.48) have been obtained, the dimensionless torque-speed curves are depicted in Fig. 8.27. These are a dimensionless version of the curves shown in Fig. 8.21 (dotted line for the vibration torque curve). Note that only one fixed point is found in this case.

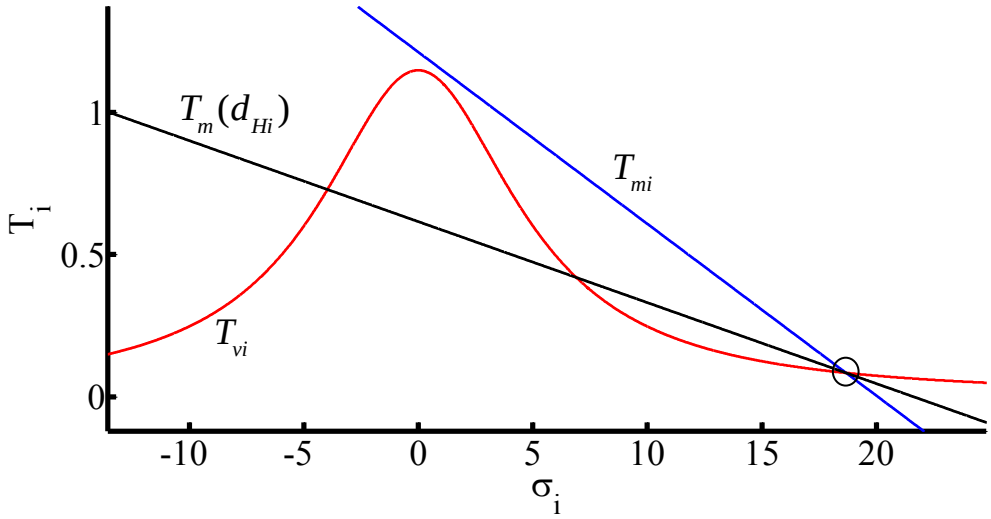

Fig. 8.27 Dimensionless torque-speed curves Case 4, with $k_i = 9.12 \cdot 10^5$ N/m (the stiffness exhibited by the system during the stationary motion)

Following the results of Section 3.4, the stability of the equilibrium depends on the value of the critical slope d_{Hi}, which is obtained through definition (3.66):

$$d_{Hi} = -0.028. \tag{8.49}$$

As depicted in Fig. 8.27, slope d_{Hi} turns out to be greater (in absolute value) than the slope of the vibration torque curve at the considered point, which implies that a Hopf bifurcation exists, according to criterion (3.67). Then, the present case belongs

to the general scenario depicted in Fig. 3.9(b.2). Note also that the actual slope of the motor characteristic is greater (in absolute value) than d_{Hi}, as highlighted in Fig. 8.27. Therefore, according to the stability regions of Fig. 3.9(b.2), the considered fixed point turns out to be stable, which is consistent with the result of the numerical simulation.

Case 5

The fifth case under study maintains all parameters (8.31) of Cases 1-4, except for the unbalanced mass, which is now doubled:

$$m_1 = 40\text{kg}. \tag{8.50}$$

This is a clear example of how the presented model can be used to analyze the influence of certain system parameters on the final result of the process. In this case, it is rather intuitive that a larger unbalanced mass will enhance the vibrocompaction process, since larger centrifugal forces in the motor will be generated.

While parameters k_0 and k_f are the same as in Case 1, there is some variation in the initial stiffness and compaction, due to the increased weight of the system:

$$k_{st} = 7.44 \cdot 10^5\ \text{N/m} \Rightarrow \gamma_{st} = 34.3\%. \tag{8.51}$$

The vibration torque curves, for $k_i \in [k_{st}, k_f]$ are plotted in Fig. 8.28. First of all, note, by comparing the scale of the vertical axis in Fig. 8.28 and Fig. 8.16, that considerably larger torque is needed in this case to make the system oscillate. This is physically sound, since the motor needs to overcome greater inertia forces on the unbalance.

Moreover, observe that the amount of compaction that can be quasistatically attained is also greater in this case. This is evidenced by the fact that the end point of curve $\Gamma(\dot{\phi})$ is now closer to the curve of total compaction, $L_v(k_f)$.

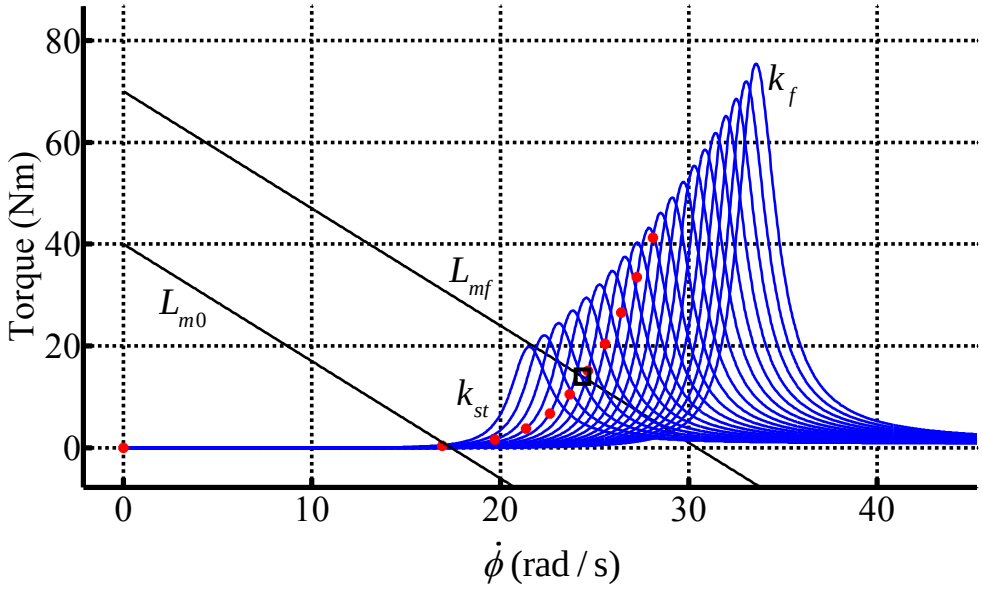

Fig. 8.28 Torque-speed curves for Case 5. The dots represent the stationary motions for a quasistatic compaction process.

Using relation (8.25), the maximum compaction can be calculated:

$$k_{max} = 1.35 \cdot 10^6 \text{ N/m} \Rightarrow \gamma_{max} = 71.2\% \tag{8.52}$$

After these analytical computations, the equations of motion (8.2) are numerically solved for the following motor control:

$$t_1 = 15\text{s}, \qquad D = -2.3\text{Nms}, \qquad \text{A}_0 = 40\text{Nm}, \qquad \text{A}_f = 70\text{Nm}. \tag{8.53}$$

The corresponding motor characteristics are represented in Fig. 8.28. As can be seen, the motor curve does not overtake the final point of $\Gamma(\dot{\phi})$. Hence compaction

γ_{max} will not be reached in this case. As a matter of fact, the expected behaviour of the machine is qualitatively the same as in Case 3, with the final operating point given by

$$\Omega_{0a} = 24.4\,\mathrm{rad/s} \tag{8.54}$$

$$k_a = 1.06 \cdot 10^6\,\mathrm{N/m} \rightarrow \gamma_a = 54\%. \tag{8.55}$$

The results of the simulations are depicted in Fig. 8.29-Fig. 8.32. The first apparent difference between this case and the preceding ones is that separations are observed here between piston and mixture, and also between mixture and mould. This is evidenced by the displacements in Fig. 8.29 and Fig. 8.30 –recall that a positive value for y_b represents separation between the mixture and the mould–and also by the contact forces in Fig. 8.32. During a time interval which roughly corresponds to the second stage of the simulation ($15\mathrm{s} < t < 30\mathrm{s}$), the contact forces become zero for certain periods, followed by an abrupt increase in the force associated to the impact between the contacting bodies. In particular, note that the impacts between the piston and the mixture produce peaks in the contact force which are around ten times the weight of the piston. Note also the complex time evolution of the forces in the close-up of Fig. 8.32(b).

From the evolution of the rotor speed in Fig. 8.31, the numerical average rotor speed during the second stage of the simulation is obtained:

$$\Omega_{0s} = 24.2\,\mathrm{rad/s}, \tag{8.56}$$

On the other hand, the numerical result for the final compaction achieved is

$$\gamma_s = 54.1\% \tag{8.57}$$

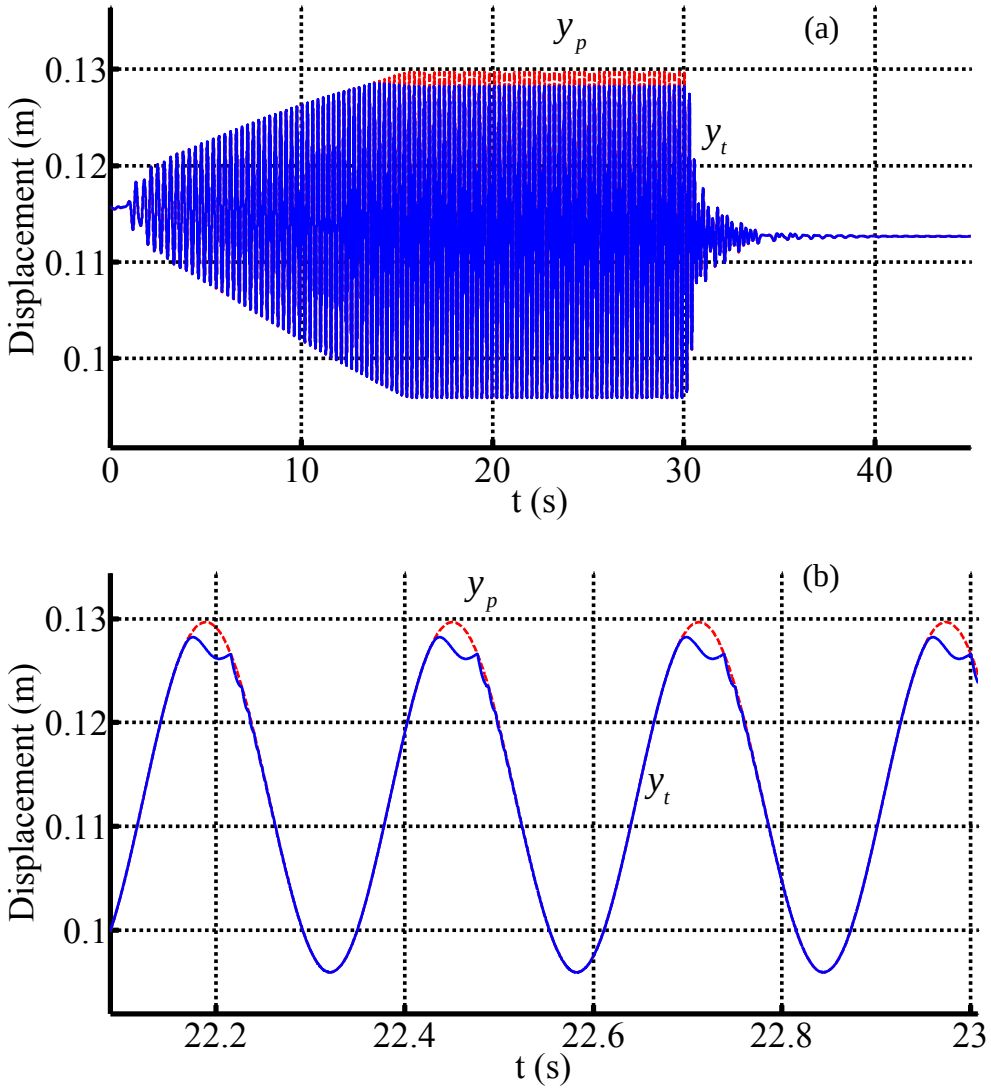

Fig. 8.29 Displacements of the piston and the top of the mixture for Case 5

(a) Full view

(b) Close-up

A comparison between (8.56), (8.57) and (8.54), (8.55) reveals a very good accordance between numerical and analytical results. Recall that the analytical results of Section 8.4 are based on the simplified model, which in turn is constructed upon the assumption of no separations between the contacting surfaces.

Hence the remarkable agreement between analytical and numerical results in this case is particularly significant, since it demonstrates that the results of 8.4 –the use of the torque-speed curves and curve $\Gamma(\dot{\phi})$ to predict the final operating point of the machine– can be useful even for conditions where separations and impacts are present in the system.

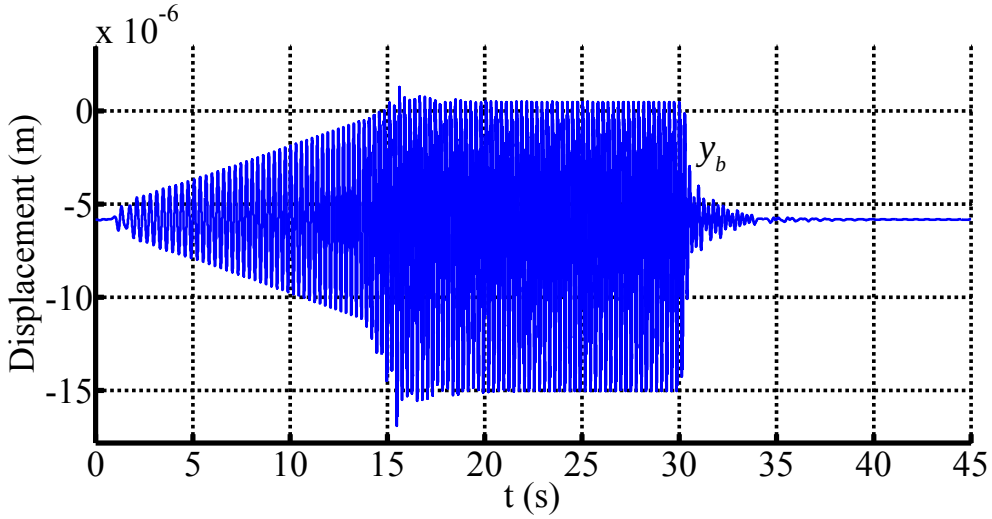

Fig. 8.30 Displacement of the bottom of the mixture for Case 5

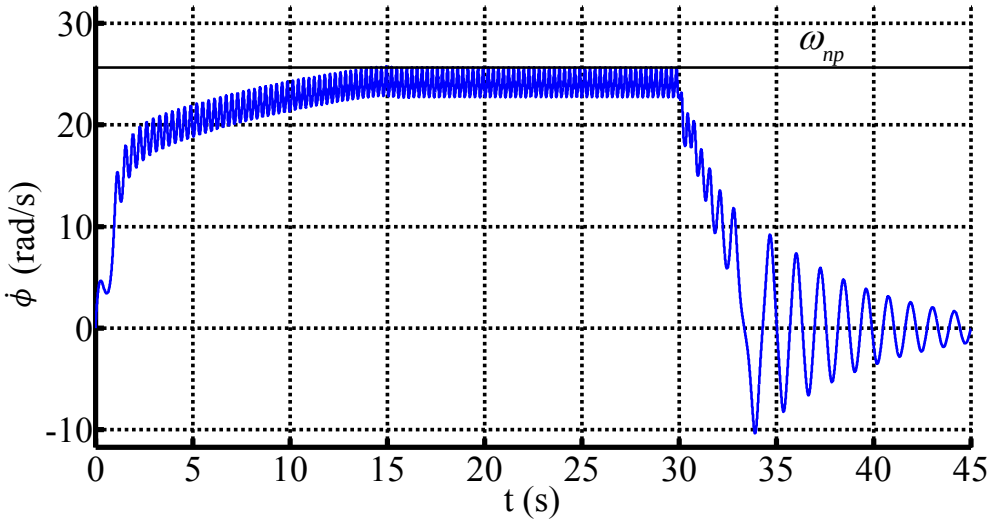

Fig. 8.31 Rotor speed for Case 5

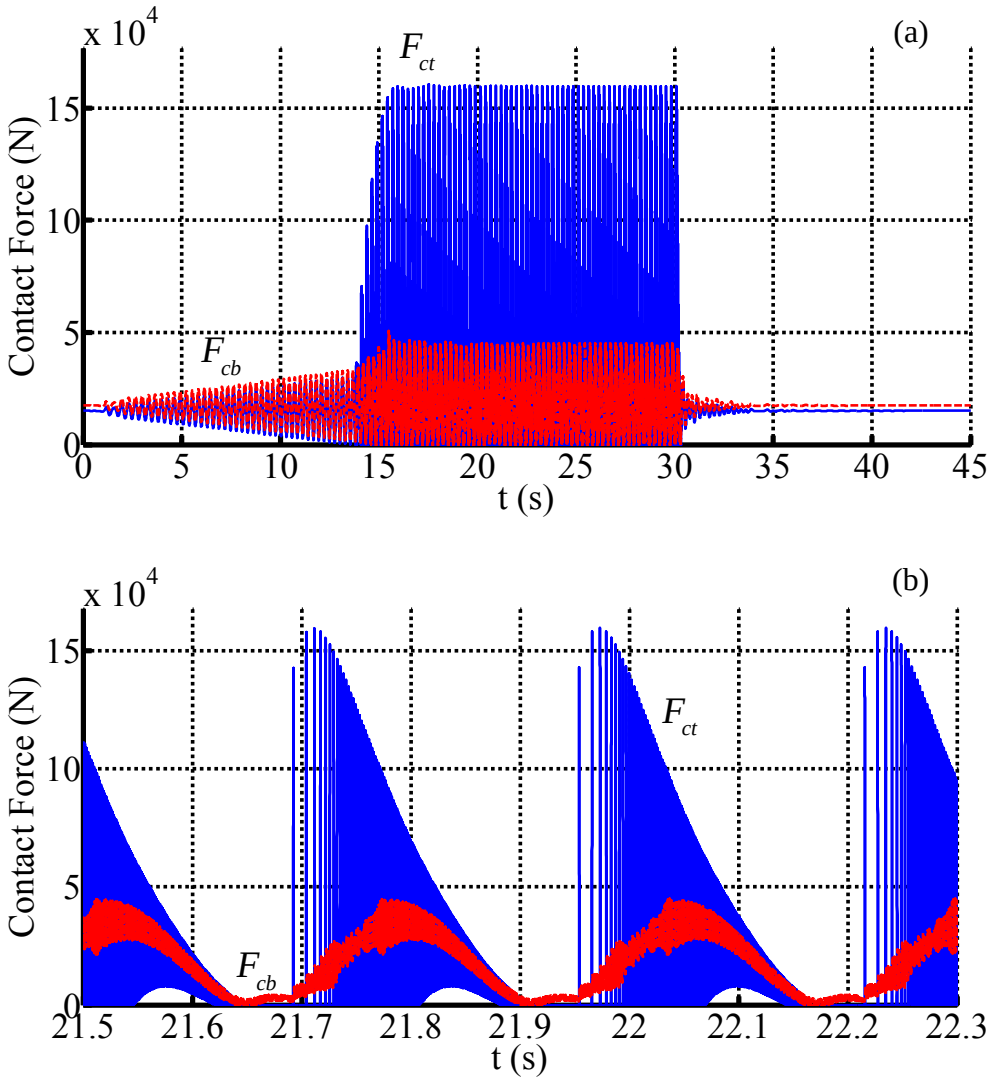

Fig. 8.32 Contact forces for Case 5

(a) Full view

(b) Close-up

Case 6

In order to further investigate the effect of impacts in the system behavior, a new scenario is considered where all parameters are exactly the same as in Case 5, with the only exception of A_f, which is now set to

$$A_f = 80\text{Nm}. \tag{8.58}$$

Therefore, the torque-speed curves do not change with respect to the previous case, except for the final the motor characteristic, which is now located further upwards (see Fig. 8.28 and Fig. 8.33). Clearly, the theoretical operating condition predicted by the intersection between $L_{mf}(\dot{\phi})$ and $\Gamma(\dot{\phi})$ –marked with a square in Fig. 8.33– is associated, in this case, with larger vibration amplitude and a greater level of compaction. Hence it is intuitive to expect that this increase in the driving torque will produce larger separations and stronger impacts between the contacting surfaces, due to the greater amplitude of oscillation.

The final stationary motion of the system predicted analytically in Fig. 8.33 is characterized by

$$\Omega_{0a} = 25.6\,\text{rad/s} \tag{8.59}$$

$$k_a = 1.14 \cdot 10^6\,\text{N/m} \rightarrow \gamma_a = 58.9\%, \tag{8.60}$$

On the other hand, the results of the numerical simulation are shown in Fig. 8.34-Fig. 8.37. As expected, larger separations between the slab and the piston, and also between the slab and the mould, can be observed in Fig. 8.34, Fig. 8.35, compared to Case 5. Accordingly, Fig. 8.37 exhibits larger peaks of the contact force during the period of impacts.

With the aim of comparing analytical and numerical results, the average rotor speed during the second stage of the motion is obtained from Fig. 8.36:

$$\Omega_{0s} = 23.8\,\text{rad/s}, \tag{8.61}$$

The level of compaction of the system during its stationary motion is also extracted from the numerical results, based on the stiffness exhibited by the nonlinear spring during the second stage of the simulation:

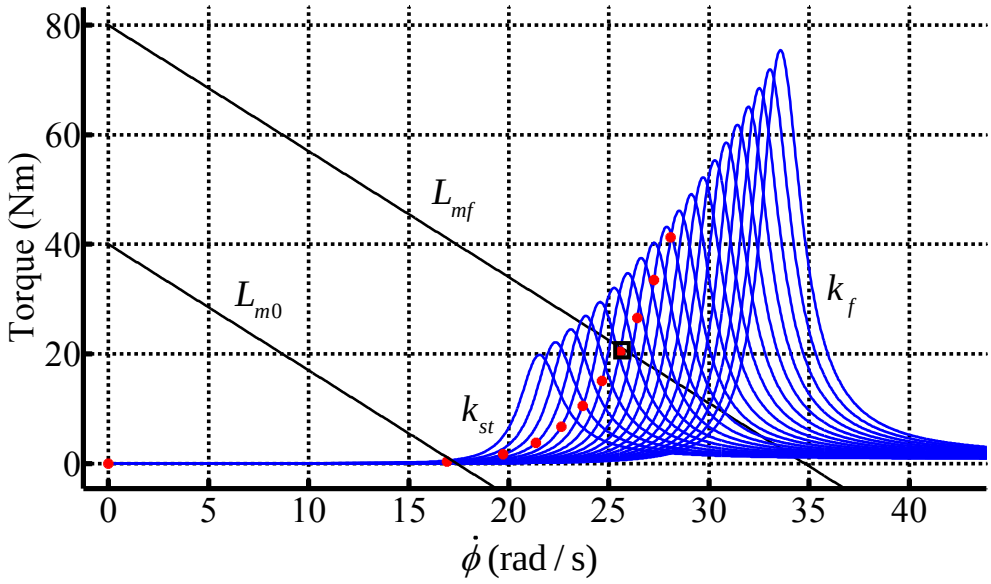

Fig. 8.33 Torque-speed curves for Case 6. The dots represent the stationary motions for a quasistatic compaction process.

$\gamma_s = 60.3\%.$ (8.62)

By comparing (8.61), (8.62) with (8.59), (8.60), a less precise accordance than in Case 5 is found. This suggests that the proposed analytical approach, while being valid when small separations exist between the contacting surfaces (Case 5), loses accuracy when the separations and impacts become more significant (Case 6). In spite of this, note that the analytical results are still reasonably close to the numerical ones in the present case. Thus, the torque-speed curves may still be useful for scenarios where severe impacts are produced, keeping in mind that the analytical predictions will not be as accurate as in a case of continuous contact.

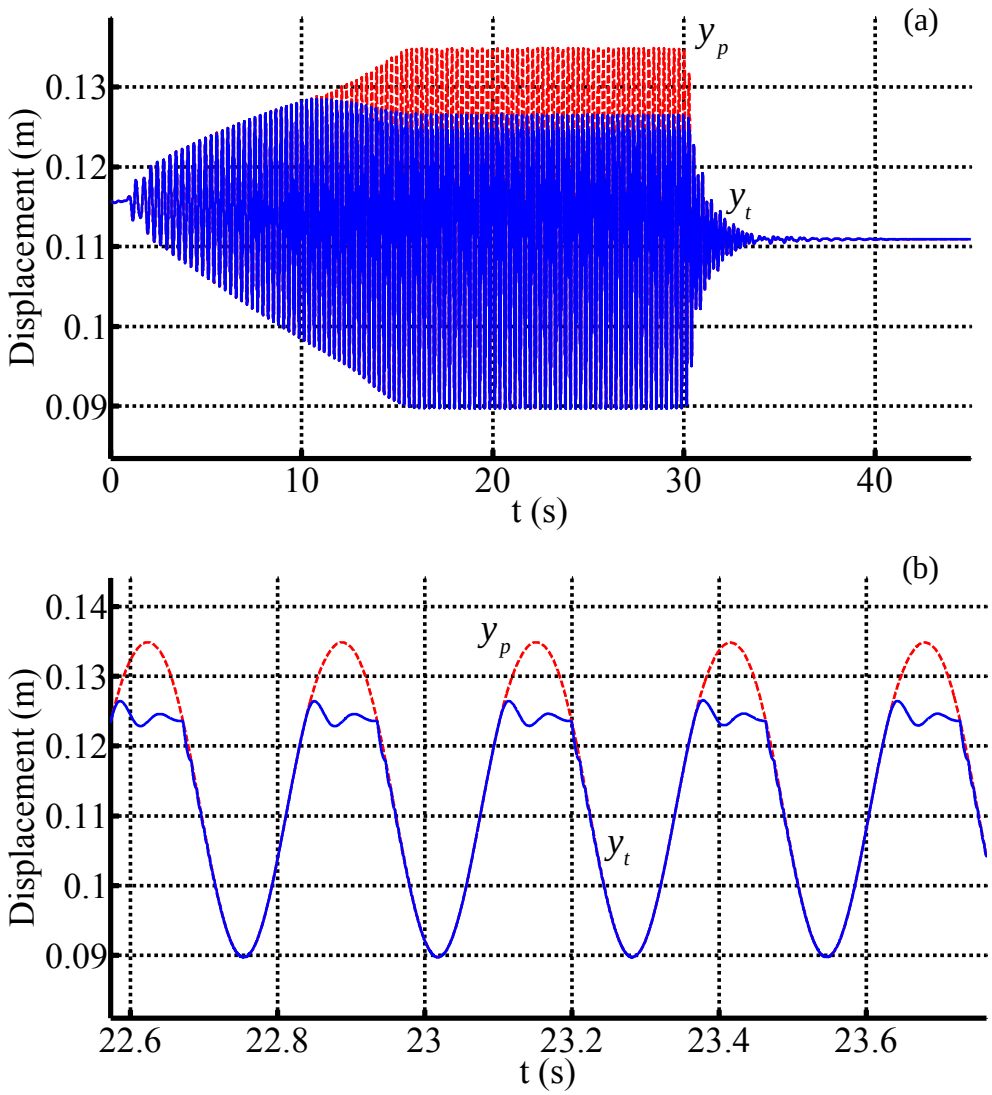

Fig. 8.34 Displacements of the piston and the top of the mixture for Case 6

(c) Full view

(d) Close-up

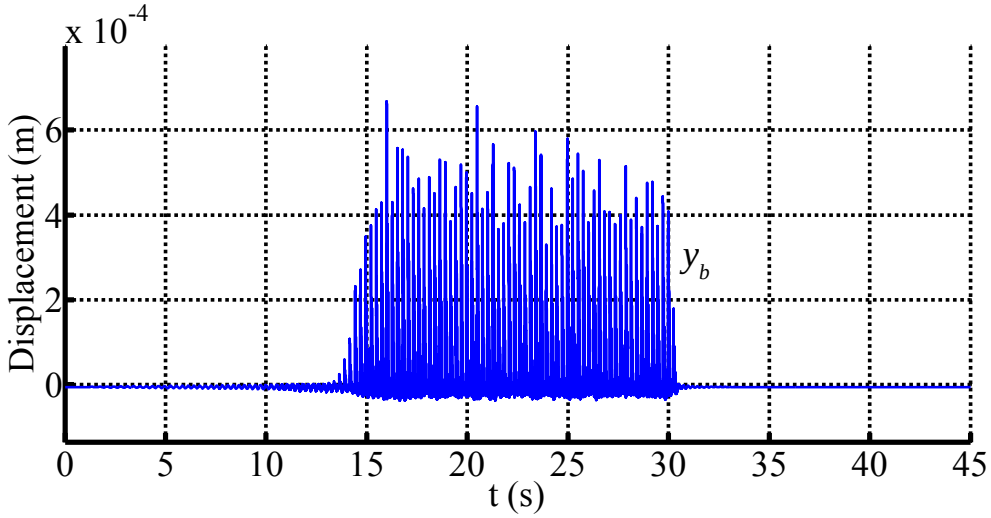

Fig. 8.35 Displacement of the bottom of the mixture for Case 6

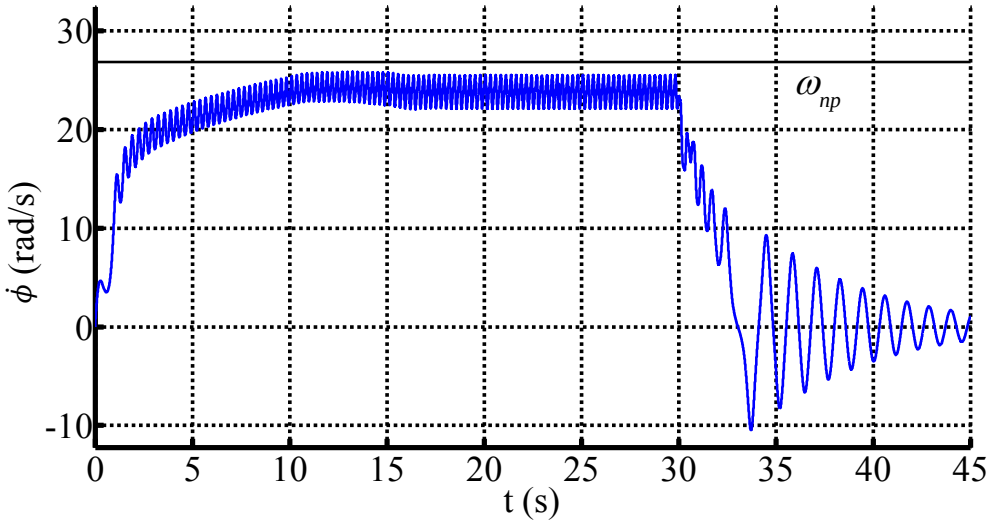

Fig. 8.36 Rotor speed for Case 6

It is also interesting to note that the numerical level of compaction (60.3%) turns out to be greater than the analytical (58.9%). This appears to be consistent, because the analytical procedure does not take into account the effect of impacts. Resorting again to physical intuition, it seems reasonable that the impacts between the piston

and the mixture are favourable to the compaction process, due to the high peaks of compressive forces generated.

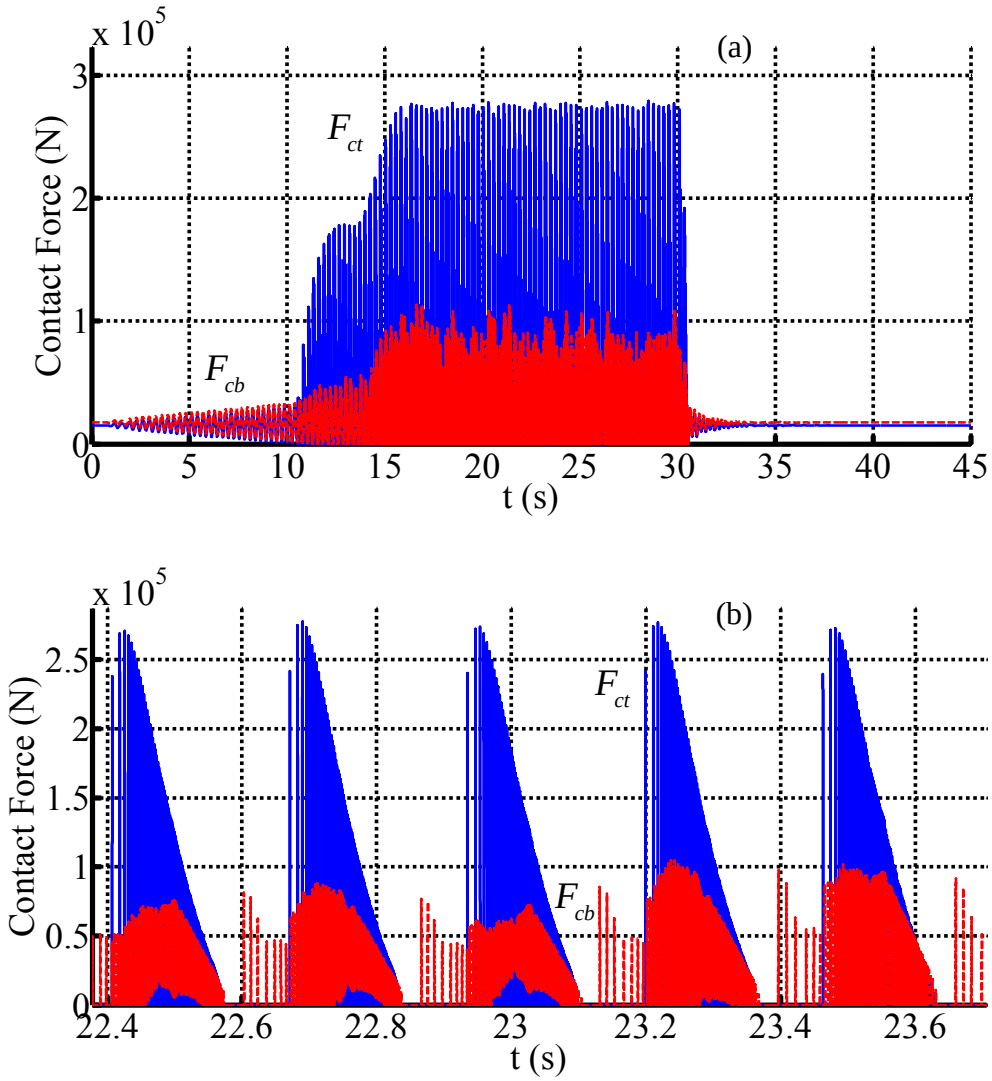

Fig. 8.37 Contact forces for Case 6

(c) Full view

(d) Close-up

Case 7

Finally, it is also illustrative to analyse the effect of the piston mass on the result of the process. To this end, the set of parameters (8.31) is maintained, except for the mass of the piston, which is doubled:

$$m_p = 3 \cdot 10^3 kg. \tag{8.63}$$

Note that, since the constitutive law of the nonlinear spring has not been modified, stiffnesses k_0 and k_f are the same as in Case 1. On the contrary, it is clear that the proposed modification will increase the static compaction due to the weight of the piston. Relations (8.12) and (8.13) yield

$$k_{st} = 1.01 \cdot 10^6 \,\mathrm{N/m} \Rightarrow \gamma_{st} = 50.9\%. \tag{8.64}$$

The torque-speed curves for the present scenario are depicted in Fig. 8.38 where, once again, it is observed that a complete compaction cannot be quasistatically achieved. These curves reveal the maximum compaction which can be obtained through a quasistatic process:

$$k_{max} = 1.19 \cdot 10^6 \,\mathrm{N/m} \Rightarrow \gamma_{max} = 61.4\% \tag{8.65}$$

After obtaining these analytical predictions a numerical simulation is conducted with the following parameters:

$$t_1 = 25\mathrm{s}, \qquad D = -1.5\mathrm{Nms}, \qquad \mathrm{A}_0 = 22\mathrm{Nm}, \qquad \mathrm{A}_f = 34\mathrm{Nm}, \tag{8.66}$$

with the corresponding motor curves depicted in Fig. 8.38. Observe that the final position of the motor curve is beyond the end point of curve $\Gamma(\dot{\phi})$. This means that, if the chosen t_1 is long enough, the expected level of compaction after the dynamic

process is γ_{max}, given in (8.65). The numerical results of the simulation are represented in Fig. 8.39 and Fig. 8.40.

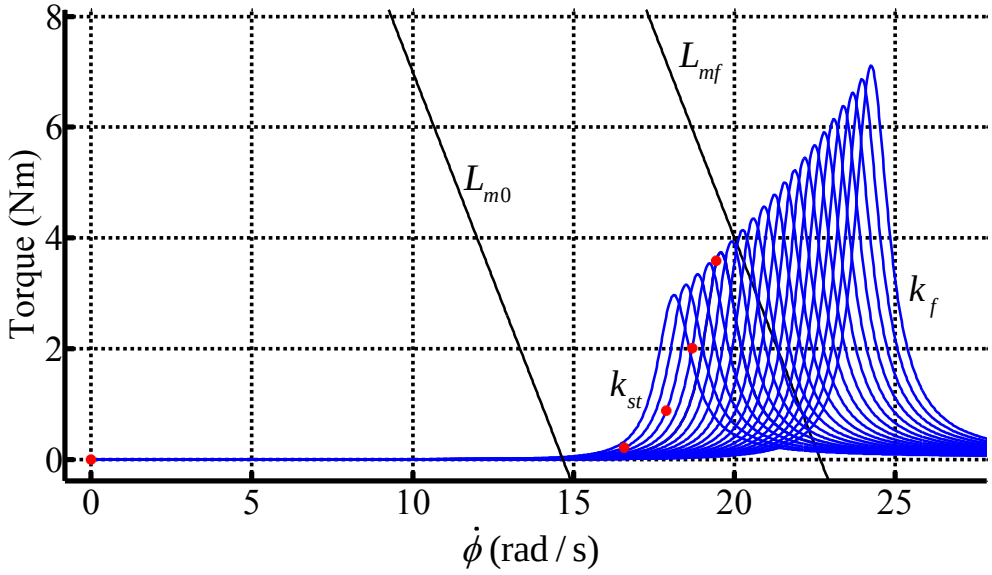

Fig. 8.38 Torque-speed curves for Case 7. The dots represent the stationary motions for a quasistatic compaction process.

It can be observed how the system follows the evolution described in Section 8.4: the vibration amplitude increases monotonically while the motor characteristic is slowly displaced upwards, until a jump phenomenon occurs, making the system reach a post-resonant state. No separations at any of the contacts were found in this case.

The final level of compaction achieved in the simulation is

$$\gamma_s = 61.2\%, \tag{8.67}$$

which is in good accordance with the analytical prediction (8.65).

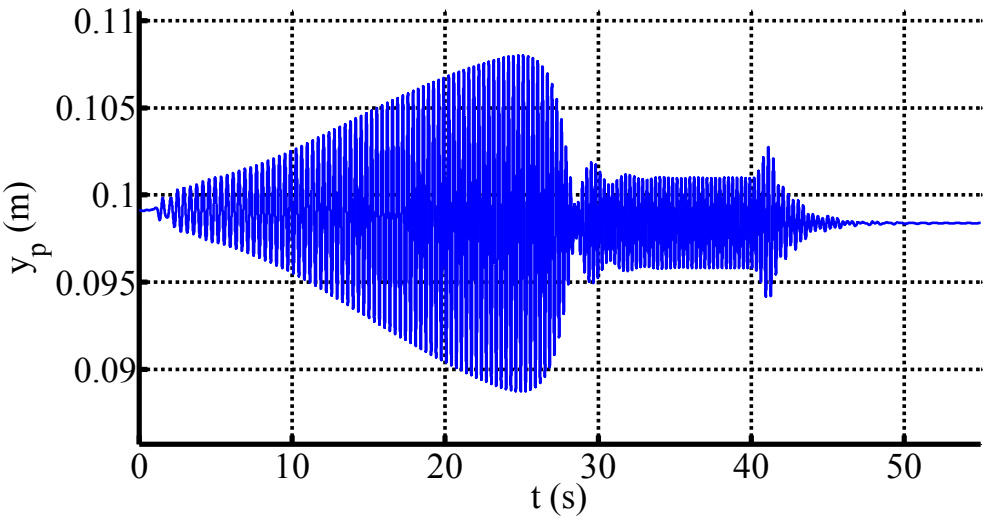

Fig. 8.39 Piston displacement for Case 7

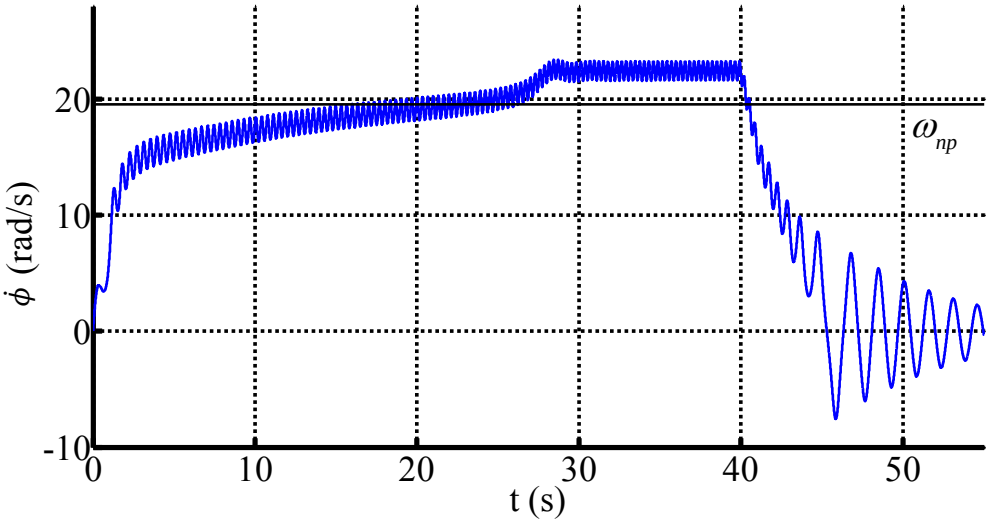

Fig. 8.40 Rotor speed for Case 7

In conclusion, the increase in the piston mass has produced a higher quality compaction. Note, however, that most of this compaction is due to the large weight of the piston, and not to the dynamic process. The results of all the conducted simulations are summarized in Table 1.

Table 1 Summary of results for the conducted simulations

Considered Scenario	**Static Compaction γ_{st}**	**Total Compaction γ_s**
Case 1	34.1%	46.5%
Case 2	34.1%	47.5%
Case 3	34.1%	47.4%
Case 4	34.1%	44.6%
Case 5	34.3%	54.1%
Case 6	34.3%	60.3%
Case 7	50.9%	61.2%

9 SUMMARY AND CONCLUSIONS

9.1 Summary

The present thesis is concerned with the nonlinear dynamics of vibrating systems excited by unbalanced motors. The main focus is the reciprocal (nonideal) interaction which in general exists between the dynamics of the exciter –the unbalanced motor– and that of the vibrating system. Two models were analytically and numerically studied. First, a 2DOF model of a general structure with a cubic nonlinearity, excited by a nonideal motor, was analysed in detail. The second model is a 4DOF simplified representation of the process of vibrocompaction of quartz agglomerates.

The first model was studied under two different assumptions: *large* and *small slope* of the motor characteristic. For the first scenario, a new analytical approach was developed, which combines two well-known perturbation techniques: the Averaging Method and the Singular Perturbation Theory. This scheme allows uncovering the system dynamics as composed of three consecutive stages of time. The first two ones occur in a short time scale and can be considered as a fast transient regime. During the third stage, the system dynamics was shown to be well represented by a reduced 2D system. A detailed analysis of this reduced system allowed obtaining its fixed points and their stability. An important outcome of this study was the existence of Hopf bifurcations making the stability region smaller than predicted by other approaches in the literature.

The Hopf bifurcations were analytically investigated and very simple conditions were derived to characterize them as subcritical and supercritical. Moreover, by using the Poincaré-Béndixson theorem, conditions were found under which all trajectories of the reduced system are attracted towards a limit cycle. This kind of motion in the reduced system corresponds to a quasiperiodic oscillation in the original one. The global bifurcations whereby the found limit cycles disappear were numerically analysed, finding homoclinic and saddle-node homoclinic bifurcations. All these results were validated by comparing numerical solutions of the original and reduced systems, which exhibited a remarkable accordance.

The case of *small slope* was also analytically studied in detail. Having found the existence of a resonance manifold in the phase space, the regions far (outer) and close (inner) to the resonance manifold were separately investigated through averaging techniques. Under certain conditions, the inner region contains two fixed points, whose stability was analysed. As an apparent limitation of the procedure, it was addressed that the time of attraction of one of the fixed points was much longer than the time of validity of the averaged system. Consequently, it is not obvious whether or not the stability of that fixed point in the averaged system is necessarily the same as in the original system. The main contribution of this part of the thesis consists in having solved the above difficulty: by using attraction arguments it was

shown that the stability properties of the inner averaged system also hold for the original system.

As in the case of large slope, numerical simulations were conducted in order to compare solutions of the original and averaged systems. A good agreement was also found in all the considered scenarios.

After the analyses of the cases of large and small slope, an alternative procedure was used to obtain the stationary motions of the system. The main advantage of this method lies in the fact that it allows representing the steady motions in a unique torque-speed plot for the whole frequency range, in contrast to previous approaches, where different graphs where needed for the near-resonant and non-resonant solutions. The use of a unique plot was especially useful for the analysis of the vibrocompaction process in the subsequent chapter.

The final part of the thesis considered a real industrial process, where a mixture of granulated quartz and polyester resin is compacted by using a piston with unbalanced electric motors. A 4-DOF model of the process was built (*full model*), including the nonideal coupling between the motor and the vibrating system, impacts and separation at two contacts (piston-mixture and mixture-mould) and a nonlinear constitutive law for the mixture which models the compaction itself. Although the model is not complex enough to give reliable quantitative results, it is a first step towards the construction of more sophisticated models which are able to predict the behaviour of actual compacting machines.

Based on the full model, a simpler 2-DOF model was built upon reasonable assumptions (*simplified model*), which turned out to be equal to the system studied in previous chapters. An analytical study of this simplified model revealed relevant information about the machine dynamics, thanks to the use of the torque-speed curves.

Several numerical simulations were conducted on the full model, with the aim of illustrating how the proposed model can be used to analyse the influence of

different parameters on the outcome of the vibrocompaction process. These simulations also provided a very significant accordance between numerical and analytical results.

9.2 Conclusions

The case of *Large Slope*

- The system exhibits three different behaviours at three consecutive stages of time. The first two stages occur on a short time interval and can be considered as a fast transient, followed by a much longer third stage.
- During the third stage of the motion, the original 4D system can be replaced by an approximate 2D system, much easier to analyse. This was validated by comparing numerical solutions of both systems.
- Conditions for the existence of a Hopf bifurcation on the right branch of the resonance curve have been found. This result is particularly significant, for it shows that the stability region of a stationary motion of the system can be smaller than predicted by usual theories. Thus, not taking the Hopf bifurcation into account may lead to unexpected instabilities in real applications.
- A very simple condition, with clear graphical interpretation, has been obtained to distinguish whether the Hopf bifurcation is subcritical or supercritical.
- Under certain known conditions, all system trajectories are attracted towards a limit cycle in the reduced system, corresponding to a quasistatic motion of the original system. This means that, irrespective of the initial conditions, the system tends to a quasiperiodic oscillation.
- The conducted numerical simulations suggest that the limit cycles, generated by Hopf bifurcations, are destroyed through homoclinic or saddle-node homoclinic bifurcations.

The case of *Small Slope*

- The time of validity for solutions of the inner averaged system close its stable fixed point has been analytically investigated, by using attraction arguments. It was found that these solutions are actually valid for all time, which implies that the stability properties of the equilibrium for the inner averaged system are also valid for the original system.

The vibrocompaction model

- The proposed model can be used to investigate how different parameters of the industrial process influence the final result of the compaction.
- Under a quasistatic control of the motor, the final level of compaction achieved can be analytically predicted by using the torque-speed curves, with no need of numerically solving the differential equations of the full model.

9.3 Original Contributions

The case of *Large Slope*

- A novel analytical approach to the problem, which combines an averaging procedure with the SPT, has been proposed. It is worth stressing that, although both the SPT and the Averaging Method are actually classical in nonlinear dynamics, they had not been used together before in the context of nonideal excitations. Thanks to this novel combination of perturbation techniques, the original 4D system is transformed into a reduced 2D system, much easier to analyse.
- The conditions for stability of equilibria of the reduced system have been analytically derived. Transcritical and Hopf bifurcations have been found. The Hopf bifurcation is particularly relevant, for it gives rise to a smaller stable region than predicted by conventional theories. Consequently, not

taking it into account may be perilous for real applications, since unexpected instabilities could occur.

- The Hopf bifurcations have been analytically investigated, in order to characterize them as subcritical or supercritical. A very simple criterion, with clear graphical interpretation, was obtained to distinguish both types of bifurcations.
- The Poincaré-Bendixson Theorem has been used to find conditions under which all trajectories in the averaged system are attracted towards a periodic orbit, corresponding to a quasiperiodic solution of the original system.
- The global bifurcations destroying the stable and unstable limit cycles have been numerically investigated. These simulations suggest that unstable LCOs are destroyed through homoclinic bifurcations, while stable LCOs can be destroyed either through homoclinic bifurcations or through saddle-node homoclinic bifurcations.

The case of *Small Slope*

- By using attraction arguments, it has been shown that solutions of the inner averaged system, near its stable fixed point, are actually valid for all time. This implies that the referred equilibrium is also asymptotically stable in the original system, which in turn gives a solid base for the possibility of resonant capture in the mechanical system of interest.

The Vibrocompaction Model

- As far as the author knows, there are not available mathematical models for the vibrocompaction of quartz agglomerates. Then, the proposed model can be considered as an original contribution which will hopefully serve as a base on which more complex models can be developed.
- An analytical procedure has been developed which allows predicting the operating point and the level of compaction achieved when the motor is quasistatically controlled.

9.4 Directions for Future Work

Since all the investigations presented in this thesis are analytical and numerical, it is clear that some experimental validation is needed. In particular, it would be especially relevant to find experimentally the quasiperiodic oscillations found in the case of large slope (see Fig. 4.10 and Fig. 4.11). This kind of behaviour had not been reported before in the context of nonideal systems and, therefore, it would be significant to find experimental evidence of its existence.

As is clear from Section 3.5, a softening nonlinearity in the structure is needed to have a supercritical Hopf bifurcation and, therefore, a stable limit cycle –see equation (3.83)–. Some experiments are already in course in the Department of Mechanical Engineering of Seville, where an unbalanced motor is mounted on a simply supported beam, one of whose ends is free to move in the axial direction. It is known that such a configuration of a beam gives rise to a cubic nonlinearity of the softening type for moderately large vibration amplitudes (Luongo et al., 1986), thereby constituting an appropriate setup to find the desired quasiperiodic motions.

Clearly, there is large space for future work concerning the vibrocompaction model. First, it would be desirable to verify, with the aid of experimental tests, whether or not the proposed nonlinear constitutive law for the mixture is able to capture the behaviour of the actual material. Besides other phenomenological models which may be developed and tested, some more fundamental research on the behaviour of three-phase mixtures would be worthwhile, in order to mathematically describe how bubbles move through the mixture during compaction.

In order to have a reliable model of the process, some aspects of the real process which were not modelled within this thesis may need to be considered, such as the vacuum system, the flexibility of the elastomer between the machine foundation and the ground or the flexibility of the piston itself.

APPENDIX

This section provides the expressions of parameters f_{ij} and g_{ij} in equation (3.80). These are simply the coefficients of the nonlinear terms of system (3.79), which result when system (3.73) is transformed according to change of variables (3.76).

$$f_{20} = -\frac{3\rho aR}{4c_2}(3c_1^2 + c_2^2) - 2c_1\left(\frac{2\xi}{aR} + \frac{3}{4}\rho a^2\right) \tag{A.1}$$

$$f_{02} = -\frac{9\rho aR\omega_0^2}{4c_2} \tag{A.2}$$

$$f_{11} = -\frac{3}{4}\rho\omega_0 a\left(a + 3R\frac{c_1}{c_2}\right) - \frac{2\xi\omega_0}{aR} \tag{A.3}$$

$$f_{30} = \frac{9\rho c_1}{4c_2}(c_1^2 + c_2^2) \tag{A.4}$$

$$f_{03} = \frac{9\rho\omega_0^3}{4c_2} \tag{A.5}$$

$$f_{21} = \frac{3\rho\omega_0}{4c_2}(3c_1^2 + c_2^2) \tag{A.6}$$

$$f_{12} = \frac{9c_1\rho\omega_0^2}{4c_2} \tag{A.7}$$

$$g_{20} = \frac{(c_1^2 + c_2^2)}{\omega_0}\left[\frac{9\rho a}{4}\left(R\frac{c_1}{c_2} + a\right) + \frac{4\xi}{aR}\right] \tag{A.8}$$

$$g_{02} = \frac{3\rho\omega_0 a}{4}\left(a + 3R\frac{c_1}{c_2}\right) \tag{A.9}$$

$$g_{11} = \frac{3}{2}\rho a^2 c_1 + \frac{3\rho aR}{4c_2}(3c_1^2 + c_2^2) + \frac{2\xi c_1}{aR} \tag{A.10}$$

$$g_{30} = -\frac{9\rho}{4\omega_0 c_2}(c_1^2 + c_2^2)^2 \tag{A.11}$$

$$g_{03} = -\frac{9c_1\rho\omega_0^2}{4c_2} \tag{A.12}$$

$$g_{21} = -\frac{9c_1\rho}{4c_2}(c_1^2 + c_2^2) \tag{A.13}$$

$$g_{12} = -\frac{3\rho\omega_0}{4c_2}(3c_1^2 + c_2^2), \tag{A.14}$$

where a_{eq} and R_{eq} have been shortly written as a and R, respectively.

REFERENCES

Alonso, E. E., Gens, A., & Josa, A. (1990). A constitutive model for partially saturated soils. *Géotechnique*, *40*(3), 405–430. http://doi.org/10.1680/geot.1990.40.3.405

Belato, D., Weber, H. I., Balthazar, J. M., & Mook, D. T. (2001). Chaotic vibrations of a nonideal electro-mechanical system. *International Journal of Solids and Structures*, *38*(10–13), 1699–1706. http://doi.org/10.1016/S0020-7683(00)00130-X

Bhasin, S., Dupree, K., Patre, P. M., & Dixon, W. E. (2008). Neural Network Control of a Robot Interacting With an Uncertain Hunt-Crossley Viscoelastic Environment. In *ASME 2008 Dynamic Systems and Control Conference, Parts A and B* (pp. 875–882). ASME. http://doi.org/10.1115/DSCC2008-2222

Blekhman, I. I. (2000). *Vibrational Mechanics-Nonlinear Dynamic Effects, General Approach*. (W. Scientific, Ed.). Singapore.

Bolla, M. R., Balthazar, J. M., Felix, J. L. P., Mook, D. T. (2007). On an approximate analytical solution to a nonlinear vibrating problem , excited by a nonideal motor. *Nonlinear Dynamics*, 841–847. http://doi.org/10.1007/s11071-007-9232-3

Boyaci, A., Lu, D., & Schweizer, B. (2015). Stability and bifurcation phenomena of Laval/Jeffcott rotors in semi-floating ring bearings. *Nonlinear Dynamics*, *79*(2), 1535–1561. http://doi.org/10.1007/s11071-014-1759-5

Brennan, M. J., Kovacic, I., Carrella, A., & Waters, T. P. (2008). On the jump-up and jump-down frequencies of the Duffing oscillator. *Journal of Sound and Vibration*, *318*(4–5), 1250–1261. http://doi.org/10.1016/j.jsv.2008.04.032

Dimentberg, M. F., Mcgovern, L., Norton, R. L., Chapdelaine, J., & Harrison, R. (1997). Dynamics of an Unbalanced Shaft Interacting with a Limited Power Supply. *Nonlinear Dynamics*, 171–187. http://doi.org/10.1023/a:1008205012232

Eckhaus, W. (1975). New approach to the asymptotic theory of nonlinear oscillations and wave-propagation. *Journal of Mathematical Analysis and Applications*, *49*(3), 575–611. http://doi.org/10.1016/0022-247X(75)90200-0

Eckhaus, W. (1979). *Asymptotic Analysis of Singular Perturbations*. Amsterdam: North- Holland Publ. Co.

El-Badawy, A. A. (2007). Behavioral Investigation of a Nonlinear Nonideal Vibrating System. *Journal of Vibration and Control*, *13*(2), 203–217. http://doi.org/10.1177/1077546307073674

Farahani, K., Mofid, M., & Vafai, A. (2000). A solution method for general contact–impact problems. *Computer Methods in Applied Mechanics and Engineering*, *187*(1–2), 69–77. http://doi.org/10.1016/S0045-7825(99)00110-3

Fidlin, A. (2006). *Nonlinear Oscillations in Mechanical Engineering*. Berlin, Heidelberg: Springer–Verlag.

Gilardi, G., & Sharf, I. (2002). Literature survey of contact dynamics modelling. *Mechanism and Machine Theory*, *37*(10), 1213–1239. http://doi.org/10.1016/S0094-114X(02)00045-9

Guckenheimer, J., & Holmes, P. (1983). *Nonlinear Oscillations, Dynamical Systems, and Bifurcations of Vector Fields* (Vol. 42). New York, NY: Springer New York. http://doi.org/10.1007/978-1-4612-1140-2

Habib, G., & Kerschen, G. (2015). Suppression of limit cycle oscillations using the nonlinear tuned vibration absorber. *Proc. R. Soc.*

Haddadi, A., & Hashtrudi-Zaad, K. (2008). A new method for online parameter estimation of Hunt-Crossley environment dynamic models. In *2008 IEEE/RSJ International Conference on Intelligent Robots and Systems* (pp. 981–986). IEEE. http://doi.org/10.1109/IROS.2008.4650575

Holtz, J., Paper, I., & Holtz, J. (2002). Sensorless control of induction motor drives. *Proceedings of the IEEE*, *90*(8), 1359–1394. http://doi.org/10.1109/JPROC.2002.800726

Hunt, K. H., & Crossley, F. R. E. (1975). Coefficient of Restitution Interpreted as Damping in Vibroimpact. *Journal of Applied Mechanics*, *42*(2), 440. http://doi.org/10.1115/1.3423596

Hunter, J. K. (2004). Asymptotic Analysis and Singular Perturbation Theory. *Department of Mathematics, University of California at Davis*.

Kononenko, V. O. (1969). *Vibrating Systems with a limited power supply*. London: Illife.

Krasnopolskaya, T. S., & Shvets, A. Y. (1993). Chaos in vibrating systems with a limited power-supply. *Chaos (Woodbury, N.Y.)*, *3*(3), 387–395. http://doi.org/10.1063/1.165946

Kuznetsov, Y. A. (1998). *Elements of Applied Bifurcation Theory, Second Edition*.

(Springer, Ed.). New York.

Lesne, A. (2006). Multi-scale Approaches. *Laboratoire de Physique de La Matière Condensée, Université Pierre et Marie Curie*.

Luongo, A., Rega, G., & Vestroni, F. (1986). On nonlinear dynamics of planar shear indeformable beams. *Journal of Applied Mechanics, 53*(3), 619–624.

Ma, O. (1995). Contact dynamics modelling for the simulation of the Space Station manipulators handling payloads. In *Proceedings of 1995 IEEE International Conference on Robotics and Automation* (Vol. 2, pp. 1252–1258). IEEE. http://doi.org/10.1109/ROBOT.1995.525453

Mason, M. T., & Wang, Y. (1988). On the inconsistency of rigid-body frictional planar mechanics. *IEEE International Conference on Robotics and Automation*, *1*, 524–528.

Mettler, E. (1962). *Handbook of Engineering Mechanics*. New York: McGraw-Hill.

Nayfeh, A. H., & Mook, D. T. (1995). *Nonlinear Oscillations*. John Wiley and Sons.

Newton, I. (1686). *Philosophiae Naturalis Principia Mathematica*. London: S. Pepsy, Reg. Soc.

Pechenev, A. V. (1992). The Averaging of Systems with a Hierarchy of Phase Rotation Speeds. *Journal of Applied Mathematics and Mechanics*, *56*(1), 20–24.

Perko, L. (2001). *Differential Equations and Dynamical Systems (Third Edition)*. New York: Springer.

Pietruszczak, S., & Pande, G. N. (1996). Constitutive Relations for Partially Saturated Soils Containing Gas Inclusions. *Journal of Geotechnical Engineering*, *122*(1), 50–59. http://doi.org/10.1061/(ASCE)0733-9410(1996)122:1(50)

Quinn, D., Rand, R., & Bridge, J. (1995). The dynamics of resonant capture. *Nonlinear Dynamics*, *8*(1), 1–20. http://doi.org/10.1007/BF00045004

Rand, R. H., Kinsey., R. J., & Mingori, D. L. (1992). Dynamics of spinup through resonance. *International Journal of Non-Linear Mechanics*, *27*(3), 489–502. http://doi.org/10.1016/0020-7462(92)90015-Y

Sanchez-Palencia, E. (1975). Méthode de centrage et comportement des trajectoires dans l'espace des phases. *Ser. A Compt. Rend. Acad. Sci.*, *280*, 105–107.

Sanders, J. A., Verhulst, F. & Murdock, J. (2007). *Averaging Methods in Nonlinear Dynamical Systems*. New York: Springer.

Shabana, A. A. (1996). *Theory of vibration (An Introduction)*. *Springer*. http://doi.org/10.1016/0378-3804(84)90129-3

Sommerfeld, A. (1904). Naturwissenchftliche Ergebnisse der Neuren Technischen Mechanik. *Verein Deutscher Ingenieur Zeitscchrift*, *18*, 631–636. http://doi.org/10.1109/COC.2000.873973

Stickel, J. J., & Powell, R. L. (2005). Fluid Mechanics and Rheology of Dense Suspensions. *Annual Review of Fluid Mechanics*, *37*(1), 129–149. http://doi.org/10.1146/annurev.fluid.36.050802.122132

Strogatz, S. (1994). *Nonlinear dynamics & chaos*.

Stronge, W. J. (1991). Unraveling paradoxical theories for rigid body collisions. *Journal of Applied Mechanics*, *58*, 1049–1055.

Thomsen, J. J. (2003). *Vibrations and Stability*. (S. Verlag, Ed.). Berlin, Heidelberg, New York.

Thomson, W. T. (1996). *Theory of Vibration with Applications*. *CRC Press*. http://doi.org/10.1121/1.1901874

Verhulst, F., & Bakri, T. (2006). The Dynamics of Slow Manifolds. *Journal of the*

Indonesian Mathematical Society, 1–16.

Vukobratović, M. K., & Potkonjak, V. (1999). Dynamics of contact tasks in robotics. Part I: general model of robot interacting with environment. *Mechanism and Machine Theory*, *34*(6), 923–942. http://doi.org/10.1016/S0094-114X(97)00091-8

Xu, M., & Marangoni, R. D. (1994). Vibration Analysis of a Motor-Flexible Coupling-Rotor System subject to Misalignment and Unbalance, Part I: Theoretical Model and Analysis. *Journal of Sound and Vibration*, *176*(5), 663–679.

Yang, J., Gao, Y., Liu, Z., Zhao, C., Kang, T., Gu, L., & Xu, B. (2016). A method for modeling and analyzing the rotor dynamics of a locomotive turbocharger. *Nonlinear Dynamics*, *84*(1), 287–293. http://doi.org/10.1007/s11071-015-2497-z